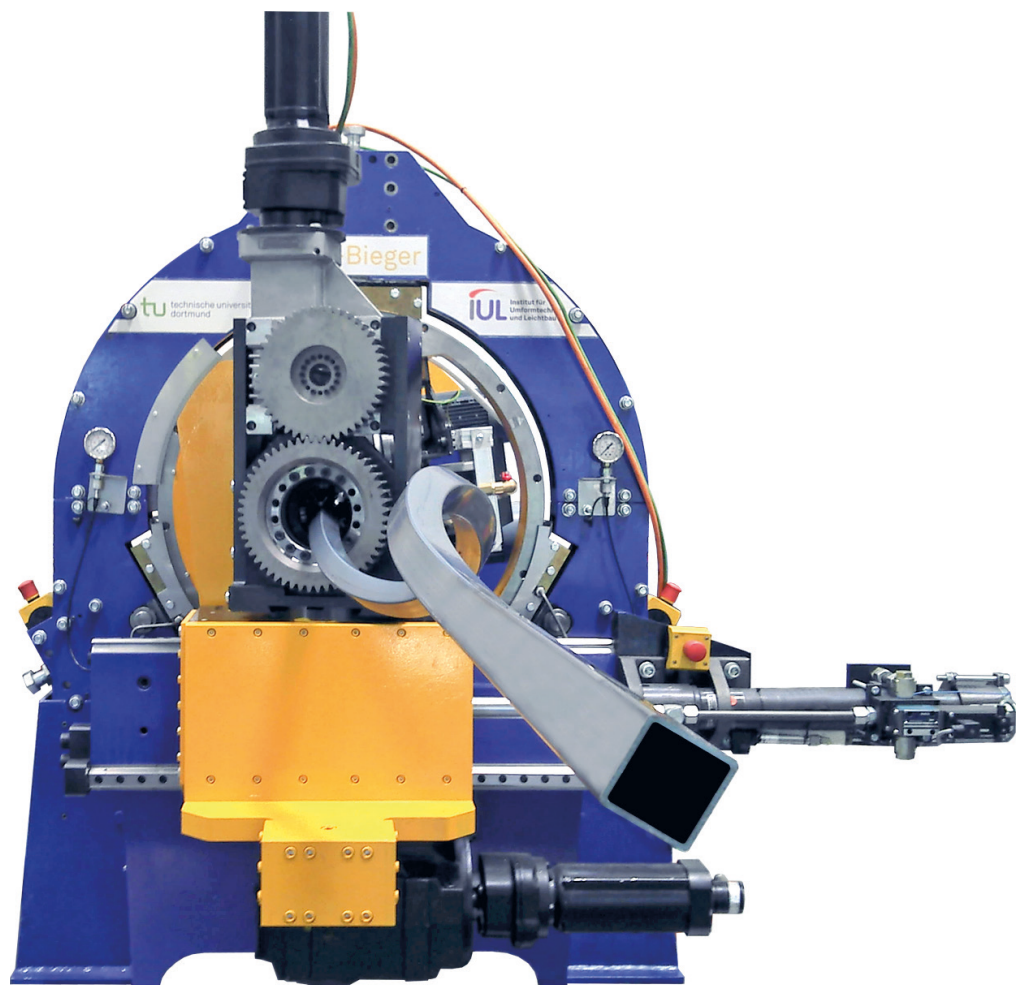


Daniel Staupendahl

## 3D Profile Bending with Five Controlled Degrees of Freedom





# **3D Profile Bending with Five Controlled Degrees of Freedom**

Zur Erlangung des akademischen Grades eines

Dr.-Ing.

von der Fakultät Maschinenbau  
der Technischen Universität Dortmund  
genehmigte Dissertation

Dipl.-Ing. Daniel Staupendahl

aus

Dortmund

Dortmund, 2020

Vorsitzender der Prüfungskommission: Prof. Dr.-Ing. Dipl.-Wirt.Ing Wolfgang Tillmann  
Berichter: Prof. Dr.-Ing. Dr.-Ing. E.h. A. Erman Tekkaya  
Mitberichter: Prof. Dr.-Ing. Bernd Engel  
Priv.-Doz. Dr.-Ing. Jobst Bickendorf  
Tag der mündlichen Prüfung: 4. Dezember 2020

Dortmunder Umformtechnik

Band 113

**Daniel Staupendahl**

**3D Profile Bending with Five Controlled Degrees  
of Freedom**

D 290 (Diss. Technische Universität Dortmund)

Shaker Verlag  
Düren 2021

**Bibliographic information published by the Deutsche Nationalbibliothek**

The Deutsche Nationalbibliothek lists this publication in the Deutsche Nationalbibliografie; detailed bibliographic data are available in the Internet at <http://dnb.d-nb.de>.

Zugl.: Dortmund, Technische Univ., Diss., 2020

Copyright Shaker Verlag 2021

All rights reserved. No part of this publication may be reproduced, stored in a retrieval system, or transmitted, in any form or by any means, electronic, mechanical, photocopying, recording or otherwise, without the prior permission of the publishers.

Printed in Germany.

ISBN 978-3-8440-8006-3

ISSN 1619-6317

Shaker Verlag GmbH • Am Langen Graben 15a • 52353 Düren

Phone: 0049/2421/99011-0 • Telefax: 0049/2421/99011-9

Internet: [www.shaker.de](http://www.shaker.de) • e-mail: [info@shaker.de](mailto:info@shaker.de)

For Katrin, Luisa, and Marie





## Acknowledgement

This dissertation is based on research that I performed during my time as a research assistant at the Institute of Forming Technology and Lightweight Components (IUL) of TU Dortmund University. During this time, I had the chance to work on and supervise many different research topics, from tube and profile bending to sheet metal forming, material characterization, and simulation, both in third-party funded projects as well as in collaborative projects with industrial partners. This present thesis represents the quintessence that I was able to extract out of all of this work.

First of all, I would like to thank Prof. Dr.-Ing. Dr.-Ing. E.h. A. Erman Tekkaya for giving me the opportunity to work at the IUL and his continuous support and belief in my professional abilities: from my first steps as a researcher over my time as manager of the Research Center of Industrial Metal Processing (ReCIMP) to my time as department head of project planning.

Next, I would like to thank Prof. Dr.-Ing. Matthias Hermes for actually introducing me to the IUL in the first place. During his time as a researcher at the IUL and my studies of mechanical engineering back in 2007 he hired me as his student assistant and sprouted the initial idea of staying at the institute for performing a dissertation; which I then eventually did, starting my career in the department of bending technology under his supervision as department head. His outstanding creativity and doer-mentality were a great inspiration and generated a fruitful work environment.

Special thanks goes to Prof. Dr. Peter Haupt for the enlightening discussions about the topics of space curves and stress superposition. He supported me in my understanding of fundamental mathematical and mechanical principles, which laid the groundwork of my analytical approaches. Here, I would also like to name my former colleague Dr.-Ing. Christoph Becker, with whom I share lots research experience at the IUL and had many constructive discussions on the topic of bending and plasticity. A great thank you also to my colleague Joshua Grodotzki who crosschecked my mathematical formulations and to my father Andreas Knobloch who proofread my text.

I wish to express my sincere gratitude to all of my student assistants that supported my research at the IUL: Jan Jaeger, Juri Martschin, Thorben Panusch, Esmaeil Nazari, Fabian Bader, Abootorab Baqerzadeh Chehreh, Sebastian Thiery, and Tim Jeschke. Here, I would like to especially thank Anna Komodromos, Jannik Grote, and Bagrat Samsonyan for their active support in the management of the ReCIMP.

Then, I would like to thank all of the former students that I supervised and greatly influenced the direction of my thesis: Jan Kersting, Carsten Westermann, Frank Schyma, Aydogan Zeyd Kaya, Daniel Schulz, Sascha Schwienke, Vignesh Selvanatarajan, Vijayarathy Anbazhagan, Christian Löbbe, Eva König, Henning Ködel, Matthias Keite,

Constantin Wissel, Benjamin Hoppe, Tobias Nitze, Bastian Janis Flick, Anastasia Bobretsova, and Siddharth Upadhyia.

A fist bump to my coffee group: Dr.-Ing. Goran Grzancic, Dr.-Ing. Peter Sieczkarek, Dr.-Ing. Stefan Ossenkemper, Dr.-Ing. Sebastian Wernicke, Lennart Tebaay, and my office-mate Alessandro Selvaggio. Thank you for all of our off-topic discussions that were definitely needed in our otherwise highly scientific workday. Moreover, without all of this coffee I do not know how I could have stayed awake in these last years of finalizing my work.

I especially and gratefully thank my parents Petra Staupendahl and Andreas Knobloch and my sister Dr. Alexandra Staupendahl for their continuous support, guidance, and love throughout all my life.

Finally and most importantly, I thank my wife Katrin and my daughters Luisa and Marie for their unconditional love, support, and especially their infinite patience. Without their trust and encouragement, this work would not have been possible.

Dortmund, December 2020

Daniel Staupendahl

## **Abstract**

In the recent decades, several processes for kinematic bending of tubes and profiles to three-dimensional (3D) contours have been developed. Although these processes offer the potential to cope with current demands for natural aesthetic design and high flexibility, they are not yet widely used in the industry. One reason has been, until now, the lack of fundamental knowledge about the forming process itself – specifically the forces and torques acting on the profile during 3D bending and the resulting stresses and strains in the cross-section.

In order to build up comprehensive process understanding, first, a general geometric description of 3D profile shapes is given. Using this geometric description, fundamental 3D-bending kinematics are derived. It is found that three controlled degrees of freedom (cDOF) are necessary to produce a 3D bending line – here, the rotation of the cross-section cannot be controlled – while at least four cDOFs are needed in order to produce profile shapes with a 3D bending line and a specified rotation, or twist, of the cross-section. Any additional cDOFs are not necessarily needed but might extend the process limits of a specific bending process. Using this knowledge, the 3-cDOF TSS bending process is extended by two additional actuators and torque measurement equipment. In order to time-efficiently analyze 3D profile shapes a new kind of 3D contour measurement device is developed and set up. To allow a thorough investigation of 3D bending with the least amount of abstraction of the material data, cold-drawn and heat-treated steel profiles are used, which can be regarded as isotropic. In addition to simple tensile tests for the generation of flow curves, cyclic tensile tests are used to measure the apparent Young's modulus degradation. In order to analyze the elastic behavior of the profile during 3D bending, a curved beam model is set up. The model can be used to represent a beam held by up to three roller/hinged supports, a single full-moment support, or a combination of a single hinged support and a single full-moment support. The model allows the accurate calculation of profile deflection as well as the calculation of the reaction forces and moments caused by an applied bending force and torque. Through thorough analyses of the stresses and strains in a profile segment during simultaneous application of a bending moment and a torque it is shown that a stress state with uniaxial stress and additional shear stress suffices to accurately model real-life profile behavior. An interesting observation is the linear decrease of shear strains from the intrados and extrados to the neutral axis of the profile.

The geometric relation of profile shape and bending kinematics is finally used together with the elastic and plastic analyses to set up a comprehensive process model, which can accurately simulate the profile behavior during 3D-profile bending and can be used to generate springback compensated NC-data for bending processes with 3-6 cDOFs.



## Publications

The following articles have been published with permission of the chairman of the doctoral committee prior to the publication of this dissertation:

- Staupendahl, D., Becker, C., Hermes, M., Tekkaya, A.E., Kleiner, M., 2011. New methods for manufacturing 3D-bent lightweight structures. In: Wieland, H.J., TEMA Technologie Marketing AG (Eds.), SCT 2011. 3<sup>rd</sup> Intern. Conf. on Steels in Cars and Trucks, Future Trends in Steel Development, Processing Technologies and Applications, Verlag Stahleisen, Düsseldorf, pp. 120-129.
- Staupendahl, D., Becker, C., Hermes, M., Tekkaya, A.E., Hudovernik, M., Quintana, G., Cavallini, B., Esteve Oró, F., Tassan, M., Servoli, G., Di Rosa, S., Tolazzi, M., Sulaiman, H., Salomon, R., 2014a. Flexible and cost-effective innovative manufacturing of complex 3D-bent tubes and profiles made of high-strength steels for automotive lightweight structures (ProTuBend). Luxembourg, Publication Office of the European Union.
- Staupendahl, D., Löbbe, C., Becker, C., Tekkaya, A.E., 2014b. Process Combinations for the Production of Load-Optimized Structural Components. In: Wieland, H.J., Brockmann, S., TEMA Technologie Marketing AG (Eds.), SCT 2014. 4<sup>th</sup> Intern. Conf. on Steels in Cars and Trucks, Future Trends in steel development, processing technologies and applications, Verlag Stahleisen, Düsseldorf, pp. 638-645.
- Staupendahl, D., Becker, C., Tekkaya, A.E., 2015. The impact of torsion on the bending curve during 3D bending of thin-walled tubes – a case study on forming helices. Key Eng. Mater., 651-653, pp. 1595-1601.
- Staupendahl, D., Chatti, S., Tekkaya, A.E. 2016. Closed-loop control concept for kinematic 3D-profile bending. In: AIP Conference Proceedings, 1769, 150002.
- Staupendahl, D., Tekkaya, A.E., 2017a. Inline-measurement of complex profile contours for the generation of process parameters used in 3D-bending, In: Proceedings of the SCT 2017 – 5<sup>th</sup> Intern. Conf. on Steels in Cars and Trucks, Future Trends in steel development, processing technologies and applications, Noordwijkerhout/Amsterdam, The Netherlands.
- Staupendahl, D., Tekkaya, A.E., 2017b. The reciprocal effects of bending and torsion on springback during 3D bending of profiles. Procedia Eng., 207, 2322-2327.
- Staupendahl, D., Schultz, D., Tekkaya, A.E., 2018a. Device for Tactile Detection and Analysis of the Geometry of Bent Profiles or Tubes. European patent EP 3 315 221 B1, priority date: 31.10.2016.

Staupendahl, D., Tekkaya, A.E., 2018b. Mechanics of the reciprocal effects of bending and torsion during 3D bending of profiles. *Journal of Materials Processing Tech.*, 262, pp. 650–659

# Table of Contents

<b>Symbols and Abbreviations</b>	<b>xiii</b>
<b>1 Introduction</b>	<b>1</b>
<b>2 State of the art</b>	<b>3</b>
2.1 Bending processes for the production of 3D tube and profile structures.....	3
2.1.1 Three-roll push bending .....	5
2.1.2 TSS Bending.....	7
2.1.3 MOS bending and process extensions.....	12
2.1.4 Parallel kinematics bending.....	13
2.1.5 Combined drawing and free-form bending .....	14
2.2 Characterization of tubular material for the use in bending process models.	15
2.2.1 Behavior of tubular material in tension and compression.....	16
2.2.2 Tensile and compression test methods .....	18
2.3 Techniques for the measurement of 3D bending contours .....	19
<b>3 Aim</b>	<b>23</b>
<b>4 Characteristics of 3D profile bending</b>	<b>25</b>
4.1 Geometrical definition of 3D contours .....	25
4.1.1 Frenet-Serret description of 3D curves .....	25
4.1.2 General mathematical description of 3D-shaped profiles .....	28
4.1.3 Extraction of contour data from structural models.....	34
4.1.4 Discrete description of 3D-contours.....	36
4.2 Characterization of free-form bending kinematics .....	41
4.2.1 Derivation of cDOFs needed for manufacturing.....	41
4.2.2 Classification of free-form bending kinematics .....	46
4.2.3 Relation of profile geometry and actuator movements .....	48
4.2.4 Location and movement of the bending force vector.....	52
<b>5 Setup of a 5-cDOF profile bending process and measuring equipment</b>	<b>55</b>
5.1 Material characterization and parametrization.....	55
5.2 Extension of 3-cDOF TSS bending to a 5-cDOF profile bending process....	60
5.2.1 Drive system of the bending head's rotational DOFs .....	65
5.2.2 Performance of the 5-cDOF TSS bending process .....	69
5.2.3 Development of an integrated torque measurement device .....	71
5.3 Development of a 3D contour measurement device .....	75
5.3.1 Design concept of a contact measurement device.....	77
5.3.2 Calculation of the profile contour data.....	79
5.3.3 Setup of the manufactured contact measurement device .....	83
5.4 Numerical model of the 5-cDOF TSS bending process and its validation....	86

5.4.1	Comprehensive numerical model .....	86
5.4.2	Simplified numerical model .....	90
<b>6</b>	<b>Elastic profile behavior during 3D profile bending</b>	<b>93</b>
6.1	Definition of a supported beam model for profile bending with $\geq 4$ cDOF ..	93
6.2	Supported beam model: die-based profile support .....	96
6.2.1	Beam deflection in the $xy$ -plane .....	98
6.2.2	Beam deflection in $z$ -direction .....	100
6.3	Supported beam model: roll-based profile support.....	107
6.3.1	Beam deflection in $xy$ -plane .....	109
6.3.2	Beam deflection in $z$ -direction .....	113
<b>7</b>	<b>The reciprocal effects of bending and torsion during 3D profile bending</b>	<b>119</b>
7.1	Analytical description of the states of strains and stresses .....	119
7.2	Influence of perimetral stress on the bending process .....	128
7.2.1	Normalized stress-strain relationship .....	130
7.2.2	Impact of the neutral axis shift on the bending moment .....	133
7.3	Influence of torsion on the bending process .....	136
7.3.1	Analytical description of pure torsion .....	138
7.3.2	Analytical description of combined bending and torsion.....	144
7.3.3	Performance of the analytical model for combined bending and torsion .	157
<b>8</b>	<b>Comprehensive process model of 3D profile bending</b>	<b>161</b>
8.1	Model procedure .....	161
8.2	Generation of springback-compensated NC-data .....	163
8.3	Process model demonstration.....	165
<b>9</b>	<b>Conclusion and outlook</b>	<b>171</b>
	<b>References</b>	<b>175</b>
	<b>Annex</b>	<b>187</b>
	<b>Curriculum vitae</b>	<b>195</b>



## Symbols and Abbreviations

Symbol	Unit	Description
$A_i$	mm <sup>2</sup>	Area of the triangle defined by the points $P_{i-1}$ , $P_i$ , and $P_{i+1}$
$A_j, B_j, C_j, D_j$	mm	Shear strain distributions
$A_m$	mm <sup>2</sup>	Area enclosed by the neutral axis of the profile wall
$dA$	mm <sup>2</sup>	Infinitesimal segment of the profile cross-section
$\vec{b}$	-	Binormal unit vector
$\vec{b}_i$	mm	Binormal vector at discrete point $P_i$
$\vec{b}_M$	-	Binormal unit vector of machine bending plane $M$
$B$	-	Bending plane
$c$	-	Profile feeding axis
$c_a$	-	Center of area
$c_L$	mm	Contact length
$c_M$	Nmm/rad	Torsional machine stiffness
$c_s$	-	Shear center
$c_W$	mm	Half of contact width
$C$	MPa	Hollomon strength coefficient
$C_1$	-	Constant of integration
$d$	mm	Depth of impression
$D$	mm	Tube diameter
$D_P$	mm	Diameter of the enclosing circle of an arbitrary cross-section
$e_1$	-	$e_1$ -axis in the plane of a profile element
$e_2$	-	$e_2$ -axis in the plane of a profile element

<b>Symbol</b>	<b>Unit</b>	<b>Description</b>
$\vec{e}_{y,cs}$	-	Unit vector along the longitudinal axis $y_{cs}$
$\vec{e}_p$	-	Unit vector tangent to neutral axis of the profile wall
$E$	MPa	Young's modulus
$E_0$	MPa	Initial Young's modulus
$E_\infty$	MPa	Asymptotic Young's modulus
$E_{\text{profile}}$	MPa	Young's modulus of profile material
$E_{\text{roll}}$	MPa	Young's modulus of roll material
$E^*$	MPa	Equivalent Young's modulus
$F$	N	Normal contact force
$F_B$	N	Bending force
$F_{B,xy}$	N	Bending force in the $xy$ -plane
$F_{B,z}$	N	$z$ -component of the bending force
$F_{B,\text{red}}$	%	Bending force reduction
$F_{B,R_{\text{th}},0}$	N	Bending force at the theoretical bending radius $R_{\text{th}}$ without twist
$F_{B,R_{\text{th}},d\phi}$	N	Bending force at the theoretical bending radius $R_{\text{th}}$ and the twist per unit length $d\phi$
$F_p$	N	Sum of Forces in perimetral direction
$F_{\beta_e}$	N	Sum of Forces along angle $\beta_e$
$\vec{F}_B$	N	Bending force vector
$G$	MPa	Shear modulus
$h$	mm	Height of rectangular cross-section
$h_1, h_2, h_3$	mm	Partial lengths along height of rectangular cross-section
$h_h$	mm	Pitch of the helix
$dh_T$	mm	Incremental deflection caused by elastic twisting of the beam by $d\alpha_T$

<b>Symbol</b>	<b>Unit</b>	<b>Description</b>
$i$	-	Discrete step on curve
$i_{CU,12}$	-	Number of increments between contact units 1 and 2, rounded to the nearest integer
$I$	$\text{mm}^4$	Second moment of area
$I_p$	$\text{mm}^4$	Polar moment of inertia
$J_T$	$\text{mm}^4$	Torsional constant
$k$	-	Index of summation
$l_{\text{step}}$	mm	Step size
$l_{\text{step},i}$	mm	Step size from $i$ to $i+1$
$l_{\text{step},i,\text{FS}}$	mm	Step size of the feed sensor from $i$ to $i+1$
$L$	mm	Length of the curve $\vec{r}$
$L_i$	mm	Initial length of straight tube during TRPB
$L_B$	mm	Lever arm of the bending force
$L_{B,\text{eff}}$	mm	Effective lever arm of the bending force, considering a displacement of the forming zone towards the bending head
$L_{B,p}$	mm	Distance of the bending force vector to the bending plane
$L_{B,x}$	mm	Distance between the profile support and the point of bending force application in $x$ -direction
$L_{B,y}$	mm	Distance between the profile support and the point of bending force application in $y$ -direction
$L_{CU,12}$	mm	Distance between contact units 1 and 2
$L_{CU,23}$	mm	Distance between contact units 2 and 3
$L_{\text{FS}}$	mm	Perpendicular distance of feed sensor to the bending line
$L_{S12}$	mm	Beam length between $S_1$ and $S_2$
$L_{S23}$	mm	Beam length between $S_2$ and $S_3$

<b>Symbol</b>	<b>Unit</b>	<b>Description</b>
$m$	-	Exponential parameter in Hockett and Sherby approximation
$m_{\text{acc}}$	%	Measurement accuracy
$M$	-	Machine bending plane
$M_{\text{B}}$	Nm	Bending moment
$M_{\text{B},i}$	Nm	Inner bending moment
$M_{\text{B},\text{max}}$	Nm	Maximum bending moment
$M_{\text{B},o}$	Nm	Outer bending moment
$M_{\text{B},n}$	Nm	Internal moment in normal direction
$M_{\text{B},z}$	Nm	Internal moment in z-direction
$M_{\text{S1},x}, M_{\text{S1},y},$ $M_{\text{S1},z}$	Nm	Reaction moments of the profile support $S_1$
$M_{\text{T}}$	Nm	Torque caused by twisting
$M_{\text{T},p}$	Nm	Parasitic torque
$M_{\text{T},\text{red}}$	%	Torque reduction
$M_{\text{T},d\phi,0}$	Nm	Torque resulting while twisting a straight profile with the twist per unit length $d\phi$
$M_{\text{T},d\phi,R_{\text{th}}}$	Nm	Torque resulting while twisting with the twist per unit length $d\phi$ and bending to the theoretical bending radius $R_{\text{th}}$
$n$	-	Number of discrete points along curve
$n_1, n_3$	mm	Distance along $x$ -axis to the vertices nearest to the neutral axis
$n_2, n_4$	mm	Distance along $x$ -axis to the intrados/extrados
$n_{\text{B}}$	mm	Distance of a profile element to the neutral axis
$n_{\text{B},0}$	mm	Distance of a profile element to the non-strained axis
$n_e$	mm	Distance from the neutral axis to the end of the elastic area

<b>Symbol</b>	<b>Unit</b>	<b>Description</b>
$n_H$	-	Strain hardening exponent
$n_{HS}$	-	Exponential parameter in Hockett and Sherby approximation
$n_m$	mm	Distance from the neutral axis to the intrados/extrados of the profile
$n_N$	-	Normalized distance of a profile element to the neutral axis
$n_{N,0}$	-	Normalized location of the non-strained axis
$\vec{n}$	-	Normal unit vector
$\vec{n}_i$	mm	Normal vector at discrete point $P_i$
$\vec{n}_M$	-	Normal unit vector of machine bending plane $M$
$\vec{n}_{M,map}$	-	Normal vector of machine bending plane $M$ mapped onto the normal plane $N$ of the bending line at point $P_{FB}$
$N$	-	Normal plane
$N_i$	-	Normal plane at discrete point $P_i$
$N_{PFB}$	-	Normal plane at point $P_{FB}$
$\vec{o}$	mm	Orientation vector
$\vec{o}_i$	mm	Orientation vector at discrete point $P_i$
$\vec{o}_{projected}$	mm	Projection of the orientation vector at $s+\Delta s$ onto the normal plane at $s$
$p$	-	Perimetral direction
$P$	mm	Length of the neutral axis of the profile wall
$P_{CU,1}$	-	Midpoint of contact unit 1
$P_{CU,2}$	-	Midpoint of contact unit 2
$P_{CU,3}$	-	Midpoint of contact unit 3
$P_{FB}$	-	Point of bending force application

<b>Symbol</b>	<b>Unit</b>	<b>Description</b>
$P_{FB,el}$	-	Point of bending force application caused by elastic beam deflection
$P_i$	-	Discrete point on a curve
$P_{LMP,1}$	-	Contact point of LMP 1 with the sensor bar 1-3
$P_{LMP,2}$	-	Contact point of LMP 2 with the sensor bar 2-4
$P_{LMP,3}$	-	Contact point of LMP 3 with the sensor bar 1-3
$P_{LMP,4}$	-	Contact point of LMP 4 with the sensor bar 2-4
$P_O$	-	Origin of the XZ-coordinate system
$P_{s,i}$	-	Discrete Point on a secondary curve
$P_S$	-	Point of profile support
$P_{SB,int}$	-	Intersection point of sensor bars
$\vec{p}_N$	mm	Position vector of any point on the normal plane $N_i$
$\vec{p}_{FB}$	mm	Position vector of the point of bending force application
$\vec{p}_{int}$	mm	Intersection point of $\vec{r}_s$ and the normal plane $N$
$\vec{p}_O$	mm	Position vector of the origin XZ-coordinate system
$\vec{p}_S$	mm	Position vector of the point of profile support
$q$	-	Ratio of height to width of the neutral axis of the profile wall
$r$	mm	Resultant
$r_{ap}$	mm	Projection of the local bending radius $r$ onto the plane of an element of the profile
$dr_{ap}$	mm	Height of the element
$r_1$	mm	Local bending radius on bending plane
$\vec{r}$	mm	Three-dimensional curve used as bending line
$\vec{r}_{cs}$	mm	Distance vector of an element of the profile wall to the center of gravity of the cross-section

<b>Symbol</b>	<b>Unit</b>	<b>Description</b>
$\vec{r}_{\text{CU},2}$	mm	Resultant vector of the movement in $x$ and $z$ -direction of contact unit 2
$\vec{r}_s$	mm	Secondary bending line
$r_{\perp}$	mm	Perpendicular distance of the vector $\vec{e}_p$ at the differential element of the profile wall to the center of gravity of the cross-section
$R$	mm	Ideal radius between the profile support and the point of bending force application
$R_B$	mm	Radius of the neutral axis
$R_{B,0}$	mm	Radius of the non-strained axis
$R_h$	mm	Radius of the helix
$R_i$	mm	Inner bending radius
$R_{i0}$	mm	Inner/outer bending radius depending on case
$R_i$	mm	Radius at discrete point $P_i$
$R_L$	mm	Loaded bending radius
$R_{L,\text{cor}}$	mm	According to Chatti et al. (2010) the loaded ideal radius $R_L$ reduced by the profile stiffness and the machine stiffness
$R_o$	mm	Outer bending radius
$R_{\text{profile}}$	mm	Radius of profile surface at the point of contact with the roll
$R_{\text{roll}}$	mm	Radius of bending head roll at the point of contact with the profile
$R_{\text{th}}$	mm	Bending radius that theoretically results from purely geometric relations of a kinematic bending process
$R_{\text{th},i}$	mm	Theoretical bending radius on bending plane at position $i$
$R_U$	mm	Unloaded bending radius
$R^*$	mm	Equivalent radius for Hertzian stress calculation
$\widehat{R}_B$	mm	Arc length of dynamic elastic region in TRPB

Symbol	Unit	Description
$R$	-	$3 \times n$ -matrix describing a discretized three-dimensional curve $\vec{r}$
$R_s$	-	$3 \times n$ -matrix describing a second discretized three-dimensional curve $\vec{r}_s$
$s$	mm	Arc length along curve (used for description of bending line $\vec{r}$ and perimeter of cross-section)
$\Delta s$	mm	Step size
$s_{PFB}$	mm	Arc length at point $P_{FB}$
$s_{PS}$	mm	Arc length at point $P_S$
$s_s$	mm	Arc length along secondary bending line $\vec{r}_s$
$s_{s,i}$	mm	Arc length along secondary bending line $\vec{r}_s$ up to step $i$
$S_{1,x}, S_{1,y}, S_{1,z}$	N	Reaction forces at profile support $S_1$
$S_{2,x}, S_{2,z}$	N	Reaction forces at profile support $S_2$
$S_{3,x}, S_{3,z}$	N	Reaction forces at profile support $S_3$
$SB_{\text{offset}}$	mm	Offset of sensor bars to origin of coordinate system
$t$	-	Path-independent variable used for curve parameterization
$t_1$	mm	Thickness of profile wall 1
$t_2$	mm	Thickness of profile wall 2
$t_3$	mm	Thickness of profile wall 3
$t_4$	mm	Thickness of profile wall 4
$t_h$	mm	Thickness of profile wall having the length $h$
$t_s$	-	Path-independent variable of a secondary line used for curve parameterization
$t_t$	mm	Thickness of profile wall
$t_w$	mm	Thickness of profile wall having the length $w$
$\vec{t}$	-	Tangent unit vector



<b>Symbol</b>	<b>Unit</b>	<b>Description</b>
$\vec{t}_i$	mm	Tangent vector at discrete point $P_i$
$\vec{t}_M$	-	Tangent unit vector of machine bending plane $M$
$u$	mm	Displacement of a differential element of the cross-section
$\vec{u}$	mm	Displacement vector of a differential element of the cross-section
$w$	mm	Width of rectangular cross-section
$w_1, w_2, w_3$	mm	Partial lengths along width of rectangular cross-section
$w_{X,B}$	mm	Displacement of the point of bending force application along the $X$ -axis because of elastic beam deflection
$w_{xy,B}$	mm	Deflection of beam in the $xy$ -plane caused by $F_{B,xy}$
$w'_{xy,B}$	rad	Slope of beam in the $xy$ -plane caused by $F_{B,xy}$
$w''_{xy,B}$	1/mm	curvature of beam in the $xy$ -plane caused by $F_{B,xy}$
$w_z$	mm	Total deflection of beam at point $P_{FB}$
$w_{z,B,F}$	mm	Deflection of beam in $z$ -direction caused by $F_{B,z}$
$w'_{z,B,F}$	rad	Slope of beam in $z$ -direction caused by $F_{B,z}$
$w''_{z,B,F}$	1/mm	curvature of beam in $z$ -direction caused by $F_{B,z}$
$w_{z,B,M}$	mm	Deflection of beam in $z$ -direction caused by $M_T$
$w'_{z,B,M}$	rad	Slope of beam in $z$ -direction caused by $M_T$
$w''_{z,B,M}$	1/mm	curvature of beam in $z$ -direction caused by $M_T$
$w_{z,T,F}$	mm	Deflection of beam in $z$ -direction resulting from beam twisting caused by $F_{B,z}$
$w_{z,T,M}$	mm	Deflection of beam in $z$ -direction resulting from beam twisting caused by $M_T$
$W_T$	mm <sup>3</sup>	Torsional section modulus
$x$	-	$x$ -axis
$x_1$	mm	$x$ -coordinate of $P_{LMP,1}$

<b>Symbol</b>	<b>Unit</b>	<b>Description</b>
$x_2$	mm	$x$ -coordinate of $P_{LMP,2}$
$x_3$	mm	$x$ -coordinate of $P_{LMP,3}$
$x_4$	mm	$x$ -coordinate of $P_{LMP,4}$
$x_{MP}$	mm	$x$ -coordinate of $P_{CU,2,i}$
$x_{MP,r}$	mm	Relative offset of the $x$ -coordinate of the midpoint $P_{CU,2,i}$ of CU 2
$X$	-	Bending axis
$y$	-	$y$ -axis
$y_{cs}$	-	Axis in longitudinal profile direction
$y_f$	mm	Feed length in TRPB
$Y$	-	$Y$ -axis
$z$	-	$z$ -axis
$z_1$	mm	$z$ -coordinate of $P_{LMP,1}$
$z_2$	mm	$z$ -coordinate of $P_{LMP,2}$
$z_3$	mm	$z$ -coordinate of $P_{LMP,3}$
$z_4$	mm	$z$ -coordinate of $P_{LMP,4}$
$z_{MP}$	mm	$z$ -coordinate of $P_{CU,2,i}$
$z_{MP,r}$	mm	Relative offset of the $z$ -coordinate of the midpoint $P_{CU,2,i}$ of CU 2
$\alpha_1$	rad	Rotation angle of the machine bending plane, in TSS bending equal to the rotation angle of the rotatable transportation system
$\alpha_2$	rad	Rotation angle of the torsional cDOF
$\alpha_T$	rad	Elastic twisting angle of beam caused by $M_T$ and $F_{B,z}$
$d\alpha_T$	rad/mm	Differential elastic twisting angle of beam caused by $M_T$ and $F_{B,z}$
$\beta$	rad	Bending angle

<b>Symbol</b>	<b>Unit</b>	<b>Description</b>
$d\beta$	rad	Incremental bending angle of a profile element lifted onto the bending plane
$\beta_0$	rad	Angle between profile support and the point of bending force application in $y$ -direction
$\beta_1$	rad	Rotation angle of $N$ around $\vec{b}_M$ , in TSS bending equal to the rotation of the compensatory axis of the bending head
$\beta_2$	rad	Rotation angle of $N$ around $\vec{n}_{M,map}$
$\beta_e$	rad	Rotation around the normal vector of a profile element in the direction of the wall thickness $t$
$d\beta_e$	rad	Incremental bending angle of a profile element
$\beta_s$	rad	Angle of circular segment between profile support and point $s$
$\gamma$	-	Nominal shear strain
$\gamma_{avg}$	-	Average nominal shear strain
$\gamma_e$	-	Shear strain at the extrados
$\gamma_i$	-	Shear strain at the intrados
$\gamma_m$	-	Maximum nominal shear strain at the intrados and extrados
$\gamma_{m,v}$	-	Nominal shear strain at a vertex closest to the neutral bending axis
$\gamma_Y$	-	Nominal shear strain at the yield point
$\dot{\gamma}$	1/s	Nominal shear strain increment
$\delta$	mm	Displacement along $X$ -axis
$\delta_{ij}$	-	Kronecker delta
$\delta_M$	mm	Machine deflection along $X$ -axis
$\delta_P$	mm	Profile deflection along $X$ -axis
$\varepsilon_\alpha$	-	Axial strain

<b>Symbol</b>	<b>Unit</b>	<b>Description</b>
$\varepsilon_{\alpha p}$	-	Shear strain
$\varepsilon_e$	-	Axial strain at the extrados
$\varepsilon_i$	-	Axial strain at the intrados
$\varepsilon_p$	-	Perimetral strain
$\varepsilon_Y$	-	Nominal strain at the yield point
$\dot{\varepsilon}_\alpha$	1/s	Axial strain increment
$\dot{\varepsilon}_{\alpha p}$	1/s	Shear strain increment in $\alpha p$ -direction
$\dot{\varepsilon}_{ij}$	1/s	General state of strain increments
$\dot{\varepsilon}_p$	1/s	Perimetral strain increment
$\dot{\varepsilon}_{pt}$	1/s	Shear strain increment in $pt$ -direction
$\dot{\varepsilon}_t$	1/s	Strain increment in thickness direction
$\dot{\varepsilon}_{t\alpha}$	1/s	Strain increment in $t\alpha$ -direction
$\dot{\bar{\varepsilon}}_{pl}$	1/s	Equivalent plastic strain increment
$\bar{\varepsilon}_{pl}$	-	Equivalent plastic strain
$\zeta$	-	Young's modulus approximation parameter
$\eta$	rad	Angle between the machine bending plane $M$ and the bending plane $B$
$\theta$	rad	Cross-section orientation
$\theta_i$	rad	Cross-section orientation at discrete point $P_i$
$\theta_{lim}$	rad	Value determining the limiting angle range when calculating $\Delta\phi_{\text{apparent},i}$
$\theta_r$	rad	Cumulative bending plane rotation
$d\theta_r$	rad/unit length	Bending plane rotation
$\theta_{r,corr}$	rad	Cumulative bending plane rotation, reduced by the machine stiffness, with added cross-section orientation $\theta$

<b>Symbol</b>	<b>Unit</b>	<b>Description</b>
$d\theta_{r,corr}$	rad/unit length	Bending plane rotation, reduced by the machine stiffness
$\theta_{r,corr, offset}$	rad	Cumulative bending plane rotation, reduced by the machine stiffness, with added cross-section orientation $\theta$ , offset by angle $\eta$
$\theta_{r,i}$	rad	Cumulative bending plane rotation at discrete point $P_i$
$\Delta\theta_{r,i}$	rad/unit length	Bending plane rotation at discrete point $P_i$
$\theta_{r,5R_h}$	rad	Cumulative bending plane rotation describing the total rotation of a helix with a helix radius $R_h = R_{h,1}$ and a pitch of $h_h = 5R_{h,1}$
$d\theta_{r,5R_h}$	rad/mm	Bending plane rotation of a helix with a helix radius $R_h = R_{h,1}$ and a pitch of $h_h = 5R_{h,1}$
$\theta_{r,CU,12,i}$	rad	Rotation angle between the point-symmetric extension of the resultant vector and the $x$ -axis
$\Delta\theta_{r,CU,12,i}$	rad/unit length	Change of the rotation angle from $P_{i-1}$ to $P_i$
$\theta_{r,TRPB}$	rad	Cumulative tube rotation during TRPB
$d\theta_{r,TRPB}$	rad/mm	Tube rotation per feed length during TRPB
$\varpi$	rad	Angle between the element plane and the bending plane
$\kappa$	1/mm	Curvature
$\kappa_{5R_h}$	1/mm	Curvature of a helix with a helix radius $R_h = R_{h,1}$ and a pitch of $h_h = 5R_{h,1}$
$\kappa_{const}$	1/mm	Constant curvature
$\kappa_i$	1/mm	Curvature at discrete point $P_i$
$\kappa_{max}$	1/mm	Maximum curvature
$\kappa_{min}$	1/mm	Minimum curvature
$\lambda$	-	Proportional parameter according to Levy-Mises
$\nu$	-	Poission's ratio

<b>Symbol</b>	<b>Unit</b>	<b>Description</b>
$\nu_{\text{profile}}$	-	Poission's ratio of profile
$\nu_{\text{roll}}$	-	Poission's ratio of roll
$\zeta$	-	Relational parameter
$\rho$	-	Ratio of bending radius $R_B$ and the profile height $D_P$
$\sigma_a$	MPa	Axial stress
$\sigma_a'$	MPa	Deviatoric axial stress
$\sigma_c$	MPa	Contact stress
$\sigma_{\text{el}}$	MPa	Von Mises stress in the elastic region
$\sigma_f$	MPa	Flow stress
$\sigma_h$	MPa	Hydrostatic stress
$\sigma_{ij}$	MPa	Stress tensor
$\sigma_{ij}^h$	MPa	Hydrostatic stress tensor
$\sigma_{ij}'$	MPa	Deviatoric stress tensor
$\sigma_p$	MPa	Perimetral stress
$\sigma_p'$	MPa	Deviatoric perimetral stress
$\sigma_t$	MPa	Stress in thickness direction
$\sigma_Y$	MPa	Yield stress
$\sigma_\infty$	MPa	Asymptotic parameter
$\tau$	MPa	Shear stress, equal to $\tau_{\alpha p}$
$\tau'$	MPa	Deviatoric shear stress
$\tau_{\alpha p}$	MPa	Shear stress in $\alpha p$ -direction
$\tau_{pt}$	MPa	Shear stress in $pt$ -direction
$\tau_{t\alpha}$	MPa	Shear stress in $t\alpha$ -direction
$U_p$	mm	Displacement of a differential element of the cross-section in tangential direction
$U_{x,i}, U_{y,i}, U_{z,i}$	mm	Position vector elements of a single point on a curve

Symbol	Unit	Description
$U_{s,x,i}, U_{s,y,i}, U_{s,z,i}$	mm	Position vector elements of a single point on a secondary curve
$\vec{U}_i$	mm	Position vector of a single point on a curve
$\vec{U}_{s,i}$	mm	Position vector of a single point on a secondary curve
$\phi$	rad	Cumulative twist
$d\phi$	rad/unit length	Twist per unit length
$\phi_{5R_h}$	rad	Cumulative twist of a helix with a helix radius $R_h = R_{h,1}$ and a pitch of $h_h = 5R_{h,1}$
$d\phi_{5R_h}$	rad/mm	Twist per unit length of a helix with a helix radius $R_h = R_{h,1}$ and a pitch of $h_h = 5R_{h,1}$
$\phi_{\text{apparent}}$	rad	Cumulative apparent twist
$d\phi_{\text{apparent}}$	rad/unit length	Apparent twist per unit length
$\Delta\phi_{\text{apparent},i}$	rad/unit length	Apparent twist per unit length at discrete point $P_i$
$\phi_{\text{CU},12,i}$	rad	Torsion angle between contact units 1 and 2
$\Delta\phi_i$	rad/unit length	Twist per unit length at discrete point $P_i$
$\Delta\phi_{\text{PCU},1,i}$	rad/unit length	Twist per unit length measured by contact unit 2 when in position of contact unit 1 at discrete point $P_i$
$d\phi_{\text{projected}}$	rad	Angle between $\vec{o}_{\text{projected}}$ and $\vec{o}$
$\phi_{\text{TRPB,dyn}}$	rad	Dynamic cumulative twist of the straight tube during TRPB
$\phi_{\text{TRPB,stat}}$	rad	Static cumulative twist of the straight tube during TRPB
$\chi_i$	-	Boolean operator describing acute or obtuse angles in the calculation of the cross-section orientation $\theta_i$
$\chi_s$	-	Boolean operator describing acute or obtuse angle in the calculation of the cross-section orientation $\theta(s)$

<b>Symbol</b>	<b>Unit</b>	<b>Description</b>
$\omega_n$	rad	Angle of the normal unit vector to the xy-plane
$\omega_t$	rad	Angle of the tangent unit vector to the xy-plane
$\omega_{t,5R_h}$	rad	Angle of the tangent unit vector of a helix with a helix radius $R_h = R_{h,1}$ and a pitch of $h_h = 5R_{h,1}$ to the xy-plane

<b>Abbreviations</b>	<b>Description</b>
2D	Two-dimensional
3D	Three-dimensional
an.	Analytical
ASTM	American Society for Testing and Materials
CAD	Computer aided design
cDOF	Controlled degrees of freedom
CNC	Computer numerical control
CNH	Case New Holland
comp.	Compensated
CSR	Cross-sectional ratio
CU	Contact unit
DIN	Deutsches Institut für Normung e.V. [German Institute for Standardization]
DP	Dual-phase
exp.	Experimental
FEM	Finite element method
GOM	Gesellschaft für Optische Messtechnik [Corporation for optical measuring technology]
IGES	Initial Graphics Exchange Specification
IMU	Inertial measurement unit



---

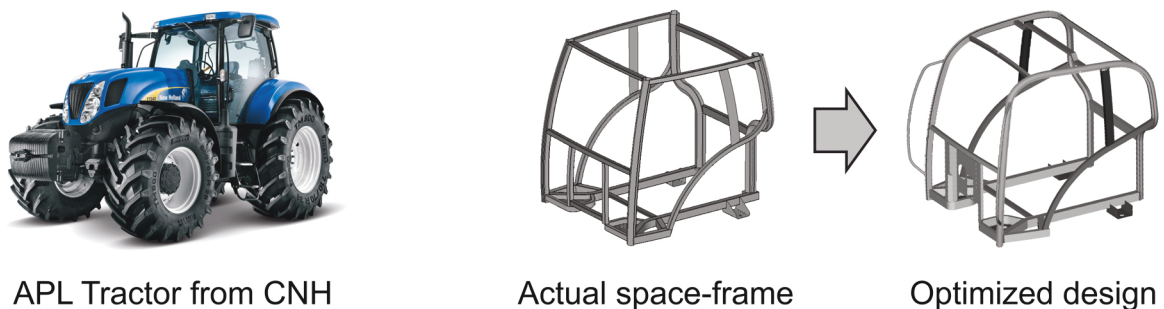
MOS	Freeform bending with a movable die developed by Murata, Ohashi, and Suzuki
NC	Numerical control
num.	Numerical
LMP	Length measurement probe
PPP	Point point point (first type of the Apollonius' Problem)
STEP	Standard for the exchange of product model data
TKS	ThyssenKrupp Steel
tnb	Frame made up of a tangent, normal, and binormal unit vector
TRB	Three-roll bending
TRPB	Three-roll push bending
TSS	Torque superposed spatial
VDI	Verein Deutscher Ingenieure [Association of German Engineers]



# 1 Introduction

After the early industrialization in the second half of the 19<sup>th</sup> century, with its main focus on part functionality, industrial design gained of great importance in the early 20<sup>th</sup> century and has steadily risen in importance since.

Since Alfred P. Sloan (1963) introduced annual model design changes to General Motors cars in the 1930s and this was adopted by competing car manufactures, automotive design has been under continuous evolution. After the boxier industrial design of the 70s and 80s with clean lines and sharp angles, the design of structural parts, especially in the transport sector, have steadily included more and more curved elements. This modern design actually more closely relates to the classic automotive design from the 50s and 60s. At that time complex curved shapes were realized by additional heat treatment in between forming steps and welding, which oftentimes needed additional manual labor (Oehler, 1951). Today's increased popularity of curved designs, in spite of increased labor costs, can be explained by advances in process automatization and process control combined with advances in 3D CAD and finite element software that allow the productive systematic design and analysis of complex shapes, necessary for cost efficient manufacturing. These techniques make possible a more aesthetic and organic design, including round shapes and continuous curves. The drive towards these designs cannot only be noticed in the automotive industry. Also, the bike industry, the furniture industry, and architecture follow a similar trend. Even the design of utility vehicles nowadays is not simply focused on functionality alone but incorporates actual emotional design (see Figure 1.1).



**Figure 1.1:** Actual space frame used in the APL tractor from CNH (Chatti et al., 2010) consisting of individual curved profile parts in comparison to an optimized design using 3D bent side elements combining the functionalities of the front pillar, roof rail, and rear pillar (Staupendahl et al., 2014a)

Profiles are being used in all of the previously mentioned industries for structural elements, enclosures, handrails, etc. To meet the current demands for 3D bent profiles in high batch production, the industry mostly relies on form-bound processes such as stretch bending or hydroforming. Because of the current additional trend towards more

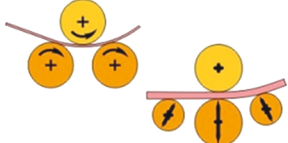
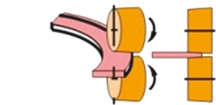
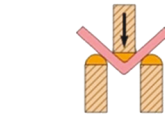
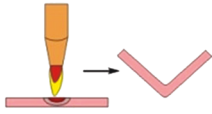
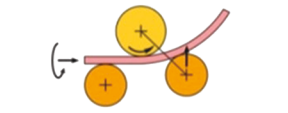

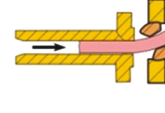
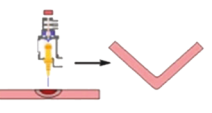
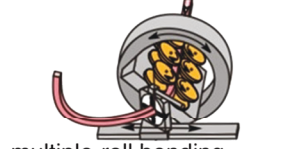
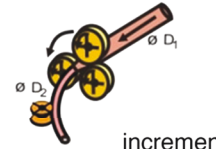
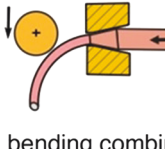
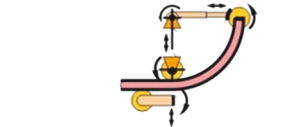
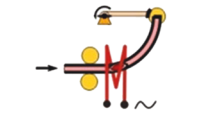
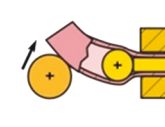

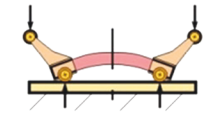
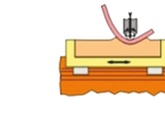

and more individuality, even high-batch industries are faced with a steady increase of product variants and are looking for more flexible processes to keep up economic production (Groche and Schneider, 2000). In bending this means replacing form-bound manufacturing methods by kinematic bending processes. Although several 3D-profile bending processes have been designed in the recent decades, these processes are not yet widely used in the industry. The most likely reason for this circumstance is the lack of knowledge about the mechanisms of 3D-profile bending and the, consequently, difficult to control processes, especially regarding part tolerances. The aim of this work is the generation of a comprehensive insight into the process of 3D-profile bending, from the geometrical interrelations over the elastic profile behavior to the reciprocal effects of stresses in the forming zone, to be used by designers and machine manufacturers in order to take full potential of this promising technology.

The thesis is subdivided into 8 chapters. Following the introduction, Chapter 2 will focus on the state of the art of 3D bending. Currently existing bending processes are introduced as well as their respective process models. Next, the behavior of tubular material is discussed. Finally, techniques for the measurement of profile contours are described along with their advantages and disadvantages. From the conclusion of the state of the art, the aim of the thesis is deduced in Chapter 3. Chapter 3 focuses on the geometrical characteristics of 3D-shaped profiles and addresses the differences between 3D profile contours with and without torsion. Using this mathematical foundation, the controlled degrees of freedom (cDOFs) for the production of these shapes are derived and used in a subsequent step to classify the currently available 3D bending processes in terms of producible part complexity. In order to investigate 3D bending with torsion, Chapter 5 describes the development of a 5-cDOF bending machine, based on the TSS bending process, and the required force and torque measurement equipment. Additionally, a comprehensive numerical process model is introduced, which is used in the following chapters to validate the process forces and the stresses and strains in the profile. Also, the development of a contour sensor is described that enables the time-efficient inline-measurement of 3D-profile contours. Chapter 6 analyzes the elastic profile behavior and the influence of the profile support and bending radius on the reaction forces and moments in the bending setup. By combining knowledge gained in Chapter 3 with knowledge gained in Chapter 6, the effect of torque on the bending plane orientation and rotation is described. Chapter 7 focuses on the plastic behavior of the profile in the forming zone. Especially, the interaction of stresses and strains is investigated and the impact of this interaction on bending force and torque. Chapter 8 finally introduces a process model that incorporates the knowledge on geometrical relations of Chapter 3, the elastic profile behavior of Chapter 6, and the plastic profile behavior of Chapter 7 and is validated with experimental equipment described in Chapter 5. Chapter 9 concludes the work and gives an outlook on potential further process extensions and combinations.

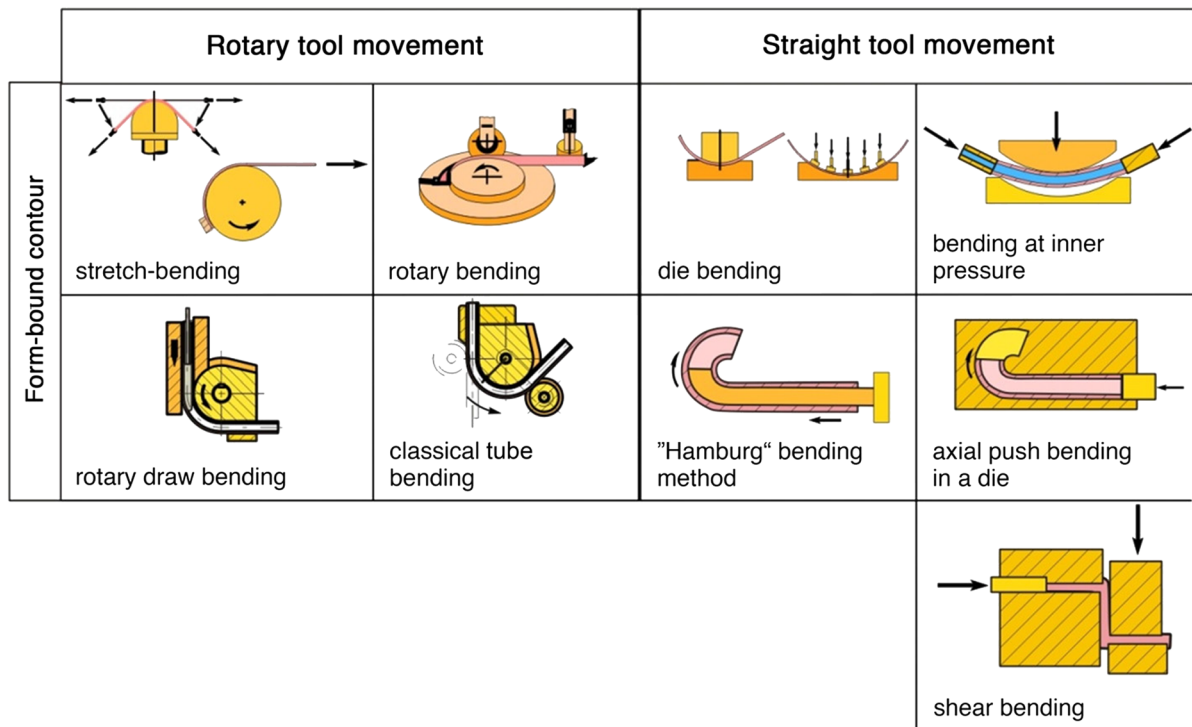
## 2 State of the art

### 2.1 Bending processes for the production of 3D tube and profile structures

The DIN 8586 divides bending processes into the categories *bending with translational movement* and *bending with rotational movement*. According to Hermes (2011) and the VDI 3430 bending processes can be further categorized into processes with a kinematic

	Rotary tool movement	Straight tool movement	Thermally induced processes	
Kinematic definition of bending contour	 (three-)roll bending	 sweeping, partial rolling out	 3-point bending	 thermally induced flame bending
	 (three-)roll push bending	 bending combined with longitudinal rolling	 freeform bending with movable die	 laser-beam bending
	 multiple-roll bending combined with torsion	 incremental tube forming	 bending combined with pushing	
	 bending with controlled moment	 bending with induction heating	 bending with expanding	
	 roll forming combined with bending	 bending without radial stress	 profile bending in an elastic die	
	 end-controlled bending			

**Figure 2.1:** Bending processes with a kinematic definition of the bending contour (Hermes, 2011, cf. VDI 3430)



**Figure 2.2:** Bending processes with a form-bound definition of the bending contour (Hermes, 2011, cf. VDI 3430)

definition of the bending contour (Figure 2.1) and processes with a form-bound contour (Figure 2.2). In form-bound processes the form of the bending tools define the shape of the part. The form-bound tools offer optimal guidance of the part and a high repeat accuracy. A major disadvantage is the low flexibility. In general, every new contour needs new tooling. Additionally, the size of the bending tools is coupled to the size of the part – large parts result in large tools. Limited flexibility is offered by rotary bending, rotary draw bending, and classical tube bending by allowing variable bending angles. Kinematic bending processes, on the other hand, purely define the bending contour by relative movements of bending tools in relation to the part. Tools only have to be adapted to the cross-section of the part. The following subsections give an overview about kinematic 3D bending processes that allow processing of tubes and, within individual limits, profiles with non-circular cross-sections.<sup>1</sup>

<sup>1</sup> Although incremental tube forming is only able to process and produce tubes with circular cross-sections, it is a highly interesting process able to produce load-adapted parts with a varying diameter and wall-thickness over the tube length. For further reading, the works of Becker et al. (2014) and Nazari et al. (2019) are recommended.

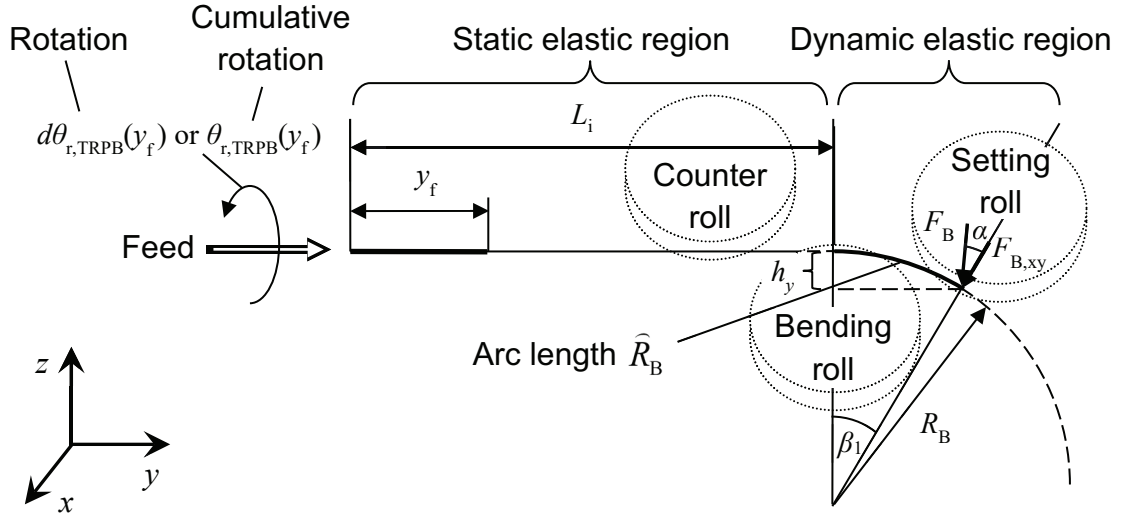
### 2.1.1 Three-roll push bending

The most widely used industrial kinematic bending process to produce 3D bent tubular structures is three-roll push bending. Extensive investigations have been done to produce stable process models that accurately predict part behavior during production. Hagenah et al. (2010) set up an FE model for three-roll push bending and increased the simulation accuracy by including machine stiffness in the calculation. Gerlach (2010) presented an analytical process model of three-roll push bending for two-dimensional bending contours. Building up on this knowledge, Engel and Kersten (2011) presented an analytical formulation that included machine stiffness to increase the accuracy in two-dimensional bending. Kersten (2013) further elaborated on this subject and presented a method to generate process parameters solely by comparing target and actual bending radii. Plettke et al. (2012) showed that bending contours produced by three-roll push bending can be efficiently described by the Frenet-Serret formulas. In their investigations, they noticed a deviation of applied tube rotation and resulting rotation angle of the bending plane and introduced an empirical correction parameter called the torsion adjustment coefficient. Using a detailed FE model, Vatter and Plettke (2013) analyzed the behavior of the torsion adjustment coefficient and proposed an empirical characteristic map that describes the tube feed, the tube rotation, and the position of the setting roll in relation to the generated tube rotation angle and curvature. They observed a slight influence of the applied tube rotation on the curvature, but could not define a clear trend. Engel and Groth (2015) performed similar investigations to analyze the torsion deformation that occurs during applied tube rotation and noticed the trend that curvatures do in fact increase slightly with increasing tube rotation. This, however, they could only observe at high curvatures.

The first analytical model to predict the tube rotation needed to produce accurate three-dimensional curves was generated by Staupendahl et al. (2015). Their hypothesis was that during three-dimensional bending of tubes, meaning profiles with circular cross-sections, plastic torsion is negligible and that the main driver for an offset of the applied tube rotation to the resulting rotation of the bending plane is the elastic tube deformation inside the machine during the bending process. As a result, a comprehensive analytical model was set up defining the applied tube rotation required to produce a specific target shape as a function of geometrical tube rotation, static elastic tube deformation, and dynamic elastic tube deformation (Figure 2.3).

The behavior of the static elastic region is described by the torsion deformation of the straight tube of an initial length  $L$ , which is reduced during the bending process by the feed  $y_f$ :

$$\phi_{\text{TRPB,stat}}(y_f) = \frac{M_T}{G \cdot I_P} (L_i - y_f) \quad (2.1)$$



**Figure 2.3:** Geometrical model of three-roll push bending with specified static elastic and dynamic elastic region (Staupendahl et al., 2015)

In the dynamic elastic region, the tube deformation resulting from the applied torsional moment is transported out of the bending process per arc length  $\hat{R}_B$  by incremental torsional springback between the bending roll and the setting roll:

$$\phi_{\text{TRPB,dyn}}(y_f) = \frac{M_T y_f}{G \cdot I_p \cdot \hat{R}_B} (L_i - y_f) \quad (2.2)$$

The static elastic deformation and the dynamic elastic deformation are now added to the targeted cumulative bending plane rotation of a targeted tube contour. Staupendahl et al. (2015) exemplarily show the resulting equations for the cumulative rotation needed to produce a helical shape:

$$\theta_{r,TRPB}(y_f) = \frac{M_T}{G \cdot I_p} (L_i - y_f) + \frac{M_T y_f}{G \cdot I_p \cdot \hat{R}_B} (L_i - y_f) + \frac{h_h \cdot y_f}{2\pi \left( R_h^2 + \left( \frac{h_h}{2\pi} \right)^2 \right)} \quad (2.3)$$

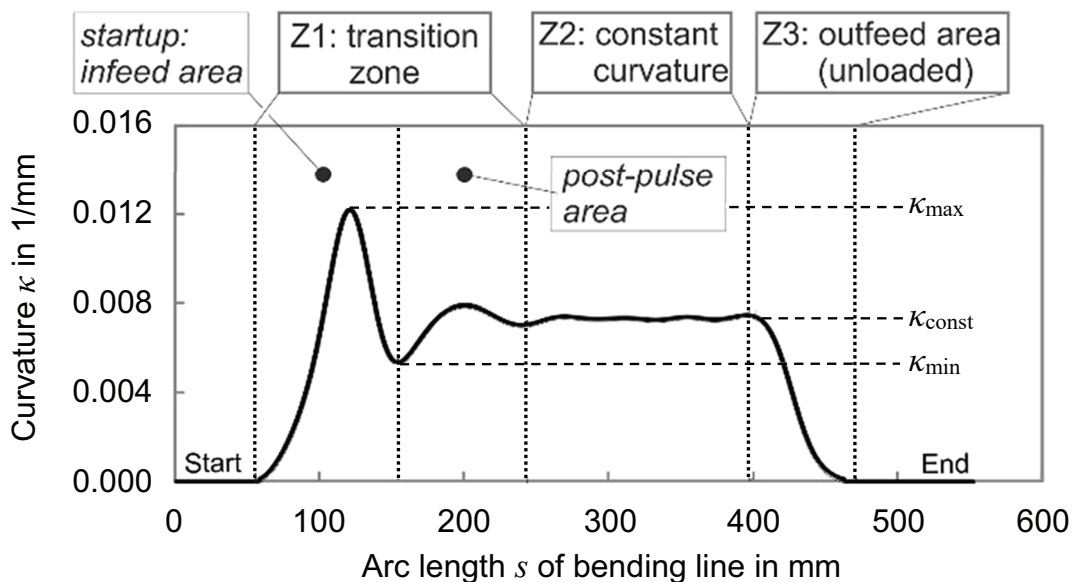
with  $R_h$  being the helix radius and  $h_h$  the pitch. The bending plane rotation that needs to be applied to the tube per feed is described by:

$$d\theta_{r,TRPB}(y_f) = \frac{M_T}{G \cdot I_p} \left( \frac{L_i}{\hat{R}_B} - \frac{2y_f}{\hat{R}_B} - 1 \right) + \frac{h_h}{2\pi \left( R_h^2 + \left( \frac{h_h}{2\pi} \right)^2 \right)} \quad (2.4)$$

In experimental validations, Staupendahl et al. (2015) noticed deviations of 2.5 % to 12.5 %, depending on the bending radius, which stand opposed to deviations of up to 33 % occurring without any compensation. The remaining deviations were assumed the result of using the geometric bending radius in the analytical model, which disregards



elastic springback, and the assumption of ideal plasticity to calculate the bending moment. Another factor was assumed non-considered friction between tube and tools. Groth and Engel laid a strong focus on the investigation of the transition zones occurring during three-roll push bending (see Figure 2.4). They analyzed the influence of the process kinematics on the length and form of the transition zone (Groth and Engel, 2017) and noticed that the strong initial curvature peak in the infeed area can be reduced by increasing the amount of tube feed per setting roll displacement. This, however, also has a direct effect on the transition gradient. Because an ideal curvature jump cannot be realized and a transition gradient cannot be avoided, Groth et al. (2018b) proposed to actually consider this gradient or curvature slope during CAD-modeling.



**Figure 2.4:** Characteristic oscillating curvature distribution generated by three-roll push bending (Groth et al., 2018c)

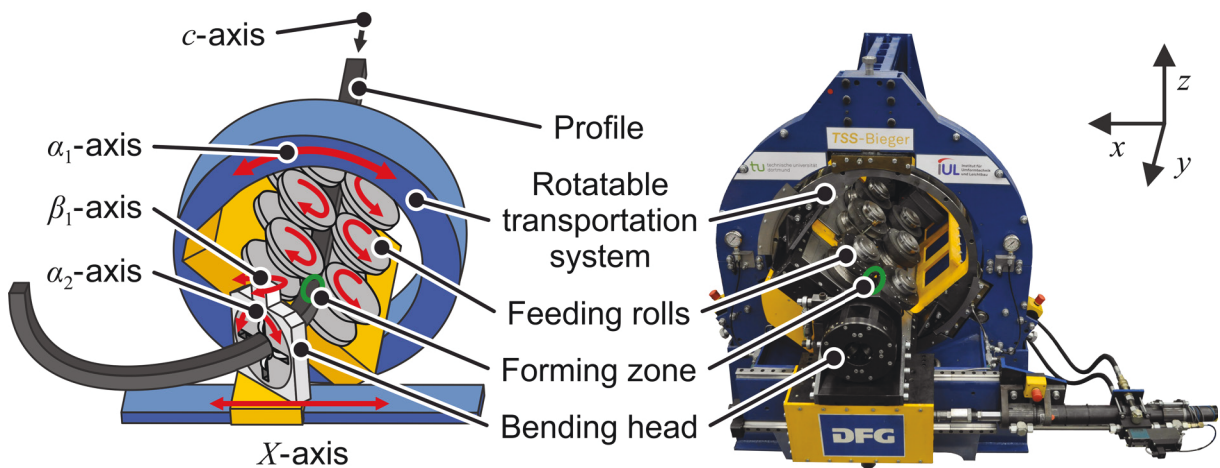
Although Gerlach (2010) has shown that profiles with non-circular cross-sections can be bent with three-roll push bending to two-dimensional bending lines, bending of three-dimensional contours necessitates specialized machines as, for instance, the Hexabend, the TKS-Mewag, the machines by Nissin and J.Neu, and the Torque Superposed Spatial (TSS) Bender (Chatti et al., 2010).

### 2.1.2 TSS Bending

The TSS-Profile bending machine was developed at the IUL with the primary focus being the flexible 3D bending of profiles with arbitrary cross-sections. A patent was filed in 2007 (Hermes and Kleiner, 2013) and, since then, the machine has been continuously extended and optimized. The flexibility is gained by a full kinematic process setup, meaning that the target contour of the profile is solely defined by the movements

of the process axes. To further increase manufacturing flexibility, the process was designed as a roll-based system, which offers continuous forming of bending contours.

The initial process design was generated by Hermes out of the idea of having a counter-roll system with single roll pairs being able to perform movements and rotations relative to the rest of the counter rolls (Hermes et al., 2008). Thereby, a profile transported through this counter-roll system would be bent and twisted according to the relative roll movements. This initial idea was extended by Hermes resulting in the process setup and machine shown in Figure 2.5. In the presented setup, the profile feed ( $c$ -axis) is achieved by 3 roll pairs mounted in a rotatable transportation system. The transportation system can be rotated around the  $\alpha_1$ -axis. During the design process, one counter-roll pair evolved into a compact bending head allowing it to be moved along a linear axis ( $X$ -axis). The bending head can freely rotate around the  $\alpha_2$  and  $\beta_1$ -axis to achieve a tangential movement relative to the profile.



**Figure 2.5:** TSS bending process (left) (Hermes et al., 2008) and TSS bending machine (right)

Hermes (2011) described 4 modes of bending that can be realized with TSS bending:

- Mode 1: Constant bending of a single radius in a single bending plane, where the  $X$ -axis has been moved to a fixed position and only the  $c$ -axis is actually moving
- Mode 2: Bending of variable contours in a single bending plane, whereby the  $X$ -axis and the  $c$ -axis are moving simultaneously
- Mode 3: Bending of 3D contours by simultaneously moving the  $X$ -axis and the  $c$ -axis while changing the bending plane by rotating the  $\alpha_1$ -axis. The  $\alpha_2$ -axis positions itself according to the profile cross-section
- Mode 4: Combined 3D bending and torsion to generate 3D contours with a twisted cross-section

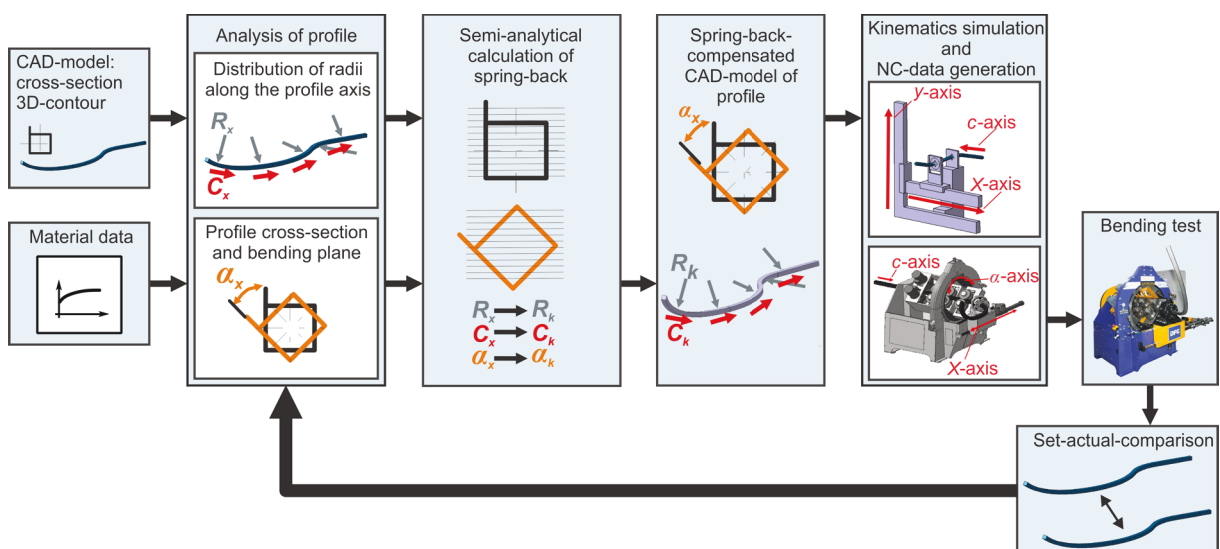
Hermes (2011) conclusion was that modes 1 through 3 are sufficient to bend profiles with arbitrary bending contours and that mode 4 is only needed to add additional twisted elements into the contour, compensate the self-twisting of unsymmetrical profiles or superpose shear stress in order to reduce bending forces and, as a result, springback. As he only focused on modes 1 through 3, Hermes looked at 3D bending as a sequence of bending single curvatures, located on different bending planes. He regarded these single bending operations as pure bending and calculated springback by (Chatti et al. 2010):

$$\frac{1}{R_{L,\text{cor}}} = \frac{1}{R_U} + \frac{F_B L_{B,y}}{EI} \quad (2.5)$$

with:

$$R_{L,\text{cor}} = \frac{L_{B,y}^2}{2(L_{B,x} - \delta_P - \delta_M)} + \frac{(L_{B,x} - \delta_P - \delta_M)}{2} \quad (2.6)$$

$R_U$  describes the radius of the profile after unloading.  $R_{L,\text{cor}}$  is the loaded ideal radius  $R_L$  reduced by the profile stiffness and the machine stiffness. Eq. (2.6) describes  $R_{L,\text{cor}}$  as a function of the bending head displacement along the  $X$ -axis  $L_{B,x}$  needed to produce the loaded ideal radius  $R_L$  and as a function of the profile deflection  $\delta_P$  as well as the machine deflection  $\delta_M$  along the  $X$ -axis caused by the applied bending force. Hermes (2011) used this formulation in a NC-data planning system to setup a compensated CAD-model of the profile part, which subsequently is used in a kinematics simulation to generate the bending axis data (see Figure 2.6). Hermes (2011) used a straight statically indeterminate beam, loaded with a bending force parallel to the  $X$ -axis, to describe the two-dimensional elastic profile behavior and reaction forces of the profile support

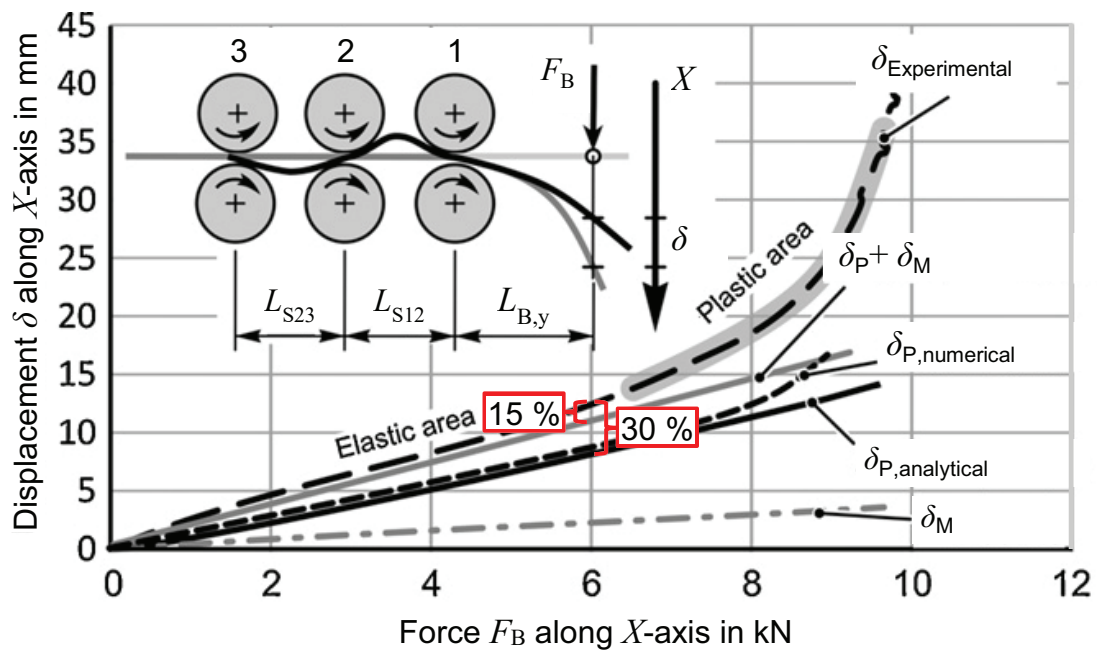


**Figure 2.6:** Process planning system for 3D bending of profiles (Hermes, 2011)

for TSS bending. He interpreted his analytical description to be in a good agreement with his experimental results during purely elastic and elastic-plastic bending. On close inspection of his results on elastic profile deformation, deviations of over 30 % are noticed (see Figure 2.7). Hermes (2011) explains these deviations with significant machine deformation, which Chatti et al. (2010) was able to describe with the following displacement function:

$$\delta_M = 1.496 \cdot 10^{-8} [\text{mm} / \text{N}^2] F_B^2 + 3.974 \cdot 10^{-4} [\text{mm} / \text{N}] F_B \quad (2.7)$$

By adding  $\delta_M$  to  $\delta_P$  the deviation to the experimental deflection was reduced to 15 %.

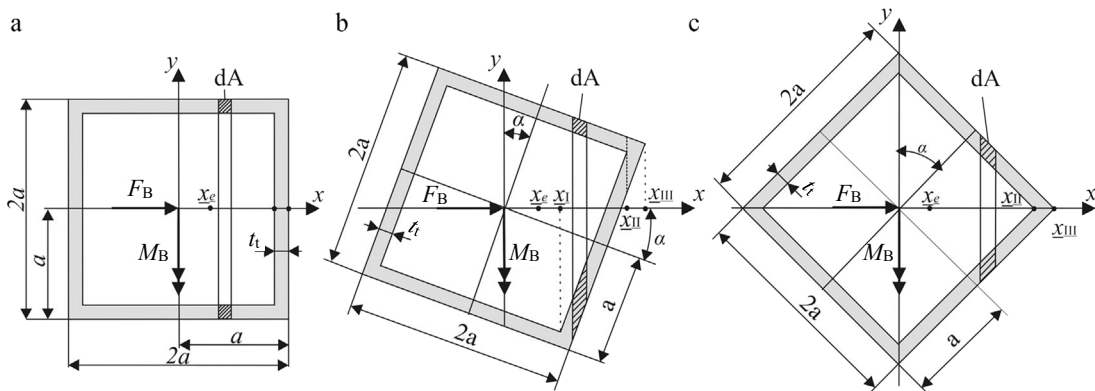


**Figure 2.7:** Experimental profile and machine deflection during TSS bending in comparison to numerical and analytical data (Chatti et al. 2010)

It is important to note that Hermes (2011) did not take into account the torsion of the bending line in his process model. He instead looked at the profile as a flexible shaft and just compensated the bending radius. This kind of mathematical formulation is acceptable as long as the inevitably resulting cross-section rotation relative to the bending plane matches the targeted profile shape or is irrelevant for the targeted application. However, in most cases during profile bending the orientation of the cross-section needs to be additionally varied to produce the desired results. The best example for such a profile is a simple handrail with a rectangular cross-section, where the top face is always supposed to point upwards.

Hudovernik (2014a) performed extensive numerical analyses of the TSS bending process and analyzed the location, size, and evolution of the forming zone. While Hermes (2011) used a CAD program to discretize the profile cross-section into a finite

amount of segments in order to calculate the bending moment according to the elementary bending theory as proposed by Vdovin (1980), Hudovernik et al. (2014b) extended the calculations of Al-Qureshi (1999), who presented an analytical solution for pure bending of tubes with circular cross-sections and material hardening, and El Megharbel et al. (2008), who presented a similar analytical solution for pure bending of profiles with square cross-sections and material hardening in the normal position (Figure 2.8a), to a square cross-section of variable orientation (Figure 2.8a-c).



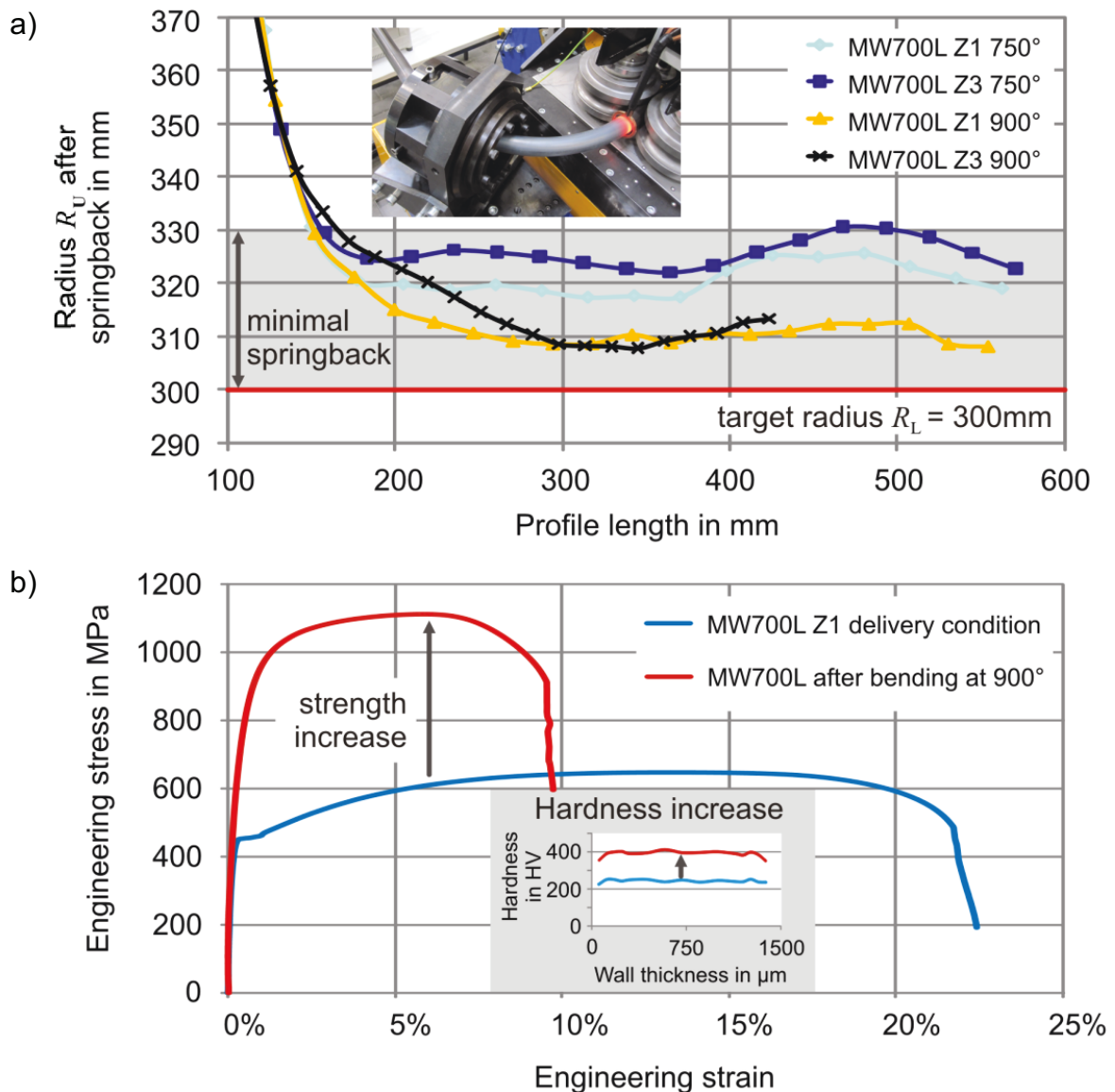
**Figure 2.8:** Thin-walled square cross-section at different orientation angles to the bending plane (Hudovernik et al., 2014b)

Hudovernik (2014a) also noticed significant deviations between the targeted bending plane rotation and experimentally bent profiles, produced via the 3-cDOF TSS bending machine.

Staupendahl et al. (2014b) investigated the possibility to combine TSS bending with an integrated induction-heating unit in order to reduce springback and produce load adapted bent profiles<sup>2</sup> (see Figure 2.9). Additionally, the possibility of combined roll forming and 3D bending was examined (Staupendahl et al. 2014b). In the course of further investigations<sup>3</sup> it became clear that, before the challenges of thermal expansion, thermal distortion, and high temperature material characterization with high heating rates could be met, bending at room temperature would have to be first thoroughly examined.

<sup>2</sup> The new process combination three-dimensional bending and integrated hardening was honored with the second place of the “Stahl-Innovationspreis” 2012 (Steel Innovation Award) in the category “Steel in research and development / Processes”

<sup>3</sup> Pivotal investigations were performed by Juri Martschin in his bachelor thesis: Entwicklung eines Formula Student Chassis unter Anwendung der Verfahrensmöglichkeiten des TSS-Profilbiegeprozesses [Development of a Formula Student chassis using the process potentials of the TSS profile bending process], 2016, supervised by: D. Staupendahl and A. E. Tekkaya

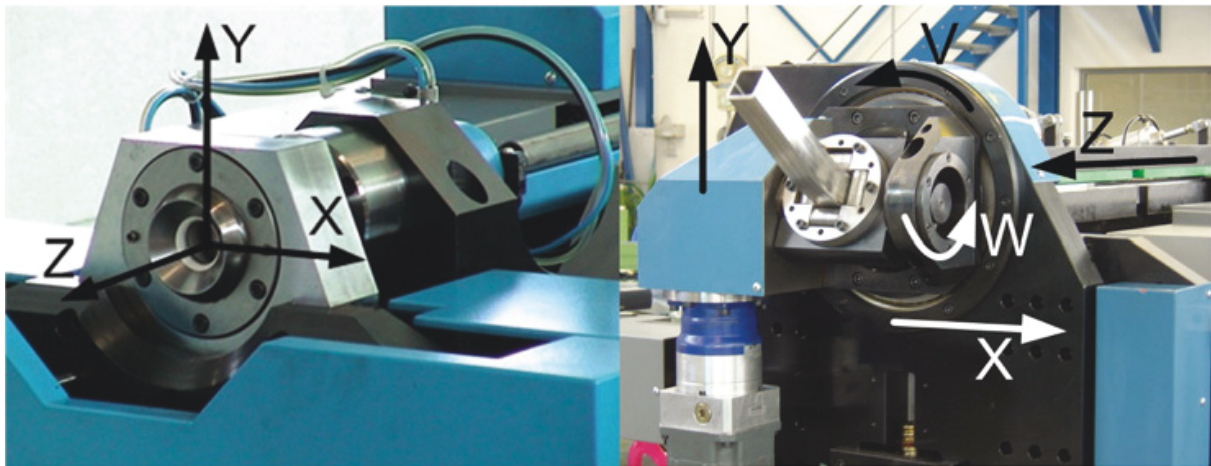


**Figure 2.9:** Springback reduction (a) and strength increase (b) of air hardening steel by combined bending and induction heating (Staupendahl et al., 2014b)<sup>4</sup>

### 2.1.3 MOS bending and process extensions

A highly flexible method to bend tubes and profiles is freeform bending with a movable die. The first of its kind was developed by Murata, Ohashi, and Suzuki in 1989. The original design of the so-called MOS bending method uses a pusher to feed a tube along the Z-axis (Figure 2.10) through a die, mounted in a spherical bearing. The bearing itself is mounted on a bending head, which is moved along the X and Y-axis and, thereby,

<sup>4</sup> The data and foto used to set up Figure 2.9a was originally generated by Christian L bbeck in his bachelor thesis: Verfahrenserweiterung des TSS-Profilbiegeprozesses mittels induktiver Wirbelstromerw rmung f r ferromagnetische Rundrohre [Process extension of the TSS profile bending process by induction heating of ferromagnetic tubes], Technische Universit t Dortmund, 2011, supervised by: D. Staupendahl, M. Hermes, and A. E. Tekkaya.

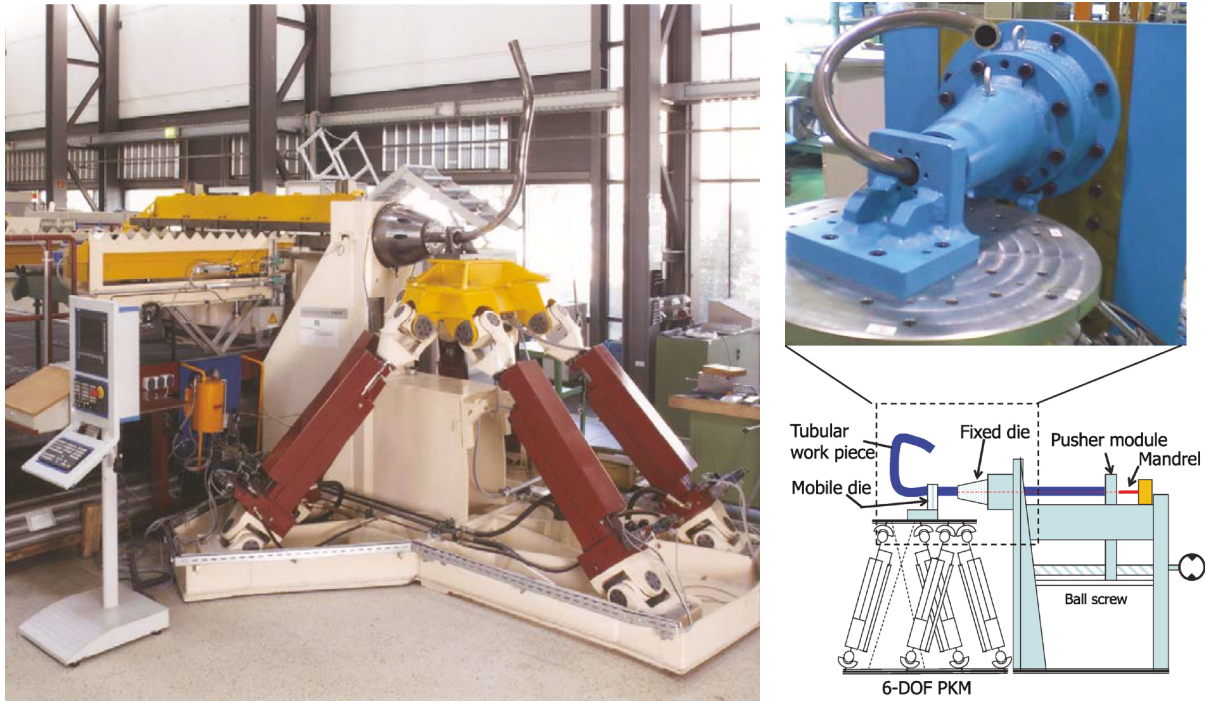


**Figure 2.10:** 3-axis Nissin bending machine (left) and 5-axis Nissin bending machine (right) (Gantner, 2005)

deflects the tube in the desired direction. In experimental investigations Murata et al. (1994) showed that radius to tube diameter ratios ( $R/D$ ) of as little as 2.5 are reachable. Using profiles with square cross-sections, this ratio increased to approximately 8 (Murata, 1996). The bending machines were originally manufactured by Nissin Precision Machines Co. Ltd. and are now licensed to J. Neu GmbH. J. Neu has continued the development and extension of the original machine design and today additionally offers 5 and 6-axis machines. The 5-axis and 6-axis machines have additional rotary axes on the bending head that can guide and twist profiles with non-circular cross-sections (Figure 2.10, right). Gantner (2005) states that the additionally possible use of a mandrel allows  $R/D$  ratios of 2. Although all 3, 5, and 6-axis machines are operated by a stable CNC-system and detailed numerical models have been developed (Beulich et al., 2017), no analytical model exists that describes the forming behavior and would allow efficient and reliable compensated NC-data generation. A compensation of bending data is currently still done with empirical correction factors for material and clearance, leading to acceptable results for single bending radii, but to errors in bending plane rotation of up to 108 % (Guo et al., 2018)

#### 2.1.4 Parallel kinematics bending

A parallel development was done in Japan and Germany on freeform bending with a movable die using parallel kinematics. Neugebauer (2001) developed the Hexabend process (Figure 2.11, left), while Goto et al. (2008) worked on 6-DOF bending. Both systems work on the Stewart-Gough platform (Tsai, 1999) using 6 servo-hydraulic cylinders. The general bending mechanism is similar to MOS bending in that a pusher feeds a tube through a die, which moves in space to deflect and, thereby, bends the profile.



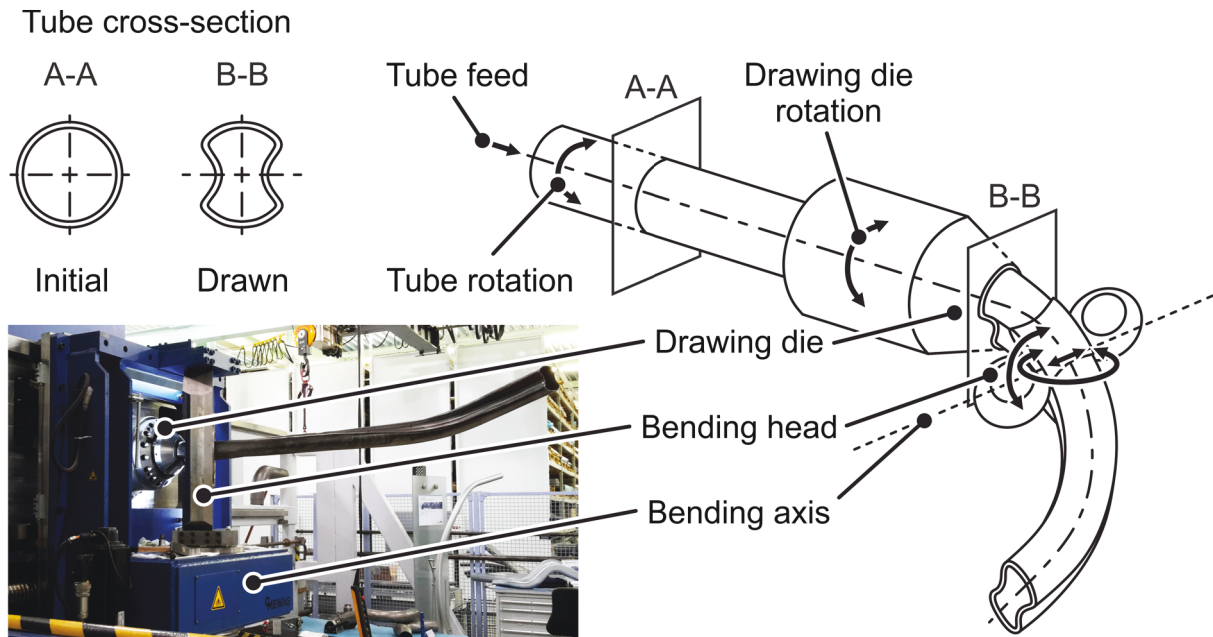
**Figure 2.11:** Left: Hexabend machine (Hoffmann et al., 2013), right: 6-DOF bending machine (Goto et al., 2012)

The difference is that translations and rotations in all three spatial directions are possible. This means that during infeed and outfeed the distance of the bending head to the feeding system can be reduced to minimize scrap. As in the 5 and 6-axis MOS bending machines, a mandrel can be used to minimize cross-section deformation and, as a result, the R/D ratio. The focus of the investigations on the Hexabend process were on system setup and possible machine extensions as for instance induction heating and controlled lubrication. No focus was laid on describing the forming behavior of the tube. Rather an empirical springback correction was performed similar to the strategy used for MOS bending. (Hoffmann et al., 2013)

### 2.1.5 Combined drawing and free-form bending

In 2006, Flehmig et al. (2009) developed a free-form bending process for tubes with circular cross-sections, which, at first glance, operates similar to MOS bending. A pusher feeds a tube through a die, or bending head, which deflects the tube to create a curved shape. The major difference is that the bending head can only move linearly along a single bending axis. The bending plane rotation, needed for 3D bending, is realized by rotating the feeding system. At a closer view, the system is actually much more similar to TSS bending, which also uses a single linear axis to guide the bending head. However, while the TSS bending system uses a roll-based transportation system and is, thus, dependent on friction based contact, the free-forming process by Flehmig et al. (2009) uses a form-closed pusher. Because the patent that Flehmig et al. had applied for was specified for tubes and the TSS bending patent was specified to use similar kine-





**Figure 2.12:** Process principle of combined drawing and free-form bending (Kibben et al., 2013) and machine setup

matics for bending profiles with arbitrary cross-sections, Flehmig et al. could not simply add the profile bending capability to their system. In order to circumvent the TSS bending patent, which specifically meant the profile twisting part, Kibben et al. (2013) combined their system with a tube drawing stage. Figure 2.12 shows the process principle of combined drawing and free-form bending and the realized machine setup. The tube is fed by the pusher through a drawing die, which changes the formerly circular cross-section to an arbitrary shape in a single stage. The drawn tube is then further fed through the bending head, which deflects the tube to create a bend. The bending plane is changed by rotating the tube and the drawing die. If both rotations are applied synchronously, just a change of the bending plane results. In order to create a twisted cross-section, an offset between both rotations needs to be set. Here, it is important to note that the profile is not actually twisted between the drawing die and the bending head – it is simply drawn through a die that has changed orientation. The mechanism is similar to how twisted cross-sections are generated via incremental profile forming (Grzancic et al., 2019). This fact leads to the ability of the machine to create helical shapes with extremely small pitches.

## 2.2 Characterization of tubular material for the use in bending process models

Profile bending is usually looked at as a biaxial process, considering only longitudinal and radial stresses. When bending large radii, as in the case of kinematic bending, radial stresses are frequently neglected to look at the process purely uniaxially. In this case, the direct use of a flow curve generated from a uniaxial tensile test seems an obvious

choice and should lead to acceptable results. In the literature, this procedure is quite common and frequently done. Ludwik (1903) used this method for sheet metal bending, Chatti (1997) and Dirksen (2008) used it for three-roll bending, Hermes (2011) used it for TSS bending, and Engel et al. (2008) used it for rotary draw bending. However, Chatti (1997) explained that the pure use of a tensile test leads to significant errors and recommends the execution of a pure bending test. For 3D bending this test would have to be done for a large amount of combinations of bending radii and bending planes leading to an extensive number of experiments. But why does the pure bending test lead to different results than a smart use of the flow curve in an advanced bending model – especially when bending large radii, where the radial stresses are low?

One reason is the cross-section deformation that might occur during bending and is also seen during a pure bending test (Chatti, 1997). In this case, a process model based on the elementary bending theory, which only considers the original cross-section of the profile, leads to greater deviations when fed with data from a flow curve rather than with data from a bending moment-curvature graph. However, depending on the kinematics of the bending process, for which material data is to be generated, the pure bending test might also overestimate the cross-section deviation – especially when generating data for processes with a localized forming zone as TSS bending, where the non-plastified profile regions stabilize the cross-section in the forming zone. In a pure bending test, the entire profile is bent the same amount at the same time, thus lacking this previously mentioned stabilizing effect.

### **2.2.1 Behavior of tubular material in tension and compression**

Another reason can be a different material behavior in the tensile and compressive direction along the longitudinal axis of the profile. It is generally accepted in the field of engineering that steel exhibits similar behavior when applied with tension or with compression. This is the case for the elastic region, as is important in machine engineering and structural engineering, as well as for the plastic region. Thus, the fairly easy to use tensile test, using probes cut from sheet material or bar stock, depending on the forming process and material used, is usually used as quick means to generate the flow curve. Using a flow criterion like, for example, von Mises, this uniaxial flow curve can then be used to set up a yield locus, which describes the state of stresses of the material in three dimensions. In the case of isotropic materials, this leads to acceptable results, or when using the results in processes, in which main stresses are applied in the tested material direction. For processes with complex stress states, the yield locus can be further optimized by performing additional tests (Yin et al., 2014b). For sheet metal forming mostly only tests in the first quadrant are performed. The most popular test in this quadrant alongside the uniaxial tensile tests is the bulge test, which shows the material behavior under biaxial tensile stress and was first introduced by Hill in 1950. Because of the possibility to perform this test on standard sheet metal testing machines, it has also found

its way into the industry. Alternatively, a stack compression test can be performed, which, because a stress is applied in the normal direction to the sheet, also describes the material behavior in the biaxial stress state. Yin (2014a) mathematically shows the equivalence of the deviatoric stress states of equibiaxial tension and stack compression. For this test, a universal testing machine can be used, making the application readily available for the industry. Special care does have to be taken to overcome the friction between the sheets, however (An and Vegter, 2005). In addition, a biaxial tensile test can be performed, which, however, needs specialized equipment. If this equipment allows changing the proportion of the applied stresses, then various points in the first quadrant of the yield locus can be gained (Verma et al., 2011). Several authors have presented shear specimen geometries that give information on the second quadrant of the yield locus. Yin (2014a) presents a thorough overview of this subject and recommends the plane torsion test with a twin bridge design over the Miyauchi-test as well as the ASTM B831 standard shear test, because of the advantages of having no parasitic reaction torque in the shear zone. In addition, other than the Miyauchi-test specimen the opposite shear zones are loaded in the same direction so that actually anisotropy or kinematic hardening can be taken into account by twisting the specimen into the opposite direction (Yin, 2014a). This means that also data can be gained about the fourth quadrant of the yield locus. However, for the plane torsion test, special equipment is needed. The ASTM B831 specimen can be tested in a standard tensile testing machine and, as the twin bridge specimen, can also be used to gain different data about quadrants two and four. Yin et al. (2014b) actually shows that the modified ASTM specimen proposed by Merklein and Biasutti in 2011 produces similar results as the twin bridge specimen when using an optical strain measurement system for the generation of flow curves, making this geometry the recommended choice for the industry. Because in-plane compression is difficult to be achieved with standard testing machines and because tensile stresses are generally more profound in sheet metal processes, the third quadrant of the yield locus including the uniaxial negative stress directions is usually not experimentally investigated. Instead, the first quadrant is inverted through the point of origin to describe the material yield in quadrant number three. By inverting the yield locus through the point of origin from quadrant one, including the positive uniaxial stress data, to the quadrant three, differences in the behavior in the tensile and compressive region are neglected.

If the profile to be bent now exhibits an anisotropic behavior because of pre-strains induced by the profile production process as, for instance, roll-forming (Weimar, 1966), a process model solely relying on the tensile tests would cause significant errors and impede a thorough investigation of the forming mechanisms themselves.

### 2.2.2 Tensile and compression test methods

Nonetheless, it is common in the industry to rely solely on the tensile test. This is especially due to the difficulty in preparing probes made from sheet metal for uniaxial and biaxial compression tests (Zillman et al., 2015). To prevent buckling of uniaxial compression probes made from sheet metal the height to width ratio has to be kept between 2 or 3 (Wiederhorn et al., 2006). Depending on the wall-thickness of the probes, this can lead to small necessary heights and overall small probes. Alternatively, anti-buckling guides can be used (Wiederhorn et al., 2006), which can lead to high friction and thus to errors in the results, especially at high strains. To reduce friction Yoshida et al. (2002) introduced teflon sheets between the anti-buckling guides and additionally applied petroleum jelly (vaseline) to further reduce the friction. Together with the adhesive bonding of several 1 mm probes to achieve a test specimen with a wall thickness of 5 mm, compressive strains up to 0.1 were achieved for mild steel and high-strength dual phase steel (DP600). Kuwabara et al. (2009) advanced this design by using upper and lower comb type anti-buckling guides that additionally reduce the friction between the tools and the test specimen. Using Copper and Aluminum alloys with a thickness of just 0.25 mm compressive strains up to 0.2 were achieved. Other than Iwata et al. (2001), Boger et al. (2005), and Cao et al. (2009), Kuwabara et al. (2009) did not have to pre-determine the friction between the sample and the guides in order to subtract it from the measured data as the friction only added an error of under 0.6 % to the flow stress of the materials.

Tisza and Lukács (2014) analyzed the springback behavior of high strength dual-phase steel sheets (DP600, DP800, and DP1000) and for this purpose developed a test setup for cyclic high strain tensile and compressive tests. To prevent buckling of the probes they developed a comb-like supporting structure, that, other than the guiding dies by Kuwabara et al. (2009) was not positioned in parallel to the probes axis but vertical to it. As the probe is lengthened or compressed, the comb-like structural elements bend in the according direction. Thus, no friction is applied to the probe. On the other hand, the force needed to bend the structures needs to be known and subtracted from the measured data. Tisza and Lukács (2014) were able to achieve compressive strains up to 0.04.

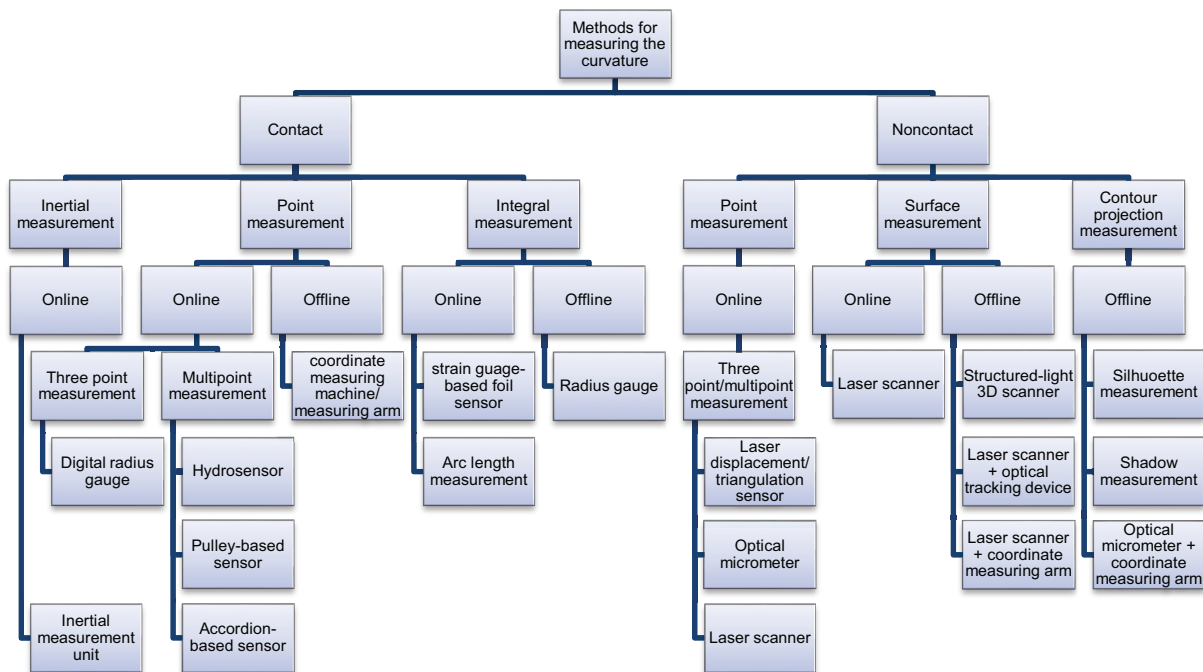
To overcome the necessity of using a buckling guide and the resulting difficulties in subtracting parasitic forces, ul Hassan et al. (2016) used miniature tensile probes with an active gauge length of 2 mm, a width of 2 mm and thickness of 1 mm. These were able to be cut directly out of the investigated 1 mm thick sheet materials, DC04, DP600 and DP1000. Due to the small gauge-length, the application of an extensometer was not possible and the strains had to be measured optically via a GOM Aramis setup. This online strain measurement system offers a great flexibility, in this case enabling the selection of the area with uniaxial stress, but also necessitates a cumbersome analysis of the gathered data, as the points to be used as a virtual extensometer have to be chosen

manually in each analysis. Ul Hassan et al. (2016) were able to compress up to strains in the region of 0.08 while DP600 buckled when exceeding compressive strains greater than 0.03. While the gauge length of 2 mm was two times the material thickness in the performed experiments, which was proposed by Wiederhorn et al. (2006) as being the lower limit to avoid buckling, the length of probe between the clamps of the test setup was 3 mm, which according to Wiederhorn et al. (2006) is the upper limit to avoid buckling. Reducing this free distance, however, might not have been possible due to limitations in the optical measurement system. A relevant observation that ul Hassan et al. (2016) made during their experiments, was that the Young's modulus significantly changes from 0 up to a strain of 0.05, showing a near linear decrease by 6 % for DC04, 21 % for DP600, and 14 % for DP1000. With TSS bending, loaded radii of 450 mm have been achieved during cold forming (Staupendahl et al., 2014b). Considering a linear strain distribution over the cross-section and a profile height of 40 mm, this equals to a maximum strain of 0.045 on the outer fiber. When bending 1000 mm radii, the strain is still 0.02. Considering these values and the findings of Hamad et al. (2015) the variation of the Young's modulus of the chosen materials should be investigated to determine the necessity of including this variation in the further analysis and especially in an analytical process model.

### 2.3 Techniques for the measurement of 3D bending contours

Chatti (1997) analyzed several methods to measure the curvature of two dimensionally bent profiles and differentiated between contact methods, which he divided into point measurement techniques and integral measurement techniques, and noncontact methods. Dirksen (2008), who himself used a laser triangulation sensor, movable relative to the profile along a linear axis to measure the bending line online during three-roll bending, extended this schema by further differentiating between online and offline measuring methods as well as methods that measure a constant curvature versus those that measure a curvature trend. Based on the classifications of Chatti and Dirksen an overview of all relevant curvature measurement techniques is given in Figure 2.13. The differentiation by Dirksen between the capability to measure only constant curvatures or curvature trends is not pursued since any sensor can be easily given this ability by the simple addition of a feed sensor.

3D contour measuring systems available on the market today that can directly compute and output a limited amount of contour data rely on two different measurement techniques. On non-contact contour projection measurement and on non-contact surface measurement. The advantage of the contour projection measurement is the fast processing time, which is in the range of seconds (Thiel, 2009). Examples of projection measurement systems are the TubeInspect products from AICON 3D Systems GmbH (Thiel, 2009), which uses silhouette measurement to determine the bending line, and the TUBOSCAN S by TRACTO-TECHNIK GmbH, which uses shadow measurement. The



**Figure 2.13:** Systems to measure curvatures of bent tubes and profiles. Extended chart based on Chatti (1997) and Dirksen (2008)

disadvantage is that these methods can actually only be used for tubes with circular cross-sections. Tubes with arbitrary cross-sections lead to irregular 2D projections and ambiguous shape computations, which the processing software cannot interpret. Readily available non-contact surface measurement systems, which directly output contour data, rely on a laser scanner fixed to a coordinate measuring arm. Measurement systems using a coordinate measuring arm and only one contact or non-contact sensor can only be used offline. For online measurement, at least three points of the profile have to be measured simultaneously to directly generate radius data. Three point measurements can be done by using contact or non-contact sensors. Non-contact sensors that supply the needed measurement accuracy are optical sensors like laser triangulation, through-beam sensors, and laser scanners. Structured light scanners also supply the needed accuracy, but the data amount of the continuously measured point cloud is too time-consuming for currently available evaluation systems to allow online measurement. Three through-beam sensors in the form of optical micrometers at fixed distances to each other have been used by Klaus (2002) to set up an online-radius sensor for the measurement of curved profile contours directly coming out of an extrusion press. Radii of profiles with non-circular cross-sections were measured by analyzing the light beam blocked in each of the sensors by one edge of the profile, running through the measurement setup. However, the setup used only allowed the analysis of two-dimensional profile contours. Although three through-beam sensors could also be used to measure three-dimensional contours, based on the sensors ability to detect only the light beam blocked by the object

moving through it and thereby not being able to detect cross-sectional details, the measurements would be limited to profiles with circular cross-sections. A single laser displacement sensor mounted on a linear guide was used by Dirksen (2008) to setup an online measurement system during three-roll bending. The three points required for a radius definition were gained by the sensor moving back and forth at a high speed relative to the profile movement during bending.

Although optical non-contact sensors offer a higher flexibility, can be easily implemented in existing processes (Döbele et al., 2009), and are not affected by wear, contact sensors are much more inexpensive and, especially in low batch production, have their *raison d'être*. Chatti (1997), for instance, successfully integrated a pulley-based multipoint contact sensor in a closed-loop control of a three-roll bending machine.

Ghiotti et al. (2017) developed a mandrel with an embedded inertial measurement unit (IMU) to monitor the bent geometry during three-roll push bending of round tubes online. The IMU comprises a 3-axis gyroscope to measure the angular velocities and a 3-axis accelerometer. Integrating the acquired values results in the rotation and displacement of the mandrel. Comparing the targeted movement with the actual movement given by the IMU, the springback of the tube was calculated. Here, Magro et al. (2019) noticed a high dependency of the accuracy on the clearance of the mandrel and the bending angle and proposed to couple the IMU rigidly to the free end of the tube.

Moreover, the company TeZet Technik AG, although offering a system to optically measure two-dimensional contours of profiles with rectangular cross-sections (TeZet, 2017), still recommends using a contact measurement technique for the measurement of profiles with three-dimensional contours (TeZet, 2010). But, although being able to analyze these contours, comparable to contact and non-contact systems from AICON, GOM and others, the system by TeZet is only able to perform offline measurements.





### 3 Aim

3D bent profiles have the potential to meet the current demand for aesthetic and organic design that includes round shapes and continuous curves. In addition, the ever-increasing demand of higher productivity, higher flexibility, and a reduced environmental footprint can potentially be met by the possibility of integrating multiple single parts and, thus, several functions in one single part. This allows the omission of additional handling and joining steps and can result in an overall reduction of processing time. Several 3D bending processes exist that were designed to meet exactly these challenges. Interesting is, however, that these processes are not yet widely used in the industry.

One reason could be that the mechanisms of 3D profile bending are not yet fully understood. As 3D profile bending is a kinematic process and, thus, does not use form-bound tools to generate the profile contour but rather solely uses actuator movements, it is extremely sensitive to imprecise actuator control. If, now, the profile bending mechanisms are not well described, the process control lacks the accuracy needed to drive the actuators to produce a part with the targeted precision. The aim of this work is to fill this knowledge gap in order to allow designers and machine manufacturers to take full use of this promising technology.

As a first step to achieve this goal, the geometrical characteristics of 3D shaped profiles have to be analyzed, especially addressing the differences between 3D profile contours with and without torsion. Based on this analysis, the essential amount and position of controlled degrees of freedom (cDOFs) will be derived that 3D bending kinematics need to incorporate for the production of these shapes. This step will lay the basis for a classification of currently available 3D bending processes in terms of producible part complexity.

After establishing the geometrical foundation for 3D profile bending, a 5-cDOF bending machine will be set up, based on the TSS bending process. In order to open up the possibilities to thoroughly investigate the process behavior, not only during bending, but also during twisting, a fully integrated torque sensor will be developed. In the following, the experimental setup will be used to set up a comprehensive numerical process model, which will be able to not only provide the process forces in all spatial directions, but also the stresses and strains in the profile. To overcome the current time-consuming task of first, optically measuring the surface contour of the profile, then, converting the recorded point cloud to a mathematically usable format and, finally, extracting the relevant contour data, an efficient inline-measurement system will be developed.

The experimental and numerical setup will, then, be used to generate fundamental process understanding of 3D bending. The underlying process analysis will be structured into an elastic analysis, which will show elastic profile deformation due to bending and twisting and the relationship and reciprocal behavior of the applied forces and torque.

An emphasis will be laid on the unwanted bending plane rotation that can be induced by applied torque. The plastic analysis will focus on describing the stresses and strains in the forming zone of the profile. Here, not only the stresses and strains in axial direction will be investigated, as has been the case in all previous investigations of 3D profile bending, but also along the perimeter of the cross-section. Additionally, shear stresses and strains over the cross-section will be analyzed that result from profile twist. An emphasis will be laid on the investigation of simultaneous profile deformation by bending and by torsion and the impact this coincidental deformation has on the resulting bending moment as well as torque.

Finally, the geometrical description of 3D profile bending will be merged with the elastic and plastic profile description to a comprehensive process model. The validation of this process model will be shown using experimentally produced sample geometries.

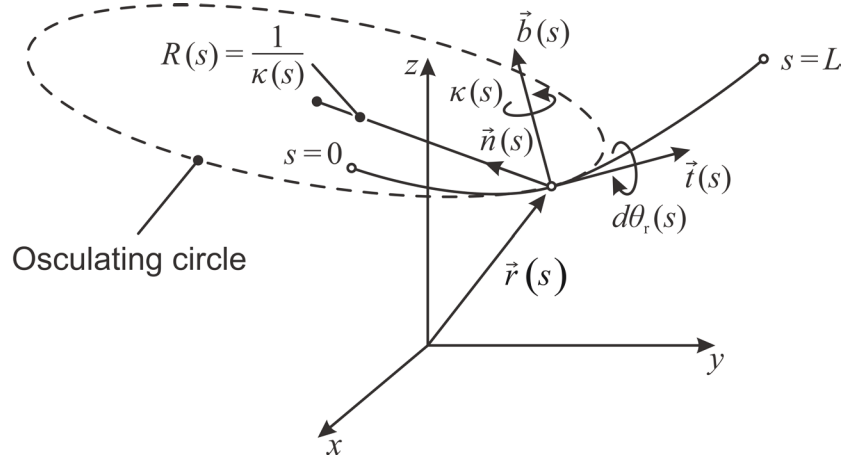
## 4 Characteristics of 3D profile bending

In Section 2.1 tube and profile bending processes were discussed that allow the production of two-dimensional and three-dimensional tubular shapes. As such, 2D profile bending can be defined as forming profiles into two-dimensional shapes where all bending radii lie in the same bending plane. Considering cross-sections with symmetry along the bending plane or point symmetry around the center of area, the bending process can fairly accurately be described by only considering longitudinal stresses and, thereby, regarding it as a uniaxial problem. Depending on the relation of wall-thickness to the cross-sectional diameter and the relation of the bending radius to the cross-sectional diameter the consideration of perimetral and radial stresses can further increase model accuracy (see Section 7.2). When bending non-symmetrical cross-sections, shear stresses are introduced into the profile because bending processes are generally set up so that the resultant of the bending force intersects the center of area of the cross-section rather than the center of shear (Groth and Engel, 2018a). These shear stresses cause an internal torque around the center of area of the cross-section and, thereby, result in profile twist. To achieve in-plane bends, this internal torque has to be compensated by an externally applied load. 3D profile bending can be defined as forming profiles into three-dimensional shapes. But what defines a three-dimensional profile shape? Section 2.1 gave an overview of 3D bending processes and their respective process models with the outcome that, up until now, three-dimensional bending is seen as a sequence of bending single curvatures, located on different bending planes. This view breaks down the three-dimensional problem into several two-dimensional ones, allowing the above-mentioned simplifications for 2D bending to be applied. But is this an accurate representation of what actually happens during 3D bending?

### 4.1 Geometrical definition of 3D contours

#### 4.1.1 Frenet-Serret description of 3D curves

In general, continuous and differentiable three-dimensional curves can be mathematically described using the Frenet-Serret formulas, originally described by Frenet (1852) and Serret (1951). The formulas describe the local behavior of a curve using a frame made up of a tangent, normal, and binormal unit vector (*tnb*-frame). The rotation of the frame around the tangent unit vector describes the mathematical torsion and the rotation of the frame around the binormal unit vector describes the curvature at arc length  $s$  of the curve. The tangent and the normal unit vector span the osculating plane on which the osculating circle lies, which has a second order contact with the curve (see Figure 4.1). The term torsion is misleading, as the mathematical torsion does not have anything to do with mechanical torsion or twist but actually describes the relative rotation



**Figure 4.1:** Curve  $\vec{r}$  with local  $tnb$ -frame and representation of the osculating circle

of one osculating plane to the next. The term torsion in its mathematical sense is, thus, replaced by the term rotation. If the three-dimensional curve  $\vec{r}$  is described in terms of the arc length  $s$ ,

$$\vec{r}(s) = \begin{pmatrix} x(s) \\ y(s) \\ z(s) \end{pmatrix} \quad (4.1)$$

then the curvature  $\kappa$ , which is regarded as a scalar, can be described by the change of the tangent  $\vec{t}$ , or in other words, by the derivative of  $\vec{t}$ . Since  $\vec{t}$  is the derivative of  $\vec{r}$ , curvature  $\kappa$  is simply the absolute value of the second derivative of  $\vec{r}$ :

$$\kappa(s) = \left\| \frac{d\vec{t}(s)}{ds} \right\| = \left\| \frac{d^2\vec{r}(s)}{ds^2} \right\| \quad (4.2)$$

Considering that

$$\vec{n}(s) = \frac{\frac{d\vec{t}(s)}{ds}}{\left\| \frac{d\vec{t}(s)}{ds} \right\|} \quad (4.3)$$

it follows that

$$\kappa(s)\vec{n}(s) = \frac{d\vec{t}(s)}{ds} = \frac{d^2\vec{r}(s)}{ds^2} \quad (4.4)$$

The derivative of  $\vec{n}$  with respect to  $\vec{r}$  is:

$$\frac{d\vec{n}(s)}{ds} = \frac{1}{\kappa} \frac{d^3\vec{r}(s)}{ds^3} \quad (4.5)$$

The binormal unit vector  $\vec{b}$  is normal to  $\vec{t}$  and  $\vec{n}$ :

$$\vec{b}(s) = \vec{t}(s) \times \vec{n}(s) \quad (4.6)$$

The change of  $\vec{b}$  is described by:

$$\frac{d\vec{b}(s)}{ds} = \frac{d}{ds} [\vec{t}(s) \times \vec{n}(s)] = \underbrace{\frac{d\vec{t}(s)}{ds} \times \vec{n}(s)}_{0 \text{ since } \frac{d\vec{t}(s)}{ds} \text{ and } \vec{n}(s) \text{ are parallel}} + \vec{t}(s) \times \frac{d\vec{n}(s)}{ds} \quad (4.7)$$

As  $d\vec{b}(s)/ds \perp \vec{t}(s)$  and  $d\vec{b}(s)/ds \perp \vec{b}(s)$  it follows that  $d\vec{b}(s)/ds$  is parallel to  $\vec{n}$ . As such, the scalar rotation  $d\theta_r$  and the change of  $\vec{b}$  can be put into the following relation:

$$-d\theta_r(s) \vec{n}(s) = \frac{d\vec{b}(s)}{ds} \quad (4.8)$$

Multiplying both sides with the unit vector  $\vec{n}$  and inserting Eq. (4.7) gives:

$$d\theta_r(s) = \left[ \frac{d\vec{n}(s)}{ds} \times \vec{t}(s) \right] \cdot \vec{n}(s) = [\vec{t}(s) \times \vec{n}(s)] \cdot \frac{d\vec{n}(s)}{ds} \quad (4.9)$$

Inserting Eqs. (4.4) and (4.5) into Eq. (4.9) yields:

$$d\theta_r(s) = \frac{1}{\kappa^2} \left[ \frac{d\vec{r}(s)}{ds} \times \frac{d^2\vec{r}(s)}{ds^2} \right] \cdot \frac{d^3\vec{r}(s)}{ds^3} \quad (4.10)$$

Eq. (4.4) relates the change of the tangent unit vector to the curvature. Eq. (4.8) relates the change of the binormal unit vector to the rotation. In order to relate the change of the normal unit vector to both scalars,  $\vec{n}$  is written as a vector product of  $\vec{b}$  and  $\vec{t}$ . Thus, the derivative of  $\vec{n}$  is:

$$\frac{d\vec{n}(s)}{ds} = \frac{d}{ds} [\vec{b}(s) \times \vec{t}(s)] = \frac{d\vec{b}(s)}{ds} \times \vec{t}(s) + \vec{b}(s) \times \frac{d\vec{t}(s)}{ds} \quad (4.11)$$

Inserting Eqs. (4.4) and (4.8) into Eq. (4.11) yields:

$$\frac{d\vec{n}(s)}{ds} = -d\theta_r(s) \vec{n}(s) \times \vec{t}(s) + \vec{b}(s) \times \kappa(s) \vec{n}(s) \quad (4.12)$$

Considering that

$$-\vec{b}(s) = \vec{n}(s) \times \vec{t}(s) \quad \text{and} \quad -\vec{t}(s) = \vec{b}(s) \times \vec{n}(s) \quad (4.13)$$

Eq. (4.12) can be written as:

$$\frac{d\vec{n}(s)}{ds} = d\theta_r(s) \vec{b}(s) - \kappa(s) \vec{t}(s) \quad (4.14)$$

Eqs. (4.4), (4.8), (4.14) are what is known as the Frenet-Serret formulas and can be written in the following matrix notation:

$$\frac{d}{ds} \begin{pmatrix} \vec{t}(s) \\ \vec{n}(s) \\ \vec{b}(s) \end{pmatrix} = \begin{pmatrix} 0 & \kappa(s) & 0 \\ -\kappa(s) & 0 & d\theta_r(s) \\ 0 & -d\theta_r(s) & 0 \end{pmatrix} \begin{pmatrix} \vec{t}(s) \\ \vec{n}(s) \\ \vec{b}(s) \end{pmatrix} \quad (4.15)$$

If curve  $\vec{r}$  is given in terms of a path-independent variable such as the time,

$$\vec{r}(t) = \begin{pmatrix} x(t) \\ y(t) \\ z(t) \end{pmatrix} \quad (4.16)$$

which, according to Plettke et al. (2012), can be the case if the curve was generated in a CAD program and saved in the IGES or STEP format, the curvature can be calculated by:

$$\kappa(t) = \frac{\left\| \frac{d\vec{r}}{dt} \times \frac{d^2\vec{r}}{dt^2} \right\|}{\left\| \frac{d\vec{r}}{dt} \right\|^3} \quad (4.17)$$

and the rotation can be calculated by:

$$d\theta_r(t) = \frac{\left( \frac{d\vec{r}}{dt} \times \frac{d^2\vec{r}}{dt^2} \right) \cdot \frac{d^3\vec{r}}{dt^3}}{\left\| \frac{d\vec{r}}{dt} \times \frac{d^2\vec{r}}{dt^2} \right\|^2} \quad (4.18)$$

The Frenet-Serret formulation of curves can be directly applied to the bending line of a profile. Following the nomenclature of VDI 3431, the osculating plane can be described as the bending plane, with the angle between two successive planes called rotation angle.

#### 4.1.2 General mathematical description of 3D-shaped profiles

In order to see if the description of the bending line is sufficient to describe a three-dimensionally shaped profile, a case study on the geometry of a helical handrail is performed. Only a geometrical analysis is performed. Elastic and plastic material behavior is neglected in this case. In the example, a helix is described whose center axis falls together with the  $z$ -axis. The radius of the helix is given the parameter  $R_h$ , the pitch of the helix is given the parameter  $h_h$ . The  $x$  and  $y$ -coordinates of the points on the curve that make up a helix are parametrically described in the same way as those of a circle. The difference is the presence of an additional  $z$ -coordinate that describes the point

movement in the  $z$ -direction. The  $z$ -coordinate has to be parametrized in such a way that the pitch  $h_h$  is 0 at  $t=0$  and linearly increases to  $h_h$  at  $t=1$ . The resulting parametric representation is:

$$\vec{r}(t) = \begin{pmatrix} x(t) \\ y(t) \\ z(t) \end{pmatrix} = \begin{pmatrix} R_h \cos(2\pi t) \\ R_h \sin(2\pi t) \\ h_h t \end{pmatrix} \quad (4.19)$$

If the parameter  $t$  is seen as time then the tangent vector  $d\vec{r}/dt$  can be regarded as the velocity vector. The absolute value of the velocity vector is the instantaneous speed:

$$\frac{ds}{dt} = \left\| \frac{d\vec{r}(t)}{dt} \right\| = \sqrt{\left[ \frac{dx(t)}{dt} \right]^2 + \left[ \frac{dy(t)}{dt} \right]^2 + \left[ \frac{dz(t)}{dt} \right]^2} = \sqrt{R_h^2 (2\pi)^2 + h_h^2} \quad (4.20)$$

The arc length of of the helix can, thus, be described by:

$$s(t) = \int_0^t \frac{ds}{dt} = t \sqrt{R_h^2 (2\pi)^2 + h_h^2} \quad (4.21)$$

Using Eq. (4.21) together with Eq. (4.19), the helix can be stated in terms of the arc length  $s$ :

$$\vec{r}(s) = \begin{pmatrix} x(s) \\ y(s) \\ z(s) \end{pmatrix} = \begin{pmatrix} R_h \cos\left(\frac{2\pi}{\sqrt{R_h^2 (2\pi)^2 + h_h^2}} s\right) \\ R_h \sin\left(\frac{2\pi}{\sqrt{R_h^2 (2\pi)^2 + h_h^2}} s\right) \\ \frac{h_h}{\sqrt{R_h^2 (2\pi)^2 + h_h^2}} s \end{pmatrix} \quad (4.22)$$

The curvature is calculated by:

$$\kappa(s) = \frac{R_h (2\pi)^2}{R_h^2 (2\pi)^2 + h_h^2} \quad (4.23)$$

The rotation is calculated by:

$$d\theta_r(s) = \frac{2\pi h_h}{R_h^2 (2\pi)^2 + h_h^2} \quad (4.24)$$

Figure 4.2 shows an exemplary helical handrail with a circular cross-section (a) in comparison to helical handrails with square cross-sections (b, c). The bending line in all three cases is described by a helix with a helix radius  $R_h = R_{h,1}$  and a pitch of  $h_h = 5R_{h,1}$  resulting in:

$$\kappa_{5R_h}(s) = \frac{(2\pi)^2}{R_h(2\pi)^2 + 25R_h} \quad (4.25)$$

and

$$d\theta_{r,5R_h}(s) = \frac{10\pi}{R_h(2\pi)^2 + 25R_h} \quad (4.26)$$

Neglecting cross-section deformation during production of the helical handrail with the circular cross-section and, thereby, seeing the cross-section as keeping its original shape, the rotation of the cross-section around the bending line can be said to have no effect on the final shape of the bent part.

For profiles with circular cross-sections, it can be followed that in a purely geometrical analysis the sole description of the bending line is sufficient to describe the shape of a 3D part. As a result, the view of 3D bending as a sequence of bending single curvatures, located on different bending planes is valid in this case.

For any helix, whose center axis falls together with the  $z$ -axis, the angle of the normal unit vector to the  $xy$ -plane is defined by:

$$\omega_n(s) = \frac{\pi}{2} - \cos^{-1}(\vec{n} \cdot \vec{e}_z) = \sin^{-1}(0) = 0 \quad (4.27)$$

where  $e_z$  is the unit vector in  $z$ -direction. At the same time the angle of the tangent unit vector of any helix to the  $xy$ -plane is defined by:

$$\omega_t(s) = \frac{\pi}{2} - \cos^{-1}(\vec{t} \cdot \vec{e}_z) = \sin^{-1}(\vec{t} \cdot \vec{e}_z) \quad (4.28)$$

For the special case of a helix with  $R_h = R_{h,1}$  and a pitch of  $h_h = 5R_{h,1}$  Eq. (4.28) becomes:

$$\omega_{t,5R_h}(s) = \sin^{-1}\left(\frac{5}{\sqrt{(2\pi)^2 + 25}}\right) \quad (4.29)$$



So, although Eq. (4.26) implies a continuously changing bending plane with a constant rotation  $d\theta_{r,5R_h}$ , Eqs. (4.27) and (4.29) show that the angle between the bending plane and the  $xy$ -plane is constant over the complete helical bending line. What this means for a profile with a square cross-section can be seen in Figure 4.2 b). The figure shows the outcome of shaping a profile with a square cross-section solely on the basis of the bending line. At  $s = 0$  the cross-section position is defined so that two parallel sides of the square are parallel to the  $xy$ -plane, while the two adjacent sides are parallel to the  $yz$ -plane. With an increasing arc length  $s$ , the bending plane rotates relative to the initial position of the cross-section. Since the angle of the bending plane relative to the  $xy$ -plane actually does not change, the result is a rotation of the cross-section around the bending line in the  $xyz$ -coordinate system. Figure 4.2 b) shows the rotation of the cross-section at arc lengths:

$$s(t) \text{ with } t = \left\{ 0, \frac{1}{5}, \frac{1}{2}, \frac{4}{5}, 1 \right\} \quad (4.30)$$

Relative to the  $tnb$ -frame, the rotation of the cross-section has the opposite sign of the bending plane rotation. In the case of the exemplary helix, the rotation  $d\theta_{5R_h}$  of the cross-section can be described by:

$$d\theta_{5R_h}(s) = -\frac{10\pi}{R_h(2\pi)^2 + 25R_h} \quad (4.31)$$

The cumulative rotation, which describes the total rotation of the cross-section at an arc length  $s$  can be calculated by:

$$\theta_{5R_h}(s) = \int_0^s d\theta_{5R_h}(s) ds = -\frac{10\pi}{R_h(2\pi)^2 + 25R_h} s \quad (4.32)$$

or, in terms of  $t$ :

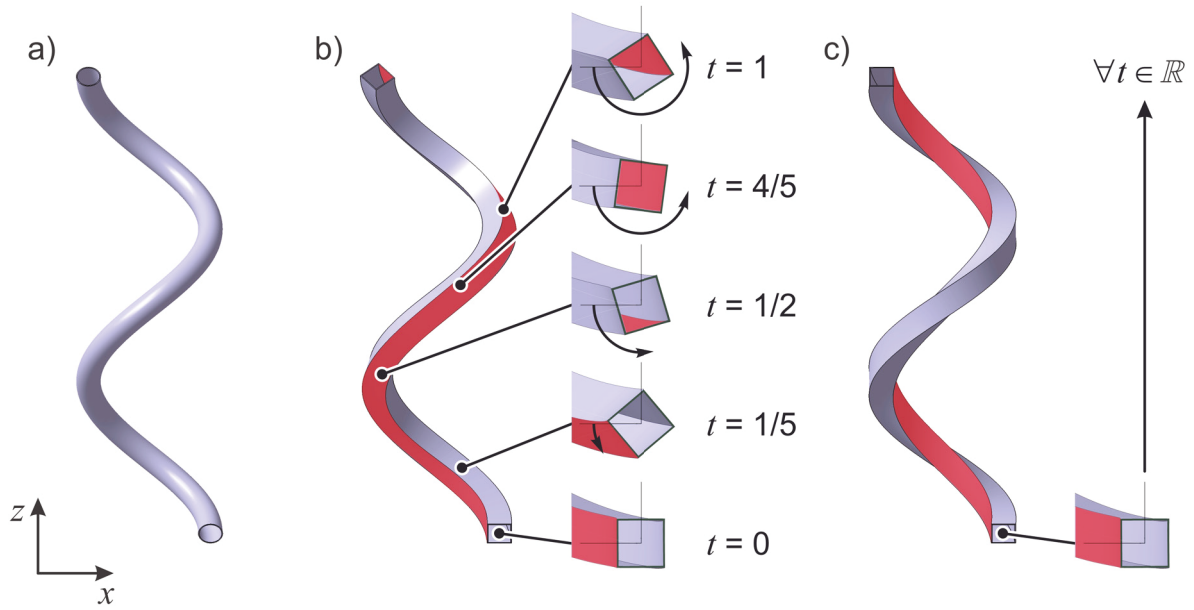
$$\theta_{5R_h}(t) = -\frac{10\pi}{\sqrt{(2\pi)^2 + 25}} t \quad (4.33)$$

Generalized for any helix the cumulative cross-section rotation can be stated as:

$$\theta(s) = \int_0^s d\theta(s) ds = -\int_0^s d\theta_r(s) ds = \frac{2\pi h_h}{R_h^2(2\pi)^2 + h_h^2} s \quad (4.34)$$

or, in terms of  $t$ :

$$\theta(t) = -\frac{2\pi h_h}{\sqrt{R_h^2(2\pi)^2 + h_h^2}} t \quad (4.35)$$



**Figure 4.2:** 3D-bent helical profiles with an identical bending line, a) circular cross-section, b) square cross section,  $d\phi = 0$ , c) square cross section,  $d\phi = d\theta_r$

Relative to  $tnb$ -frame, the cross-section rotation appears to be twisted. Thus, in the following this relative rotation will be called apparent twist  $\phi_{\text{apparent}}$ . The relation of the cumulative rotation  $\theta_{r,5R_h}$  and the cumulative twist  $\phi_{5R_h}$  for the helix shown in 4.2 b) and the resulting apparent twist over the arc length  $s$  is shown in Figure 4.3 a). In order to produce a shape as shown in Figure 4.2 c), whose cross-section does not rotate relative to the  $tnb$ -frame and, hence, shows no apparent twist, the cross-section has to actively be twisted around the tangent unit vector with the same amount as the bending plane rotates. For the helix this means that the twist per unit length  $d\phi_{5R_h}$  of the cross-section has to be equal to  $d\theta_{r,5R_h}$  and, as a result, the cumulative twist  $\phi_{5R_h}$  equal to the cumulative rotation  $\theta_{r,5R_h}$ . The relation of the parameters is shown in Figure 4.3 b).

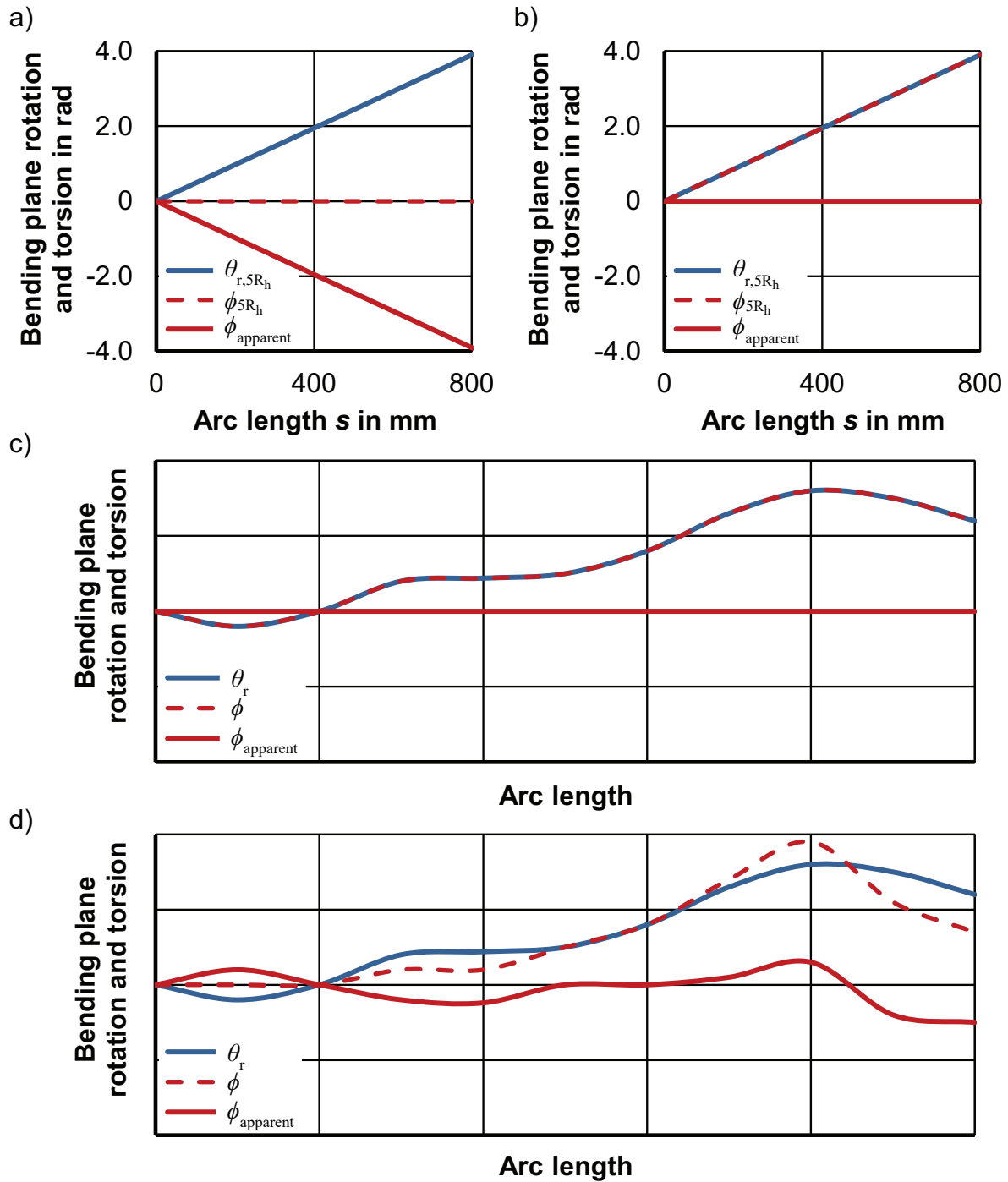
This interaction can actually be generalized to any three-dimensional shape: If the apparent cross-sectional twist of profile geometry is supposed to be zero, the twist per unit length  $d\phi$  of the cross-section has to be equal to  $d\theta_r$  and, as a result, the cumulative twist  $\phi$  equal to the cumulative rotation  $\theta_r$ . Figure 4.3 c) shows this effect qualitatively. To generate a specific non-zero apparent twist, the difference between  $d\phi$  and  $d\theta_r$  ( $\phi$  and  $\theta_r$  accordingly) has to be controlled. A qualitative representation is shown in Figure 4.3 d). The general formula for the apparent twist per unit length is:

$$d\phi_{\text{apparent}} = d\phi - d\theta_r \quad (4.36)$$

and for the cumulative apparent twist is:

$$\phi_{\text{apparent}} = \phi - \theta_r \quad (4.37)$$

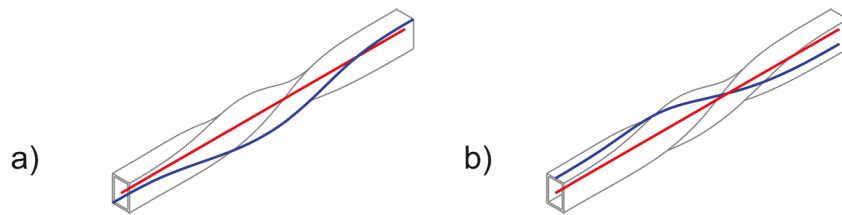
In conclusion it can be said, that in a purely geometrical analysis while for profiles with circular cross-sections it is sufficient to solely describe the bending line, profiles with non-circular cross-sections necessitate the additional information about the cross-sectional twist aka torsion  $d\phi(s)$  to describe arbitrary 3D shapes.



**Figure 4.3:** Cumulative bending plane rotation  $\theta_r$  and apparent twist  $\phi_{\text{apparent}}$  for a helix with a square cross-section and a)  $d\phi = 0$  and b)  $d\phi = d\theta_r$ , qualitative representation of general interaction of  $\theta_r$  and  $\phi$  for c)  $d\phi = d\theta_r$  and d) varying  $d\phi$

### 4.1.3 Extraction of contour data from structural models

Profile contours, especially complex three-dimensional ones, are generally designed with CAD software as part of comprehensive parametric structural models. Usually the contours are first designed as line models, with the line representing the bending line of the shape. In a next step, a profile is extruded along this bending line. Following the elementary bending theory and the VDI 3431, the bending line should pass through the center of area of the cross-section, used as a basis for the extrusion. For 3D-bending it is now necessary to extract the relevant curvature, rotation, and torsion data to be further processed in the bending process control. In the case that a three times differentiable parametric spline or B-spline curve is used as the bending line, Eqs. (4.4) or (4.17) can be used to calculate the local curvatures and Eqs. (4.10) or (4.18) can be used to calculate the local bending plane rotation. To extract the data about profile torsion, another secondary line  $\vec{r}_s$  is needed that passes through another point other than the center of area of the cross-section. Depending on how the profile was extruded in the CAD software, a secondary line might already exist. If not, then a new secondary line needs to be derived from the CAD shape. An effective way is to generate a line along an edge of the profile or along a surface as shown in Figure 4.4.



**Figure 4.4:** Bending line (red) needed to describe 3D-curve and secondary line (blue) needed to describe torsion with a) the secondary line lying on an edge of the profile and b) the secondary line lying on an arbitrary surface of the profile<sup>5</sup>

To extract the torsion data from the profile that is now described by a central bending line  $\vec{r}$  and a secondary line  $\vec{r}_s$ , first of all an orientation vector  $\vec{o}$  between these two lines has to be generated, lying on the normal plane spanned by  $\vec{n}$  and  $\vec{b}$ , parameterized either as a function of  $s_s$  or  $t_s$ . In the following all further parametrization will be based on the arc length, so  $s$  for the bending line and  $s_s$  for the secondary line. In a first step, the intersection point  $\vec{P}_{\text{int}}$  of  $\vec{r}_s$  and the normal plane  $N$  has to be calculated. If the plane

<sup>5</sup> Based on a figure by Jan Kersting from his student thesis: Entwicklung eines Prozesssimulationsmodells für das TSS-Biegen [Development of a Process Simulation Modell for TSS Bending], Technische Universität Dortmund, 2012, supervised by: D. Staupendahl and A. E. Tekkaya

is stated in the point-normal form, then  $\vec{r}$  simply has to be inserted as the point vector and  $\vec{r}_s$  as the position vector. Thus,  $\vec{P}_{\text{int}}$  can be described by:

$$\vec{P}_{\text{int}}(s) = \vec{r}_s(s_s) \quad (4.38)$$

where  $\vec{r}_s(s_s)$  can be found by solving Eq. (4.39) for  $s_s$ :

$$[\vec{r}_s(s_s) - \vec{r}(s)]\vec{t}(s) = 0 \quad (4.39)$$

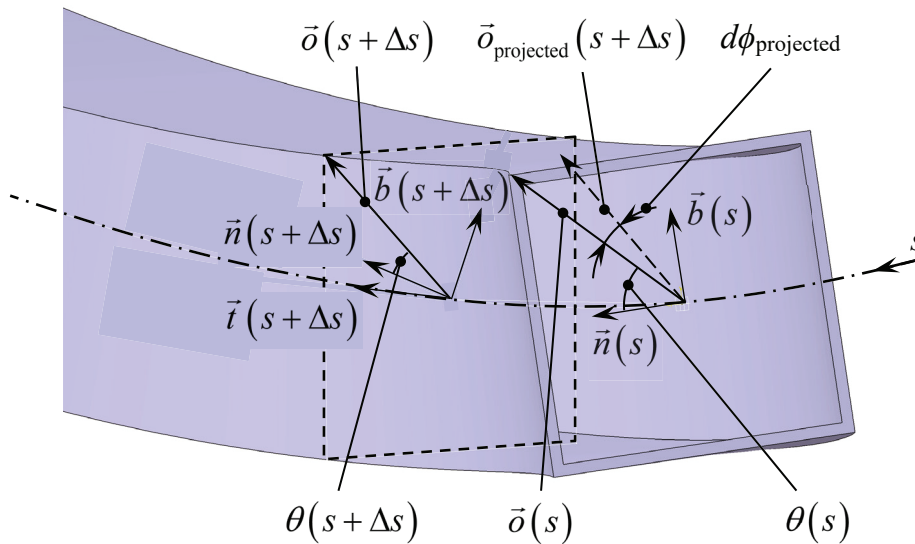
The orientation vector  $\vec{o}$  at position  $s$  is then calculated by:

$$\vec{o}(s) = \vec{P}_{\text{int}}(s) - \vec{r}(s) \quad (4.40)$$

The angle between  $\vec{o}$  and  $\vec{n}$  is called the cross-section orientation  $\theta$  and is calculated by:

$$\theta(s) = \begin{cases} 0 & \text{for } \chi_s = 0 \\ \cos^{-1} \left[ \frac{\vec{o}(s)}{\|\vec{o}(s)\|} \cdot \vec{n}(s) \right] & \text{for } \chi_s = 1 \\ 2\pi - \cos^{-1} \left[ \frac{\vec{o}(s)}{\|\vec{o}(s)\|} \cdot \vec{n}(s) \right] & \text{for } \chi_s = -1 \end{cases} \quad \text{with } \chi_s = \frac{\vec{o}(s) \cdot \vec{b}(s)}{|\vec{o}(s) \cdot \vec{b}(s)|} \quad (4.41)$$

The value  $\chi_s$  describes if the angle between  $\vec{o}$  and  $\vec{b}$  is acute (1) or obtuse (-1) and, thus, if the angle between  $\vec{o}$  and  $\vec{n}$  is less or greater than  $\pi$ . As a result, Eq. (4.41) outputs values of  $\theta$  in the range  $0 \leq \theta < 2\pi$ .



**Figure 4.5:** Angle measured between the orientation vector at  $s$  and the projection of the orientation vector at  $s + \Delta s$  onto the normal plane at  $s$  for the helix with  $d\phi = 0$

The VDI3431 defines the torsion angle as the angle of twist between two successive cross-sections. It might now seem straightforward to calculate the profile torsion by calculating the angle between the orientation vectors at  $s$  and  $s+\Delta s$ . However, the problem here is that for 3D bending lines the angle calculated would actually be the resultant angle generated by the rotations of  $\vec{o}$  around the tangent, normal, and binormal vector and not by the rotation of  $\vec{o}$  around the tangent alone. Another potential straightforward solution is to project the orientation vector at  $s+\Delta s$  onto the normal plane at  $s$  or vice versa. Here, the remaining problem is that this projection also is a resultant of the rotation of  $\vec{o}$  around the above-mentioned three axes.

Depending on the shape of the bending line, a rotation could be calculated even though the profile is not actually twisted (see Figure 4.5). This effect cannot be neglected because, although showing small deviations locally, the error accumulates with accumulating torsion and causes large deviations in the calculated cumulative twist.

This can be overcome by first calculating the angle between the vector  $\vec{o}$  at arc length  $s$  and the bending plane at the same arc length  $s$ . Secondly, the angle between the vector  $\vec{o}$  at arc length  $s+\Delta s$  and the bending plane at  $s+\Delta s$  is calculated. Because the calculated angles depend on the bending plane rotation, the rotation angle of  $\vec{o}$  between arc lengths  $s$  and  $s+\Delta s$  does not directly yield the twist per unit length but the apparent twist (see Section 4.1.2):

$$d\phi_{\text{apparent}} = \lim_{\Delta s \rightarrow 0} \Delta\phi_{\text{apparent}} = \begin{cases} \lim_{\Delta s \rightarrow 0} [\theta(s + \Delta s) - \theta(s)] & \text{for } \lim_{\Delta s \rightarrow 0} [\theta(s + \Delta s) - \theta(s)] + d\theta_r \rightarrow 0 \\ \lim_{\Delta s \rightarrow 0} [2\pi + \theta(s + \Delta s) - \theta(s)] & \text{for } \lim_{\Delta s \rightarrow 0} [\theta(s + \Delta s) - \theta(s)] + d\theta_r \rightarrow -2\pi \\ \lim_{\Delta s \rightarrow 0} [-2\pi + \theta(s + \Delta s) - \theta(s)] & \text{for } \lim_{\Delta s \rightarrow 0} [\theta(s + \Delta s) - \theta(s)] + d\theta_r \rightarrow 2\pi \end{cases} \quad (4.42)$$

Values of  $\lim_{\Delta s \rightarrow 0} [\theta(s + \Delta s) - \theta(s)] + d\theta_r$  approaching  $-2\pi$  as well as  $2\pi$  indicate a rotation of  $\vec{o}$  crossing  $\vec{n}$ . In order to avoid the resulting error in  $d\phi_{\text{apparent}}$   $2\pi$  and  $-2\pi$  are added to the equation, respectively. Following Eq. (4.36), the twist per unit length can then be calculated by:

$$d\phi = d\phi_{\text{apparent}} + d\theta_r \quad (4.43)$$

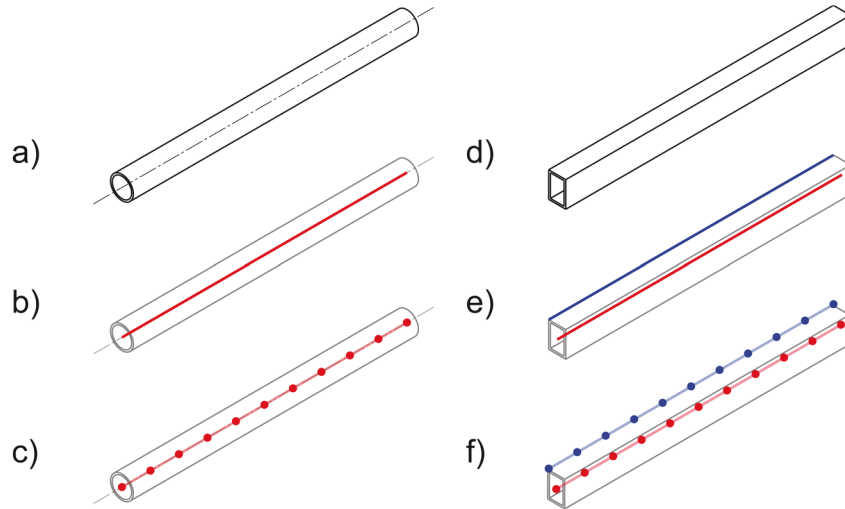
The calculation of  $d\phi$  is especially relevant for the shear strain and shear stress calculation shown in Section 7.3 and has a direct impact on the resulting torque and bending moment, as shown in Section 7.3.3.

#### 4.1.4 Discrete description of 3D-contours

When designed in CAD, complex 3D parts are often not designed from one single parametric spline or B-spline that is three times differentiable. Oftentimes several design methods are used to set up one single shape. A shape might, for instance, be made up of

a spline, a line, and a radius. These separate geometric constructs might be tangent to each other, but still show discontinuities in the second derivative of the complete curve. In such a case, the curve has to be described discretely.<sup>6</sup>

As described in Section 4.1.3, first, the bending line  $\vec{r}$  needs to be extracted from the 3D shape. If the profile has a non-circular cross-section, then a secondary curve  $\vec{r}_s$  needs to be defined, as described in the same section. The next step is the discretization of the two curves (see Figure 4.6).



**Figure 4.6:** Discretization of bending line (red) for the case of a)-c) a profile with a circular cross-section, discretization of bending line (red) and secondary line (blue) for the case of d)-f) a profile with an arbitrary non-circular cross-section

In a CAD program the discretization of  $\vec{r}$  can efficiently be done by automatically defining a finite amount of points along the curve set apart by a fixed arc-length:

$$P_i \text{ with } \{i \in \mathbb{Z} \mid 1 \leq i \leq n\} \quad (4.44)$$

The curve can then be described as a  $3 \times n$ -matrix, where each column vector represents the position vector of a single point on the curve:

$$\mathbf{R} = \begin{pmatrix} v_{x,i} & v_{x,i+1} & \cdots & v_{x,n} \\ v_{y,i} & v_{y,i+1} & \cdots & v_{y,n} \\ v_{z,i} & v_{z,i+1} & \cdots & v_{z,n} \end{pmatrix} \quad (4.45)$$

<sup>6</sup> The figures in this subsection are based on drawings by Jan Kersting from his student thesis: Entwicklung eines Prozesssimulationsmodells für das TSS-Biegen [Development of a Process Simulation Modell for TSS Bending], Technische Universität Dortmund, 2012, supervised by: D. Staupendahl and A. E. Tekkaya.

To be able to later extract the orientation vectors needed to describe profile torsion, the curve  $\vec{r}_s$  needs to be discretized so that each of the discrete points lie on a normal plane of the curve  $\vec{r}$ . To describe the normal plane  $N_i$  at a point  $P_i$ , first, the tangent  $\vec{t}_i$  needs to be found. If three points on  $\vec{r}$  are always thought to describe an ideal circle and all points are, as described above, evenly spaced apart, then  $\vec{t}_i$  is simply  $\overline{P_{i-1}P_{i+1}}$ . The normal plane at position  $i$  can, thus, be described in the point-normal form by:

$$N_i: (\vec{p}_N - \vec{v}_i) \overline{v_{i-1}v_{i+1}} = 0 \quad (4.46)$$

where  $\vec{p}_N$  is the position vector of any point on the plane. To discretize  $\vec{r}_s$ , the curve needs to be inserted as  $\vec{p}_N$  into Eq. (4.46) and solved for  $s_{s,i}$ . The procedure is similar to the procedure described for continuous curves in Section 4.1.3. Parallel to Eq. (4.38), the points:

$$P_{s,i} \text{ with } \{i \in \mathbb{Z} \mid 1 \leq i \leq n\} \quad (4.47)$$

on the secondary curve  $\vec{r}_s$  are defined by the position vectors:

$$\vec{v}_{s,i}(s) = \vec{r}_s(s_{s,i}) \quad (4.48)$$

The secondary curve can then be described as a  $3 \times n$ -matrix, where each column vector represents the position vector of a single point on  $\vec{r}_s$ , as in the matrix  $R$  defining the bending line  $\vec{r}$ :

$$R_s = \begin{pmatrix} v_{s,x,i} & v_{s,x,i+1} & \cdots & v_{s,x,n} \\ v_{s,y,i} & v_{s,y,i+1} & \cdots & v_{s,y,n} \\ v_{s,z,i} & v_{s,z,i+1} & \cdots & v_{s,z,n} \end{pmatrix} \quad (4.49)$$

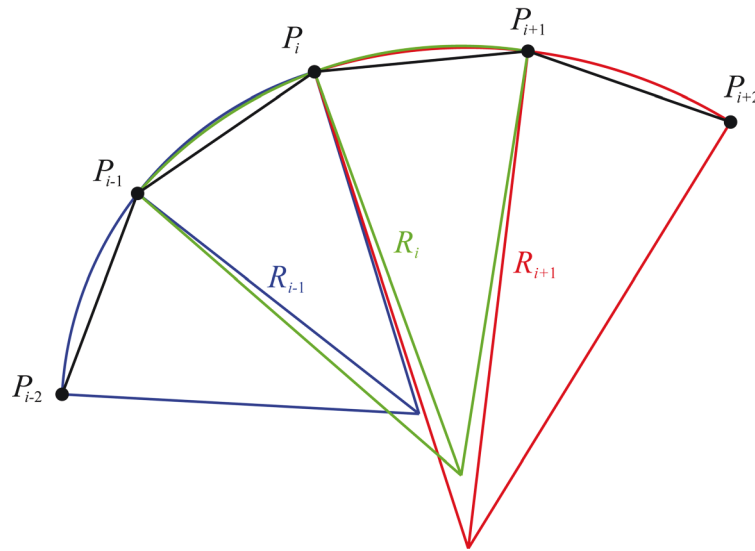
To calculate the curvature of the bending line at the point  $P_i$ , the directly preceding point  $P_{i-1}$  and subsequent point  $P_{i+1}$  are used together with  $P_i$  to describe the ideal radius  $R_i$  (see Figure 4.7). The task of calculating the radius of the circle touching three points is known as the first type of the Apollonius' Problem, or PPP problem (Viète, 1600) and can be solved by using the law of sines (Walther, 1931):

$$R_i = \frac{\|\overline{P_{i-1}P_{i+1}}\|}{2 \sin \sphericalangle(\overline{P_{i-1}P_i}, \overline{P_iP_{i+1}})} \quad (4.50)$$

Using the magnitude of the cross product between  $\overline{P_{i-1}P_i}$  and  $\overline{P_iP_{i+1}}$  Eq. (4.50) can be rewritten as:

$$\kappa_i = \frac{1}{R_i} = \frac{2 \|\overline{P_{i-1}P_i} \times \overline{P_iP_{i+1}}\|}{\|\overline{P_{i-1}P_i}\| \cdot \|\overline{P_iP_{i+1}}\| \cdot \|\overline{P_{i-1}P_{i+1}}\|} \quad (4.51)$$





**Figure 4.7:** Geometrical definition of the radii at points  $P_{i-1}$ ,  $P_i$ , and  $P_{i+1}$

or alternatively, as the magnitude of a cross-product equals the Area of the parallelogram spanned by the two adjacent vectors:

$$\kappa_i = \frac{1}{R_i} = \frac{4A_i}{\|\overline{P_{i-1}P_i}\| \cdot \|\overline{P_iP_{i+1}}\| \cdot \|\overline{P_{i-1}P_{i+1}}\|} \quad (4.52)$$

where the  $A_i$  is the area of the triangle defined by the points  $P_{i-1}$ ,  $P_i$ , and  $P_{i+1}$ . To calculate  $A_i$  Heron's formula can be used, which is named after Heron of Alexandria and is thought to date back to Archimedes (Heath, 1921):

$$A_i = \sqrt{p_s \left( p_s - \|\overline{P_{i-1}P_{i+1}}\| \right) \left( p_s - \|\overline{P_iP_{i+1}}\| \right) \left( p_s - \|\overline{P_{i-1}P_i}\| \right)} \quad (4.53)$$

with  $p_s = \frac{1}{2} \left( \|\overline{P_{i-1}P_{i+1}}\| + \|\overline{P_iP_{i+1}}\| + \|\overline{P_{i-1}P_i}\| \right)$

Expanded, Eq. (4.53) can be rewritten as:

$$A_i = \frac{1}{4} \sqrt{\left( 2 \|\overline{P_{i-1}P_i}\| \|\overline{P_{i-1}P_{i+1}}\| \right)^2 - \left( \|\overline{P_{i-1}P_i}\|^2 + \|\overline{P_{i-1}P_{i+1}}\|^2 - \|\overline{P_iP_{i+1}}\|^2 \right)^2} \quad (4.54)$$

For the description of the discrete bending plane rotation  $\Delta\theta_{r,i}$ , the geometric definition of the dot product is used to calculate the angles between the binormal vectors  $\vec{b}_i$  and  $\vec{b}_{i+1}$ , whereby:

$$\vec{b}_i = \overline{P_{i-1}P_i} \times \overline{P_iP_{i+1}} \quad \text{and} \quad \vec{b}_{i+1} = \overline{P_iP_{i+1}} \times \overline{P_{i+1}P_{i+2}} \quad (4.55)$$

Knowing the direction of bending plane rotation around the tangent is crucial for a proper description of the bending line. However, this knowledge cannot be directly gained from the dot product. The dot product can, though, be used to define the angle

between two vectors to be acute or obtuse. If the binormal vector  $\vec{b}_{i+1}$ , now, forms an obtuse angle with the normal vector:

$$\vec{n}_i = \vec{b}_i \times \overrightarrow{P_{i-1}P_{i+1}} \quad (4.56)$$

which indicates a positive bending plane rotation, the normalized dot product is equal to -1. If  $\vec{b}_{i+1}$  and  $\vec{n}_i$  form an acute angle, then the normalized dot product is equal to 1. As a result:

$$\Delta\theta_{r,i} = -\cos^{-1} \left( \frac{\vec{b}_i \cdot \vec{b}_{i+1}}{\|\vec{b}_i\| \|\vec{b}_{i+1}\|} \right) \cdot \frac{\vec{b}_{i+1} \cdot \vec{n}_i}{|\vec{b}_{i+1} \cdot \vec{n}_i|} \quad (4.57)$$

and the cumulative bending plane rotation  $\theta_{r,i}$  is:

$$\sum_{i=1}^n \Delta\theta_{r,i} \quad (4.58)$$

To calculate the torsion of the profile, first, the orientation vectors at positions  $i$  and  $i+1$  are calculated by:

$$\vec{o}_i = \vec{v}_{s,i} - \vec{v}_i \quad \text{and} \quad \vec{o}_{i+1} = \vec{v}_{s,i+1} - \vec{v}_{i+1} \quad (4.59)$$

Similar to Eq. (4.41) the cross-section orientation  $\theta_i$  is calculated by:

$$\theta_i = \begin{cases} 0 & \text{for } \chi_i = 0 \\ \cos^{-1} \left( \frac{\vec{o}_i \cdot \vec{n}_i}{\|\vec{o}_i\| \|\vec{n}_i\|} \right) & \text{for } \chi_i = 1 \\ 2\pi - \cos^{-1} \left( \frac{\vec{o}_i \cdot \vec{n}_i}{\|\vec{o}_i\| \|\vec{n}_i\|} \right) & \text{for } \chi_i = -1 \end{cases} \quad \text{with} \quad \chi_i = \frac{\vec{o}_i \cdot \vec{b}_i}{|\vec{o}_i \cdot \vec{b}_i|} \quad (4.60)$$

in the range  $0 \leq \theta < 2\pi$ . As a next step, similar to Eq. (4.42), the discrete apparent twist  $\Delta\phi$  is calculated by:

$$\Delta\phi_{\text{apparent},i} = \begin{cases} \theta_{i+1} - \theta_i & \text{for } -\theta_{\text{lim}} < \theta_{i+1} - \theta_i + \Delta\theta_{r,i} < \theta_{\text{lim}} \\ \theta_{i+1} - \theta_i + 2\pi & \text{for } -2\pi < \theta_{i+1} - \theta_i + \Delta\theta_{r,i} < \theta_{\text{lim}} - 2\pi \\ \theta_{i+1} - \theta_i - 2\pi & \text{for } 2\pi - \theta_{\text{lim}} < \theta_{i+1} - \theta_i + \Delta\theta_{r,i} < 2\pi \end{cases} \quad (4.61)$$

Similar to the term  $\lim_{\Delta s \rightarrow 0} [\theta(s + \Delta s) - \theta(s)] + d\theta_r$  in Eq. (4.42), the term  $\theta_{i+1} - \theta_i + \Delta\theta_{r,i}$  in Eq. (4.61) should give values close to zero, while values near  $-2\pi$  or  $2\pi$  signal a rotation of  $\vec{o}$  crossing  $\vec{n}$ . As in Eq. (4.42), in the case of a vector crossing,  $2\pi$  and  $-2\pi$  are added to the equation, respectively.

Although the step size:

$$l_{step} = \frac{L}{n-1} \quad (4.62)$$

in discrete curve representations should be small, the specific value can be chosen arbitrarily. In order to define “close to” or “near”, the term  $\theta_{lim}$  is used.  $\theta_{lim}$  should be chosen in the range of  $\pi/4$  to incorporate even very large step sizes.

Finally, and similar to Eq. (4.43), the discrete twist per unit length can then be calculated by:

$$\Delta\phi_i = \Delta\phi_{\text{apparent},i} + \Delta\theta_{r,i} \quad (4.63)$$

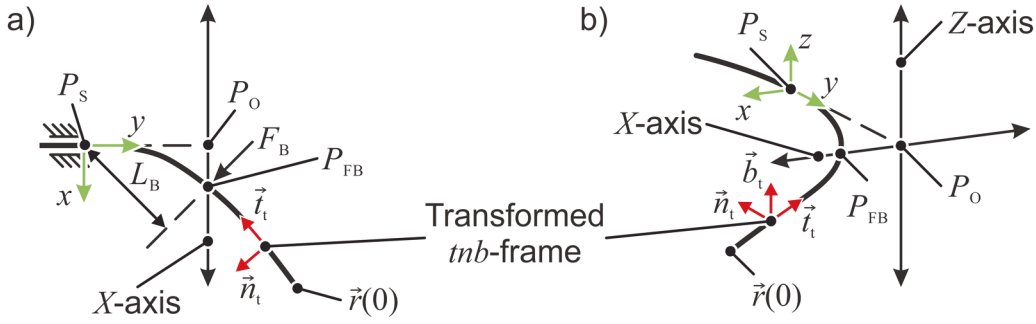
The difference between Eqs. (4.10) and (4.43), and (4.57) and (4.63) is the step size  $\Delta s$ . While the step size approaches 0 in Eqs. (4.10) and (4.43),  $\Delta s$  is finite in Eqs. (4.57) and (4.63). For easier legibility and a more compact setup of the rest of this work, in the following sections and chapters only the differential representations will be used.

## 4.2 Characterization of free-form bending kinematics

In Section 4.1 it was learned that 3D profiles with circular cross-sections can solely be described by their bending line, while 3D profiles with non-circular cross-sections necessitate the additional information about the profile torsion aka twist. What does this now mean for bending kinematics and, as a result, for bending machines? How many controlled axes or actuators are needed to bend a profile?

### 4.2.1 Derivation of cDOFs needed for manufacturing

To bend a profile, a bending moment needs to be generated in a targeted position of the initially straight profile. To generate this bending moment, part of the profile needs to be fixed in space, while a moment or a force is applied to another part of the profile. All of the bending processes mentioned in Section 2.1 of the state of the art use bending force application instead of bending moment application, which is why all further analyses will focus on applied bending force. Furthermore, the point of bending force application  $P_{FB}$  is defined to move on a plane, which is located at a specified distance to the plane that is orthogonal to the profile axis at the fixed profile part. If the bending kinematics are thought to be fixed in space, the profile fixture or support can be defined to be at point  $P_S (x = 0, y = 0, z = 0)$  and the plane of the movement of the point of bending force application  $P_{FB}$  can be defined to be parallel to the  $xz$ -plane. In the plane of  $P_{FB}$  movement, the two dimensional movement of  $P_{FB}$  can be described by a local two-dimensional coordinate system made up of the  $X$ -axis and the  $Z$ -axis. The origin  $P_O$  of this local coordinate system lies at the global coordinates  $(0, y_{P_{FB}}, 0)$ . The  $X$  and  $Z$ -axes follow the directions of the  $x$  and  $z$ -axes, respectively. The resulting geometric process model



**Figure 4.8:** a) Top view of the generalized geometric 3D bending process model, b) 3D view of the bending process model

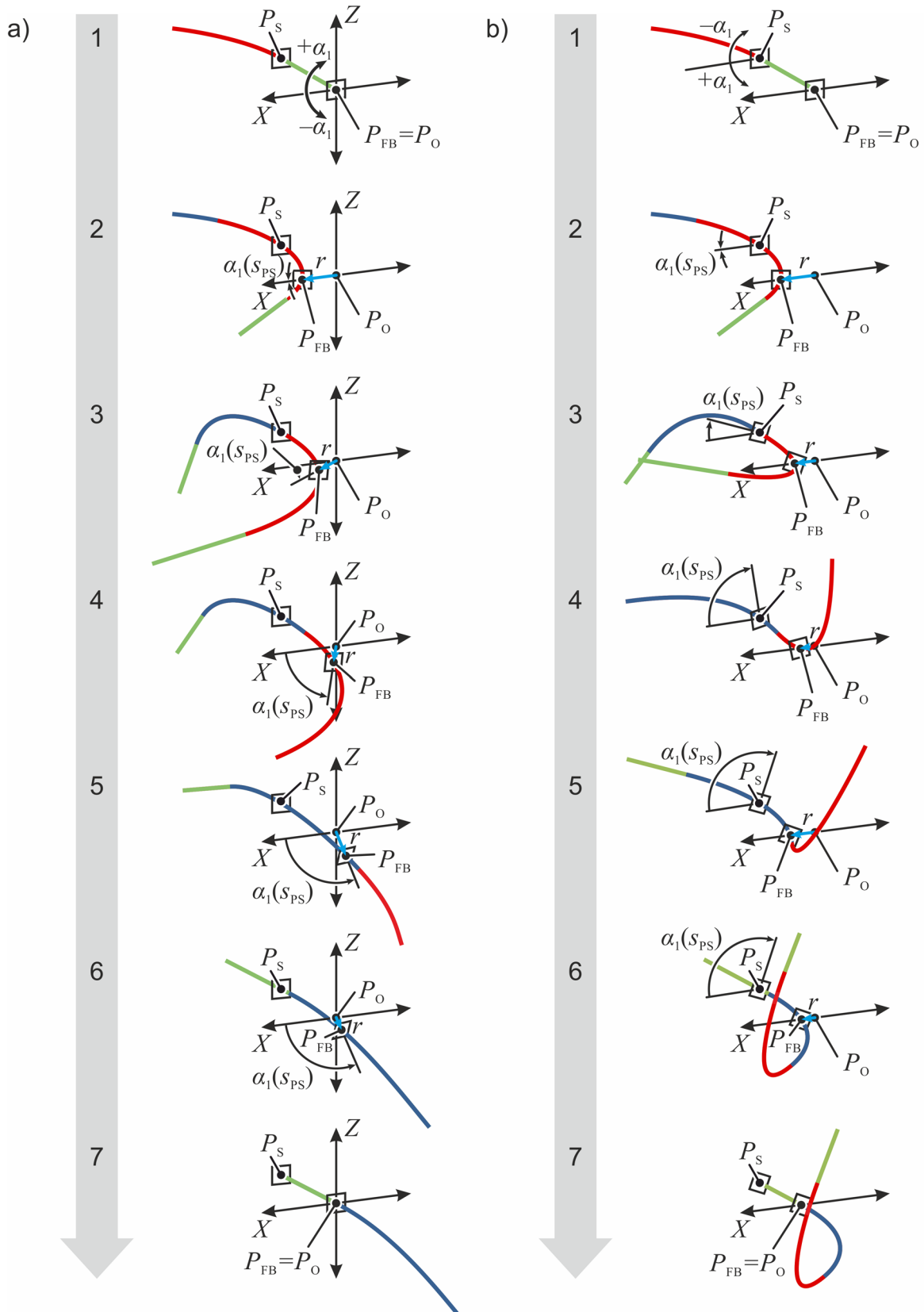
is shown in Figure 4.8. Figure 4.8a shows bending of a single radius in the  $xy$ -plane, while Figure 4.8b shows the three-dimensional view.

By defining the profile support to lock all profile movements but the movement in the  $y$ -direction, the movement of  $P_{FB}$  of an arbitrary profile can now be tracked by continuously moving the profile through the profile support. The function of the curve  $\vec{r}$  or, in case of a discrete curve description, the matrix  $R$  need to be continuously transformed into the coordinate system of the bending process model based on the profile movement. Figure 4.9 a) shows a sequence of  $P_{FB}$  movements for an exemplary profile with a bending line made up of two consecutive bending radii in two different bending planes. The first bending radius is marked red, the second blue. To overcome the distance between the profile support and the plane of movement of  $P_{FB}$ , straight elements are added to the front and back end of the bending line, marked in green.

During the movement of the first radius (red) through the profile support (Figure 4.9 a) steps 1-2),  $P_{FB}$  solely moves along the  $X$ -axis, with the value of  $X$  actually being fixed in step 2. Steps 3 and 4 mark the transition from the first bending radius to the second (blue) and, thus, from the first bending plane to the second. Here,  $P_{FB}$  moves both in  $X$  and in  $Z$ -direction. Step 5 shows the movement of the second radius through the profile support and  $P_{FB}$ .  $P_{FB}$  does not change its position in this case, similar as in step 2. In steps 6 and 7 the point  $P_{FB}$  moves back to its central starting position. Hereby, the point moves in the bending plane of the second radius. The ratio of  $X$  to  $Z$  values, thus, stays constant.

Considering a continuous curve description,  $P_{FB(s_{PS})}$  refers to the position of the point of bending force application when the point  $\vec{r}(s_{PS})$  of the bending line is in the profile support. The movement of  $P_{FB}$  can be described either in Cartesian coordinates or in polar coordinates:

$$P_{FB}(s_{PS}) = \begin{pmatrix} X(s_{PS}) \\ Z(s_{PS}) \end{pmatrix} = \begin{pmatrix} r(s_{PS}) \cos[\alpha_1(s_{PS})] \\ r(s_{PS}) \sin[\alpha_1(s_{PS})] \end{pmatrix} \quad \text{with} \quad r(s_{PS}) = \sqrt{X^2(s_{PS}) + Z^2(s_{PS})} \quad (4.64)$$



**Figure 4.9:** Movement of the point of bending force application  $P_{FB}$  for an exemplary profile with a bending line with two different subsequent radii in different bending planes using a cross table (a) or a single linear axis (b)

In the range  $-\pi \leq \alpha_1 < \pi$  the angle  $\alpha_1(s_{PS})$  relates to movements in  $X$  and  $Z$ -direction by:

$$\alpha_1(s_{PS}) = \begin{cases} 0 & \text{for } X(s_{PS}) = 0 \text{ and } Z(s_{PS}) = 0 \\ \cos^{-1} \left[ \frac{X(s_{PS})}{r(s_{PS})} \right] & \text{for } Z(s_{PS}) \geq 0 \\ -\cos^{-1} \left[ \frac{X(s_{PS})}{r(s_{PS})} \right] & \text{for } Z(s_{PS}) < 0 \end{cases} \quad (4.65)$$

Eq. (4.64) shows that the movement of  $P_{FB}$  can either be described by two translations (one in  $X$  and one in  $Z$ -direction), or by one translation (the resultant  $r$ ) and one rotation (angle  $\alpha_1$ ). This rotation does not necessarily need to be in the plane of movement of  $P_{FB}$ . The two parameters – translation and rotation – can be separated so that the rotation is applied at the profile support and a linear translation along a single axis is left in the original plane of  $P_{FB}$  movement. It is important to note here that the sign convention of  $\alpha_1$  changes in this case. Using this adapted kinematic setup, the resulting sequence of  $P_{FB}$  movements for the above stated exemplary profile is shown in Figure 4.9 b). The profile and axis movements in steps 1 and 2 are identical to the movements in Figure 4.9 a). However, in the transition from one bending plane to the next (steps 3 and 4), instead of allowing a  $P_{FB}$  movement in the  $Z$ -direction, the profile itself rotates until the bending plane of the second radius (blue) is equal to the  $xy$ -plane (step 5). No further profile rotation is needed to complete the profile movements of steps 6 and 7. It is imperative to note that the movement of  $P_{FB}$  along the single linear  $X$ -axis of Figure 4.9 b) is not identical to the  $X$ -axis movement of  $P_{FB}$  but equal to the resultant  $r$  as calculated with Eq. (4.64).

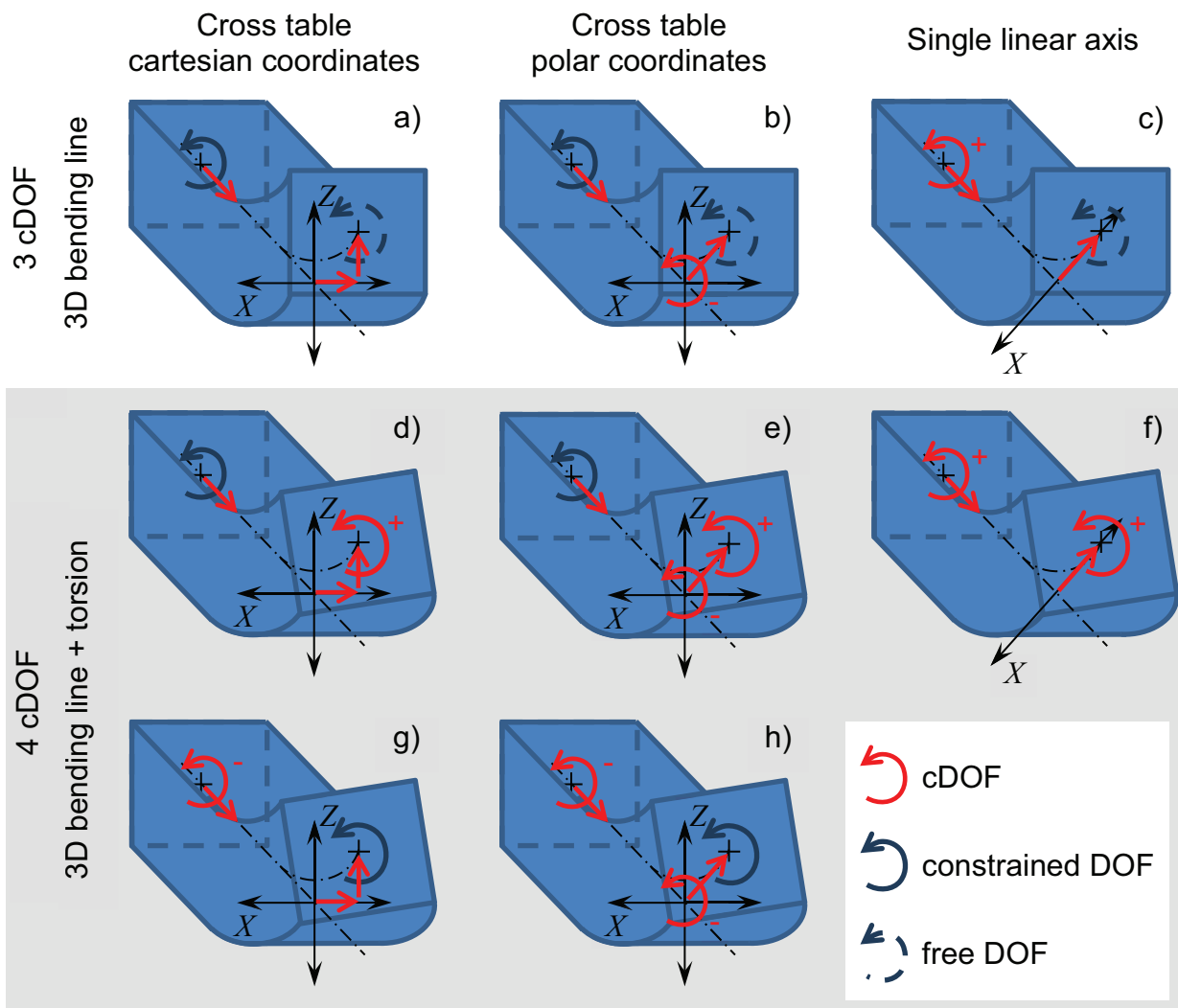
Figure 4.9 additionally shows the plane  $N_{PFB}$  at the point  $P_{FB}$  that is congruent to the normal plane  $N$  of the bending line at this same point. The tangent  $\vec{t}_t$  of the bending line at this point represents the orientation of  $N_{PFB}$  in the coordinate system of the bending process model. In terms of the bending kinematics, the angle of  $N_{PFB}$  relative to the  $XZ$ -plane can be defined by individual rotations around the  $X$  and  $Z$ -axis. Although, the plane only rotates around the  $Z$ -axis in the case of single radii (Figure 4.9 b) steps 1-2 and steps 5-7), the plane also rotates around an axis parallel to the  $x$ -axis in the transition zones shown in steps 3 and 4. As these plane rotations are not necessary to describe the movement of the point of force application  $P_{FB}$ , they can be called compensatory movements.

An interesting observation that can be made by comparing the kinematics shown in Figure 4.9 is that the Cartesian and polar coordinate description of a) as well as the polar

coordinate description of b) need 3 parameters to track the profile geometry. It can, thus, be concluded that the three variables that describe a bending line:

1. curvature,
2. bending plane rotation,
3. and arc length,

directly define the minimum controlled degrees of freedom (cDOF) necessary to bend a 3D profile with a circular cross-section. This realization also directly implies, that a 3-cDOF process cannot be used to bend profiles with non-circular cross-sections to arbitrary bending contours. A 3-cDOF process can only be used to generate a 3D shaped profile, if the targeted apparent twist is exactly opposite to the bending plane rotation, so in other words if  $d\phi_{\text{apparent}} = -d\theta_r$  (see Eq. (4.36)). In all other geometrical cases, at least 4 cDOF are needed, with the 4<sup>th</sup> cDOF imperatively being an actuator to twist the profile. Any additional cDOFs are theoretically optional, but might support a smooth



**Figure 4.10:** cDOFs (red) needed to produce 3D bending lines with and without a twisted cross-section

operation of the machine and prevent jamming of the profile in critical machine positions (compensatory axes based on the above stated compensatory plane movements), or a more efficient material usage (controllable lever arm by adjusting the distance of the profile support to the plane of  $P_{FB}$  movement).

As was already hinted when looking at Figure 4.9, the positions of the cDOFs are flexible. Figure 4.10 schematically shows the possible locations of cDOFs required to produce profiles with 3D bending lines with and without torsion. The shown profile segment represents the profile part between the profile support, marked by the arrow in axial profile direction and the plane of  $P_{FB}$  movement, marked by the  $X$  and  $Z$ -axis (cross table) and the resultant  $X$ -axis (single linear axis). Cases a) and b) represent the same kinematics as used in Figure 4.9 a) while case c) represents the same kinematics as Figure 4.9 b). In the case of cross table kinematics the 4<sup>th</sup> cDOF needed to twist the profile can be either located in the compensatory plane at the point of bending force application  $P_{FB}$  or in the profile support. In the case of bending kinematics with a single linear axis, the rotation in the profile support is already used to change the bending plane rotation. Thus, in the latter case, the only possible position for the 4<sup>th</sup> cDOF is the point  $P_{FB}$ .

#### 4.2.2 Classification of free-form bending kinematics

Based on the controlled degrees of freedom (cDOFs), defined in the previous sections, that are needed to produce profiles with arbitrary 3D shapes, and the tool used to apply the bending force, the currently available bending machines were assessed. The resulting process classification can be seen in Table 4.1.

“1D bending actuator” means that only a single actuator is used to apply the bending force. “2D bending actuator” describes the use of two actuators, independent of the location of the mechanisms. So both the cross-table and the single linear axis used together with a rotational cDOF at the profile support are encompassed.

In the classification, only processes were regarded that allow fully automatic bending of single profiles and do not require manual intervention during the process to, for instance, change the position of the profile. As such, only three-roll bending without any additional vertical actuators was regarded. Although three-roll bending allows limited 3D bending, contours are constricted to helical shapes and require constant manual engagement by the operator. Three-roll bending and three-roll push bending are classified as processes with a single linear bending axis. At first glance, this assessment might not fit because in three-roll bending generally two rolls can be moved and in three-roll push bending the bending roll can be moved along the  $x$  and the  $y$ -axis. However, only one of these movements in each of the processes is actually needed to bend profiles. In the case of TSS bending only the 3-DOF process has been realized until now. However, possible 4-DOF and 5-DOF setups have been proposed by (Hermes and Kleiner, 2013).





In the Gigalus combined drawing and free-form bending machine, the profile is actually not twisted as in the other processes with  $\geq 4$  cDOFs. The classification as 5 cDOF is justified because, although the profile is not mechanically twisted, still a rotation is needed to produce the contoured profile.

Although the basic movements of the bending head in the Hexabend process and the 6-DOF bending process follow the movements of a bending head mounted on a cross-table with a variable distance to the profile support and, thereby, a variable lever arm, the calculation of the actual movements of the actuators is so complex that both processes were placed in a separate parallel kinematics class.

### 4.2.3 Relation of profile geometry and actuator movements

In Section 4.2.1 the relation of  $\alpha_1$  to the  $X$  and  $Z$ -axis movement of the bending kinematics was shown. In order to establish the relation of  $\alpha_1$ ,  $X$  and  $Z$  to the shape of the profile, it is most convenient to visualize how the plane spanned by the vectors  $\overline{P_S P_O}$  and  $\overline{P_O P_{FB}}$  moves along the bending line. The plane is equal to the bending plane  $B$  at  $\vec{P}_S$ :

- If  $d\theta_r \in \mathbb{R} \setminus \{0\}$  in between points  $\vec{P}_S$  and  $\vec{P}_{FB}$ , and  $\|\overline{P_S P_O}\| \rightarrow 0$
- or if  $d\theta_r = 0$  in between points  $\vec{P}_S$  and  $\vec{P}_{FB}$ , and  $\|\overline{P_S P_O}\| \geq 0$

If one of these cases is not met, however, then these two planes are unequal. Since the distance  $\|\overline{P_S P_O}\|$  is dependent on the bending machine setup, the plane will be called the machine bending plane  $M$  in the further work. Figure 4.12 shows the different rotations of  $M$  and  $B$  for an exemplary profile with a bending line with two different subsequent radii in different bending planes, also used in Figure 4.9.  $\vec{P}_S$  is used as the point vector of  $M$ , which defines its position in space.  $\vec{P}_S$  moves along the bending line from  $\vec{r}(0)$  to  $\vec{r}(l)$  with:

$$\vec{P}_S = \vec{r}(s_{PS}) \quad (4.66)$$

$\vec{P}_O$  is calculated by:

$$\vec{P}_O = \vec{r}(s_{PS}) - \underbrace{\vec{t}(s_{PS})}_{\frac{d\vec{r}(s_{PS})}{ds}} \|\overline{P_S P_O}\| \quad (4.67)$$

The second term is subtracted because the vector  $\overline{P_S P_O}$  is directed into the opposite direction of  $\vec{t}(s_{PS})$ .  $\vec{P}_{FB}$  is gained by calculating the point on the bending line  $\vec{r}(s_{PFB})$  that is located at a distance of  $\|\overline{P_S P_O}\|$  from the normal plane  $N$  at  $\vec{P}_S$ :

$$\vec{P}_{FB} = \vec{r}(s_{PFB}) \quad \text{with} \quad [\vec{r}(s_{PFB}) - \vec{r}(s_{PS})] \vec{t}(s_{PS}) = \|\overline{P_S P_O}\| \quad (4.68)$$

In order to generate data starting from  $\vec{P}_S = \vec{r}(0)$  and ending up with  $\vec{P}_{FB} = \vec{r}(l)$ , a valid geometry needs to be added to  $\vec{r}$  for values of  $s < 0$  and  $s > l$ . Since profile bending

generally always starts out with a straight profile that is bent to the desired shape with the chosen bending process, the addition of a straight-line segment to the beginning and end of  $\vec{r}$  with the length of  $\|\overrightarrow{P_S P_O}\|$  is the most straightforward choice. Figuratively this is shown in Figure 4.9 (added straight line segments are marked green).  $\vec{r}(s_{PS})$  and  $\vec{r}(s_{PFB})$  are, thus, adapted to:

$$\vec{r}(s_{PS}) = \begin{cases} \vec{r}(s_{PS}) & \text{for } 0 \leq s_{PS} \leq l \\ \vec{r}(l) + \vec{t}(l)s_{PFB} & \text{for } l < s_{PFB} \leq l + \|\overrightarrow{P_S P_O}\| \end{cases} \quad (4.69)$$

and:

$$\vec{r}(s_{PFB}) = \begin{cases} \vec{r}(s_{PFB}) & \text{for } 0 \leq s_{PS} \leq l \\ \vec{r}(0) + \vec{t}(0)s_{PFB} & \text{for } -\|\overrightarrow{P_S P_O}\| < s_{PFB} < 0 \end{cases} \quad (4.70)$$

In order to describe the movement and rotation of  $M$  relative to the bending line a  $t_M n_M b_M$ -frame is introduced, with:

$$\vec{t}_M(s_{PS}) = \vec{t}(s_{PS}) \quad (4.71)$$

$$\vec{b}_M(s_{PS}) = \vec{t}(s_{PS}) \times \frac{\overrightarrow{P_O P_{FB}}}{\|\overrightarrow{P_O P_{FB}}\|} \quad (4.72)$$

$$\vec{n}_M = \vec{b}_M \times \vec{t}_M \quad (4.73)$$

The angle between  $M$  and the bending plane  $B$  at position  $s_{PS}$  is calculated by:

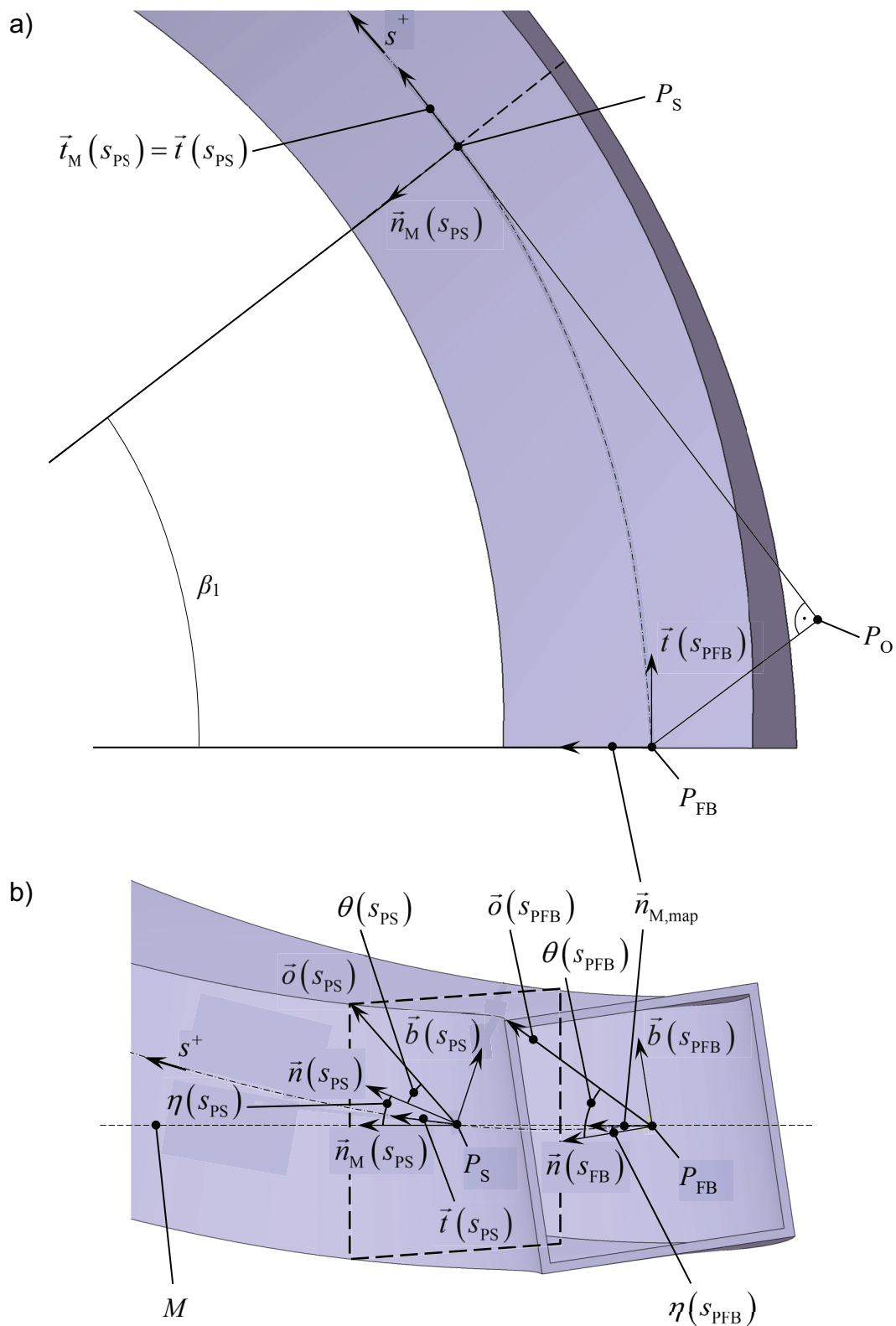
$$\eta(s_{PS}) = \begin{cases} 0 & \text{for } \chi_s = 0 \\ \cos^{-1}[\vec{n}_M(s_{PS}) \cdot \vec{n}(s_{PS})] & \text{for } \chi_s = 1 \\ 2\pi - \cos^{-1}[\vec{n}_M(s_{PS}) \cdot \vec{n}(s_{PS})] & \text{for } \chi_s = -1 \end{cases} \quad \text{with } \chi_s = \frac{\vec{n}_M(s_{PS}) \cdot \vec{b}(s_{PS})}{|\vec{n}_M(s_{PS}) \cdot \vec{b}(s_{PS})|} \quad (4.74)$$

The value  $\chi_s$  describes if the angle between  $\vec{n}_M$  and  $\vec{b}$  is acute (1) or obtuse (-1) and, thus, if the angle between  $\vec{n}_M$  and  $\vec{n}$  is less or greater than  $\pi$ . As a result, Eq. (4.74) outputs values of  $\eta$  in the range  $0 \leq \theta < 2\pi$ .

The angle  $\alpha_1$  is now defined as the difference of  $\eta$  and the cross section orientation  $\theta$  at the position  $s_{PS}$ :

$$\boxed{\alpha_1(s_{PS}) = \eta(s_{PS}) - \theta(s_{PS})} \quad (4.75)$$

Graphically this is shown in Figure 4.11. The resultant  $r(s_{PS})$ , which can be directly used as the displacement along the  $X$ -axis in the case of a bending process with a single linear axis (Figure 4.10c,f), or, in the case of bending kinematics that use a cross-table (Figure 4.10a,b,d,e,g,h), inserted into Eq. (4.64) together with  $\alpha_1(s_{PS})$  in order to obtain



**Figure 4.11:** a) top view of the machine bending plane  $M$  and the points  $P_S$ ,  $P_O$  and  $P_{FB}$  b) front view and visualization of the angles  $\eta$  and  $\theta$  at the points  $P_S$  and  $P_{FB}$ ,

the axes movements in the  $X$  and  $Z$ -direction, is calculated by:

$$\boxed{r(s_{PS}) = \left\| \overline{P_O P_{FB}} \right\|} \quad (4.76)$$

The torsional cDOF is defined by analyzing the rotation of the profile cross-section at the point of bending force application  $P_{FB}$ . The angle between  $M$  and the bending plane  $B$  at this position is gained by first mapping  $\vec{n}_M$  onto the normal plane  $N$  of the bending line at point  $P_{FB}$ . Essentially, this vector is the intersection line of  $N$  and  $M$  and, as a unit vector is calculated by:

$$\vec{n}_{M, \text{map}} = \frac{\vec{b}_M(s_{PS}) \times \vec{t}(s_{PFB})}{\left\| \vec{b}_M(s_{PS}) \times \vec{t}(s_{PFB}) \right\|} \quad (4.77)$$

The angle between  $\vec{n}_{M, \text{map}}$  and the bending plane  $B$  at position  $s_{PS}$  is calculated by:

$$\eta(s_{PFB}) = \begin{cases} 0 & \text{for } \chi_s = 0 \\ \cos^{-1} \left[ \vec{n}_{M, \text{map}} \cdot \vec{n}(s_{PFB}) \right] & \text{for } \chi_s = 1 \\ 2\pi - \cos^{-1} \left[ \vec{n}_{M, \text{map}} \cdot \vec{n}(s_{PFB}) \right] & \text{for } \chi_s = -1 \end{cases} \quad \text{with } \chi_s = \frac{\vec{n}_{M, \text{map}} \cdot \vec{b}(s_{PFB})}{\left| \vec{n}_{M, \text{map}} \cdot \vec{b}(s_{PFB}) \right|} \quad (4.78)$$

The rotation angle  $\alpha_2$  of the torsional cDOF is finally gained by:

$$\boxed{\alpha_2(s_{PFB}) = \eta(s_{PFB}) - \theta(s_{PFB})} \quad (4.79)$$

Using the exemplary helix with the helix radius  $R_h = R_{h,1}$  and a pitch of  $h_h = 5R_{h,1}$  from Section 4.1.2 (Figure 4.2b,c) combined with the distance  $\left\| \overline{P_S P_O} \right\| = R_{h,1}$ , to calculate the angular difference  $\Delta\alpha = \alpha_2 - \alpha_1$ , it can be observed that  $\Delta\alpha = 0$  for  $d\phi = 0$  and  $\Delta\alpha = 0.52$  rad for  $d\phi = d\theta_r$ . These values are identical to the values of cumulative torsion between the points  $P_{FB}$  and  $P_{PS}$ . Thus, the angle  $\alpha_2$  can also be stated in terms of  $\alpha_1$  and  $d\phi$ :

$$\boxed{\alpha_2(s_{PS}) = \alpha_1(s_{PS}) + \int_{s_{PFB}}^{s_{PS}} d\phi(s) ds} \quad (4.80)$$

In the case of bending kinematics using a single linear axis, the compensatory rotations of the normal plane  $N$  at point  $P_{FB}$  can be directly calculated. The rotation angle of  $N$  around  $\vec{b}_M$  is computed by:

$$\boxed{\beta_1(s_{PS}) = \cos^{-1} \left[ \vec{n}_{M, \text{map}} \cdot \vec{n}_M(s_{PS}) \right]} \quad (4.81)$$

$\beta_1$  is always positive with an angle range of  $0$  to  $\pi$ , because in case of a direction change of the vector  $\overline{P_O P_{FB}}$ , the  $t_M n_M b_M$ -frame also rotates around  $\vec{t}_M(s_{PS})$ . For the rotation

angle of  $N$  around  $\vec{n}_{M,\text{map}}$ , the angle between  $N$  and  $\vec{b}_M$  is calculated by:

$$\beta_2(s_{\text{PS}}) = -\sin^{-1} \left[ \vec{t}(s_{\text{FB}}) \cdot \vec{b}_M(s_{\text{PS}}) \right] \quad (4.82)$$

Eq. (4.82) produces angles between  $-\pi/2$  and  $\pi/2$ .

#### 4.2.4 Location and movement of the bending force vector

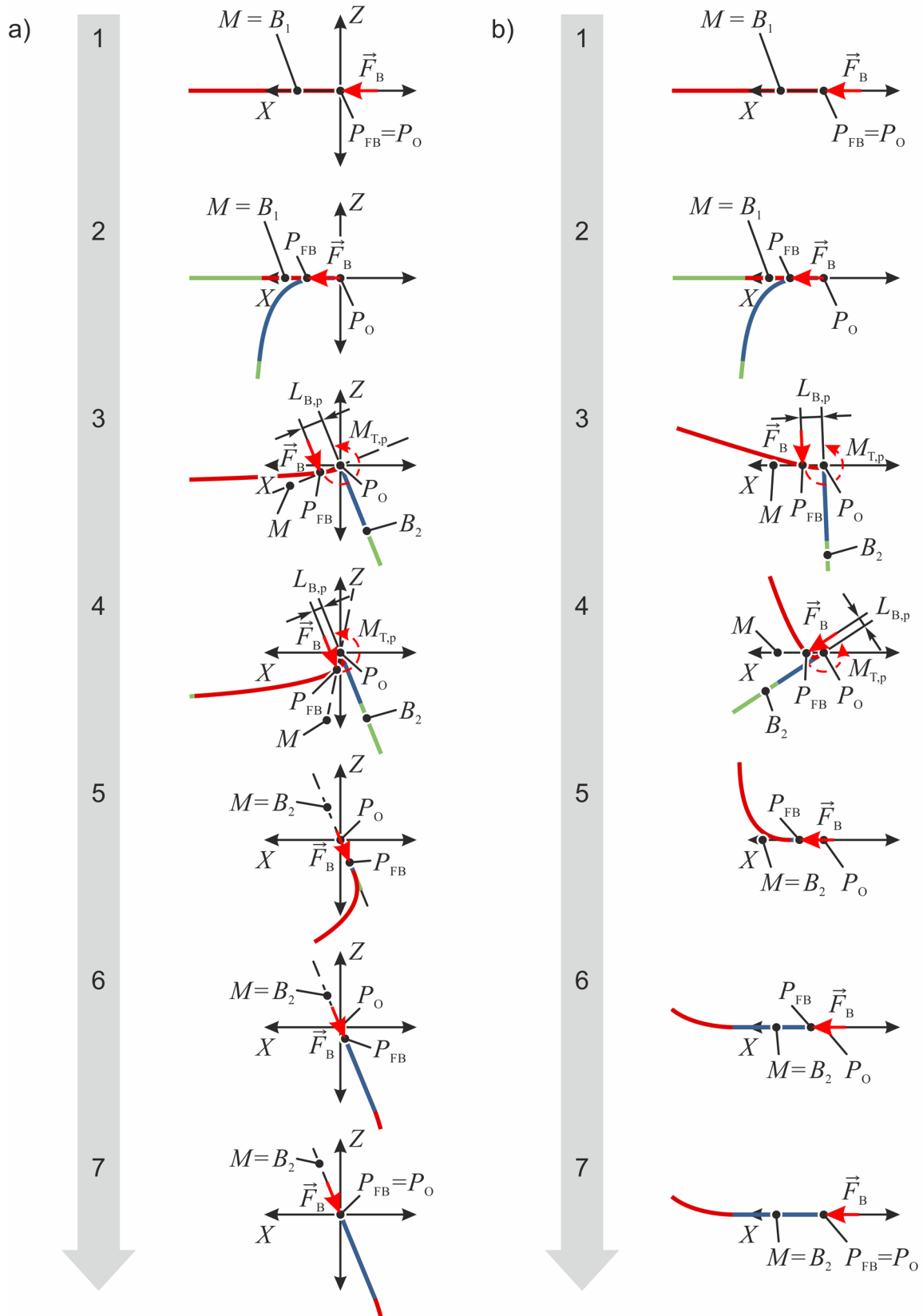
Figure 4.12 shows the front view of the sequence of kinematic movements initially presented in Figure 4.9 for an exemplary profile with a bending line made up of two consecutive bending radii in two different bending planes  $B_1$  and  $B_2$ . A close look is now taken at the bending force vector, which always necessarily passes through the point  $P_{\text{FB}}$ . In steps 1 and 2 of both sequences a) and b) it can be seen that  $P_{\text{FB}}$  lies in the same plane as the single radius, going from the profile support to point  $P_{\text{FB}}$ . The same is true for steps 5 through 7. If the radius is now considered to be actually bent, a bending force needs to be applied at  $P_{\text{FB}}$  to generate the necessary bending moment. As only single radii are considered in the above-mentioned steps, which each lie in single bending planes, the bending force vector  $\vec{F}_B$  necessarily lies in this same plane. But what happens in the transition from one bending radius lying in one bending plane to the next radius lying in another bending plane?

Once the second radius is supposed to be bent, the bending force vector needs to instantly change direction to be parallel to the bending plane of the second radius. However, the force vector still needs to pass through  $P_{\text{FB}}$ . This means that the bending force vector does not lie in the bending plane but at a distance  $L_{B,p}$  to it. This effect can be seen in steps 3 and 4. What can be noticed in comparing these two steps in sequences a) and b) is that, although the absolute direction of the bending force vector is different in both sequences, the direction relative to the profile as well as the distance  $L_{B,p}$  are equal. This implies that the movement of the bending force vector relative to the profile is independent of the specific bending process design. Together with the knowledge that the value of the bending force vector is only influenced by the contour to be produced, it can be implied that a general formulation of 3D bending can be found that can be applied to all kinematic bending processes.

A bending force vector, set at a distance to the bending plane, results in an unwanted or parasitic torque  $M_{T,p}$  in the forming zone at the profile support:

$$M_{T,p} = F_B L_{B,p} \quad (4.83)$$

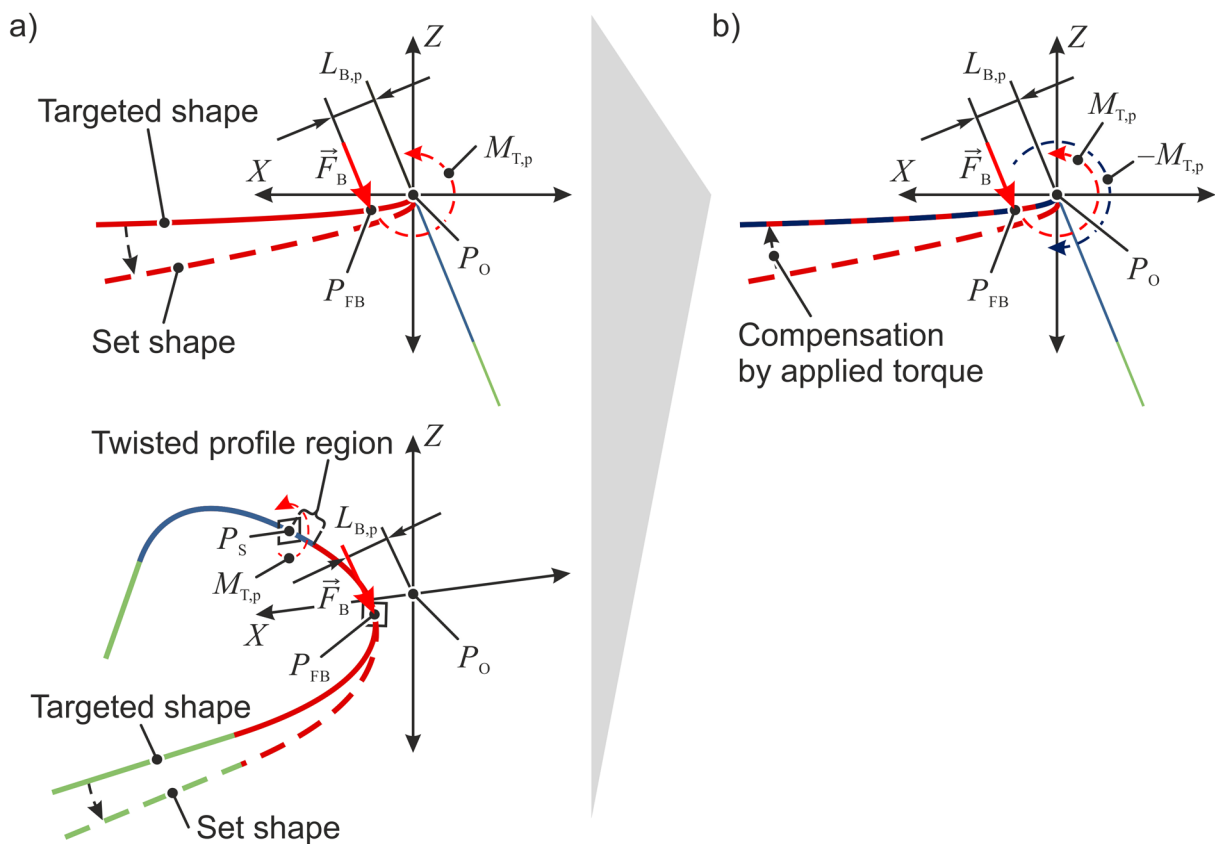
This can lead to unwanted twisting of the profile. This unwanted twisting of the profile not only results in unwanted torsion of the cross-section but also results in deviations of the bending plane rotation.



**Figure 4.12:** Movement of the bending force vector  $F_B$  for an exemplary profile with a bending line with two different subsequent radii in different bending planes ( $B_1, B_2$ ) using a cross table (a) or a single linear axis (b)

Figure 4.13a) explains how local twisting of the profile in transition zones can affect the angle between two subsequent bending planes using step 3 of the kinematic sequence shown in Figure 4.12a). This phenomenon has a direct influence on the applicability of 3-cDOF processes on profiles with non-circular cross-sections. It was stated before in Section 4.2.1 that a 3-cDOF process can be used on these profiles if the targeted apparent twist is exactly opposite to the bending plane rotation, so in other words if  $d\phi_{\text{apparent}} = -d\theta_r$  (see Eq. (4.36)). Depending on the magnitude of the parasitic torque  $M_{T,p}$  in transition areas, the resulting profile shape, specifically the bending plane rotation and the cross-sectional twist, might vary greatly from the targeted shape. Hudovernik (2014a), for instance, noticed deviations of around 15 % between targeted and set bending plane rotations in his investigations.

If the profile has a circular cross-section or if the predicted unwanted twist of a profile with a non-circular cross-section is insignificant for the application, then the targeted bending line can still be achieved if the deviation in the bending plane rotation is compensated by bending axes movements. If the cross-section position is essential for the application of a profile, a compensation of  $M_{T,p}$  can only be done using a 4<sup>th</sup> cDOF to apply a compensatory torque of  $-M_{T,p}$  to the forming zone as seen in Figure 4.13b).



**Figure 4.13:** Deviation of the bending plane rotation caused by profile torsion in the transition zone from one bending plane to the next



## **5 Setup of a 5-cDOF profile bending process and measuring equipment**

The conclusion of Section 4.2.1 was that 3D bending of profiles with non-circular cross-sections to arbitrary shapes can only be performed with bending processes that encompass at least 4 controlled degrees of freedom (cDOF). This chapter focuses on the setup of such a process and the development of measuring equipment to monitor the torque applied during bending and simultaneous twisting. Additionally, the development of a contour sensor is described as well as the setup of a comprehensive numerical process model. However, before diving into the experimental hardware and numerical methods, the material used in the investigations is presented.

### **5.1 Material characterization and parametrization**

As was described in Section 2.2 of the state of the art, the accuracy of kinematic profile bending processes is very sensitive to accuracy of the material data used in the process model. Tubes and profiles are often roll formed and are, thus, pre-strained in axial direction (Weimar, 1966) and along the perimeter of the cross-section (Eichhorn, 1974). Together with the necessity to weld the profiles longitudinally to produce closed sections, this makes roll-formed profiles highly anisotropic. Compared to sheet material, profiles only offer flat surface areas of an extremely limited width – width in this case meaning length along the perimeter. Tubes do not even have any flat surfaces at all. This makes a thorough material characterization difficult, time consuming, and not realizable with standard measuring equipment. Since material characterization is not the focus of this work, it was decided to use profile material that can be robustly characterized simply by uniaxial tensile tests. The only possible ways to produce reasonably isotropic profiles are either by hot rolling (Halmos, 2006) or by a cold forming step such as roll forming or cold drawing and subsequent heat treatment (Hubmer, 2017).

For the investigations, it was decided to use cold-drawn and heat-treated seamless precision tubes from Mannesmann Precision Tubes GmbH (formerly known as Salzgitter Mannesmann Precision GmbH). Specifically, the air hardening steel MW700L was selected in its soft-annealed state (Z1) and its air-hardened and tempered state (Z3). As profile geometry, a square cross-section was chosen with the size 40x40x2.5 mm. Tensile tests complying with DIN EN ISO 6892-1:2009-12 using a non-proportional A80 tensile probe as described in Appendix B of the DIN standard (gauge length = 80 mm, probe width = 20 mm) were conducted on a Zwick Z250 SN universal testing machine equipped with an Xforce K load cell.

In order to achieve a continuous mathematical description of the stress-strain relationship of the material with the aim of generating a monotonically increasing function well suited for FE-simulations, a flow curve approximation has to be performed. Because

maximum strains reached in kinematic profile bending are generally below 0.1, an accurate approximation has to be used for exactly this range of small strains. The elongated yield point of the material in the Z1 state gives the experimental data an initial convex appearance, followed by a concave trend. This kind of material behavior cannot accurately be described by the methods proposed by Ludwik (1909), Hollomon (1945), Swift (1952), or Voce (1948) as these methods only allow purely concave approximations and, thus, deviate from the experimental data points in the relevant strain range. The approximation method proposed by Hockett and Sherby (1975) is based on the method set up by Voce, but includes an additional power function in the exponential term (see Eq. (5.1)).

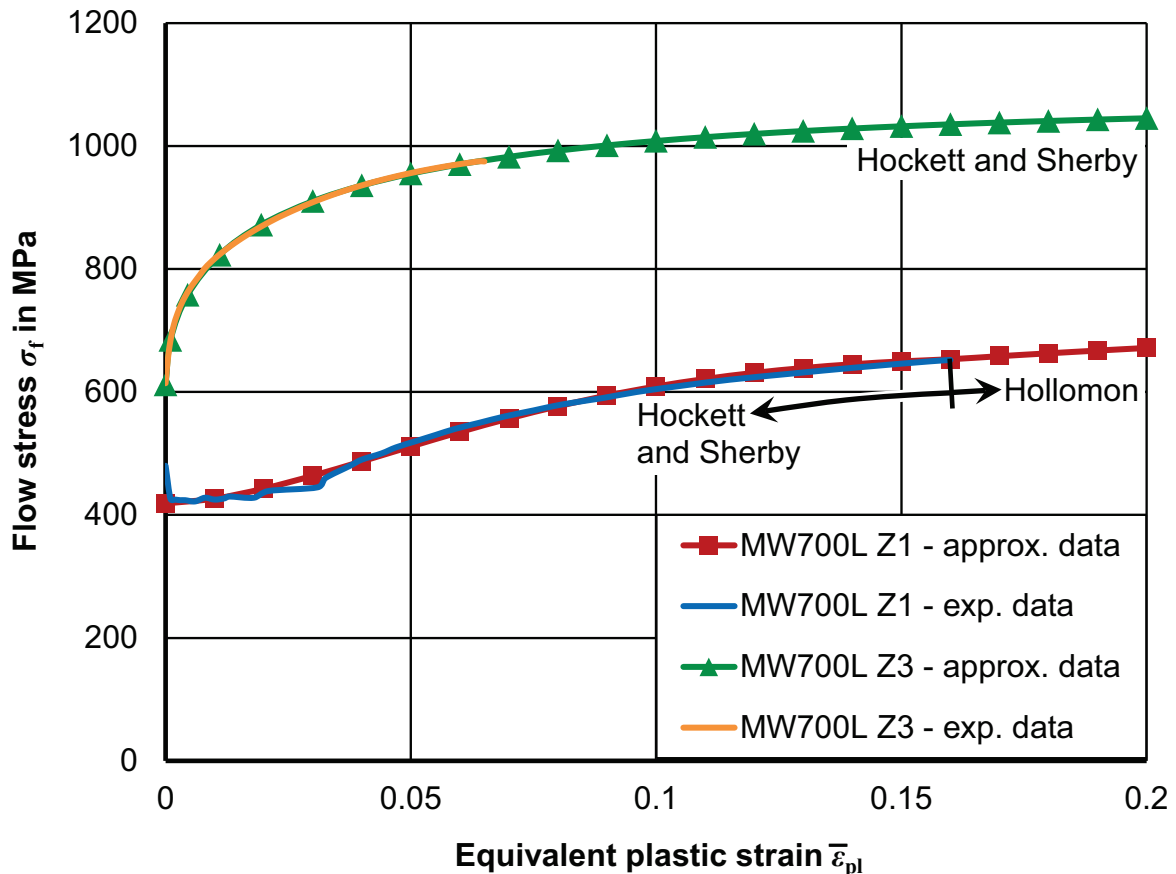
$$\sigma_f(\bar{\varepsilon}_{pl}) = \sigma_\infty - (\sigma_\infty - \sigma_Y) \cdot e^{-m \cdot (\bar{\varepsilon}_{pl})^{n_{HS}}} \quad (5.1)$$

This additional exponent actually allows the function to exhibit an inflection point, making it the optimal choice for the present flow curve approximation. Since the elongated yield point covers a small strain range compared to the complete flow curve, the initial convex curve trend can only be reached with a Hockett and Sherby approximation if the asymptotic parameter  $\sigma_\infty$  is relatively low. In cases where exact approximations are

**Table 5.1:** Flow curve approximations for MW700L Z1 and MW700L Z3

<b>MW700L Z1: Hockett and Sherby + Hollomon</b>	
$\sigma_f(\bar{\varepsilon}_{pl}) = \begin{cases} \sigma_\infty - (\sigma_\infty - \sigma_Y) \cdot e^{-m \cdot (\bar{\varepsilon}_{pl})^{n_{HS}}} & \text{for } \bar{\varepsilon}_{pl} < 0.17 \\ C \cdot \bar{\varepsilon}_{pl}^{n_H} & \text{for } \bar{\varepsilon}_{pl} \geq 0.17 \end{cases} \quad (5.2)$	
Hockett and Sherby parameters	Hollomon parameters
$\sigma_Y = 418 \text{ MPa}$ $\sigma_\infty = 661.99 \text{ MPa}$ $n_{HS} = 1.6676$ $m = 70.802$	$C = 820 \text{ MPa}$ $n_H = 0.124$
<b>MW700L Z3: Hockett and Sherby</b>	
$\sigma_f(\bar{\varepsilon}_{pl}) = \sigma_\infty - (\sigma_\infty - \sigma_Y) \cdot e^{-m \cdot (\bar{\varepsilon}_{pl})^{n_{HS}}} \quad (5.3)$	
Hockett and Sherby parameters	
$\sigma_Y = 612 \text{ MPa}$ $\sigma_\infty = 1071.2 \text{ MPa}$ $n = 0.5312$ $m = 6.7548$	

needed in low as well as in high strains, the combination of a Hockett and Sherby approximation and another approximation is recommended. Here, the approach by Hollomon is adequate, because while being simple, it offers a realistic approximation of material hardening (Yin, 2014a). Table 5.1 shows the approximation functions used for MW700L Z1 and Z3 and the parameters found using a least-square data fitting method. Figure 5.1 displays the flow curve approximations for MW700L Z1 and Z3 in comparison with the experimental data.



**Figure 5.1:** Experimental and approximated flow curve of MW700L Z1

But not only the plastic material behavior has to be accurately described to allow a robust operation of kinematic bending processes. Also, the elastic material behavior plays a crucial role, especially in the determination of springback. The standard method to describe the elastic behavior of metals is by determining the Young's modulus. The standard testing procedure in metal forming is by regarding the experimental stress-strain data, gained from the tensile test, up to the yield point and approximating the stress-strain relationship of a selected region in this sector by linear regression. In materials without an elongated yield point, the yield point definition itself depends on the Young's modulus. This interdependency of parameters makes the Young's modulus determination with a tensile test highly dependent on the interpretation by the operator. A method to reduce the range of Young's modulus interpretations is described in the DIN EN

ISO 6892-1:2009-12, whereby the sample is first tensioned up to the expected yield strength and, upon exceeding this value, the applied tensile force is reduced down to 10 % of the force value at the expected yield point. A subsequent force increase above the initial force value generates a hysteresis loop, whose middle line or chord, specifically, its slope shall serve as the Young's modulus. Other methods to determine the Young's modulus use acoustic analyses as, for instance, resonance measurement (Gerstein et al., 2017) or ultrasonic pulse-echo measurement (Krautkrämer and Krautkrämer, 1990), whereby the wave propagation in the longitudinal and transverse direction through a probe is first used to calculate the Poisson's ratio and subsequently the Young's modulus (Krautkrämer and Krautkrämer, 1990). The resonance measurement is standardized in the ASTM E1875-13 (Standard Test Method for Dynamic Young's Modulus, Shear Modulus, and Poisson's Ratio by Sonic Resonance) and ASTM E1876-15 (... by Impulse Excitation of Vibration) but necessitates a complex setup to measure the resonance frequency of a sample. The ultrasonic pulse-echo method, on the other hand, can be performed with readily available ultrasonic thickness gauges (Olympus, 2018). However, measurements of the latter are highly dependent on accurate thickness measurements and are sensitive to applied stresses on the samples, which make the material double refracting (Krautkrämer and Krautkrämer, 1990).

In tube and profile bending, and actually in metal forming in general, the Young's modulus is used in springback calculations. And this is done even though Lems investigated the change in Young's modulus after material deformation as early as 1963. Morestin and Boivin showed in 1996 that the Young's modulus of construction steel, of non-alloy quality special steel and high-strength low-alloy steels reduces by 5-15 % in tension and compression up to an equivalent plastic strain of 0.05, with insignificant further reductions up to 0.1 in tension. Recent investigations have extended these observations to dual-phase steel, specifically DP600, for which Yoshida et al. (2002) noted a reduction of 21 % and ul Hassan et al. (2016) noted a reduction of 28 % up to an eq. plastic strain of 0.1, DP800, for which Chongthairungruang et al. (2012) observed a reduction of 14-21 % depending on the rolling direction, and DP1000, for which ul Hassan et al. (2016) observed a reduction of 26 % and saturation up to a strain of 0.09. As shown by Gerstein et al. (2016) for DP600, this high apparent reduction of Young's modulus cannot be measured by the resonance method. Instead of values between 21 % and 28 %, only a reduction of 3 % was observed at a strain of 0.01. This difference is due to the fact that the material actually does not act purely elastic during unloading. Rather, the unloading strain can be separated into a linear elastic contribution and an anelastic<sup>7</sup> contribution

---

<sup>7</sup> Anelasticity refers to short-range reversible movements of dislocations, which result in a reversible non-linear strain recovered during unloading alongside the pure elastic strain (Torkabadi et al., 2017) and is not to be confused with inelasticity.

(Torkabadi et al., 2017). While the non-destructive resonance method can apparently only measure the linear elastic contribution, the total unloading strain can only be measured by a destructive method such as the tensile test.

As such, the apparent Young's modulus degradation of MW700L Z1 and Z3 was determined by cyclic tensile tests. The selected range of nominal strains is 0 to 8 %, where 8 % is the theoretical nominal strain reached in the extrados of a profile with a square cross-section of the size 40x40 mm, bent to the loaded radius 250 mm in normal direction. During the tensile tests, the tensile force was reduced down to 0 in 1 % intervals, generating a set of 8 hysteresis loops per test. The chord moduli were determined by approximating the data during unloading and loading using linear regression. Figure 5.2 shows the experimental apparent Young's modulus degradation and the approximation by Yoshida et al. (2002):

$$E(\bar{\varepsilon}_{pl}) = E_0 - (E_0 - E_\infty) \cdot (1 - e^{-\zeta \cdot \bar{\varepsilon}_{pl}}) \quad (5.4)$$

which, when simplified, is actually identical to the approximation by Voce (1948):

$$E(\bar{\varepsilon}_{pl}) = E_\infty - (E_\infty - E_0) \cdot (e^{-\zeta \cdot \bar{\varepsilon}_{pl}}) \quad (5.5)$$

As in the parameter identification of the flow curve, the parameters of the Young's modulus approximation were found using a least-square data fitting method. The Parameters are listed in Table 5.2, while the degradation curves are shown in Figure 5.2.

**Table 5.2:** Parameters for the Young's modulus approximation for MW700L Z1 and MW700L Z3

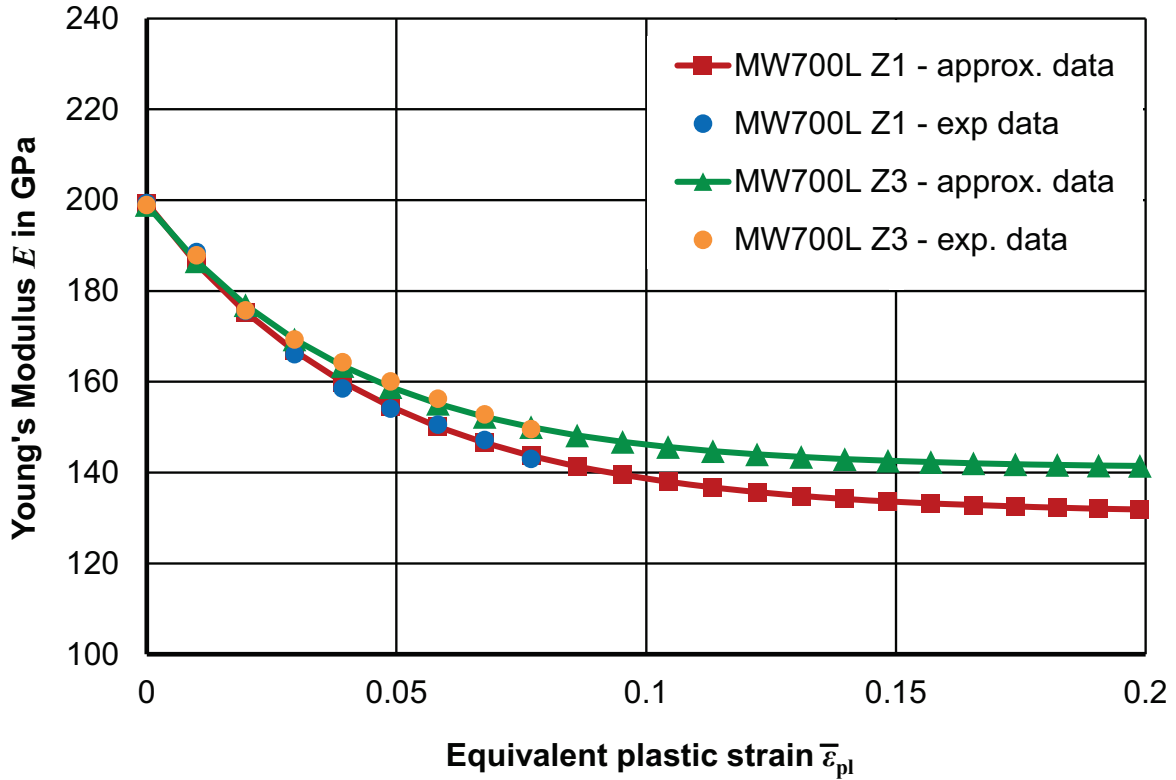
MW700L Z1	MW700L Z3
$E_0 = 199,350 \text{ MPa}$	$E_0 = 198,920 \text{ MPa}$
$E_\infty = 131,000 \text{ MPa}$	$E_\infty = 141,000 \text{ MPa}$
$\zeta = 21.874$	$\zeta = 24.163$

Since MW700L Z1 shows an elongated yield point (Figure 5.1) with a sharp transition from elastic to elastic-plastic behavior, the Young's modulus  $E_0$  was stably measured as 199,350 MPa without the need for an additional hysteresis loop. The apparent Young's modulus degradation from 0 to the equivalent plastic strain of 0.077 is 28 %. The approximation function predicts a further degradation down to a total of 34 %.

For MW700L Z3 a Young's modulus  $E_0$  of 198,920 MPa was determined. The apparent Young's modulus degradation from 0 to the equivalent plastic strain of 0.077 is 25 %. The approximation function predicts a further degradation down to a total of 29 %.

The profiles are regarded as isotropic so that the shear modulus can be related to the Young's modulus by:

$$G = \frac{1}{2(1+\nu)}E \quad \text{with} \quad \nu = 0.3 \quad (5.6)$$

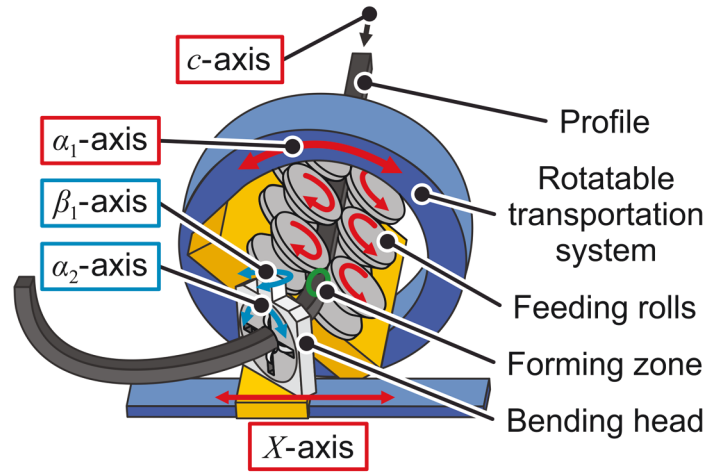


**Figure 5.2:** Experimental and approximated apparent Young's modulus degradation

## 5.2 Extension of 3-cDOF TSS bending to a 5-cDOF profile bending process

The TSS bending process, as it was set up by Hermes et al. (2008), only offers 3 cDOF (see Figure 5.3). Using the insight found in Section 4.2.1 it follows that this process can only be used in a limited fashion to bend 3D contours in which the targeted apparent twist is exactly opposite to the bending plane rotation. The capability of the 3-cDOF TSS bending process to produce such profiles was shown by Chatti et al. (2010) and Hudovernik (2014a). Especially the latter noticed large deviations between targeted and set bending plane rotations in his investigations. The most likely cause for the presented high contour deviation is the incapability of the 3-cDOF process to compensate the parasitic torque (see Section 4.2.4) that occurs during bending plane transitions.

Considering the classification presented in Table 4.1, TSS bending is a kinematic bending process with a bending head on a single linear axis ( $X$ -axis). By consulting Figure 4.10, which shows the possible locations of cDOFs required to produce profiles with



**Figure 5.3:** 3-cDOF TSS bending process (Hermes et al., 2008), cDOFs are marked red, free DOFs are marked blue

3D bending contours with and without torsion in different process designs, it can be inferred that the only option to apply twist in TSS bending is by controlling the rotary DOF ( $\alpha_2$ -axis) of the bending head (Figure 4.10f). Controlling the  $\alpha_2$ -axis would convert the 3-cDOF TSS bending process into a 4-cDOF process.

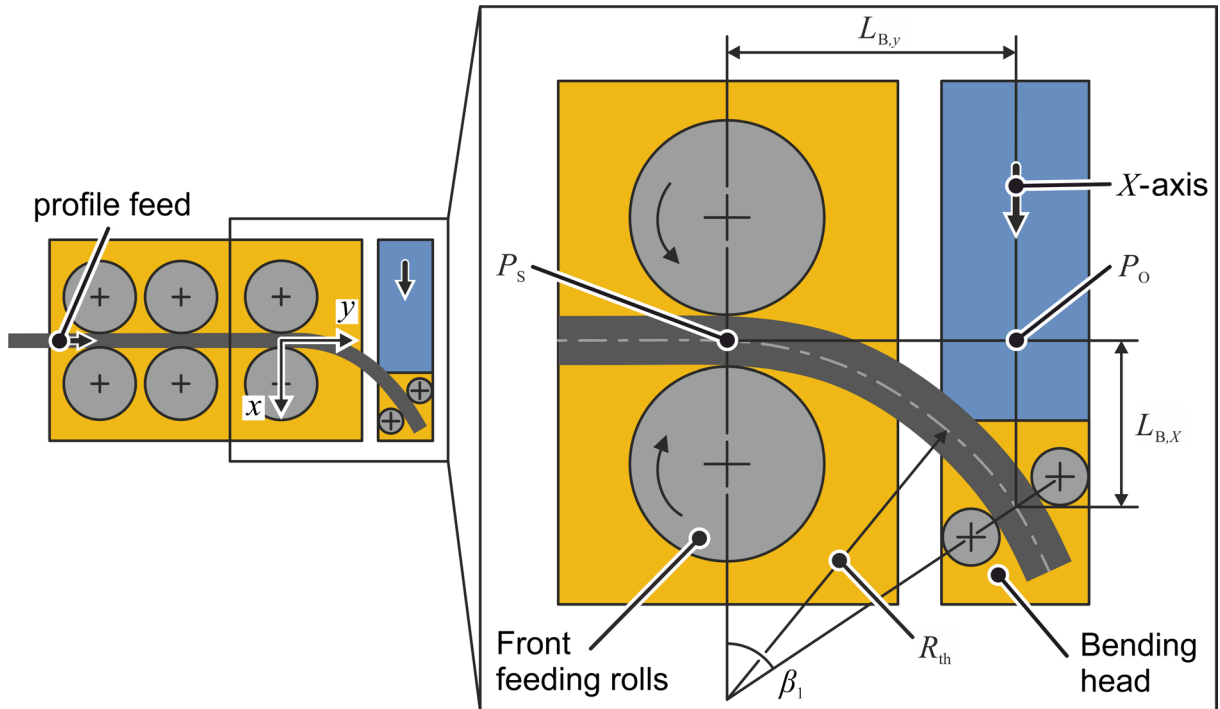
In kinematic bending processes with a bending head on a single linear axis, the bending head should move along the  $X$ -axis according to the point of bending force application  $P_{FB}$  and rotate according to the rotations of the plane  $N_{P_{FB}}$  at  $P_{FB}$  that is congruent to the normal plane  $N$  of the bending line at this same point (see Section 4.2.1). In Section 4.2.3 these rotations were named  $\beta_1$ , the rotation angle of  $N$  around the normal vector  $\vec{b}_M$  of the machine bending plane  $M$ , and  $\beta_2$ , the rotation angle of  $N$  around  $\vec{n}_{M, \text{map}}$ , which is equal to the directional vector of the  $X$ -axis, rotated by  $\beta_1$  to lie in  $N$  and put in unit length. Looking at the dimensions of the set up 3-cDOF TSS bending machine and taking the distance from the front feeding roll pair to the  $X$ -axis ( $L_{B,y} = \left\| \overline{P_S P_O} \right\| = 390 \text{ mm}$ ) and the maximum  $X$ -axis value of 250 mm, and neglecting machine stiffness and profile elasticity, the minimal producible theoretical bending radius would be 429.2 mm. The maximum angle of  $\beta_1$  would be 1.14 rad or  $65.3^\circ$  in this case. The general relation is given by:

$$R_{\text{th}} = \frac{1}{2} \left( \frac{L_{B,X}^2 + L_{B,y}^2}{L_{B,X}} \right) \quad (5.7)$$

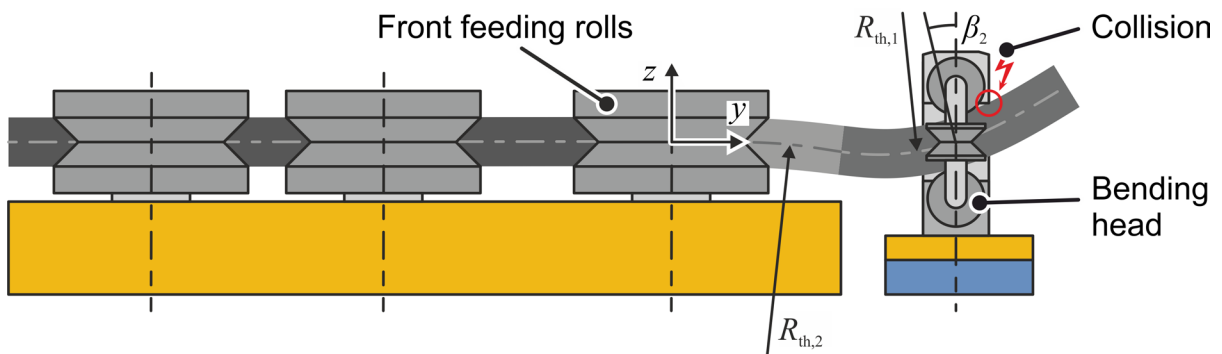
and:

$$\beta_1 = \sin^{-1} \left( \frac{L_{B,y}}{R_{\text{th}}} \right) \quad (5.8)$$

Figure 5.3 shows that the 3-cDOF TSS bending process does not include a  $\beta_2$ -axis and, thus, cannot perform an according bending head rotation. If the profile now switches



**Figure 5.4:** Geometrical relations of bending head movement and resulting ideal bending radius and  $\beta_1$  angle



**Figure 5.5:** Angular offset of bending head to the bending line of the profile during 3D-bending using the 3-cDOF TSS bending process

from one radius  $R_{th,1}$  on one bending plane to the next radius  $R_{th,2}$  on the next bending plane, as shown for an exemplary profile in Figure 4.9, the bending head is offset from the normal plane  $N$  of the bending line by exactly  $-\beta_2$ . The maximum angle of  $\beta_2$  can be calculated by considering two consecutive radii of 429.2 mm and a bending plane rotation  $\Delta\theta_r$  of  $\pi$  from the first radius ( $R_{th,1}$ ) to the second ( $R_{th,2}$ ). If a third consecutive radius now lies on a bending plane perpendicular to the bending plane of  $R_{th,2}$ , the profile is positioned in the machine as shown in Figure 5.5 resulting in  $\beta_2 = 0.384 \text{ rad} = 22.0^\circ$ . This large offset can pose problems for the bending process by causing collisions in the bending head. Furthermore, jamming of the profile in the bending head rolls can occur when the  $y$ -component of the bending force exceeds the feeding force of the feeding



system or because of excessive Hertzian stress between the bending head rolls and the profile and the resulting deformation of the profile surface. In the calculation of the Hertzian stress between the bending head rolls and the profile, the roll is considered as elastic and the profile is thought of as an elastic half-space with a plane surface. The contact problem can then be defined as the interaction of two cylinders, whereby one cylinder has an infinite radius (the profile). According Popov (2010) the contact stress between two cylinders with parallel axes can be calculated by:

$$\sigma_c = \frac{E^*}{2} \frac{d}{c_w} = \frac{E^*}{2} \sqrt{\frac{d}{R^*}} = \sqrt{\frac{E^* F}{\pi c_L R^*}} \quad (5.9)$$

Whereby  $c_L$  is the contact length,  $d$  is the depth of impression and,  $c_w$  is half of the contact width:

$$c_w = \sqrt{R^* d} \quad (5.10)$$

The equivalent radius  $R^*$  is given by:

$$\frac{1}{R^*} = \frac{1}{R_{\text{roll}}} + \frac{1}{R_{\text{profile}}} \xrightarrow{\text{when } R_{\text{profile}} = \infty} 0 \quad (5.11)$$

and, thus, is equal to the radius of the bending head roll  $R_{\text{roll}}$ . The equivalent Young's Modulus  $E^*$  is computed by:

$$\frac{1}{E^*} = \frac{1 - \nu_{\text{roll}}^2}{E_{\text{roll}}} + \frac{1 - \nu_{\text{profile}}^2}{E_{\text{profile}}} \quad (5.12)$$

where  $\nu$  is the Poisson's ratio.  $F$  is the normal contact force and given by:

$$F = \frac{\pi}{4} E^* c_L d \quad (5.13)$$

Using the contact length of 28 mm, a bending roll radius of 40 mm and assuming a Poisson's ratio of 0.3 and a Young's modulus of 210 GPa for both the bending head roll and the profile, Figure 5.6 shows the bending head offset and the geometrically linked impression depth for different contact stresses. The maximum contact stress of 2000 MPa is given by the material of the bending head roll. The rolls are made of quenched and tempered 42CrMo4 (DIN EN ISO 683-1, Steel number: 1.7225), surface hardened by gas nitriding reaching a surface hardness of 55-64 HRC.

From Figure 5.6 it can be seen that even the slightest bending head offsets can potentially affect the surface quality of the profile. Considering that the shown impression depths are below 0.05 mm the possible surface defect could be described as burnishing. On the one hand, higher bending head offsets than shown in Figure 5.6 would damage the bending head rolls. On the other hand, these low offsets would greatly reduce the

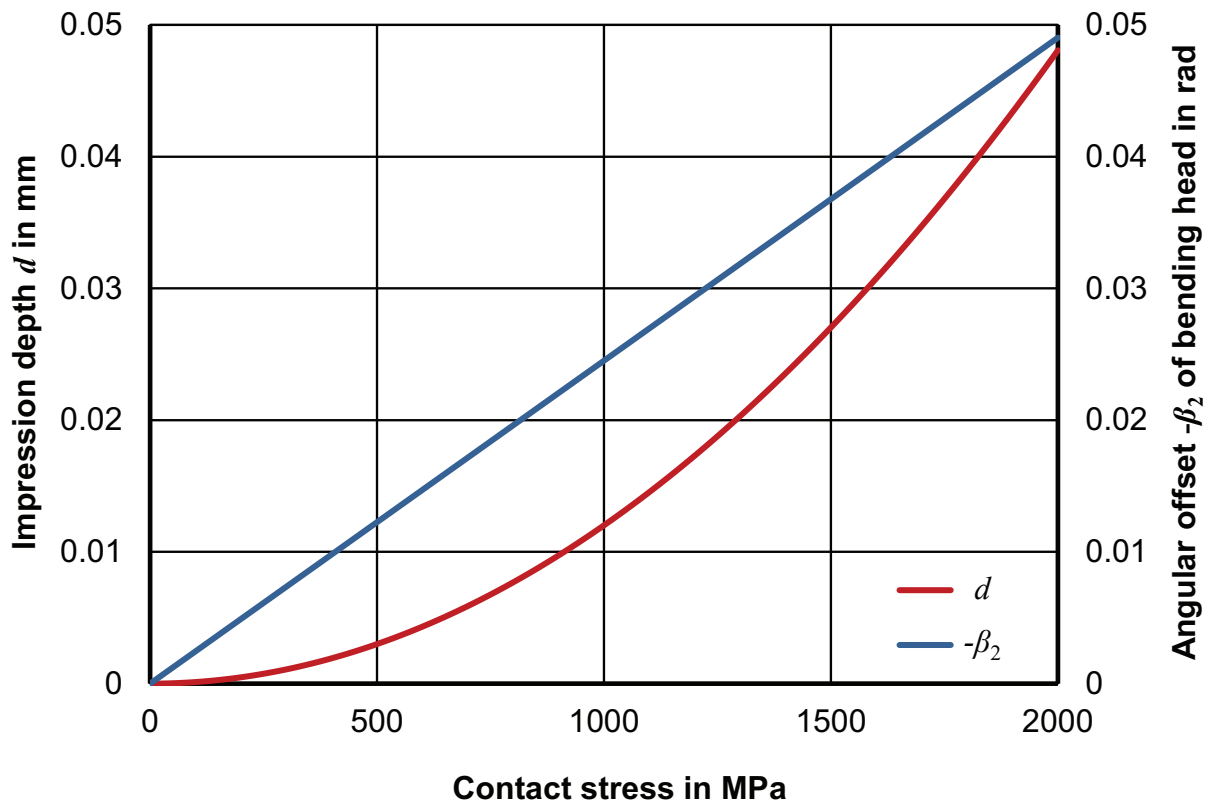


Figure 5.6: Impression depth and the geometrically linked bending head offset for different contact stresses

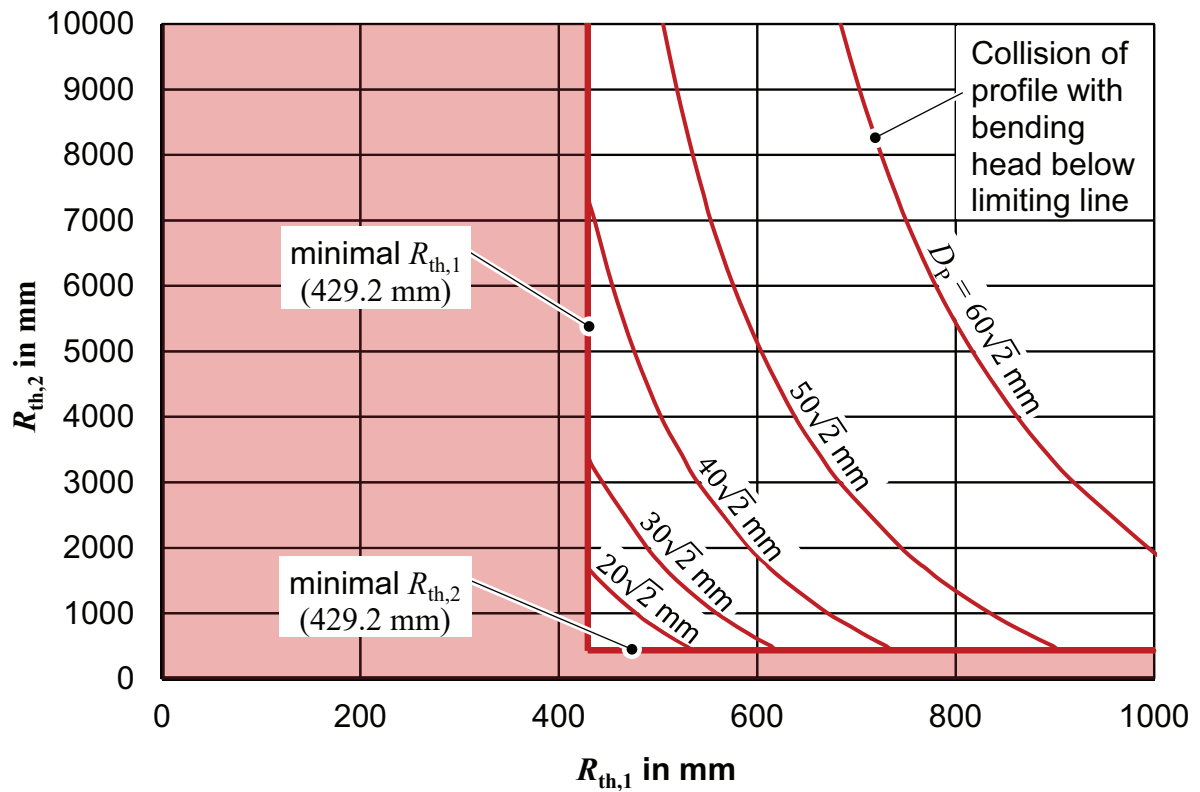


Figure 5.7: Process window considering minimal producible radii without collisions

applicability of the TSS bending process to bend 3D-contours. To overcome this limitation, the bending head rolls must be adjusted to create a gap in between the rolls and the profile. Based on an analysis of the circular runout tolerance of the rotatable transportation system, which resulted in measurements of  $\pm 0.2$  mm (Staupendahl et al. 2014a) at the point  $P_O$ , the size of the gap was defined to be 0.2 mm. With the additional consideration of the profile elasticity between the points  $P_S$  and  $P_{FB}$ , the process window shown in Figure 5.7 is achieved. The combinations of  $R_{th,1}$  and  $R_{th,2}$  in the red area are not producible because of the limited  $X$ -axis movements ( $\pm 250$  mm), independent of the profile cross-section. The red curved lines further limit the process window based on the collision of the profile with the bending head, whereby the possible radius combinations are to the top right of the lines. The limits are shown for sizes of arbitrary cross-sections ranging from  $D_P = 20\sqrt{2}$  mm to  $D_P = 60\sqrt{2}$  mm, where  $D_P$  is defined as the diameter of the enclosing circle having its midpoint at the center of gravity of the cross-section.

### 5.2.1 Drive system of the bending head's rotational DOFs

As explained in the previous section, controlling the  $\alpha_2$ -axis would convert the 3-cDOF TSS bending process into a 4-cDOF process and theoretically allow 3D bending of profiles with non-circular cross-sections to arbitrary bending contours. However, the missing  $\beta_2$ -axis and the resulting angular offset between the profile and the bending head can cause jamming of the free  $\beta_1$ -axis. To overcome the limitations of the process concerning profile shape and part tolerances, the process is, thus, extended by two additional actuators. One to drive the  $\alpha_2$ -axis and one to drive the  $\beta_1$ -axis. For the development of the controlled bending head system<sup>8</sup>, the systematic engineering design approach of Pahl and Beitz (1977) was used, standardized in the VDI guideline VDI 2221, which divides the development and design process into the single steps:

- Planning and clarifying the task
- Conceptual design
- Embodiment design
- Detail design

The major requirements in the planning step were:

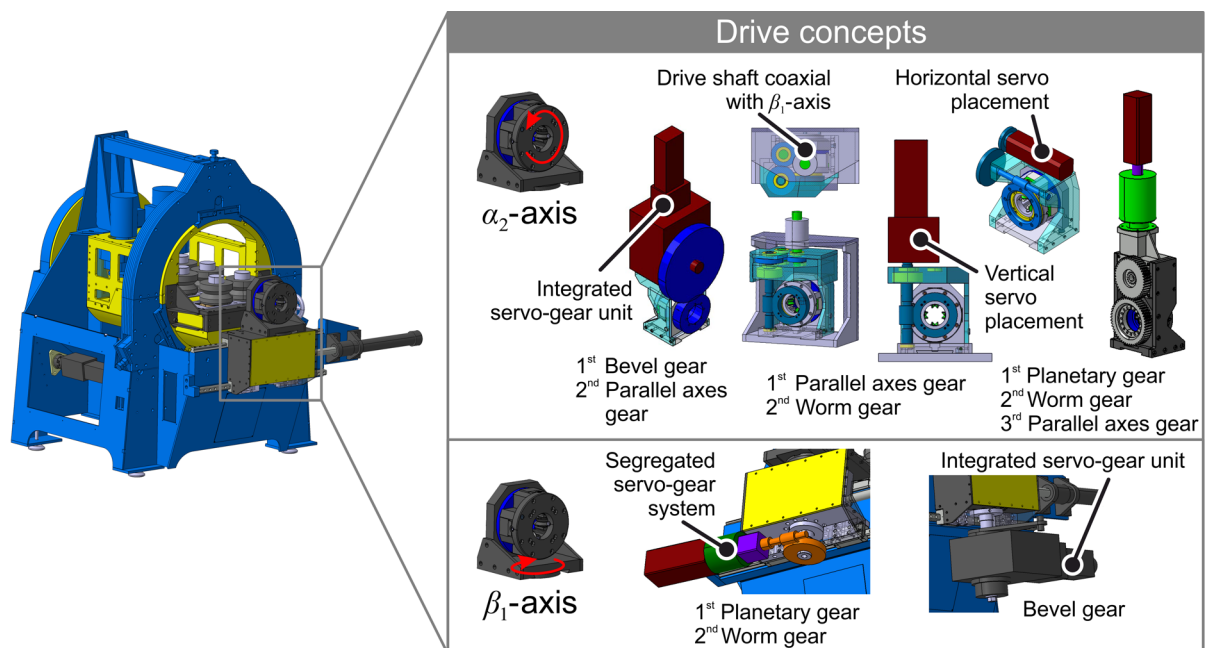
- The torque and rotation speed of the  $\alpha_2$ -axis actuator must match or be greater than the maximum torque and speed of the  $\alpha_1$ -axis actuator (3000 Nm,  $1.89 \text{ min}^{-1}$ )

---

<sup>8</sup> The design and assembly of the bending head drive system was done by Aydogan Zeyd Kaya in the course of his diploma thesis: Konstruktive Erweiterung der TSS-Profilbiegemaschine um zwei zusätzliche CNC-Servoachsen [Extension of the TSS Profile Bending Machine by two additional CNC-Servo Axes], Fachhochschule Aachen, 2011, supervised by: D. Staupendahl, M. Hermes, A. E. Tekkaya, and H. Heinrichs.

- The rotation speed of the  $\beta_1$ -axis actuator must not reduce the overall process time
- The process window must not be reduced by more than 5 %

During this systematic process, different drive concepts were evaluated regarding their complexity, efficiency, installation size, cost, as well as the torque and rotation speed requirements. Segregated and integrated servo-gear systems were compared, the advantages and disadvantages of different angular gears, namely bevel gears and worm gears, were analyzed, and the advantages and disadvantages of different axial gear systems, based on parallel axes gears and planetary gears, were assessed. Figure 5.8 gives an overview of the drive concepts that were investigated.



**Figure 5.8:** Drive concepts for the  $\alpha_2$ -axis and the  $\beta_1$ -axis (Staupendahl et al. 2014a)

Since the bending head itself is quite compact, a compact gear system is needed. For the drive of the  $\alpha_2$ -axis, the least interference with the bending process proved to be a vertical placement of the servo. The horizontal placement would either limit the rotation angles of the  $\beta_1$ -axis or greatly increase the distance  $L_{B,y}$ . However, a vertical placement of the servo entailed an angular gear with an operating angle of  $90^\circ$ . Gear concepts involving bevel gears or worm gears as a last stage did not meet the requirements concerning maintaining the process window inside the previously defined tolerance. Also, bevel gear boxes used as a first stage proved to need too much installation space and result in premature collision of the profile with the bending head (see Figure 5.5). Worm gear boxes, on the other hand, allowed much more compact setups. Yet, worm gears only allow the transmission of high torques at low speed ratios. In order to reach high torques, worm gears either have to be driven by high torque servos, whose diameter is too large for the present use case, or be combined with additional axial transmissions.

Applicable axial gearboxes either use planetary gears or parallel axes gears based on spur or helical gears. Parallel axes gearboxes proved the more cost effective choice. The finally chosen concept uses a vertically placed servo, which drives the following gear stages:

1. Parallel axes gear box → increases torque output of servo
2. Worm gear box → 90° direction change, further torque increase
3. Parallel axes gear → transmission of torque to  $\alpha_2$ -axis

In the embodiment design it was finally decided to use a compact helical servo gear motor with an internal speed ratio of 66.12 from *KEB Automation* as stage 1, which offers a maximum continuous torque output of 610 Nm (standstill) and a maximum rotational speed of 45 min<sup>-1</sup>. As a second stage, a high-torque worm gear unit from *Atlanta Antriebssysteme* was chosen with a transmission ratio of 4.75, a center distance of 80 mm, and an allowable static torque to avoid tooth fracture of 3000 Nm. The allowable static torque was seen as the determining parameter because the speed of the driving shaft is considerably lower than the specified maximum driving speed of the gear of 3000 min<sup>-1</sup>. The advantage of using a worm gear with a low speed ratio is the higher transmittable torque and higher efficiency compared to worm gears with high-speed ratios. The efficiency of the selected worm gear at 1500 min<sup>-1</sup> is stated as 94 % and is reduced to 77 % at standstill (Atlanta, 2012). As a third stage, a spur gear with a modulus of 5, a width of 50 mm, and a transmission ratio of 1.16 was especially designed to be fully integrated into the bending head, replacing the outer housing of the bending head's thrust bearing. In order to enable the transmission of torques up to 3000 Nm from the worm to the spur gear, the bolted connection interface according to DIN EN ISO 9409-1 was strengthened by 4 hardened cylindrical pins. The selection of a spur gear over a helical gear was mainly done to avoid additional thrust loads in axial direction and realize the highest possible transmission efficiency. The close to 100 % transmission efficiency is important for the integration of an accurate flange-based torque measurement device in between the worm gear and the spur gear as explained in Section 5.2.3.

The total speed ratio including the internal ratio of the gear motor is 364.32. The resulting nominal rotational speed of the  $\alpha_2$ -axis is 8.17 min<sup>-1</sup>. Since the  $\alpha_1$ -axis speed is limited to 1.89 min<sup>-1</sup>, as stated in the design requirements, the servo driving the  $\alpha_2$ -axis will, thus, mostly rotate up to around 23 % of its nominal speed. The torque output in this speed range is close to the servo's standstill torque. Using the total efficiency of the gear unit of 77 %, the continuous torque output of the  $\alpha_2$ -axis can be specified as 2588 Nm. The overloading capacity of the used servo is three times higher than the continuous torque at standstill, which allows a short-time torque output of 3480 Nm, limited by the 3000 Nm tooth fracture torque of the worm gear.

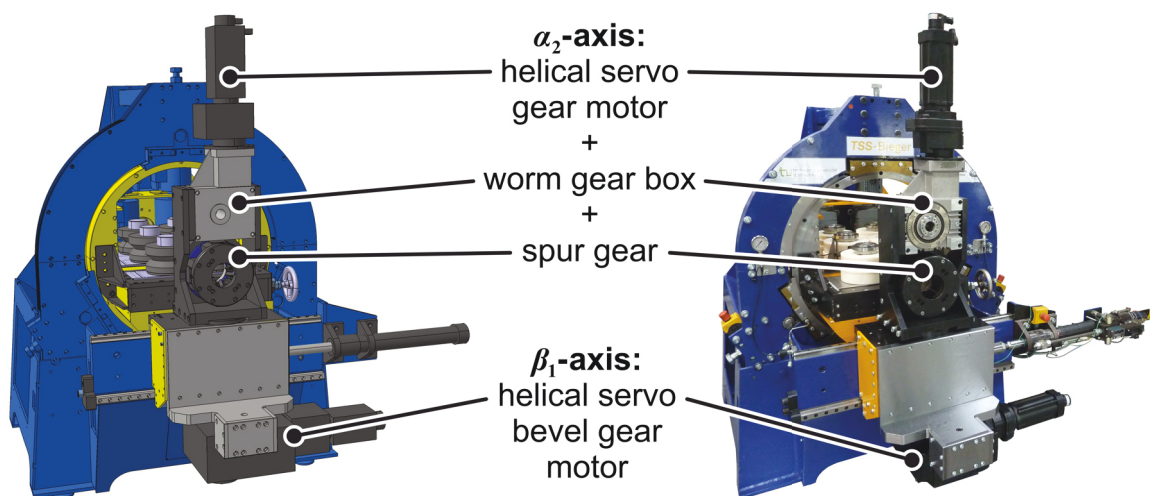
The connection of the bending head to the linear  $X$ -axis unit is realized through a vertical shaft, fixed to the bending head and supported in polymer sleeve and thrust bearings

inside the  $X$ -axis unit (Hermes, 2011). This support setup permits the free rotation of the shaft and, with it, the bending head around the  $\beta_1$ -axis. The shaft protrudes the lower casing of the  $X$ -axis unit and calls for a plug-on drive solution. A vertical placement of the servo with an axial connection to the shaft would cause collisions with the ground if mounted below the  $X$ -axis unit and decrease the process window if mounted in front of the unit. It was, thus, focused on a horizontal placement of the servo. As mentioned before in the description of the  $\alpha_2$ -axis drive, a worm gear of a certain size or, more specifically, a certain center distance withstands higher torques at lower speed ratios. If high-speed ratios are required to realize a specific final torque, a worm gear must be combined with additional gear units. In the case of the  $\alpha_2$ -axis, the installation space was the crucial factor that necessitated this kind of combination. As installation space below the  $X$ -axis unit is abundant, the main deciding factors were the drive complexity, cost, and efficiency. The finally chosen concept uses a:

- single integrated servo-bevel gear unit → Integrates the following functions:  
servo, increased torque output,  
90° direction change

In the embodiment design, it was decided to use a helical servo bevel gear motor with an internal speed ratio of 336.18 from *KEB Automation*, which offers a maximum continuous torque output of 2970 Nm (standstill) and a maximum rotational speed of 8.9 min<sup>-1</sup>. The vertical shaft holding the bending head was replaced by a shaft of increased length to fit through the entire hollow shaft of the servo-bevel gear unit and connected via a shrink disk. The bolted connection interface between the shaft and the bending head limits the transmittable torque to 2000 Nm.

Figure 5.9 shows the finalized detailed design of the bending head drive system and the realized machine extension. The slightly eccentric position of the bending head, which was previously needed for a robust operation of the undriven  $\beta_1$ -axis was not needed



**Figure 5.9:** Finalized bending head drive design and realized machine extension

anymore in the case of a driven axis. By centering the bending head, the distance from the front feeding roll pair to the  $X$ -axis ( $L_{B,y}$ ) was increased from 390 mm to 396.92 mm, which results in an increase of the minimal producible radii  $R_{th,min}$  from 429.2 mm to 440.1 mm. The process window is, thus, decreased by 2.5 %, which is well within the initially stated maximum required value of 5 %. By simply changing the lower limits of the process window shown in Figure 5.7 to the new minimal producible radii, the process window is still valid for the extended bending machine.

### 5.2.2 Performance of the 5-cDOF TSS bending process

Due to the changes made to the bending head, the stiffness of the bending machine was re-evaluated. The measurement strategy presented by Hermes (2011) was used to set up a displacement function for the point of bending force application as explained by Chatti et al. (2010). The new displacement function (Eq. (5.14) in Table 5.3) produces significantly lower values in the range 0.1 kN (factor 6) to 50 kN (factor 2) than the values calculated for the original setup using Eq. (2.7) and, hence, suggest a significantly higher machine stiffness. Additionally, the torsional stiffness of the machine was measured and is stated as the torsional spring constant  $c_m$  (Eq. (5.15) in Table 5.3).

Together with the extension of the machine by two additional driven axes, the complete control hardware and software of the machine was upgraded. Table 5.3 gives an overview of the characteristics of the upgraded 5-cDOF TSS bending machine. Originally, the  $\alpha_1$ -axis communicated over the serial bus RS-485, the  $c$ -axis was controlled by  $\pm 10V$ , and the  $X$ -axis communicated over CAN bus – all axes and sensors being connected to a process control unit made up of a dual-core PC (Pentium D 3.4 GHz, 1 GB RAM) with LabVIEW used as control software. The initial idea of integrating the additional bending head rotational axes into the process control via Ethernet was quickly abandoned due to high program cycle times caused by too many hardware interfaces and a slow PC hardware. In tests, these high cycle times caused the software-PID-controlled bending axis to jitter because of constant parameter overshooting at  $c$ -axis feed speeds above 30 mm/s, which eventually led to process failure. To overcome this problem, all communication with the axes was changed to one single interface: Profibus DP. The control hardware was upgraded to a current 4-core system and used as an embedded system. As control software, the LabVIEW Real-Time Module was used. Programming was done in LabVIEW 2012. The processors capability of hyper-threading was disabled due to compatibility issues with the real-time software.

As shown in Section 4.2.1, all axes movements can be related to profile feed. So, as realized by Hermes (2011) in his original process control, the  $c$ -axis is used as the master axis. In order to increase the stability of this axis and allow proper speed and velocity control when no profile is placed into the machine or if the rotary encoder used as a feed

Table 5.3: Characteristics of the 5-cDOF TSS bending machine

Features		Specifications
$\alpha_1$ -axis		<ul style="list-style-type: none"> <li>• Servo drive</li> <li>• Nominal torque: 3000 Nm</li> <li>• Nominal rotational speed: <math>1.89 \text{ min}^{-1}</math></li> <li>• Travel: <math>3600^\circ</math></li> </ul>
$\alpha_2$ -axis		<ul style="list-style-type: none"> <li>• Servo drive</li> <li>• Nominal torque: 3480 Nm</li> <li>• Nominal rotational speed: <math>8.17 \text{ min}^{-1}</math></li> <li>• Travel: continuous</li> </ul>
$c$ -axis		<ul style="list-style-type: none"> <li>• Asynchronous motor</li> <li>• Nominal torque: 2945 Nm</li> <li>• Nominal rotational speed: <math>6.9 \text{ min}^{-1}</math> (feed rolls)</li> <li>• Nominal feed speed: 70 mm/s (feed roll <math>\varnothing = 200 \text{ mm}</math>)</li> <li>• Travel: continuous</li> <li>• rotary encoder on motor shaft</li> <li>• rotary encoder connected to profile with measuring wheel</li> </ul>
$X$ -axis		<ul style="list-style-type: none"> <li>• Hydraulic cylinder</li> <li>• Nominal force: 50 kN</li> <li>• Travel: <math>\pm 250 \text{ mm}</math></li> <li>• Distance <math>L_{B,y}</math>: 396.92 mm</li> <li>• <math>R_{th,min}</math>: 440.1 mm</li> <li>• linear encoder integrated in cylinder</li> </ul>
$\beta_1$ -axis		<ul style="list-style-type: none"> <li>• Servo drive</li> <li>• Nominal torque: 2000 Nm</li> <li>• Nominal rotational speed: <math>8.9 \text{ min}^{-1}</math></li> <li>• Travel: continuous</li> </ul>
Machine stiffness	$X$ -axis	$\delta_M = 1.496 \cdot 10^{-8} [\text{mm/N}^2] F_B^2 + 6.342 \cdot 10^{-5} [\text{mm/N}] F_B$ (5.14)
	Torsion	$c_M = 2.552 \cdot 10^7 \text{ Nmm/rad}$ (5.15)
Data transmission		<ul style="list-style-type: none"> <li>• Profibus DP</li> </ul>
Control Hardware		<ul style="list-style-type: none"> <li>• Embedded system</li> <li>• Core i7-2600 3.4 GHz (4 cores, hyper-threading disabled)</li> <li>• 8 GB RAM</li> </ul>
Control Software		<ul style="list-style-type: none"> <li>• LabVIEW Real-Time Module</li> </ul>
Programming Environment		<ul style="list-style-type: none"> <li>• LabVIEW 2012</li> </ul>



sensor loses contact, an additional encoder was connected to the motor shaft of the asynchronous drive. The upgraded control hardware and software, together with object-oriented multithread programming reduced the program cycle times by 10 and resulted in PID response times able to handle the axes speeds mentioned in Table 5.3 (Staupendahl et al., 2014a).

### 5.2.3 Development of an integrated torque measurement device

A torque sensor was designed<sup>9</sup> in order to measure the torque  $M_T$ , applied by the  $\alpha_2$ -axis to twist the profile, and the parasitic torque  $M_{T,p}$  generated during 3D bending by a bending force vector, set at a distance to the bending plane as explained in Section 4.2.4. As for the bending head drive system, the design approach laid out in the VDI 2221 guideline was used.

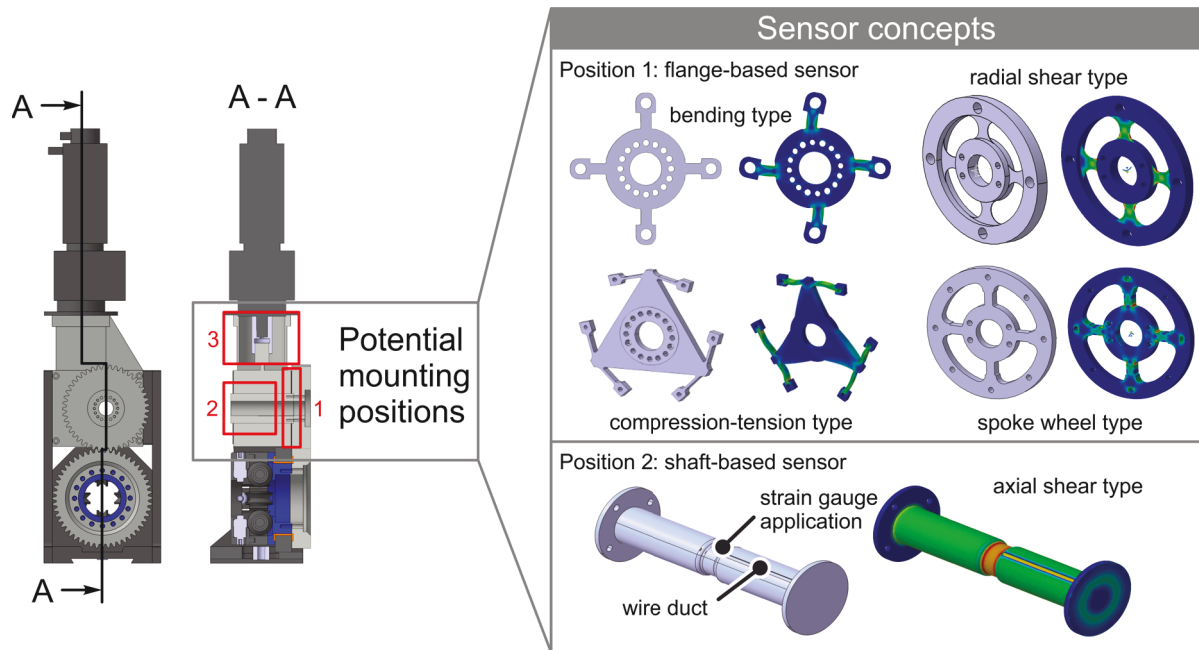
First, potential mounting positions for the torque sensor were analyzed (see Figure 5.10). The potential positions are:

1. The bolted connection interface between the worm gear and spur gear.
2. The hollow shaft of the worm gear
3. The connection of the helical servo motor to the worm gear

Of these three positions, position 3 can be directly discarded. The efficiency of the worm gear of solely 77 % (see Section 5.2.1) would greatly impede the accuracy of the downstream torque sensor. Position 2, the hollow shaft, allows the design of a very compact measuring setup. An axial shear type shaft-based sensor could be used of which one side is directly connected to the spur gear and the other side is connected to the bolted connection interface on the opposite side of the worm gear on which the spur gear is placed. In the sectional drawing A-A, one side of the shaft sensor would be connected to the left connection interface of the worm gear while the other side would be connected to the spur gear on the right side of the worm gear. The torque would be, thus, completely transmitted by the shaft-based sensor inside the hollow shaft of the worm gear. Because the shaft-based sensor would need to take up the shear forces acting on the spur gear during torque transmission, the sensor would have to be supported by bearings or bushings inside of the hollow shaft. This reduces the maximum possible outer diameter of the sensor and causes excessive stress in the area of strain gauge application. Also, the stiffness of the  $\alpha_2$ -axis would be negatively influenced by the elastic twist of the slender shaft.

---

<sup>9</sup> The design of the torque measurement device was done by Frank Schyma in the course of his bachelor thesis: Konstruktion einer Drehmoment-Messvorrichtung für das Tordieren von asymmetrischen Profilen während des TSS-Profilbiegeprozesses [Design of a Torque Measurement Device for the Twisting of Asymmetric Profiles during the TSS Bending Process], Fachhochschule Südwestfalen, 2012, supervised by: D. Staupendahl and W. Stolp



**Figure 5.10:** Sensor concepts for an integrated torque measurement device

Position 1, the connection interface between the worm gear and the spur gear, calls for a compact flange-based sensor. Different sensor designs were investigated:

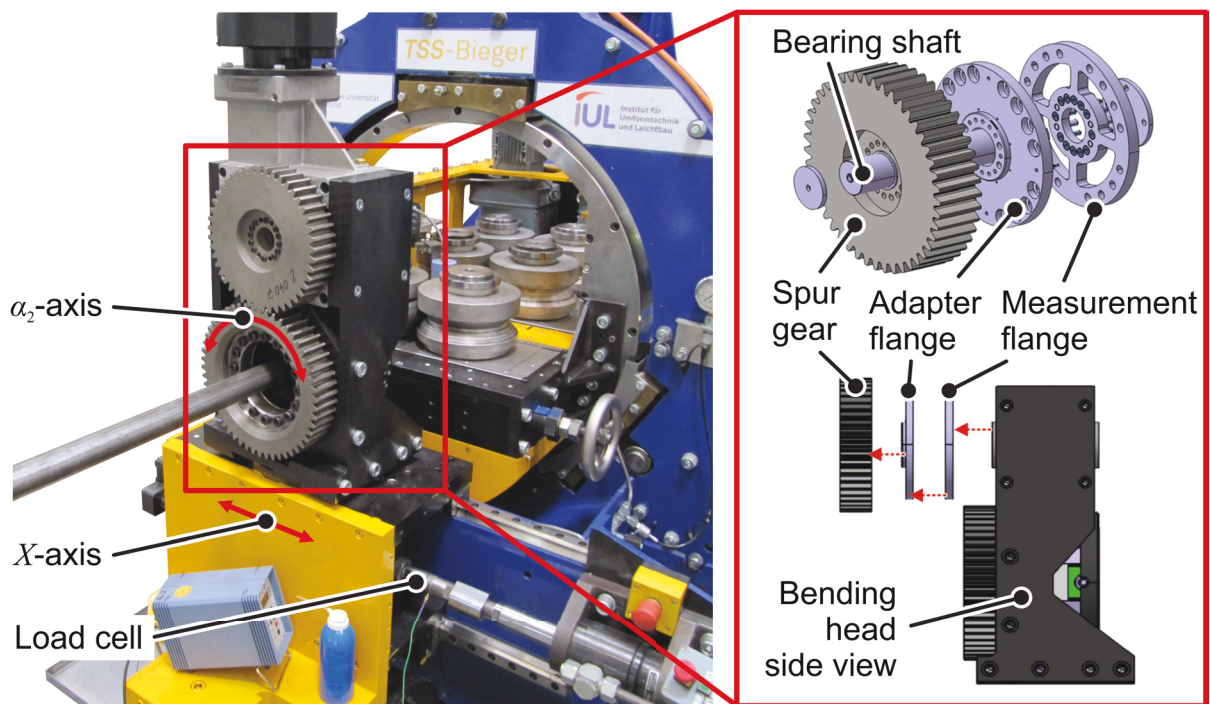
- A bending type sensor, where the outer ends of the bending beams are supported by bushings or needle bearings.
- A compression-tension type, where the outer edges of the sensor are supported by transversely placed tension-compression beams.
- A radial shear type, where the spokes of the flange are sheared radially.
- And, last, a spoke wheel type, in which the individual spokes of the flange are bent in an S-shape, with a radial shear zone occurring in the middle of each spoke.

The bending type sensor has very homogeneous stress and strain fields on the individual bending beams, and negligible radial stresses. The design with the outer end supports requires very accurate production in order to avoid pre-stressing the sensor during assembly. This is also true for the compression-tension type sensor. Additionally to the required high production accuracy, the transverse beams in this design do not experience pure tension and compression but a combination of tension and compression and S-shape bending. The sensor design is, therefore, especially sensitive to strain gauge placement. The radial shear type sensor and the spoke wheel type sensor are both robust designs, whereby the spoke wheel design offers a higher overall stiffness and a high stability against parasitic off-center shear forces.

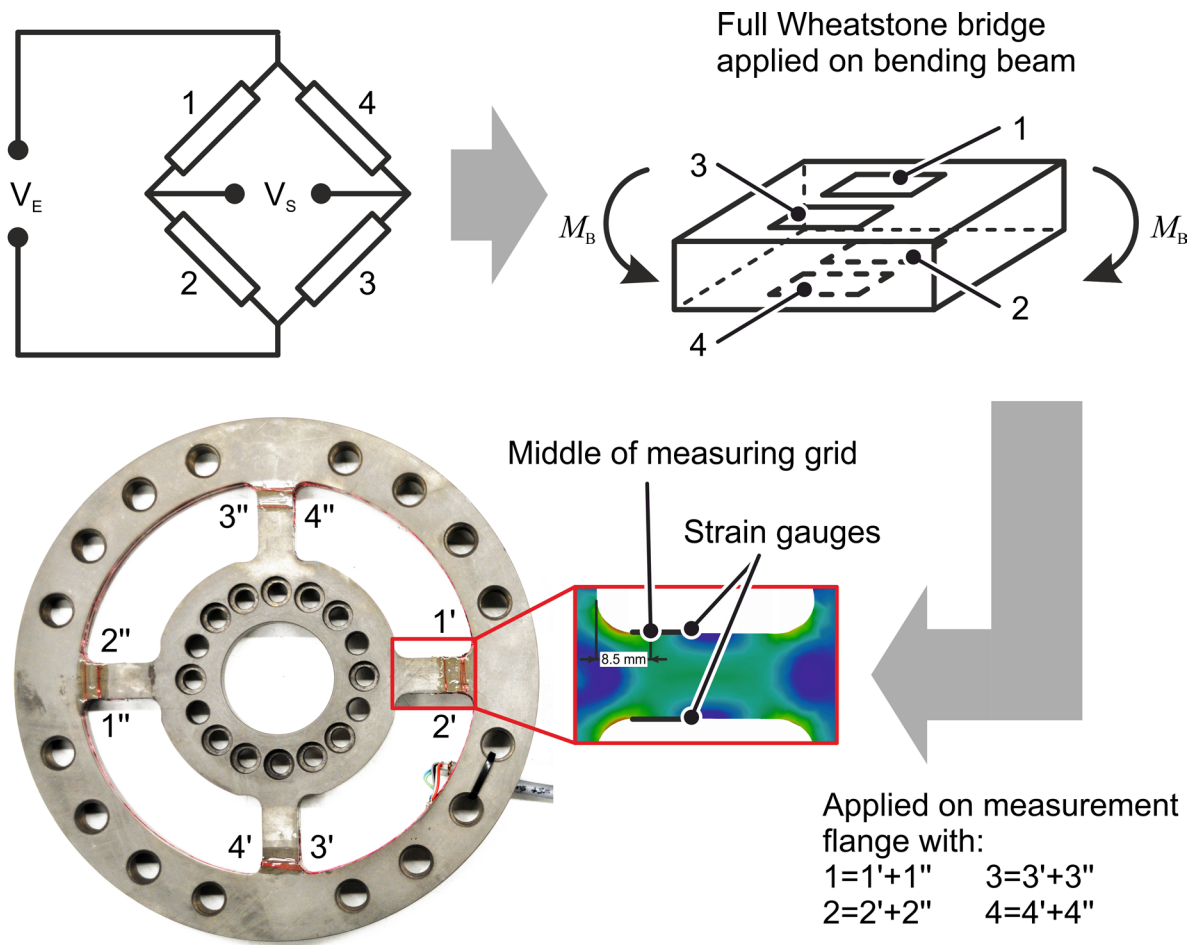
A technical and economic value analysis, as stated in the VDI 2225, showed the spoke wheel type design to be the most promising design. The final design and integration into the bending head is shown in Figure 5.11. The connection interface of the worm gear connects to the center hub of the measurement flange. The torque is transmitted via four

spokes to the outer ring of the flange, which is bolted to an adapter flange. The center hub of the adapter flange is finally connected to the spur gear. To increase the resistance of the setup to shear forces caused by the spur gear transmission, an additional shaft is mounted into the hollow shaft of the worm gear, with needle bearings supporting the spur gear and the adapter flange. In order to decrease friction as much as possible and thereby increase measurement accuracy, all polymer sleeve bearings and thrust washers used in the  $\alpha_2$ -axis (Hermes, 2011) were replaced by radial and axial needle bearings.

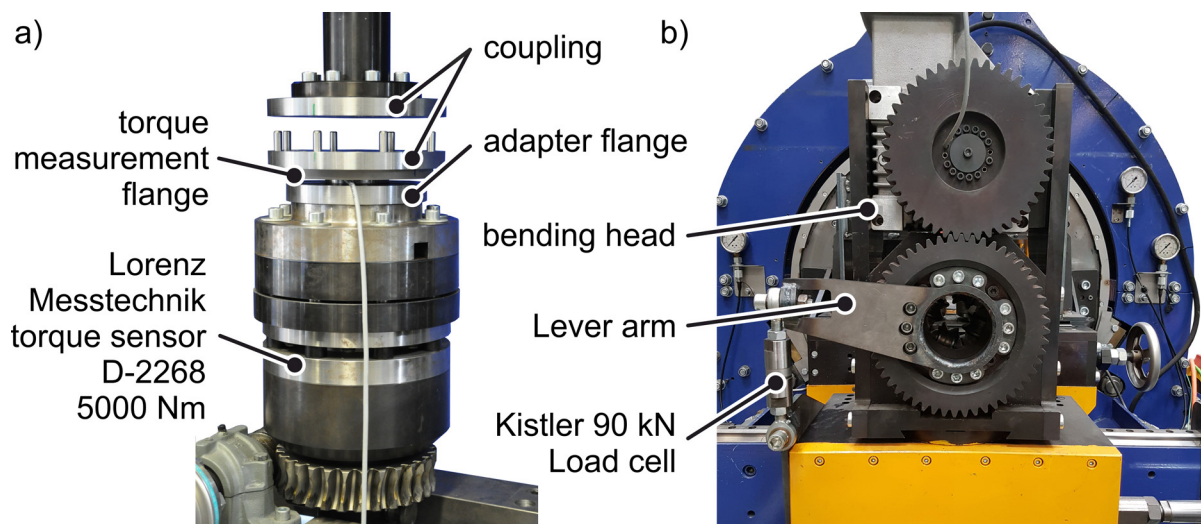
For the strain gauge circuitry, a full Wheatstone bridge is used. Figure 5.12 shows the general strategy of applying a full Wheatstone bridge on a beam under pure bending (Hoffmann, 1987). With the presented strain gauge placement, axial strain, torsion, and thermal expansion can be compensated. In the designed torque measurement flange, axial shear loads that would twist the individual spokes are not expected. Radial shear loads caused by the spur gear transmission are unavoidable, however. This is why the strain gauge pairs 1-2 and 3-4 are each placed on spokes set  $90^\circ$  apart from each other. To increase the overall measurement stability, the strain gauges 1-4 are each replaced by two individual strain gauges connected in series (e.g.  $1 = 1' + 1''$  as shown in Figure 5.12). The placement of the strain gauges on the spokes of the measurement flange was done as a result of finite element analysis showing the areas of axial strain during loading. Using gas nitrided 42CrMo4 (DIN EN ISO 683-1, Steel number: 1.7225) with a surface hardness of 55-64 HRC and a tensile strength of about 1900 MPa, the measuring range was initially specified from 100 to 3000 Nm. The strains in the middle of the



**Figure 5.11:** TSS bending machine with included force and torque sensors



**Figure 5.12:** Strain gauge circuitry and application on manufactured torque sensor



**Figure 5.13:** Torque sensor calibration using the in-plane torsion setup by Yin et al. (2011) (a) and using a load cell setup inside the 5-cDOF TSS bending machine (b)

measuring grid of the strain gauges, hereby, range from 0.005 % at 100 Nm to 0.16 % at 3000 Nm.

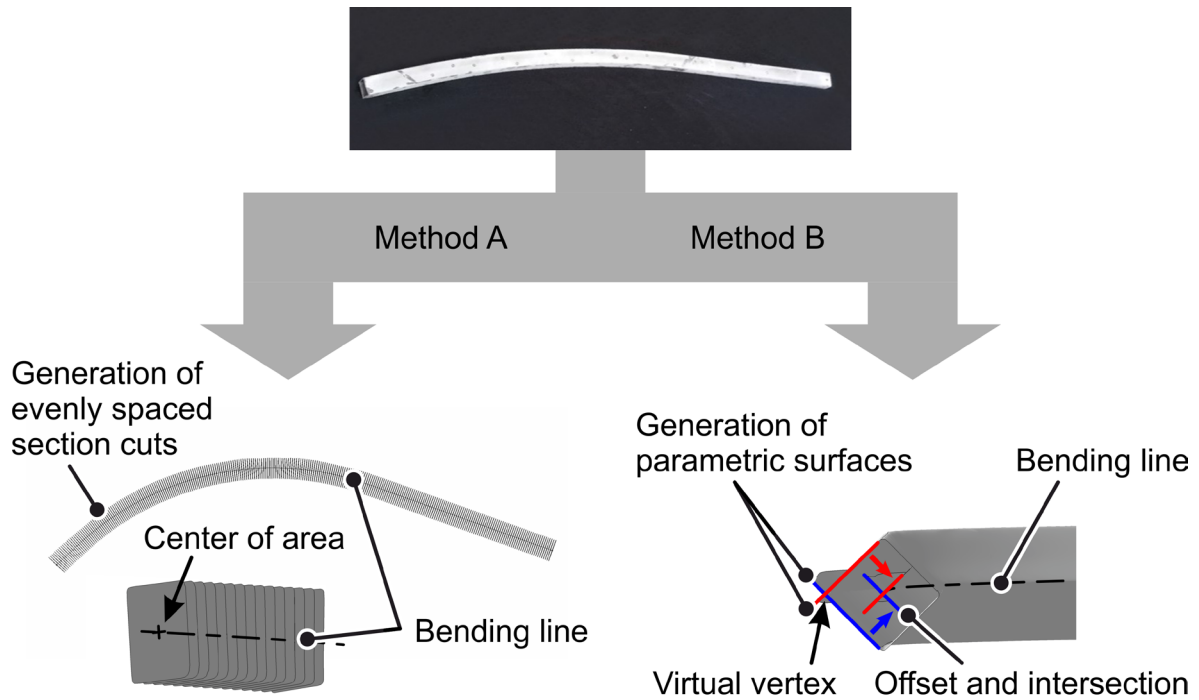
The sensor was calibrated using the in-plane torsion setup designed by Yin et al. (2011) up to 1200 Nm using adapter flanges (Figure 5.13 a). The setup can also be seen in Yin et al. (2015). The final calibration was performed with the fully assembled measurement setup inside of the 5-cDOF TSS bending machine (Figure 5.13 b). By calibrating the torque measurement flange, the measurement range could finally be specified from 250 Nm to 3000 Nm with an accuracy ranging from 5 % at 250 Nm to 0.7 % at 3000 Nm. Using the approximation function by Voce (1948), the measurement accuracy  $m_{acc}$  over the whole range can be described by:

$$m_{acc} [\%] = 0.7 + 8.3e^{-0.002676 \cdot M_T} \quad (5.16)$$

### 5.3 Development of a 3D contour measurement device

Additionally to the process data made up of actual axes movements and force and torque measurements, the knowledge of the produced profile shape is needed in order to analyze and understand the mechanisms of 3D-profile bending.

Chatti et al. (2010), Staupendahl et al. (2011), Hermes (2011), and Hudovernik et al. (2014b) used the structured-light 3D scanner GOM Atos I 350, a noncontact offline surface measurement technique, to scan the outer surfaces of profiles after bending. In order to generate the bending lines further extensive processing of the data is needed. The first step is a cleanup of the files, deleting excess points that do not belong to the profile but to objects that surrounded the profile during scanning. In a next step, the surfaces are smoothed and meshed with triangular facets in order to allow the generation of an STL-file. This file can be further processed either in the GOM Atos software or in other CAD programs. Chatti et al. (2010) and Hermes (2011) used the GOM Atos software to perform deviation analyses of 3D-bent profiles, specifically set-actual comparisons. The bending line and torsion was not investigated. Staupendahl et al. (2011) and Hudovernik et al. (2014b), on the other hand, used the CAD program CATIA by Dassault Systèmes to generate the bending lines from mesh data. In the course of the research, two methods for bending line generation were found (see Figure 5.14). In method A, evenly spaced section cuts are produced along the longitudinal axis of the profile. Since this longitudinal axis initially does not exist as a geometrical element, it has to be manually approximated. In the next step, the center of area of each individual section cut is generated. Following the VDI 3431, the bending line is finally produced by connecting the centers of area with a continuous curve, specifically a spline. Errors can occur because of a poor initial longitudinal axis definition or by failing section cut definitions caused by a poorly cleaned up or smoothed STL-file. In method B two or more outer surfaces are parameterized and offset to the middle of the profile. Here, the



**Figure 5.14:** Generation of the bending line by the processing of section cuts (Method A) and the outer surfaces of the profile (Method B)

intersection of two surfaces generate a line, which can ultimately serve as the bending line. The accuracy of this method can be increased by averaging the intersections of several surface pairings and thus countering potential errors caused by cross-section deformation. Both methods describe the generation of the bending line. As explained in Section 4.1.3, additionally to the bending line  $\vec{r}$ , a secondary line  $\vec{r}_s$  is needed to describe profile torsion. In order to generate said secondary line, an additional point needs to be created in the same relative position on each section cut. For the square cross-section shown in Figure 5.14 two adjacent sides could be extrapolated in each cut and intersected to create this point. Performing these steps manually is unjustifiable and the automatization of the necessary steps is highly complex. Method B on the other hand can efficiently be adapted to not only produce the bending line by offsetting the outer surfaces and intersecting the same, but to also produce a secondary line in a virtual vertex by extruding the outer surfaces so that they exceed this virtual vertex and then create the intersection line between these two extruded parts. Once the bending line  $\vec{r}$  and the secondary line  $\vec{r}_s$  are generated, the mathematical calculation described in Section 4.1.3 (if the curve description is continuous and three times differentiable) or in Section 4.1.4 (if the curves show discontinuities). As can be sensed from the above description, the analysis of a profile using the structured-light 3D scanning technique is very time consuming and can actually take up to 3-5 hours for a 2 meter long profile (including preparation of the profile and post-processing). Another disadvantage is that the system can

only perform offline-measurements. In order to simplify this procedure and additionally allow for online-measurements, a new 3D contour measurement device was developed.

### 5.3.1 Design concept of a contact measurement device

As for the drive system of the bending head and the torque sensor, the design approach described in the VDI 2221 guideline was used. Following the results and recommendations of the state of the art (Section 2.3), the focus in the sensor design was placed on contact measurement methods. But not only the experience of leading measurement expert companies speaks for contact measurement methods when analyzing 3D-bent profiles, also a significant cost benefit exists – e.g. comparing digital length measurement probes and laser triangulation sensors or laser scanners. Additionally, measurement difficulties caused by reflections and thermal radiation can be avoided.

The main requirements of the new sensor design were:

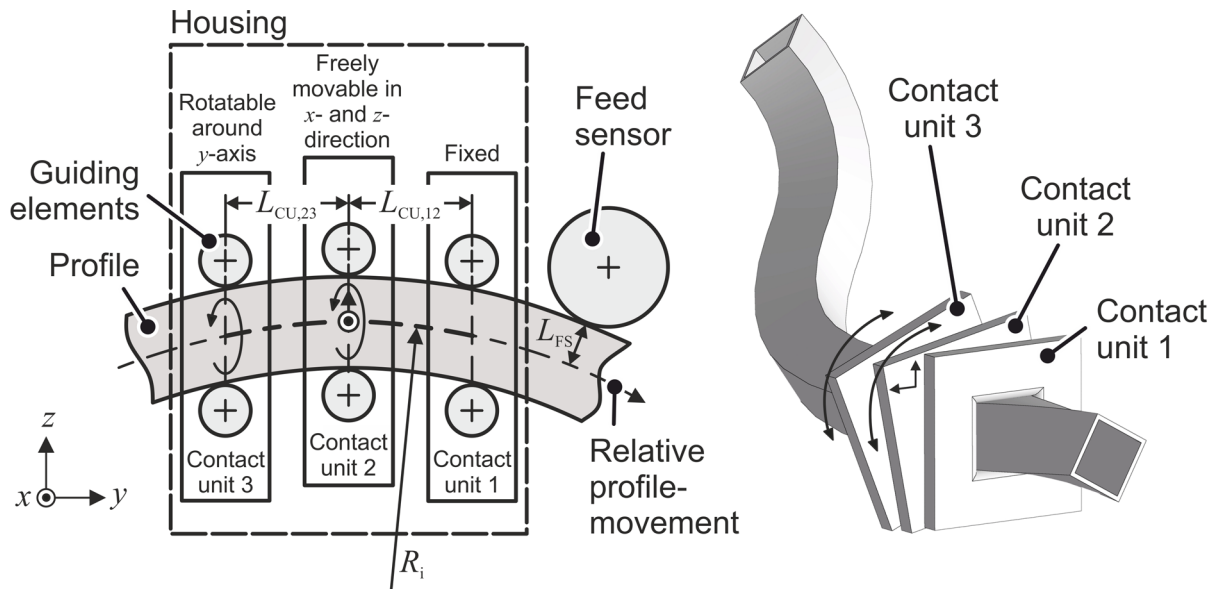
- Analysis of bending line: curvature and bending plane rotation relative to the arc length  $s$
- Measurement of profiles with cross-sections fitting into a square of 65x65 mm and radii from 250 mm to 2000 mm
- Analysis of twist relative to the arc length  $s$
- Compact setup
- Capability to perform online measurements

The compact setup was targeted so that the sensor could be integrated into a wide range of kinematic bending processes and placed as near to the forming zone as possible. Since kinematic bending processes form the profile contour incrementally and the ability to perform online measurements was also targeted, the actual contour measurement process is required to work incrementally as well. This means that only one specific partition of the profile can be measured at a single time step, with the overall profile contour being a combination or addition of the individual partition measurements.

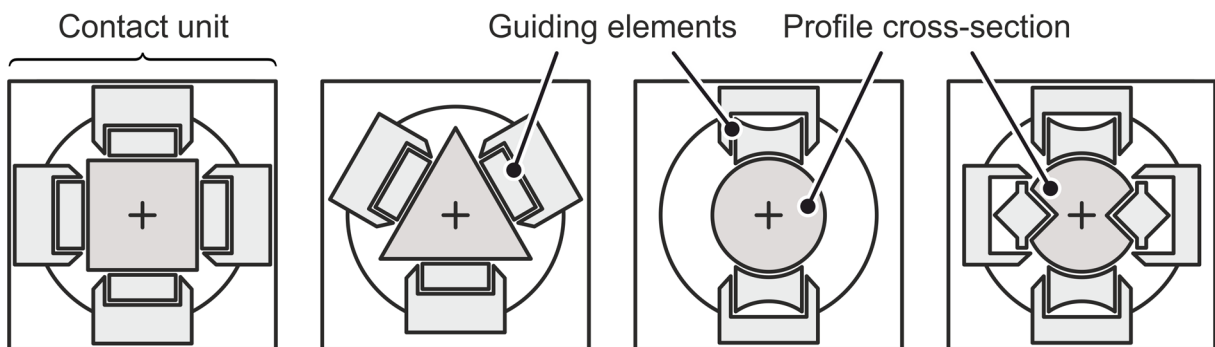
The simplest way to describe a radius is by three points (see Section 4.1.4). For the analysis of two-dimensional curves, where the bending plane is always oriented in the same direction, a sensor is sufficient that is only able to measure concave and convex radii. A sensor of this kind only needs to be in contact with the profile at a defined position on the inner or outer radius. However, in three-dimensional curves the orientation of the bending planes varies necessitating an enclosing sensor.

Following the recommendations of the VDI 2222 a morphological analysis was used in the conceptual design phase of the sensor to generate potential designs from a combination of several partial solutions. Figure 5.15 shows the ultimately chosen measurement concept of the newly developed sensor. The sensor is made up of three contact units: Two outer units, where one is fixed in an enclosing housing and one is rotatable around

the  $y$ -axis, and a center contact unit, which is freely movable in the  $x$  and  $z$  direction and additionally rotatable around the  $y$ -axis. A feed sensor is used to determine the position of the sensor along the profile axis. The contact units can be adapted to arbitrary cross-section shapes by simple change and flexible positioning of guiding elements (see Figure 5.16). By this simple setup for which a European patent was granted under the patent number EP 3 315 221 B1<sup>10</sup> all of the above targets can be achieved. The mid-points of the contact units 1, 2, and 3 define the local radius of of a 3D shaped profile, running through the sensor, and the local bending plane (see Figure 5.17 a).



**Figure 5.15:** Measurement concept of the 3D contour sensor (Staupendahl and Tekkaya, 2017a)

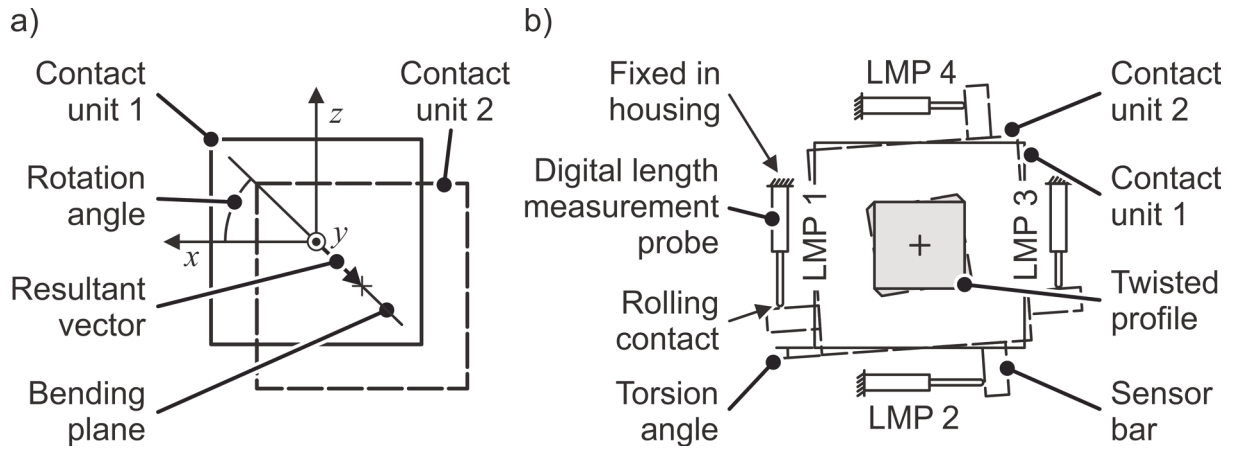


**Figure 5.16:** Contact units with mounted exemplary guiding elements (Staupendahl and Tekkaya, 2017a)

<sup>10</sup> Staupendahl, D., Schultz, D., Tekkaya, A.E., 2018a. Device for Tactile Detection and Analysis of the Geometry of Bent Profiles or Tubes. European patent EP 3 315 221 B1, priority date: 31.10.2016.



The twist per unit length is obtained by analyzing the rotation of contact unit 2 around the  $y$ -axis of the sensor. The movement of contact unit 2 is tracked by digital length measurement probes (LMP 1-4), placed parallel to the sides of the sensor as seen in Figure 5.17 b, sensing the position and motion of sensor bars, protruding from contact unit 2. The placement of the LMPs was chosen to allow a compact sensor setup. The detailed calculation of the profile data is shown in the next section.



**Figure 5.17:** Determination of the bending plane rotation  $\theta_{r,CU,12,i}$  relative to the sensors  $x$ -axis and the torsion angle  $\phi_{CU,12,i}$  (Staupendahl and Tekkaya, 2017a)

### 5.3.2 Calculation of the profile contour data

The mid-points of the contact units 1, 2, and 3 ( $P_{CU,1}$ ,  $P_{CU,2}$ ,  $P_{CU,3}$ ) define the radius  $R_i$  of a curve. Here, the relevant parameter of the freely movable contact unit (CU) 2 is the length of the resultant vector  $\vec{r}_{CU,2}$  of the movement in  $x$  and  $z$ -direction (see Figure 5.17 a). In order to calculate  $\vec{r}_{CU,2}$ , first of all, the movement of  $P_{CU,2}$  needs to be related to the measurements of the LMPs (see Figure 5.18). The contact points of the LMPs with the sensor bars are described as  $P_{LMP,1}$  through  $P_{LMP,4}$ . As a result, the sensor bars can be represented by straight-line equations in the point slope form. The angle between the sensor bar 1-3 and the  $x$ -axis is equal to the angle between the sensor bar 2-4 and the  $z$ -axis and is described by:

$$\phi_{CU,12,i} = \tan^{-1} \left( \frac{z_1 - z_3}{x_1 - x_3} \right) = \tan^{-1} \left( \frac{x_4 - x_2}{z_2 - z_4} \right) \quad (5.17)$$

Thus, a clockwise rotation of CU 2 relative to CU 1, which is actually a negative rotation around the  $y$ -axis, results in a positive  $\phi_{CU,12,i}$ . Taking this sign convention into account, the sensor bar line 1-3 can be defined with the point  $P_{LMP,1}$  as:

$$z = \tan(\phi_{CU,12,i}) \cdot x + z_1 - \tan(\phi_{CU,12,i}) \cdot x_1 \quad (5.18)$$

Using point  $P_{LMP,2}$  as the known point, the sensor bar line 2-4 is defined by:

$$z = -\frac{1}{\tan(\phi_{CU,12,i})} \cdot x + z_2 + \frac{1}{\tan(\phi_{CU,12,i})} \cdot x_2 \quad (5.19)$$

The coordinates of the intersection point  $P_{SB,int}$  are obtained by equalizing Eqs. (5.18) and (5.19):

$$x = \left[ \frac{\tan(\phi_{CU,12,i})}{\tan^2(\phi_{CU,12,i}) + 1} \right] \left[ \tan(\phi_{CU,12,i}) \cdot x_1 + \frac{1}{\tan(\phi_{CU,12,i})} \cdot x_2 + z_2 - z_1 \right] \quad (5.20)$$

$$z = \left[ \frac{\tan^2(\phi_{CU,12,i})}{\tan^2(\phi_{CU,12,i}) + 1} \right] \left[ \tan(\phi_{CU,12,i}) \cdot x_1 + \frac{1}{\tan(\phi_{CU,12,i})} \cdot x_2 + z_2 - z_1 \right] + z_1 - \tan(\phi_{CU,12,i}) \cdot x_1 \quad (5.21)$$

The coordinates of  $P_{CU,2,i}$  are finally calculated by adding the relative offsets  $x_{MP,r}$  and  $z_{MP,r}$  to the respective coordinates of  $P_{SB,int}$ :

$$x_{MP} = \left[ \frac{\tan(\phi_{CU,12,i})}{\tan^2(\phi_{CU,12,i}) + 1} \right] \left[ \tan(\phi_{CU,12,i}) \cdot x_1 + \frac{1}{\tan(\phi_{CU,12,i})} \cdot x_2 + z_2 - z_1 \right] + \underbrace{SB_{offset} \sqrt{2} \cdot \sin\left(\frac{\pi}{4} - \phi_{CU,12,i}\right)}_{x_{MP,r}} \quad (5.22)$$

$$z_{MP} = \left[ \frac{\tan^2(\phi_{CU,12,i})}{\tan^2(\phi_{CU,12,i}) + 1} \right] \left[ \tan(\phi_{CU,12,i}) \cdot x_1 + \frac{1}{\tan(\phi_{CU,12,i})} \cdot x_2 + z_2 - z_1 \right] + z_1 - \tan(\phi_{CU,12,i}) \cdot x_1 + \underbrace{SB_{offset} \sqrt{2} \cdot \cos\left(\frac{\pi}{4} - \phi_{CU,12,i}\right)}_{z_{MP,r}} \quad (5.23)$$

The length of the resultant vector  $\vec{r}_{CU,2}$  then becomes:

$$\|\vec{r}_{CU,2}\| = \sqrt{x_{MP}^2 + z_{MP}^2} \quad (5.24)$$

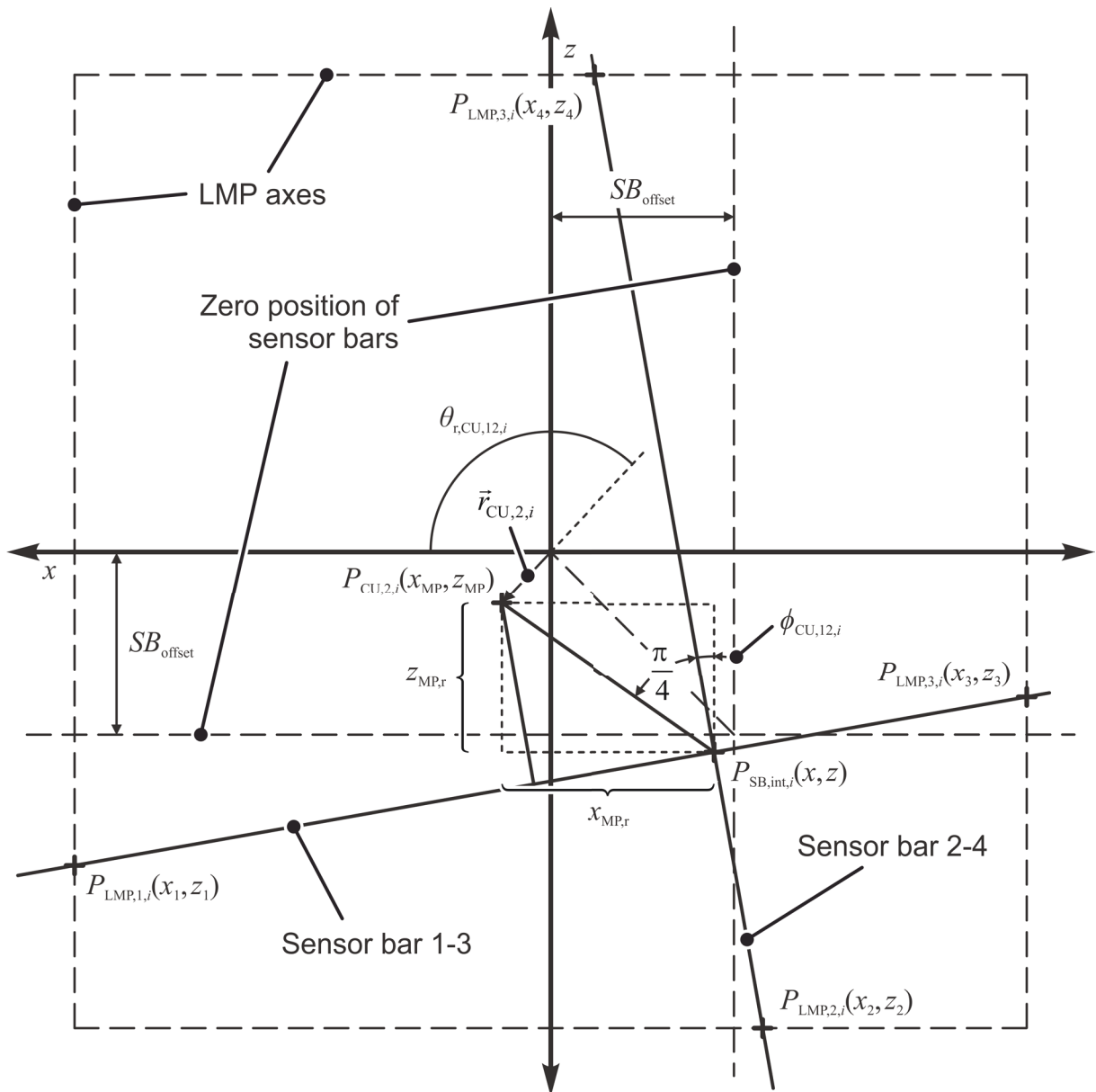
Eqs. (4.50), (4.51), or (4.52) can be used for the calculation of the radius. Here, instead of  $\overrightarrow{P_{i-1}P_i}$ ,  $\overrightarrow{P_iP_{i+1}}$ , and  $\overrightarrow{P_{i-1}P_{i+1}}$ , the vectors between the midpoints of the contact units  $\overrightarrow{P_{CU,1,i}P_{CU,2,i}}$ ,  $\overrightarrow{P_{CU,2,i}P_{CU,3,i}}$ , and  $\overrightarrow{P_{CU,1,i}P_{CU,3,i}}$  are used.

Since CU 1 and 2 are set the distance  $L_{CU,12}$  apart  $\phi_{CU,12,i}$  has to be divided by the arc length of the curve between CU 1 and 2 in order to obtain the twist per unit length of

the profile  $\Delta\phi_i$ . As an idealization, the arc is defined to have the shape of a circle:

$$\Delta\phi_i = \frac{\phi_{\text{CU},12,i}}{\sin^{-1}\left(\frac{L_{\text{CU},12}}{R_i}\right) \cdot R_i} \quad (5.25)$$

As for  $\phi_{\text{CU},12,i}$ , a clockwise rotation, so a negative rotation around the  $y$ -axis, signals positive torsion. This sign convention can be understood when imagining the profile's local  $tnb$ -frame during its movement through the sensor. Similar to the profile movement through the generalized geometric 3D bending process model seen in Figure 4.8,



**Figure 5.18:** Geometrical relations between the contact points of the LMPs and the sensor bars as well as the midpoint  $P_{\text{CU},2,i}$

the  $t$ -direction of the  $tnb$ -frame at the origin of the  $xyz$ -coordinate system is exactly opposite to the  $y$ -axis. The rotation angle  $\theta_{r,CU,12,i}$  between the point-symmetric extension of the resultant vector and the  $x$ -axis (see Figure 5.17 a and Figure 5.18) is used to calculate the discrete rotation angle  $\Delta\theta_{r,i}$  of the bending plane. The point-symmetric extension is relevant in this case because the normal vector of the curve, passing through the sensor, is always directed in the opposite direction of the resultant vector. As a result, the rotation angle and the torsion angle measured by the sensor have the same sign, which is what is expected when looking at Section 4.1. In the range  $0 \leq \theta_{r,CU,12,i} < 2\pi$  the angle  $\theta_{r,CU,12,i}$  relates to movements in  $x$  and  $z$ -direction by:

$$\theta_{r,CU,12,i} = \begin{cases} 0 & \text{for } x_{MP} = 0 \text{ and } z_{MP} = 0 \\ \cos^{-1}\left(\frac{x_{MP}}{\|\vec{r}_{CU,2}\|}\right) & \text{for } z_{MP} \geq 0 \\ -\cos^{-1}\left(\frac{x_{MP}}{\|\vec{r}_{CU,2}\|}\right) & \text{for } z_{MP} < 0 \end{cases} \quad (5.26)$$

Since the rotation angle  $\theta_{r,CU,12,i}$  is measured relative to the current cross-section position in CU 1, a twisted cross-section affects the rotation measurements. In the extreme case in which the bending plane rotation is equal to the twist per unit length as shown in Figure 4.2 c, the sensor would measure no rotation at all. It is, thus, essential to add the torsion that CU 1 has already undergone to the measured rotation angle. Mathematically this can be described by:

$$\boxed{\Delta\theta_{r,i} = \Delta\theta_{r,CU,12,i} + \Delta\phi_{PCU,1,i}} \quad (5.27)$$

with:

$$\Delta\theta_{r,CU,12,i} = \theta_{r,CU,12,i} - \theta_{r,CU,12,i-1} \quad (5.28)$$

The twist per unit length  $\Delta\phi_{PCU,1,i}$  is the value that CU 2 measured when it was in the position of CU 1. If the feed sensor only tracks the movement of a single line on the outer surface of the profile facing in the  $z$ -direction as shown in Figure 5.15, the step size output by the sensor  $l_{step,i,FS}$  needs to be converted into the step size of the bending line  $l_{step,i}$ :

$$l_{step,i} = l_{step,i,FS} \left( \frac{R_i}{R_i - L_{FS} \sin(\theta_{r,CU,12,i})} \right) \quad (5.29)$$

$\Delta\phi_{P_{CU,1,i}}$  can, thus, be described as:

$$\Delta\phi_{P_{CU,1,i}} = \Delta\phi_{i-i_{CU,12}} \quad \text{with} \quad i_{CU,12} = \left\lceil \left( \sin^{-1} \left( \frac{L_{CU,12}}{R_i} \right) \cdot R_i + 0.5 \right) \frac{i - i_{CU,12}}{\sum_{k=i-i_{CU,12}}^i l_{\text{step},i}} \right\rceil \quad (5.30)$$

Here, the parameter  $i_{CU,12}$  describes the number of increments between contact units 1 and 2, rounded to the nearest integer.

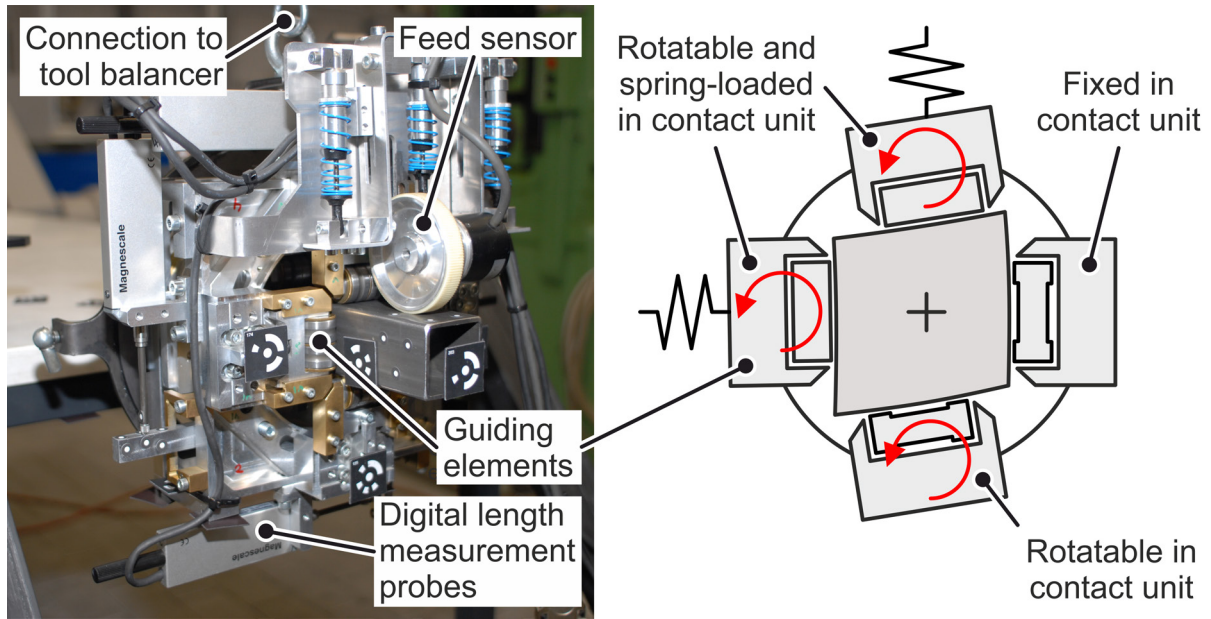
### 5.3.3 Setup of the manufactured contact measurement device

Figure 5.19 shows the manufactured 3D contour sensor. As planned in the conceptual design, the finalized setup allows flexible positioning of guiding elements on contact units 1 through 3. During first tests, it was noticed that the contact rolls of the guiding elements were not in line contact with the profile cross-section if it had undergone severe distortion during bending. To overcome this contact issue, only one guiding element was fixed in each contact unit. One adjacent element was mounted rotatable into the contact unit. The remaining two elements were designed rotatable and spring-loaded in radial direction. In order to allow inline-measurements directly in sequence to a bending process, the sensor is supported by a tool balancer. The tool balancer balances out the complete weight of the contour sensor in order to avoid additional force on the profile, which could affect the bending process.<sup>11</sup>

As LMPs, digital sensors from Magnescale (DT32N) were used, which allow a maximum range of 32 mm, a resolution of 5  $\mu\text{m}$  and a measurement accuracy of 10  $\mu\text{m}$ . The measurement of the accuracy of the fully assembled contour sensor was performed in two steps. First, the geometry of the finalized sensor setup was analyzed with GOM Tritop. The coded and uncoded measurement points used in the analysis can be seen in Figure 5.19 a. The geometrical aspects verified were the parallel positioning of the LMPs to the center as well as the distances of contact points  $P_{LMP,1}$  through  $P_{LMP,4}$  to the center in  $x$  and  $z$ -direction.

The actual measurement accuracy of the sensor was gained by a comparison of measured radius, bending plane and torsion data with data gained via the structured light scanner GOM Atos. Radii between 700 mm and 1300 mm and bending plane rotations

<sup>11</sup> The embodiment and detail design as well as the assembly of the contour sensor with solely fixed guiding elements was done by Daniel Schultz in the course of his master thesis: Entwicklung einer Messvorrichtung für das Analysieren von Konturen dreidimensional gebogener Profile [Development of a Measurement Device for the Contour Analysis of Three-Dimensionally Bent Profiles], Technische Universität Dortmund, 2014, supervised by: D. Staupendahl and A. E. Tekkaya,

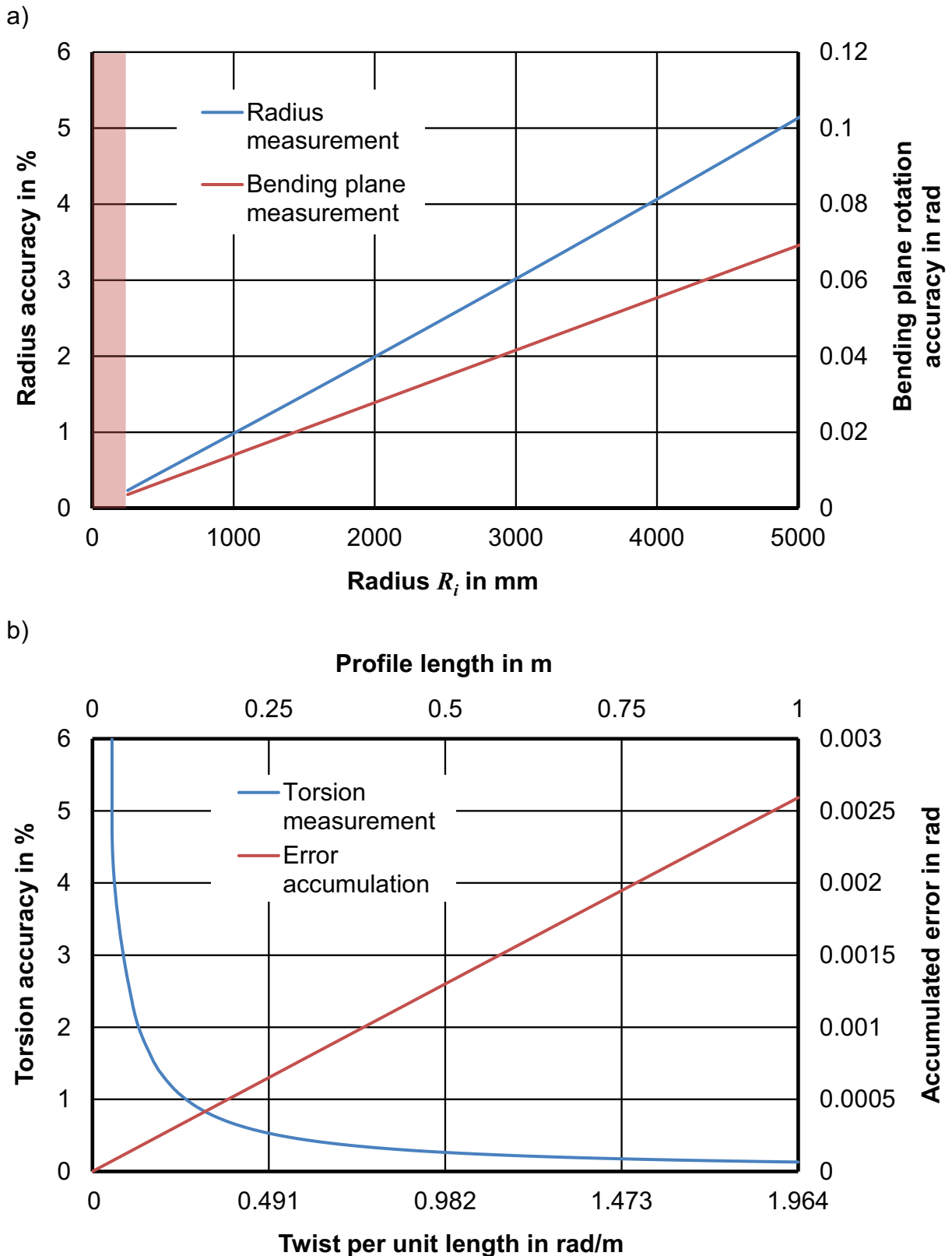


**Figure 5.19:** Manufactured 3D contour sensor (left) (Staupendahl and Tekkaya, 2017a) and guiding element setup used to allow accurate measurement during cross-section deformation (right)

and twist per unit length data from 0 to 0.982 rad/m were used in the analysis. Using the CAD program Catia from Dassault Systèmes, Method A from Figure 5.14 was used to generate the bending line and Method B was used to generate the secondary line needed to describe profile torsion. The section cuts defining the bending line in Method A were distributed at an interval of 5 mm along the length the profile. For the analysis of the bending line and torsion data, three evenly spaced points on the bending line and their corresponding points on the secondary line, with the outer points on the bending line being 128 mm apart from each other. This exactly matches the 64 mm spacing between the CUs of the contour sensor and avoids deviations because of different discretizations. The radius accuracy data was extrapolated to cover the range 250 mm until 5000 mm.

Figure 5.20 shows the accuracy of the different measurement parameters in relation to the currently measured radius  $R_i$  and the twist per unit length  $\Delta\phi_i$ . These relations are significant because the resolution of the LMPs relative to the measured parameters actually changes with changing parameters. E.g., the relative resolution is high when measuring small radii and decreases with increasing radii. Thus, the radius and bending plane measurement accuracy decreases. This effect can be seen in Figure 5.20 a.

In the analysis of the data, it was noticed that the absolute accuracy of the contour sensor is about two times lower than what is mathematically calculated from the accuracy of the LMPs. This can be mainly related to manufacturing tolerances but also to non-optimal contact when handling profiles with cross-section deformation. In the range 250 mm to 2000 mm, the radius measurement accuracy goes from 0.23 to 2.0 %. No relative accuracy can be specified for the bending plane rotation. Instead, the accuracy



**Figure 5.20:** a) Relation of radius measurement accuracy and bending plane rotation measurement accuracy to currently measured radius  $R_i$ , b) Relation of torsion measurement accuracy to currently measured  $\Delta\phi_i$  and error accumulation over profile length

is specified in terms of radians. The expected deviations in both cases increase about linearly up to  $R_i = 15000$  mm although only data up to  $R_i = 5000$  mm are shown. This is because deviations above 5 % are too high for the validation of the effects analyzed in Sections 6.3 and 8. It is important to note that for the radius measurement, no error accumulation exists because the instantaneous radius is only dependant on the instantaneous CU midpoint positions. Figure 5.20 b shows the error accumulation resulting during torsion measurement and the consequential accuracies at different twists per unit length. Because of the relation between torsion and bending plane rotation shown in Eq. (5.27) the error accumulation of the measured torsion has a direct effect on the bending plane rotation and has to be accounted for additionally to the instantaneous deviation shown in Figure 5.20 a. All in all the presented accuracies show that the designed 3D contour sensor is feasible for the analysis of 3D profile contours.

## 5.4 Numerical model of the 5-cDOF TSS bending process and its validation

In two-dimensional plane bending, the force data in the  $X$ -direction, collected by the force sensor that is integrated into the  $X$ -axis of the 5-cDOF TSS bending machine (load cell in Figure 5.11), can be used, together with the rotation of the bending head around the  $\tau$ -axis, to directly calculate the bending force. In three-dimensional bending, the application of torque by the bending head rotation around the  $\alpha_2$ -axis causes additional loads and, thereby, increases frictional forces on the linear guiding system of the bending head, resulting in a reduced measurement accuracy. As such, the experimental data of plane bending of profiles to the theoretical radii  $R_{th}$  of 600, 800, and 1000 mm as well as pure torsion of a profile to  $d\phi = 1.964$  rad/m was used to calibrate a numerical model of the process, which was, in turn, used to analyze the stresses and strains during bending (Section 7.1) and generate the bending force data for the investigations with applied torque in Section 7.3.

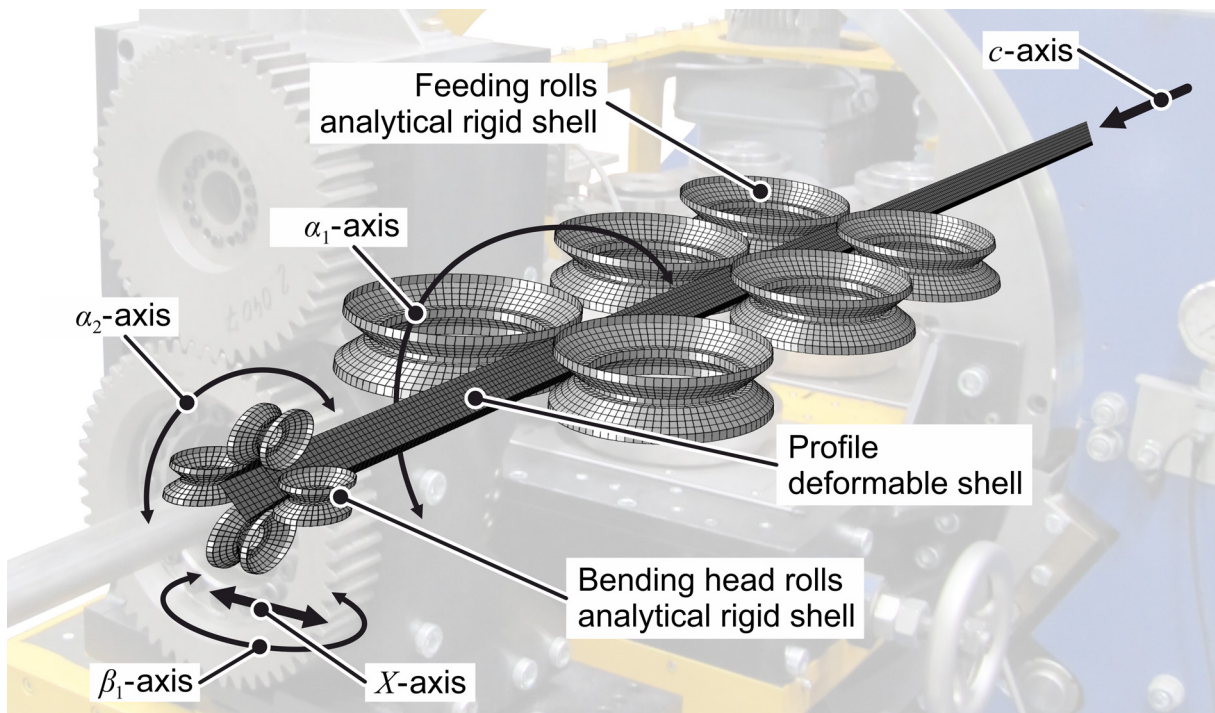
### 5.4.1 Comprehensive numerical model

The numerical model used is based on the model first described by Hudovernik et al. (2014b) and set up with the numerical software Abaqus from Dassault Systèmes. As kinematic bending is a dynamic process with continuously changing contact conditions, the explicit solver is used. The feeding rolls and the bending head rolls are modeled using analytically rigid shells, with the profile being modeled as a deformable shell. Specifically the profile is described by the extruded middle axis of the profile wall (a square with the dimensions 37.5x37.5 mm), meshed using 4-node, quadrilateral, general purpose shell elements with a Gauss thickness integration using five integration points. The feeding rolls are completely fixed, with the bending head rolls being rigidly linked to a central reference point, whose movement is controlled along the  $X$ -axis and, other than described by Hudovernik et al. (2014b), also around the  $\alpha_2$  and  $\beta_1$ -axis. This setup idealizes the stiffness of the actual 5-cDOF TSS Bending machine and, as such, does

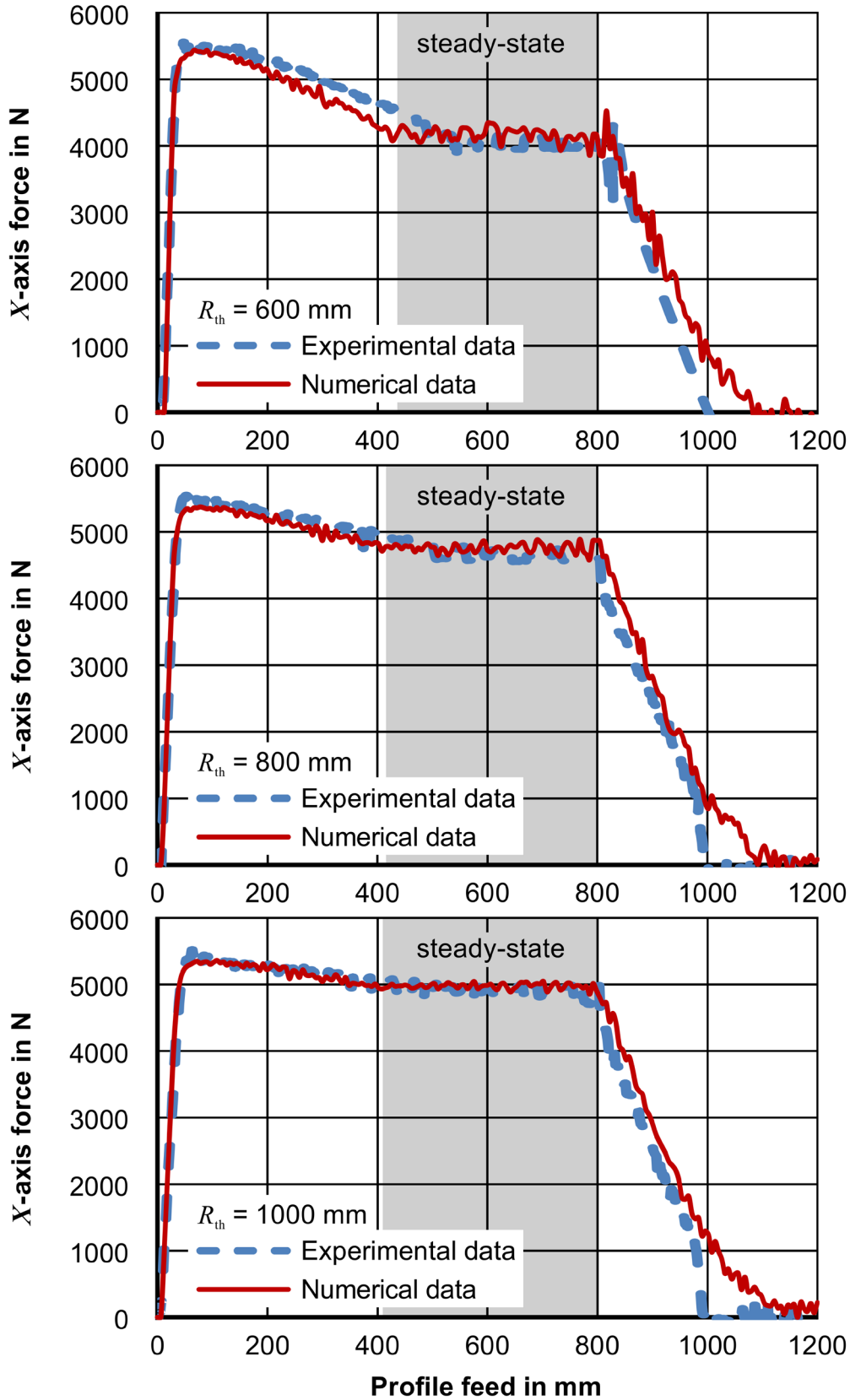


not consider bending roll and feeding roll deflections. A frictionless surface-to-surface penalty contact is defined between profile and rolls. As a result, other than in the actual process, the feeding rolls are not used to transport but only to guide the profile, whereby the feed is being applied to the rear end of the profile, acting similar to a pusher in tube bending. The impact of this simplification on the bending force component in the  $X$ -direction was previously investigated by Hudovernik (2014a), with the outcome that the difference between the two feed strategies is negligible. The advantage of the pusher strategy, however, is the clearly reduced calculation time of the numerical model. Figure 5.21 displays the model setup. The controlled axes are marked with arrows.

The numerical analyses were performed using the flow curve approximated for the material MW700L Z1 from Eq. (5.2) in combination with the von Mises yield criterion and isotropic hardening. No mass scaling was applied, but while the plane bending experiments were performed at a constant velocity of 4 mm/s, the numerical simulations were performed with a velocity of 200 mm/s. A further decrease of the velocity did not bring improvements to the simulation, while higher values negatively affected the force output. Below 200 mm/s the bending process can, thus, be regarded as quasi-static. In previous investigations (Staupendahl and Tekkaya, 2017b) a feed velocity of 600 mm/s was actually used in the numerical simulations, which explains the slight differences in the calculated strain and bending force data. Figure 5.22 shows the experimental and numerical force components in  $X$ -direction for the theoretical radii 600 mm, 800 mm,



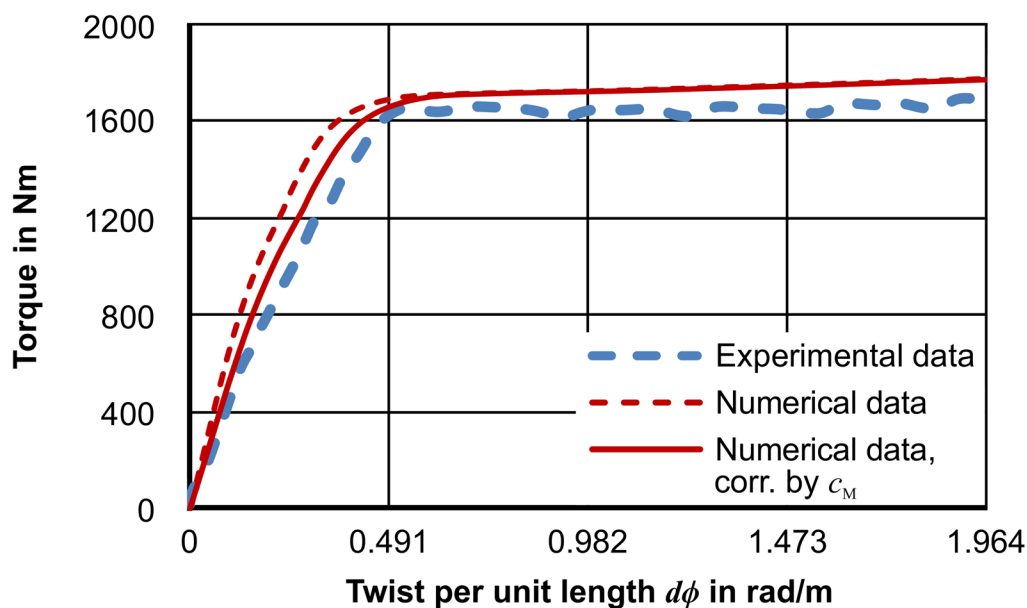
**Figure 5.21:** FE model of the 5-cDOF TSS bending machine used for the calculation of bending forces in two-dimensional and three-dimensional bending (Staupendahl and Tekkaya, 2018b)



**Figure 5.22:** Experimental and numerical  $X$ -axis force component data during bending of MW700L Z1 to  $R_{th} = 600$  mm,  $R_{th} = 800$  mm, and  $R_{th} = 1000$  mm (Staupendahl and Tekkaya, 2018b)

and 1000 mm in relation to the profile feed. The graph can be divided into three regions: loading, steady-state, and unloading. During the loading stage, which begins at a profile feed of 0 mm, the bending head moves along the  $X$ -axis and rotates around the  $\beta_1$ -axis until it reaches its steady-state position. It stays at this position until a profile feed of 800 mm, after which the unloading stage begins. In this last stage, the bending head moves and rotates back to the initial center starting position until the profile feed reaches 1200 mm. The movements of the axes are defined using an ideal profile made up of a 400 mm straight part, followed by an 800 mm curved part with the target radius  $R_{th}$ , and finalized by a 400 mm straight part in combination with a digital kinematic mock-up as described by Staupendahl (2011) and used by Hudovernik et al. (2013), which is built up like the generalized geometric 3D bending process model shown in Figure 4.9 b. According to the  $X$ -axis force data comparison shown in Figure 5.22, the numerical data can be rated to be in good agreement with the experimental results with errors lying well within a 5 % range at the force peak in the loading section and over the whole steady-state region.

The validation of the numerical model during pure torsion was performed without profile feed in order to focus solely on the torque response of the model. The profile was twisted to  $d\phi = 1.964$  rad/m at an angular speed of the  $\alpha_2$ -axis of 0.00393 rad/s in the experiment while it was twisted at 0.196 rad/s in the numerical simulation, keeping the previously established speed factor 1:50. The experimental and numerical torque data in relation to twist per unit length of the profile is shown in Figure 5.23. The slope of the numerical curve in between 0 and 0.491 rad/m deviates significantly from the experimental slope, causing an error of 30 % at 0.246 rad/m. This deviation can be

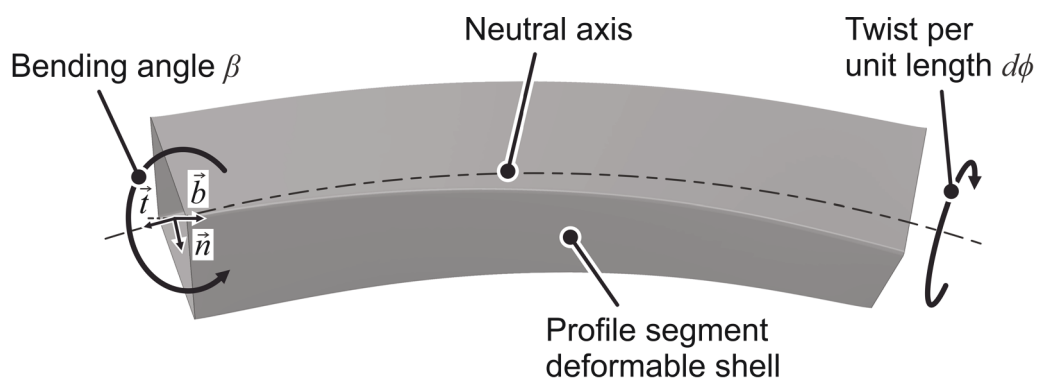


**Figure 5.23:** Experimental and numerical torque data during twisting the MW700L Z1 profile to different values of  $d\phi$

attributed to the machine stiffness, which, in case of torsion, is calculated with Eq. (5.15). The slope of the numerical data corrected by the torsional stiffness  $c_M$  as seen in Figure 5.23 is in much better agreement with the experimental data, showing a maximum error of 14 % at 0.246 rad/m and an average error of 7 % from 0.246 rad/m to 0.491 rad/m. The average error between the numerical and the experimental results in the range from 0.491 to 0.982 rad/m is below 5 % and only increases to 6 % from 0.982 to 1.964 rad/m.

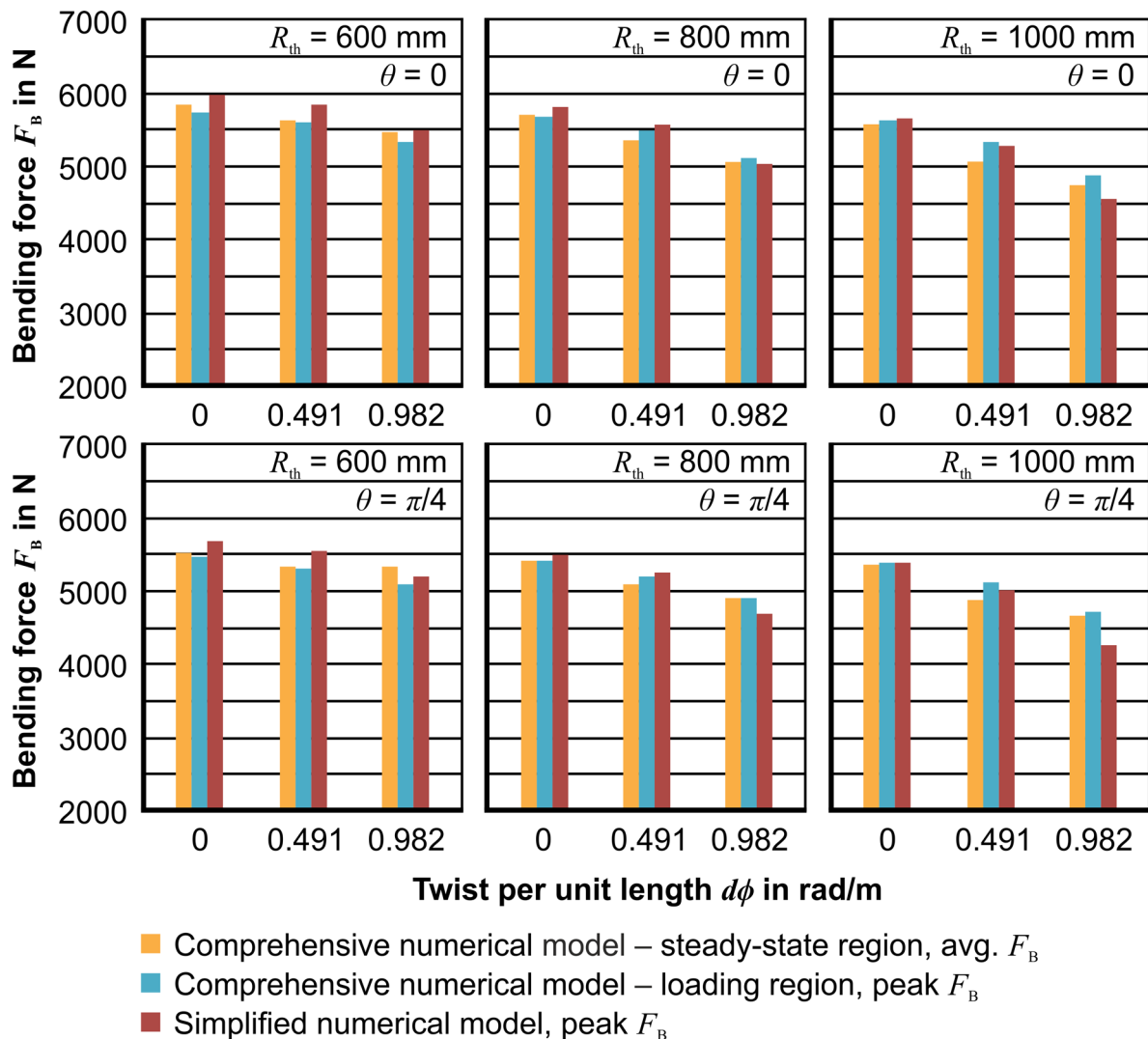
### 5.4.2 Simplified numerical model

In order to analyze the shear strain over the cross-section without the influence of tool contact and, thus, contact stresses, a simplified implicit FE model was additionally set up in which bending and twisting were applied by boundary conditions (see Figure 5.24). Due to the non-existence of contact interfaces in this approach and the quasi-static nature of the actual 3D profile bending process in the investigated range of feed velocities, the simplified FE model was regarded as a static problem and solved using the implicit solver. The advantage of using this calculation scheme is that equilibrium equations are solved in each time step, thereby upholding the static equilibrium throughout the entire simulation (Belytschko et al., 2014). This allows a reliable analysis of mathematical constructs that cannot be directly validated experimentally. As the explicit model, the simplified implicit model was set up using 4-node, quadrilateral, general purpose shell elements. In order to avoid tool contact, only a 400 mm long profile segment was regarded, which represents the length of the profile between the front feeding rolls and the bending head, with boundary conditions at both ends of the profile simulating bending and twisting. To further simplify the simulation and increase the calculation efficiency, only half of the profile length was actually analyzed. Here, twist was applied to one end of the profile segment by a rotational boundary condition around the neutral axis of the profile, while bending was simulated by a rotational boundary condition around the binormal vector  $\vec{b}$  at the other end of the segment. The rotation around  $\vec{b}$  is



**Figure 5.24:** Simplified FE model to simulate combined bending and twisting without tool contact (Staupendahl and Tekkaya, 2018b)

given by the bending angle  $\beta$ , which, in the specific case of a 200 mm long profile segment, is equal to  $200 \text{ mm}/R_{\text{th}}$ . The vertices of the cross-section were filleted with 1.25 mm radii, closely resembling the experimentally used profile material, which was presented in Section 5.1. The main reason behind the filleting was overcoming convergence issues during solving of the numerical model. A mesh size of 0.2 mm was chosen in the areas in proximity to the fillet and in the middle section of the profile. The middle section was used to extract the stress and strain data in Section 7.3. Figure 5.25 compares the bending force data calculated with the simplified model to the bending force data calculated with the comprehensive numerical model. In the simplified simulations with bending and simultaneous twisting, twisting and bending were initialized in the same instant and reached their final values at the same increment.



**Figure 5.25:** Comparison of bending force data calculated by the comprehensive numerical in the loading region and the steady-state region to the bending force calculated by the simplified numerical model at profile positions  $\theta = 0$  and  $\theta = \pi/4$

In the comprehensive simulations, the  $\alpha_2$ -axis movements were initialized parallel to the  $X$ -axis and  $\beta_1$ -axis movements at a profile feed of 0 mm. All axis movements were finalized upon reaching the steady state region. On average, the difference between  $F_B$  obtained with the simplified model and  $F_B$  obtained with the comprehensive model is in the same range as the difference between the average  $F_B$  in the steady-state region and the peak  $F_B$  of the comprehensive model. As a result, the simplified FE-model is declared feasible for the stress and strain analyses performed in Section 7.3.

## 6 Elastic profile behavior during 3D profile bending

Depending on the position of  $P_{FB}$ , a torque  $M_T$  applied to the profile in order to twist its cross-section can result in a parasitic force that is oriented orthogonally to the bending force. Similar to the parasitic torque discussed in Section 4.2.4, this parasitic force can result in deviations of the bending plane rotation. The calculations necessary to set up the relation between an applied torque and a parasitic force in a 4-cDOF bending process is addressed in the next section.

### 6.1 Definition of a supported beam model for profile bending with $\geq 4$ cDOF

In order to calculate the forces and moments acting on a profile during 3D profile bending, an analogous model has to be set up. An efficient way to do this is by converting the complex real-life bending process with its profile feeding system and enclosing bending head into a supported beam model. The state of the art of 3D profile bending machines with  $\geq 4$  cDOF shows two general kinds of profile supports:

- A die-based support, through which the profile is fed and which acts like a sleeve bearing, taking up radial forces and moments. Processes that use a die-based support are the Gigalus combined drawing and free-form bending machine, the Nissin processes, the Hexabend process, and the 6-DOF bending process.
- A roll-based support, where the individual feeding rolls take up different forces and moments depending on the general roll setup and the roll positions. The only system that currently uses this kind of support is the TSS bending process.

As explained in Section 2.1.2, Hermes (2011) used a straight statically indeterminate beam, loaded with a bending force parallel to the  $X$ -axis, to describe the in-plane elastic profile behavior in TSS bending. This simplification lead to displacement deviations along the  $X$ -axis of 30 %, which were reduced to 15 % by the consideration of machine stiffness (see Figure 2.7). However, a remeasurement of the machine stiffness (see Section 5.2.2) has actually yielded a much higher machine stiffness with displacement values at the point of force application 2 to 6 times lower than Hermes' values, depending on the applied bending force (2 at  $F_B = 50$  kN, 6 at  $F_B = 0.1$  kN). A reason for Hermes' high deviation between experimental and analytical values could be his simplification of the elastic bending problem as a straight beam. Thus, for an increased real-life representation of the bending process, a curved beam is regarded in the following sections.

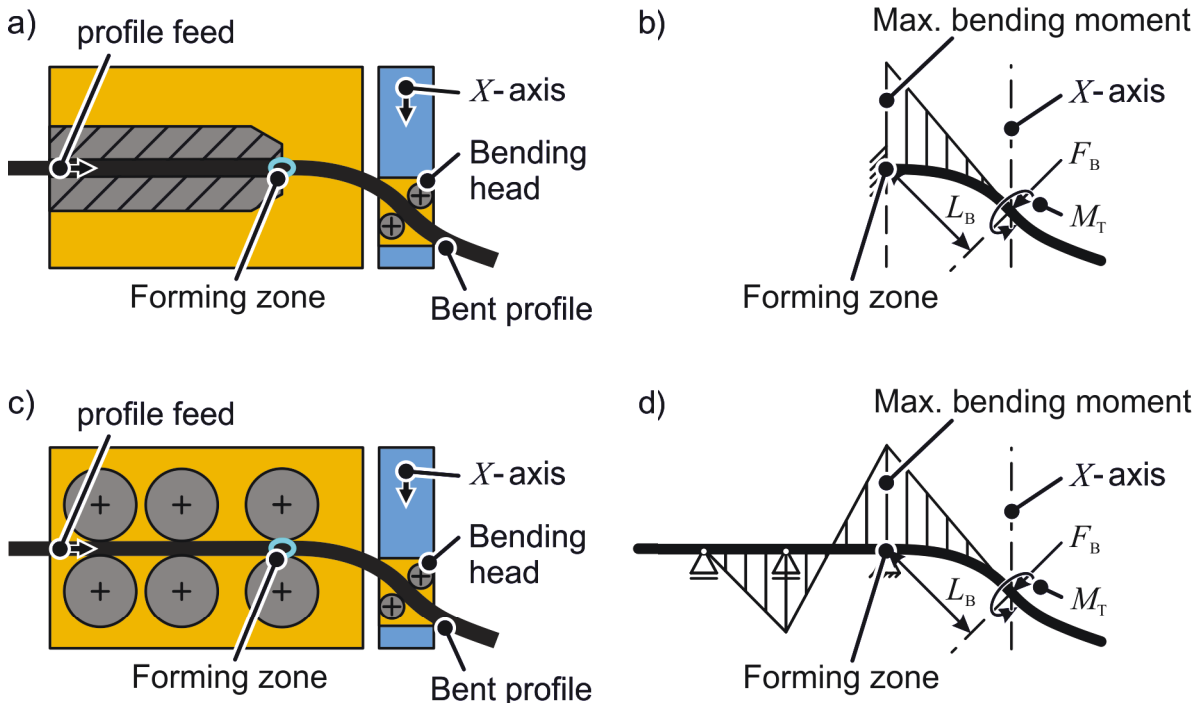
For the setup of the supported beam model, it is assumed that the curve describes an ideal radius and lies in the  $xy$ -plane. The top view of a 3D bending process in the  $xy$ -plane with a die support and its simplification are shown in Figure 6.1a) and b). In the illustrated process setup, the profile is replaced by a cantilever beam, while the die is simplified as a full moment connection.

Figure 6.1 c) and d) show a roll-based support, as it is applied in the TSS bending process, and its simplification as a statically indeterminate beam. The left and middle pair of the feeding rolls are replaced by two roller supports, constraining the translations of the beam in  $x$  and  $z$ -direction. The right pair (front pair) is replaced by a hinged support, constraining the translations in  $x$ ,  $y$ , and  $z$ -direction. Additionally to the respective translations, the supports also constrain the rotation of the beam around the  $y$ -axis.

Should more or less feeding roll pairs be used in the roll-based support, the beam model can be extended with further roller supports left of the hinged support, or the amount of roller supports can be reduced. In the case of combining the roll-based support with a form-closed feeding mechanism as, for instance, a pusher or booster, the beam model can be extended by a full moment connection left of the roller supports. The bending head, in all cases, is replaced by a simple support, solely constraining the translation of the beam in  $z$ -direction, and a force vector with the magnitude  $F_B$  and a torque  $M_T$ .

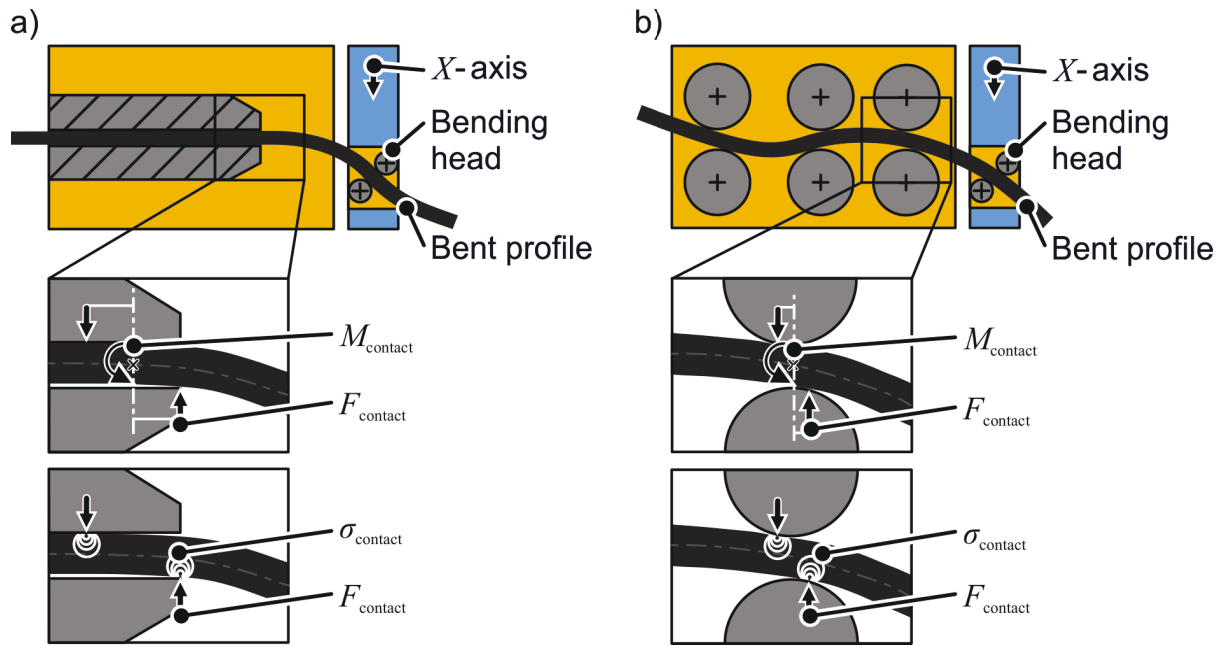
The real-life surface-to-surface contact is, thus, simplified to a point contact implicating the following additional simplifications:

- No transmission of additional moments into the profile by an oblique positioning of the profile in the supporting system (Figure 6.2)
- No effect of contact pressure on the stresses generated inside of the beam (Figure 6.2)



**Figure 6.1:** 3D bending process with a die support (a) and roll-based support (c) and their respective simplified supported beam models including qualitative bending moment diagrams (b, d)





**Figure 6.2:** a) Contact stresses caused by oblique positioning of profile in a die-based support (a) and a roll based support (b)

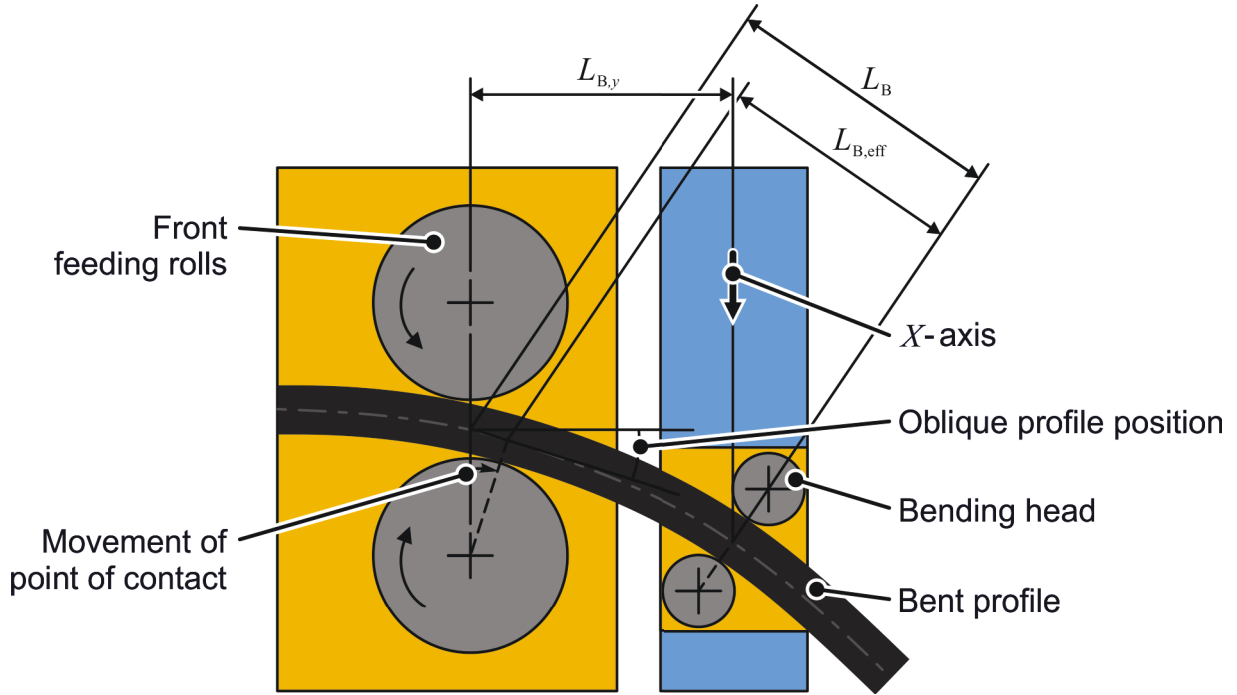
- No movement of the forming zone due to a change of the point of contact on the front feeding roll (Figure 6.3)

Hudovernik (2014a) suggested that the forming zone begins before the front feeding rolls and ends after, with a shift of the forming zone center towards the bending head, not only because of a moving contact point on the feeding roll (Figure 6.3) but also because of cross-section deformation and resulting changes in the second moment of area. He defined the center of the forming zone as the mid-point of the line described by the points of maximum von Mises stress in the compressive and tensile region of the profile as given by a FE-simulation. His results suggest forming zone displacements towards the bending head, which reduce the ideal bending lever arm  $L_B$  as much as 10 % creating the effective lever arm  $L_{B,\text{eff}}$ . The validity of Hudovernik's approach is not completely clear, however, because the von Mises stress data that he extracted from his simulations were affected by contact stresses, applied to the profile by the feeding rolls. The figures in his work, showing the von Mises stress distribution along the profile during bending, could also be interpreted in the way that the center of the forming zone is actually much closer to the front feeding rolls than he stated, which would match observations done by Hermes (2011).

The supported beam model, that is set up in this work will, thus, use the ideal lever arm  $L_B$  that does not consider a shift of the forming zone. As a result, the maximum bending moment that acts on the forming zone, as shown in the supported beam models in Figure 6.1b) and d), can be calculated with the bending force  $F_B$  and the ideal lever arm  $L_B$ :

$$M_{B,\max} = F_B L_B \quad (6.1)$$

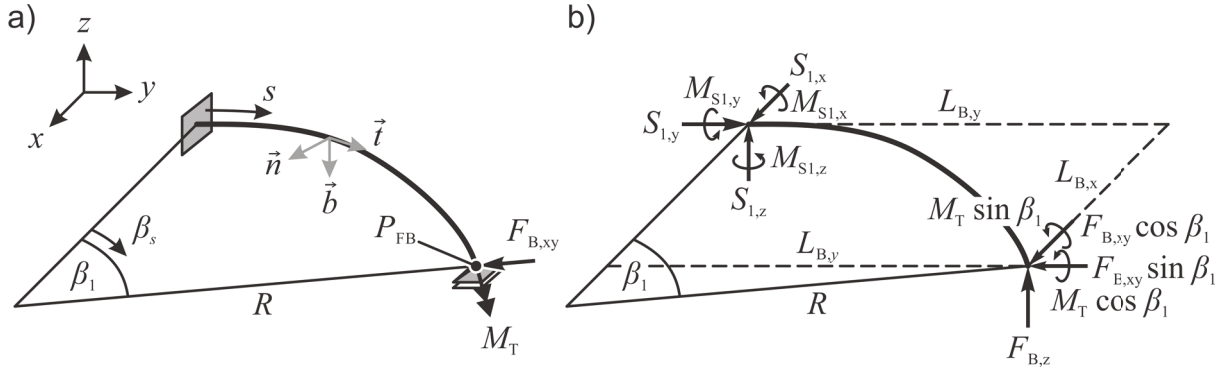
In the case of an ideal bending radius,  $L_B$  is equal to the distance  $L_{B,y}$  from the profile support to plane of  $P_{FB}$  movement, or, when looking at the process in the  $xy$ -plane as pictured in Figure 6.3, from the front feeding rolls to the  $X$ -axis:



**Figure 6.3:** Movement of the point of contact between profile and front feeding roll because of oblique profile position in feeding roll pair

## 6.2 Supported beam model: die-based profile support

Figure 6.4 shows the isometric view of a supported beam model of a 3D bending process with a die support and the corresponding free-body diagram. Since the movement of the beam is constrained in the  $z$ -direction at the point of bending force application  $P_{FB}$  by a simple support, the beam has to be regarded as a statically indeterminate beam. The most effective way to calculate the loads and the bending line in the present case is by the method of superposition, which allows a separation of loads in order to set up statically determinate beams. In the free body diagram, the simple support is, therefore, replaced by the force  $F_{B,z}$  in the  $z$ -direction. In the point  $P_{FB}$  the beam is, thus, loaded by the bending force in the  $xy$ -plane  $F_{B,xy}$ , by the force  $F_{B,z}$ , and by the torque  $M_T$ . In order to calculate the individual forces and the bending line of the beam, first, the deflection caused by each individual forces is calculated. Using the constraint that the total deflection  $w_{z,P_{FB}}$  in the point  $P_{FB}$  must be zero, the unknown force  $F_{B,z}$  can be calculated and used to solve the equilibrium equations. An ideal radius  $R$  between the profile support and the point of bending force application is considered.



**Figure 6.4:** a) Supported beam model of a 3D bending process with a die support, b) free-body diagram

The beam is positioned so that the osculating plane is parallel to the  $xy$ -plane with the binormal axis being positioned in the opposite direction of the  $z$ -axis. The simplification of the ideal radius results in the following relations:

$$L_{B,x} = R - R \sin \beta_1 \quad (6.2)$$

$$L_{B,y} = R \sin \beta_1 \quad (6.3)$$

The equilibrium equations of the beam:

$$\sum F = 0 = \begin{bmatrix} S_{1,x} \\ S_{1,y} \\ S_{1,z} \end{bmatrix} + \begin{bmatrix} F_{B,xy} \cos \beta_1 \\ -F_{B,xy} \sin \beta_1 \\ F_{B,z} \end{bmatrix} \quad (6.4)$$

$$\sum M = 0 = \begin{bmatrix} M_{S1,x} \\ M_{S1,y} \\ M_{S1,z} \end{bmatrix} + \begin{bmatrix} L_{B,x} \\ L_{B,y} \\ 0 \end{bmatrix} \begin{bmatrix} F_{B,xy} \cos \beta_1 \\ -F_{B,xy} \sin \beta_1 \\ F_{B,z} \end{bmatrix} + \begin{bmatrix} M_T \sin \beta_1 \\ M_T \cos \beta_1 \\ 0 \end{bmatrix} \quad (6.5)$$

lead to the following reaction forces:

$$S_{1,x} = -F_{B,xy} \cos \beta_1 \quad (6.6)$$

$$S_{1,y} = F_{B,xy} \sin \beta_1 \quad (6.7)$$

$$S_{1,z} = -F_{B,z} \quad (6.8)$$

and reaction moments of the support:

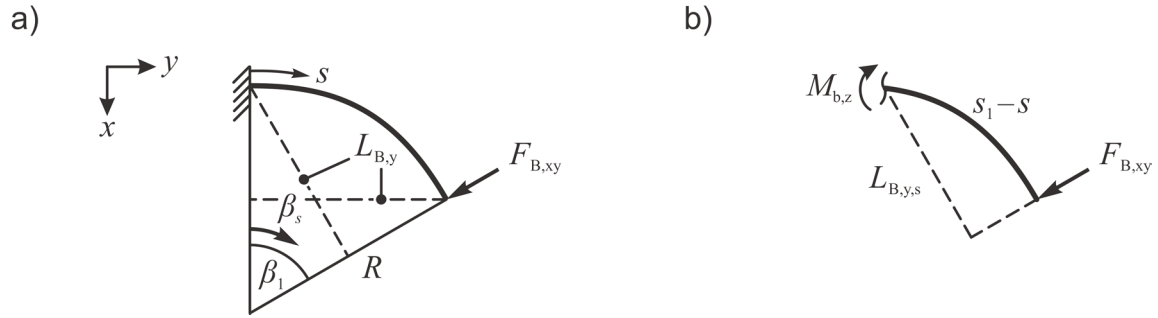
$$M_{S1,x} = -F_{B,z} L_{B,y} - M_T \sin \beta_1 \quad (6.9)$$

$$M_{S1,y} = F_{B,z} L_{B,x} - M_T \cos \beta_1 \quad (6.10)$$

$$M_{S1,z} = F_{B,xy} L_{B,y} \quad (6.11)$$

### 6.2.1 Beam deflection in the $xy$ -plane

In the  $xy$ -plane the beam is statically determined so that the beam deflection in the plane can be directly calculated from the applied load  $F_{B,xy}$ . The supported beam model and the respective free-body diagram are pictured in Figure 6.5.



**Figure 6.5:** a) Supported beam model with just the bending force  $F_{B,xy}$  applied  
b) free-body diagram

The internal moment in terms of  $\beta_s$  is calculated by:

$$M_{B,z}(\beta_s) = F_{B,xy} L_{B,y,s} = F_{B,xy} R \sin(\beta_1 - \beta_s) \quad (6.12)$$

With the relation:

$$\beta_s = \frac{s}{R} \quad (6.13)$$

Eq. (6.12) can be put in terms of the arc length  $s$ :

$$M_{B,z}(s) = F_{B,xy} R \sin\left(\beta_1 - \frac{s}{R}\right) \quad (6.14)$$

Integrating the curvature-bending moment equation:

$$w''_{xy,B}(s) EI = -M_{B,z}(s) \quad (6.15)$$

with the constraint  $w'_{xy,B}(0) = 0$  (full moment connection), the beam's slope equation is derived:

$$w'_{xy,B}(s) = \frac{F_{B,xy} R^2}{EI} \left[ \cos\left(\frac{s}{R} - \beta_1\right) - \cos \beta_1 \right] \quad (6.16)$$

or, in terms of  $\beta_s$ :

$$w'_{xy,B}(\beta_s) = \frac{F_{B,xy} R^2}{EI} \left[ \cos(\beta_s - \beta_1) - \cos \beta_1 \right] \quad (6.17)$$

with the constraint  $w_{xy,B}(0) = 0$  the beam deflection is calculated:

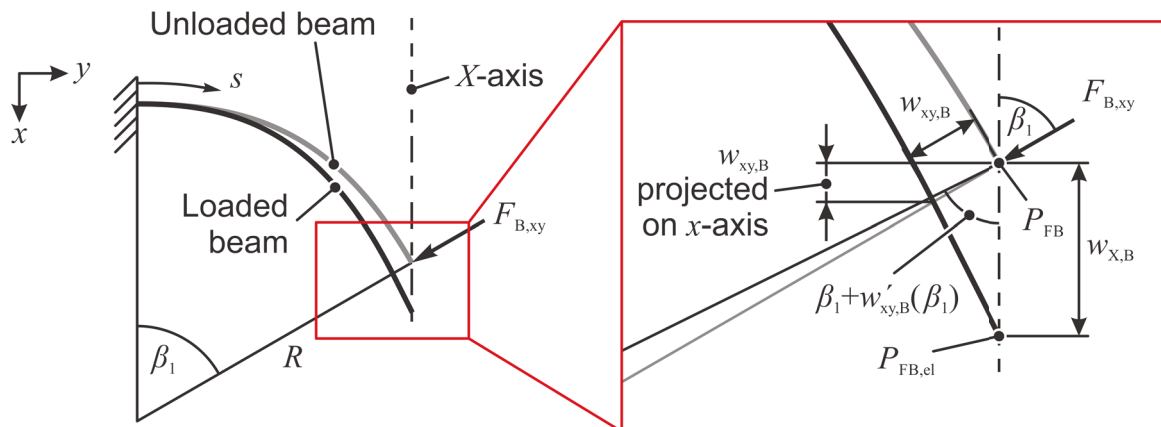
$$w_{xy,B}(s) = \frac{F_{B,xy}R^3}{EI} \left[ \sin\left(\frac{s}{R} - \beta_1\right) - \frac{s}{R} \cos \beta_1 + \sin \beta_1 \right] \quad (6.18)$$

or, in terms of  $\beta_s$ :

$$w_{xy,B}(\beta_s) = \frac{F_{B,xy}R^3}{EI} \left[ \sin(\beta_s - \beta_1) - \beta_s \cos \beta_1 + \sin \beta_1 \right] \quad (6.19)$$

The displacement  $w_{xy,B}$  describes the repositioning of each infinitesimal point of the beam in normal direction to the beam's original geometry. This means that the total deflection at  $\beta_1$  is in direction of the applied load  $F_{B,xy}$ . In the case of a movement of the point of bending force application  $P_{FB}$  on a plane parallel to the  $xz$ -plane (Figure 4.9), as it is the case with all die-based 3D-profile bending process with  $\geq 4$  cDOF but the parallel-kinematics-based processes (see Table 4.1), the resulting deflection in this plane is needed. In the present calculation this means calculating the deflection  $w_{x,B,F}$  in  $x$ -direction. Here, a projection of  $w_{xy,B}$  at  $\beta_1$  onto the  $x$ -axis does not lead to the required results because this vector component breakdown implies a possible movement of  $P_{FB}$  in  $y$ -direction. This is hindered, however, by the constraint of  $P_{FB}$  to movements along the  $X$ -axis. The profile, on the other hand can move freely through  $P_{FB}$ . The resulting geometric dependencies are shown in Figure 6.6. In order to allow a movement of the profile point initially in contact with  $P_{FB}$ , the curved beam is extended with a straight beam element tangent to the endpoint. The intersection point of the extended beam and the  $X$ -axis represents the position of  $P_{FB,el}$  with the total displacement along the  $X$ -axis  $w_{X,B}$  being calculated by:

$$w_{X,B}(\beta_1) = \frac{w_{xy,B}(\beta_1)}{\cos[\beta_1 + w'_{xy,B}(\beta_1)]} \quad (6.20)$$

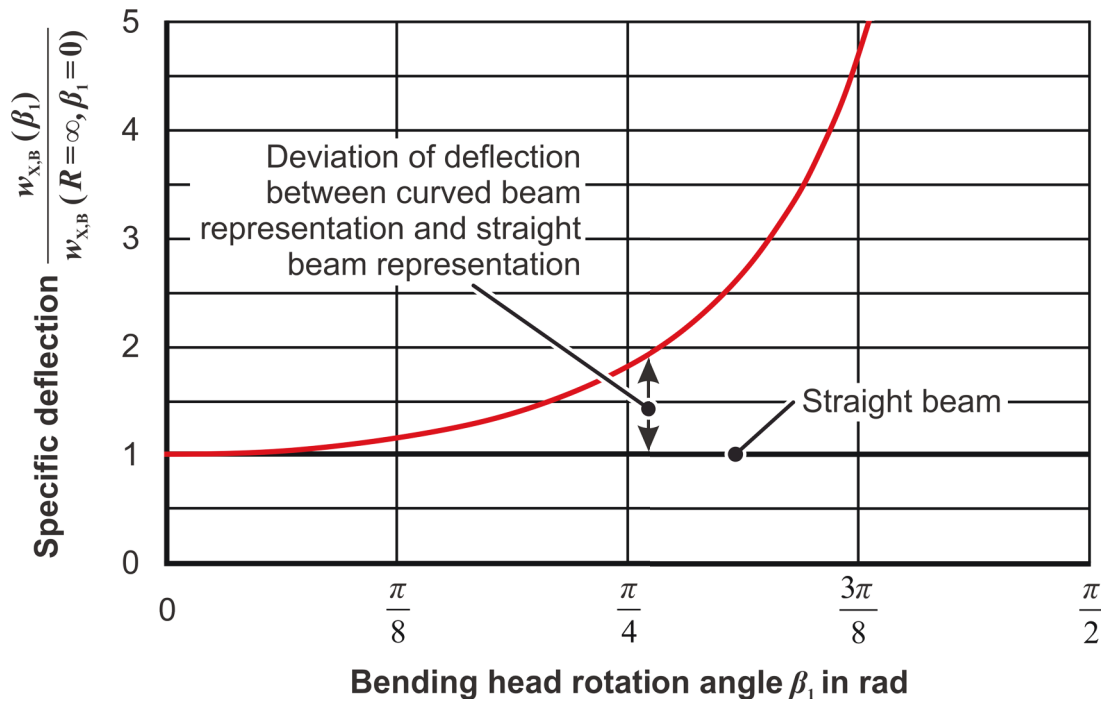


**Figure 6.6:** Elastic deformation of beam causing deflection  $w_{X,B}$  along  $X$ -axis

The difference of  $w_{X,B,F}$  to the displacements calculated with a straight profile are significant. Figure 6.7 shows the specific deflection of a curved beam in relation to the rotation angle  $\beta_1$ . The specific deflection is given by:

$$\frac{w_{X,B}(\beta_1)}{w_{X,B}(R=\infty, \beta_1=0)} = \frac{3(\tan \beta_1 - \beta_1)}{\sin^3 \beta_1} \quad \text{with} \quad w'_{xy,B}(\beta_1) = 0 \quad (6.21)$$

Taking the distance  $L_{B,y}$  to be 396.92 mm, as it is the case in the 5-cDOF TSS bending machine, and a radius  $R$  of 2000 mm ( $\beta_1 = 0.200$ ), the difference between the calculated deflection using the curved beam representation and the straight beam representation is 4 %. At a radius of 1000 mm ( $\beta_1 = 0.408$ ) this deviation increases to 17 %, however. At 600 mm ( $\beta_1 = 0.723$ ) the deviation further increases to 65 %.



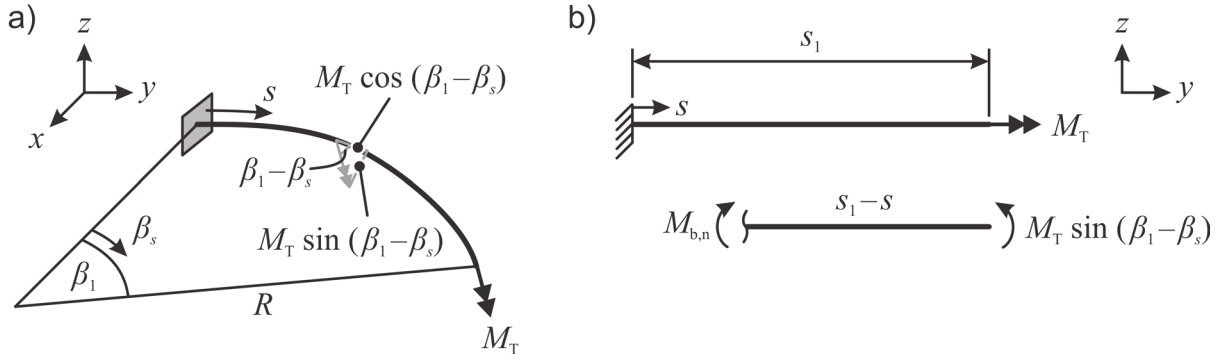
**Figure 6.7:** Specific deflection of curved beam in relation to the rotation angle  $\beta_1$

## 6.2.2 Beam deflection in $z$ -direction

In the  $z$ -direction the beam is statically indeterminate. Here, a separation of the individual loads on the beam –  $F_{B,z}$  and  $M_T$  – has to be performed. The impact of these loads on beam deflection, aka bending, has to be calculated as well as the impact on beam torsion.

### 6.2.2.1 Impact of $M_T$ on beam bending

In the point of torque application, the torque vector is tangential to the beam. Thus, no bending moment is generated by the torque in this point. As the torque is moved along the curve, hereby staying parallel to its initial position at  $s = s_0$ , the torque splits up into



**Figure 6.8:** a) Supported beam model with just the torque  $M_T$  applied  
b) free-body diagram in order to calculate beam bending

a tangential and a normal component (see Figur 6.8a). While the tangential component twists the beam, the normal component acts as a bending moment. As such, the internal bending moment in terms of  $\beta_s$  is calculated by:

$$M_{B,n}(\beta_s) = M_T \sin(\beta_1 - \beta_s) \quad (6.22)$$

Using Eq. (6.13) the internal moment can be put in terms of  $s$ :

$$M_{B,n}(s) = M_T \sin\left(\beta_1 - \frac{s}{R}\right) \quad (6.23)$$

When setting the second derivative of the beam deflection equal to the internal moment, it is imperative to use the correct sign. In Eq. (6.15) the second derivative was set equal to  $-M_{B,z}$ , which is the common convention in the literature if positive forces to the right side of the origin rotate into the opposite direction of the bending moment. E.g., the positive bending moment rotation in Section 6.2.1 is counterclockwise, while positive forces to the right of the origin lead to a clockwise rotation. Setting  $M_{B,n}$  negative in this case, leads to deflections that are positive when going into the same direction as the positive forces. Since the bending moment in the case of a beam deflection in  $z$ -direction ( $M_{B,n}$ ) rotates into the same direction as positive forces to the right of the origin (counterclockwise) the second derivative of the beam deflection must be set equal to  $+M_{B,n}$ :

$$w''_{z,B,M}(s)EI = M_{B,n}(s) \quad w'_{z,B,M}(0) = 0 \quad (6.24)$$

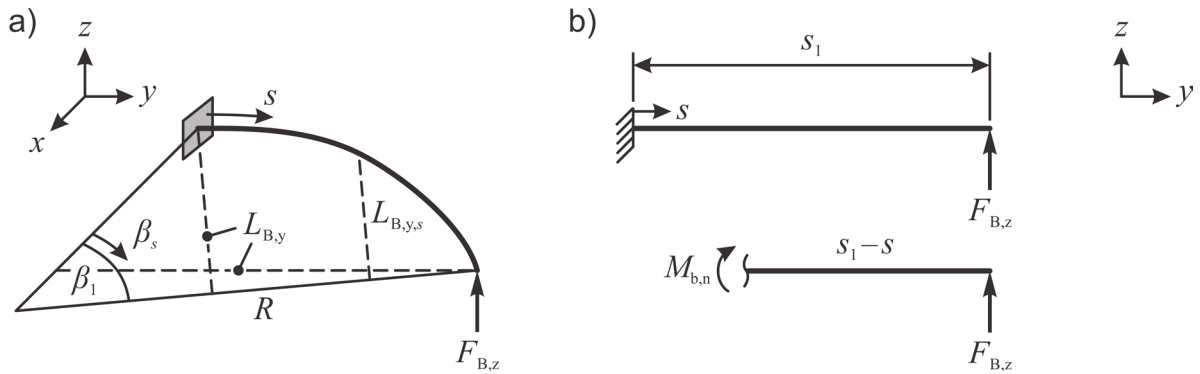
Using the constraints  $w_{z,B,M}(0) = 0$  and  $w'_{z,B,M}(0) = 0$  yields the beam deflection:

$$w_{z,B,M}(s) = \frac{M_T R^2}{EI} \left[ \sin\left(\frac{s}{R} - \beta_1\right) - \frac{s}{R} \cos \beta_1 + \sin \beta_1 \right] \quad (6.25)$$

In terms of  $\beta_s$  Eq. (6.25) can be written as:

$$w_{z,B,M}(\beta_s) = \frac{M_T R^2}{EI} \left[ \sin(\beta_s - \beta_1) - \beta_s \cos \beta_1 + \sin \beta_1 \right] \quad (6.26)$$

### 6.2.2.2 Impact of $F_{B,z}$ on beam bending



**Figure 6.9:** a) Supported beam model with just the force  $F_{B,z}$  applied  
b) free-body diagram in order to calculate beam bending

The force  $F_{B,z}$  acts on each individual position  $s$  of the profile with the bending lever  $L_{B,y,s}$  (see Figure 6.9a):

$$L_{B,y,s} = R \sin(\beta_1 - \beta_s) \quad (6.27)$$

In combination with Eq. (6.13), the internal bending moment in terms of  $s$  is calculated by:

$$M_{B,n}(s) = F_{B,z} R \sin\left(\beta_1 - \frac{s}{R}\right) \quad (6.28)$$

Double integrating the equation:

$$w''_{z,B,F}(s) EI = M_{B,n}(s) \quad (6.29)$$

and using the constraints  $w_{z,B,F}(0) = 0$  and  $w'_{z,B,F}(0) = 0$  yields the beam deflection:

$$w_{z,B,F}(s) = \frac{F_{B,z} R^3}{EI} \left[ \sin\left(\frac{s}{R} - \beta_1\right) - \frac{s}{R} \cos \beta_1 + \sin \beta_1 \right] \quad (6.30)$$

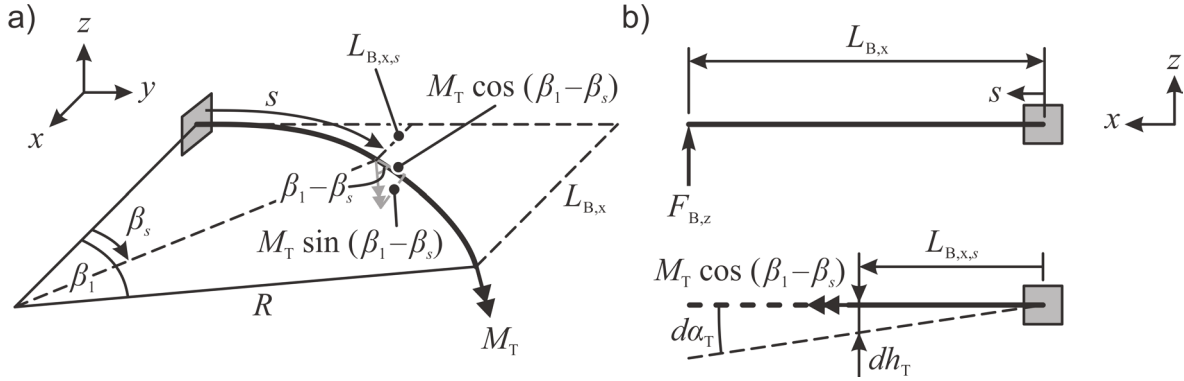
In terms of  $\beta_s$ , Eq. (6.25) can be written as:

$$w_{z,B,F}(\beta_s) = \frac{F_{B,z} R^3}{EI} \left[ \sin(\beta_s - \beta_1) - \beta_s \cos \beta_1 + \sin \beta_1 \right] \quad (6.31)$$

### 6.2.2.3 Impact of $M_T$ on beam twisting

The component of the torque tangent to the beam causes the beam to twist around its neutral axis. Since the neutral axis of the beam is shaped in form of a partial circle with the radius  $R$  (see Figure 6.10a), twisting of the beam causes a deflection in the  $z$ -direc-





**Figure 6.10:** a) Supported beam model with just the torque  $M_T$  applied  
b) free-body diagram in order to calculate beam twisting

tion. Specifically, the beam twists with the angle  $d\alpha_T$  at the lever arm  $L_{B,x,s}$ , causing the deflection  $dh_T$ . The relation between  $d\alpha_T$ ,  $L_{B,x,s}$ , and  $dh_T$  is given by:

$$\tan d\alpha_T = \frac{dh_T}{L_{B,x,s}} \quad (6.32)$$

At small displacements, Eq. (6.32) can be simplified to:

$$d\alpha_T = \frac{dh_T}{L_{B,x,s}} \quad (6.33)$$

Integrating the incremental displacement  $dh_T$  over  $d\alpha_T$  leads to the deflection  $w_{z,T,M}$ :

$$w_{z,T,M}(\alpha_T) = -\int dh_T = -\int L_{B,x,s} \cdot d\alpha_T \quad (6.34)$$

Since the final value  $\alpha_T$  is unknown,  $d\alpha_T$  can be related to the angle  $\beta_s$  by using the Saint Venant formulation (Venant, 1855):

$$d\alpha_T = \frac{M_T \cos(\beta_1 - \beta_s) \cdot ds}{GJ_T} \quad \text{with} \quad ds = R \cdot d\beta_s \quad (6.35)$$

Together with the geometric relation:

$$L_{B,x,s} = R - R \cos \beta_s \quad (6.36)$$

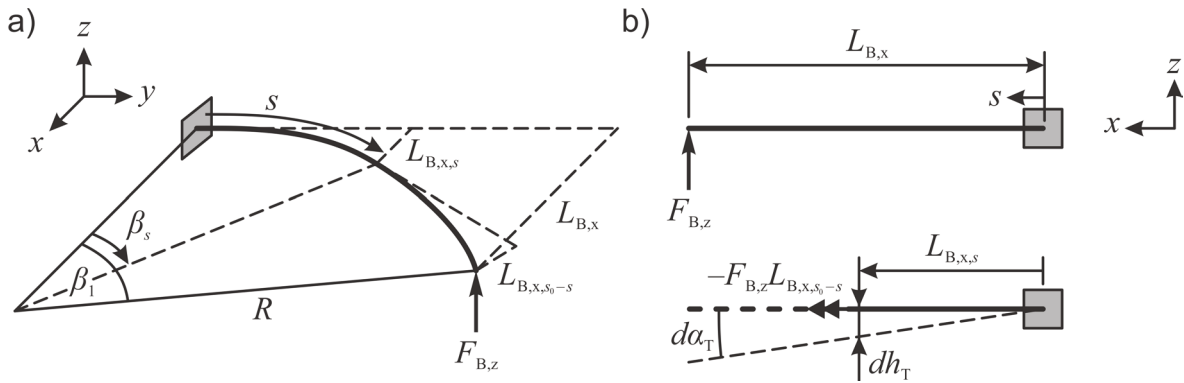
it follows that:

$$w_{z,T,M}(\beta_s) = \frac{-M_T R^2}{GJ_T} \int [(1 - \cos \beta_s) \cdot \cos(\beta_1 - \beta_s) \cdot d\beta_s] \quad (6.37)$$

The integral can be solved by considering the constraint  $w_{z,T,M}(0) = 0$ :

$$w_{z,T,M}(\beta_s) = \frac{M_T R^2}{GJ_T} \left[ -\sin(\beta_s - \beta_1) + \frac{1}{4} \sin(2\beta_s - \beta_1) + \frac{1}{2} \beta_s \cos \beta_1 - \frac{3}{4} \sin \beta_1 \right] \quad (6.38)$$

### 6.2.2.4 Impact of $F_{B,z}$ on beam twisting



**Figure 6.11:** a) Supported beam model with just the torque  $F_{B,z}$  applied  
b) free-body diagram in order to calculate beam twisting

The impact of  $F_{B,z}$  on beam twisting is calculated in a similar fashion as the impact of  $M_T$  in the previous section. In this case, beam twisting in a beam element at position  $s$  is caused by the force  $F_{B,z}$  at the lever arm  $L_{B,x,s_0-s}$ .

$$L_{B,x,s_0-s} = R - R \cos(\beta_1 - \beta_s) \quad (6.39)$$

This lever arm is maximal at  $s = 0$  and minimal at  $s = s_0$ . Figure 6.11 shows the geometric relations of the supported beam model and the free-body diagram. As  $F_{B,z}$  at the lever arm  $L_{B,x,s_0-s}$  causes a torque around the neutral axis of the beam with a negative sign, the deflection at point  $P_{FB}$  in the  $z$ -direction is calculated by:

$$w_{z,T,F}(\alpha_T) = \int dh_T = \int L_{B,x,s} \cdot d\alpha_T \quad (6.40)$$

As  $d\alpha_T$  can be related to the angle  $\beta_s$  by:

$$d\alpha_T = \frac{F_{B,z} [R - R \cos(\beta_1 - \beta_s)] \cdot ds}{GJ_T} \quad \text{with} \quad ds = R \cdot d\beta_s \quad (6.41)$$

and  $L_{B,x,s}$  to  $R$  and  $\beta_s$  by Eq. (6.36), the deflection  $w_{z,T,F}$  can be written as:

$$w_{z,T,F}(\beta_s) = \frac{F_{B,z} R^3}{GJ_T} \int \left\{ (1 - \cos \beta_s) \cdot [1 - \cos(\beta_1 - \beta_s)] \cdot d\beta_s \right\} \quad (6.42)$$

The integral can be solved by considering the constraint  $w_{z,T,F}(0) = 0$ :

$$w_{z,T,F}(\beta_s) = \frac{F_{B,z} R^3}{GJ_T} \left[ \beta_s - \sin \beta_s - \sin(\beta_s - \beta_1) + \frac{1}{4} \sin(2\beta_s - \beta_1) + \frac{1}{2} \beta_s \cos \beta_1 - \frac{3}{4} \sin \beta_1 \right] \quad (6.43)$$

### 6.2.2.5 The relation of $F_{B,z}$ and $M_T$

As the total deflection  $w_z$  at point  $P_{FB}$  must be zero, the sum of all individual deflections calculated in Sections 6.2.2.1 to 6.2.2.4 must be zero as well:

$$w_z(\beta_1) = 0 = w_{z,B,M}(\beta_1) + w_{z,B,F}(\beta_1) + w_{z,T,M}(\beta_1) + w_{z,T,F}(\beta_1) \quad (6.44)$$

By inserting Eqs. (6.26), (6.31), (6.38) and (6.43) into Eq. (6.44), the unknown force  $F_{B,z}$  can be determined in terms of the applied torque  $M_T$ :

$$F_{B,z} = -\frac{M_T}{R} \left[ \frac{\left(1 - \frac{EI}{2GJ_T}\right)(\sin \beta_1 - \beta_1 \cos \beta_1)}{(\sin \beta_1 - \beta_1 \cos \beta_1) - \frac{EI}{2GJ_T}(3 \sin \beta_1 - \beta_1 \cos \beta_1 - 2\beta_1)} \right] \quad (6.45)$$

From Eq. (6.45) it can be seen that the relation of  $F_{B,z}$  to  $M_T$  is dependent on the beam radius  $R$ , the bending head angle  $\beta_1$ , and the ratio bending stiffness  $EI$  to torsional stiffness  $GJ_T$ . Figure 6.12 shows this relation for radii from 200 mm to 10,000 mm for  $\beta_1$  values of 0 to  $\pi/2$  and stiffness ratios of 1.25, 1.50, and 1.75. At a radius of 10,000 mm  $F_{B,z}$  is only between 1 and 4 %/m of  $M_T$ , and can be neglected. However, at a radius of 2000 mm  $F_{B,z}$  is already between 6 and 19 %/m of  $M_T$ . The effect of  $M_T$  on  $F_{B,z}$  steadily increases with a decreasing radius and reaches values between 63 and 188 %/m at 200 mm.

Considering the square profile shape and material data introduced in Section 5.1, a stiffness ratio of 1.74 results. At a beam radius of 600 mm, the ratio of  $F_{B,z}$  to  $M_T$  is 0.21 1/m, at 800 mm the ratio is 0.16 1/m, and at 1000 mm the ratio is 0.13 1/m.

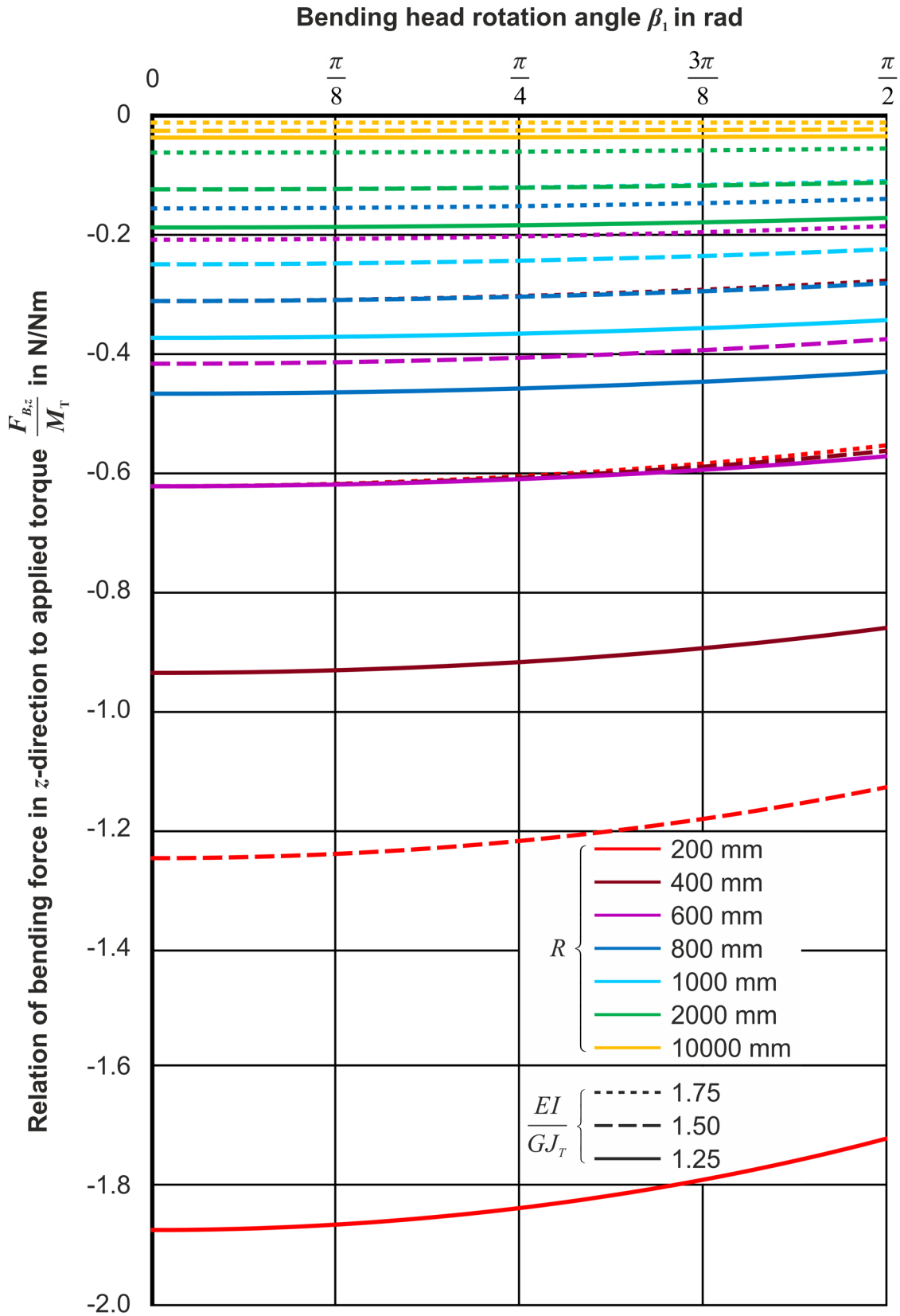
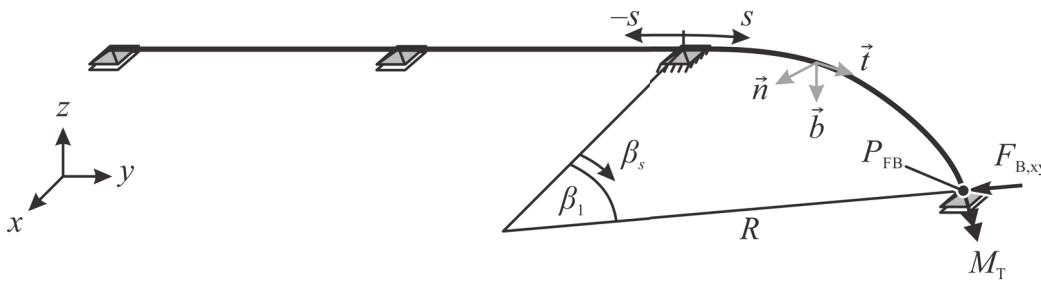


Figure 6.12: Ratio of bending force  $F_{B,z}$  to applied torque  $M_T$  for different radii and ratios of bending stiffness  $EI$  to torsional stiffness  $GJ_T$

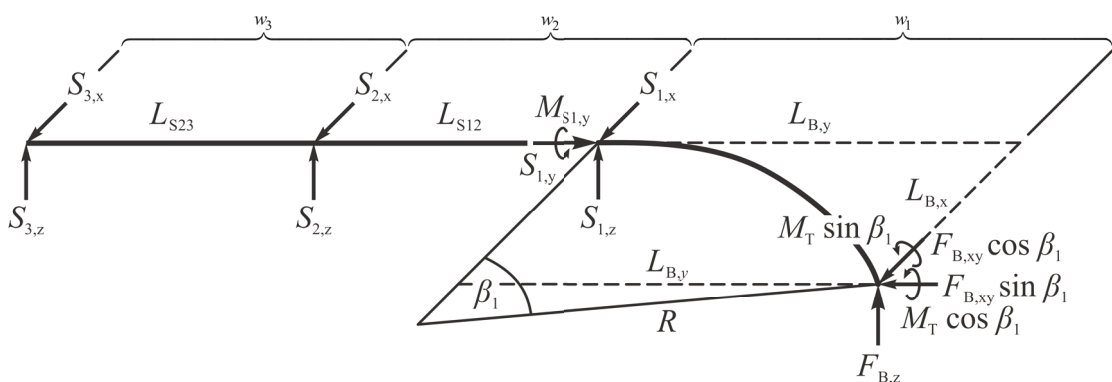
### 6.3 Supported beam model: roll-based profile support

Figure 6.13 shows the isometric view of a supported beam model adapted for a roll-based profile support with 3 supports as used in the 5-cDOF TSS bending process. The model is set up similar to the model of the die-based support with the difference that support  $S_1$  only constrains the rotation around the  $y$ -axis while allowing rotations around the  $x$  and  $z$ -axis. This means that bending moments in the  $xy$  and  $yz$ -plane are transferred to the beam on the left side of  $S_1$ . In order to take up the resulting reaction forces in  $x$  and in  $z$ -direction the support  $S_2$  is located at a distance of  $-L_{S12}$  from the origin and  $S_3$  is located at a distance of  $-L_{S12}-L_{S23}$  from the origin. The free rotations in the point  $S_1$  result in a nonzero slope of the beam in the  $xy$  and  $yz$ -plane and, thus, in non-zero boundary conditions for the beam bending calculations in this point. The two additional supports also make the beam statically indeterminate in the  $xy$ -plane and actually two times statically indeterminate in the  $yz$ -plane.

a)



b)



**Figure 6.13:** a) Supported beam model of a 3D bending process with a roll-based support b) free-body diagram

Although the same calculation strategy as in Section 6.2 can be used, the calculation is much more extensive. Only the twisting calculation using the applied moment  $M_T$  and the applied force  $F_{B,z}$  is identical to Section 6.2 because all torque (only torque around the  $y$ -axis is generated) is taken up by rotary constraint of  $S_1$ .

The equilibrium equations of the beam are:

$$\sum F = 0 = \begin{bmatrix} S_{3,x} \\ 0 \\ S_{3,z} \end{bmatrix} + \begin{bmatrix} S_{2,x} \\ 0 \\ S_{2,z} \end{bmatrix} + \begin{bmatrix} S_{1,x} \\ S_{1,y} \\ S_{1,z} \end{bmatrix} + \begin{bmatrix} F_{B,xy} \cos \beta_1 \\ -F_{B,xy} \sin \beta_1 \\ F_{B,z} \end{bmatrix} \quad (6.46)$$

$$\begin{aligned} \sum M_{S_1} = 0 = & \begin{bmatrix} 0 \\ -L_{S12} & -L_{S23} \\ 0 \end{bmatrix} \times \begin{bmatrix} S_{3,x} \\ 0 \\ S_{3,z} \end{bmatrix} + \begin{bmatrix} 0 \\ -L_{S12} \\ 0 \end{bmatrix} \times \begin{bmatrix} S_{2,x} \\ 0 \\ S_{2,z} \end{bmatrix} + \begin{bmatrix} 0 \\ M_{S1,y} \\ 0 \end{bmatrix} \\ & + \begin{bmatrix} L_{B,x} \\ L_{B,y} \\ 0 \end{bmatrix} \begin{bmatrix} F_{B,xy} \cos \beta_1 \\ -F_{B,xy} \sin \beta_1 \\ F_{B,z} \end{bmatrix} + \begin{bmatrix} M_T \sin \beta_1 \\ M_T \cos \beta_1 \\ 0 \end{bmatrix} \end{aligned} \quad (6.47)$$

and lead to the following reaction forces:

$$S_{1,x} = S_{3,x} \left( \frac{L_{S23}}{L_{S12}} \right) - F_{B,xy} \left( \frac{L_{B,y}}{L_{S12}} + \cos \beta_1 \right) \quad (6.48)$$

$$S_{1,y} = F_{B,xy} \sin \beta_1 \quad (6.49)$$

$$S_{1,z} = S_{3,z} \left( \frac{L_{S23}}{L_{S12}} \right) - F_{B,z} \left( \frac{L_{B,y} + L_{S12}}{L_{S12}} \right) - M_T \sin \beta_1 \left( \frac{1}{L_{S12}} \right) \quad (6.50)$$

$$S_{2,x} = -S_{3,x} \left( \frac{L_{S12} + L_{S23}}{L_{S12}} \right) + F_{B,xy} \left( \frac{L_{B,y}}{L_{S12}} \right) \quad (6.51)$$

$$S_{2,z} = -S_{3,z} \left( \frac{L_{S12} + L_{S23}}{L_{S12}} \right) + F_{B,z} \left( \frac{L_{B,y}}{L_{S12}} \right) + M_T \sin \beta_1 \left( \frac{1}{L_{S12}} \right) \quad (6.52)$$

$$S_{3,x} = -S_{2,x} \left( \frac{L_{S12}}{L_{S12} + L_{S23}} \right) + F_{B,xy} \left( \frac{L_{B,y}}{L_{S12} + L_{S23}} \right) \quad (6.53)$$

$$S_{3,z} = -S_{2,z} \left( \frac{L_{S12}}{L_{S12} + L_{S23}} \right) + F_{B,z} \left( \frac{L_{B,y}}{L_{S12} + L_{S23}} \right) + M_T \sin \beta_1 \left( \frac{1}{L_{S12} + L_{S23}} \right) \quad (6.54)$$

and the following reaction moment of  $S_1$ :

$$M_{S1,y} = F_{B,z} L_{B,x} - M_T \cos \beta_1 \quad (6.55)$$

### 6.3.1 Beam deflection in $xy$ -plane

Using  $S_1$  as the origin of the coordinate system, the following set of differential equations is set up to describe elastic beam bending and the resulting deflection in the  $xy$ -plane:

$$w''_{xy,B,1}(s)EI = -F_{B,xy}R \sin\left(\beta_1 - \frac{s}{R}\right) \quad (6.56)$$

$$w''_{xy,B,2}(s)EI = -F_{B,xy}R \sin\beta_1 \left(1 + \frac{s}{L_{S12}}\right) - S_{3,x} \frac{L_{S23}}{L_{S12}} s \quad (6.57)$$

$$w''_{xy,B,3}(s)EI = S_{3,x} (s + L_{S12} + L_{S23}) \quad (6.58)$$

The set of equations can be solved using the method of superposition similar to the case shown for the cantilever beam in Section 6.2 and using the following boundary conditions in the  $xy$ -plane:

$$w_{xy,B,1}(0) = w_{xy,B,2}(0) = w_{xy,B,2}(-L_{S12}) = w_{xy,B,3}(-L_{S12}) = w_{xy,B,3}(-L_{S12} - L_{S23}) = 0$$

$$w'_{xy,B,1}(0) = w'_{xy,B,2}(0) \quad (6.59)$$

$$w'_{xy,B,2}(-L_{S12}) = w'_{xy,B,3}(-L_{S23})$$

Consequently, the supporting force  $S_{3,x}$  is defined by:

$$S_{3,x} = -\frac{1}{2} F_{B,xy} R \left[ \frac{L_{S12} \sin\beta_1}{L_{S23} (L_{S12} + L_{S23})} \right] \quad (6.60)$$

resulting in the beam slope  $w'_{xy,B}$  and the deflection  $w_{xy,B}$ :

$$w'_{xy,B}(\beta_s) = \frac{F_{B,xy} R^2}{EI} \left[ \cos(\beta_s - \beta_1) - \cos\beta_1 + \psi \right] \quad (6.61)$$

$$w_{xy,B}(\beta_s) = \frac{F_{B,xy} R^3}{EI} \left[ \sin(\beta_s - \beta_1) - \beta_s \cos\beta_1 + \sin\beta_1 + \psi\beta_s \right] \quad (6.62)$$

with:

$$\psi = \frac{1}{3} \frac{L_{S12}}{R} \sin\beta_1 - \frac{1}{12R} \left( \frac{L_{S12}^2 \sin\beta_1}{L_{S12} + L_{S23}} \right) \quad (6.63)$$

As in the die-based model, Eqs. (6.61), (6.62) and (6.63) can be put in terms of  $s$  by replacing  $\beta_s$  by  $s/R$ . Eqs. (6.61) and (6.62) are similar to Eqs. (6.17) and (6.19) with the difference of the added terms  $\psi$  and  $\psi\beta_s$ .

Different support geometries can be modelled with Eq. (6.62):

- Die-based support (full-moment support):  $L_{S12} = L_{S23} = 0$
- 2-roll support:  $L_{S23} \gg L_{S12}, L_{S12} \neq 0$
- 2-roll support + chuck:  $L_{S23} = 0, L_{S12} \neq 0$
- 3-roll support:  $L_{S12} \neq 0, L_{S23} \neq 0$

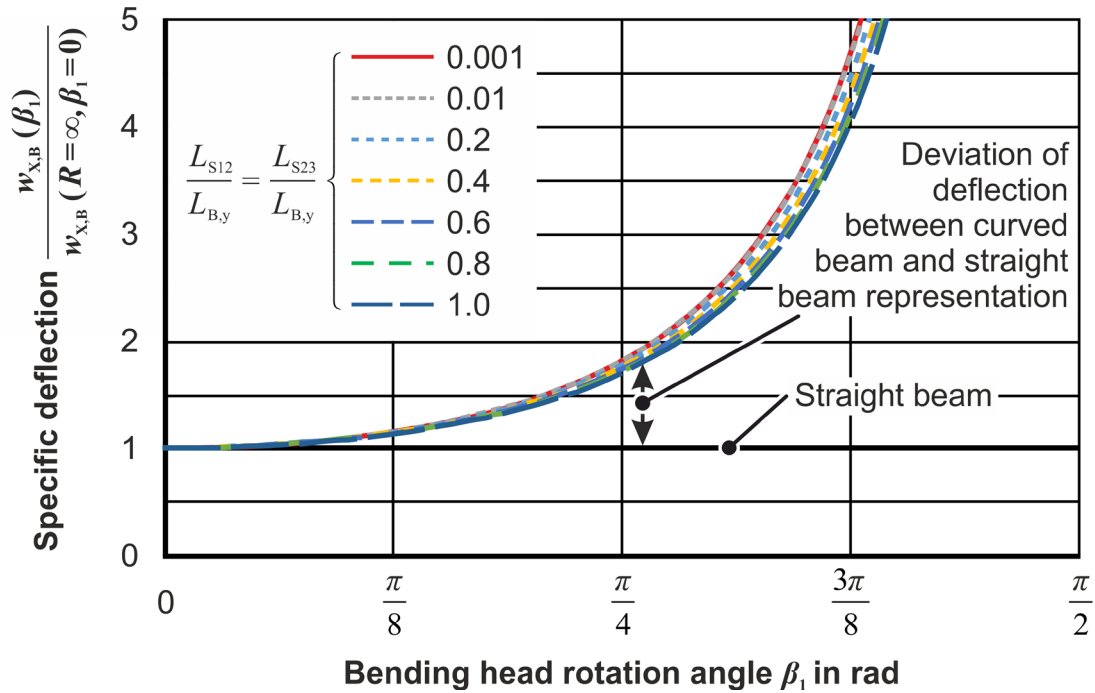
As explained in Section 6.2.1  $w_{xy,B}$  defines the repositioning of each infinitesimal point of the beam in normal direction to the beam's original geometry. In order to calculate the displacement along the  $X$ -axis  $w_{X,B}$  is calculated by Eq. (6.20). Figure 6.14 shows the specific deflection of a curved beam in relation to the rotation angle  $\beta_1$  for different ratios of  $L_{S12}/L_{B,y}$  and  $L_{S23}/L_{B,y}$ . Here, the ratios  $L_{S12}/L_{B,y} = L_{S23}/L_{B,y} = 0.001$  and  $0.01$  produce similar results as the specific deflection of the die-based support shown in Figure 6.7. If  $L_{S12}$  and  $L_{S23}$  have different lengths, then solely the ratio  $L_{S12}/L_{B,y}$  can be used to analyze the deviation between the curved beam model and the straight beam model, as the effect of  $L_{S12}$  on the deflection is much greater than the effect of  $L_{S23}$ .

Taking the distance  $L_{B,y}$  to be 396.92 mm, the ratio  $L_{S12}/L_{B,y} = 0.82$  and the ratio  $L_{S23}/L_{B,y} = 0.63$  as is the case in the 5-cDOF TSS bending machine, and a radius  $R$  of 2000 mm ( $\beta_1 = 0.200$ ), the difference between the calculated deflection using the curved beam representation and the straight beam representation is 3 %. At a radius of 1000 mm ( $\beta_1 = 0.408$ ) this deviation increases to 15 %, however. At 600 mm ( $\beta_1 = 0.723$ ) the deviation further increases to 57 %.

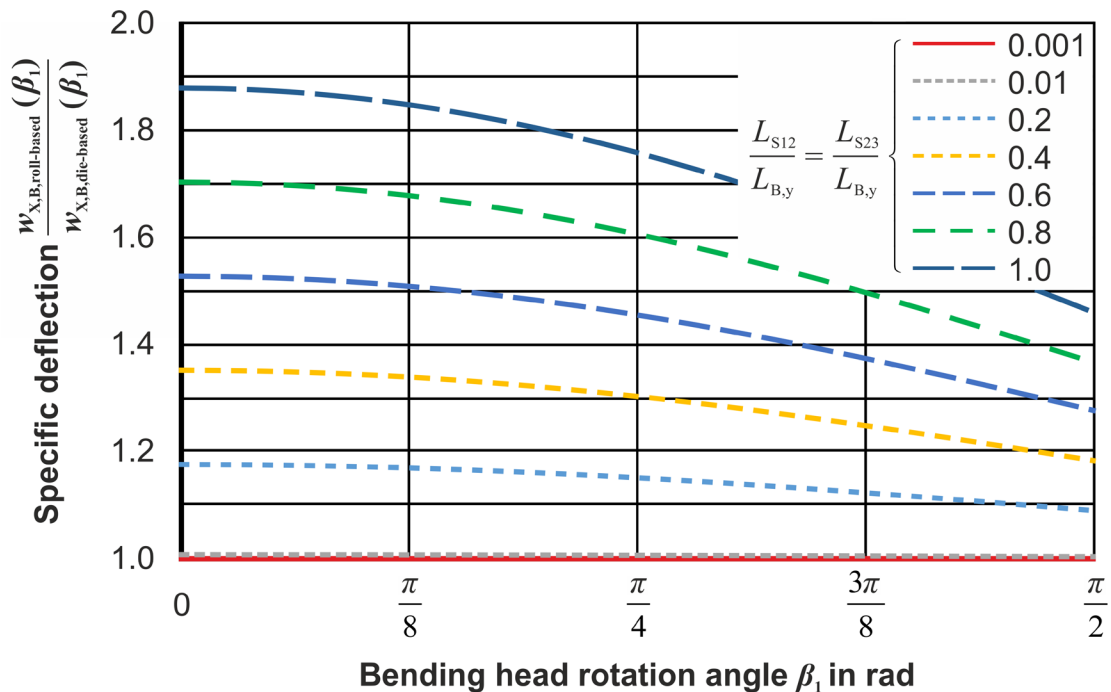
Since the calculation effort to set up a three-support beam model is quite extensive in comparison to a beam with a die-based support, it might seem attractive to simplify the three-support model and combine the supports into a full moment connection. This, however, produces quite high deviations as can be seen in Figure 6.15. As explained before, the ratios  $L_{S12}/L_{B,y} = L_{S23}/L_{B,y} = 0.001$  and  $0.01$  simulate a full moment connection quite satisfactorily. But already at ratios of 0.2 the three-support model calculates deflections that are up to 17 % higher than the die-based model. Considering the geometry of the 5-cDOF TSS bending machine and the radii 2000 mm ( $\beta_1 = 0.200$ ), 1000 mm ( $\beta_1 = 0.408$ ), and 600 mm ( $\beta_1 = 0.723$ ) the three-support model calculates deflections that are 70 %, 68 %, and 62 % higher, respectively.

Figure 6.16 shows the experimentally measured springback along the  $X$ -axis of profiles bent to the theoretical radii 600 mm, 800 mm, and 1000 mm in relation to analytically calculated beam deflection using a curved beam as described in this section and a straight beam as was done by Hermes (2011). The experimental data was gained by first bending a profile to the respective theoretical radius, then pausing the process, and finally relieving the profile by moving the bending head until the  $X$ -axis force sensor registered a remaining load of 0 N. The experimental deflection data was reduced by the deflection caused by machine stiffness (for the material MW700L Z1: 0.8 mm, for



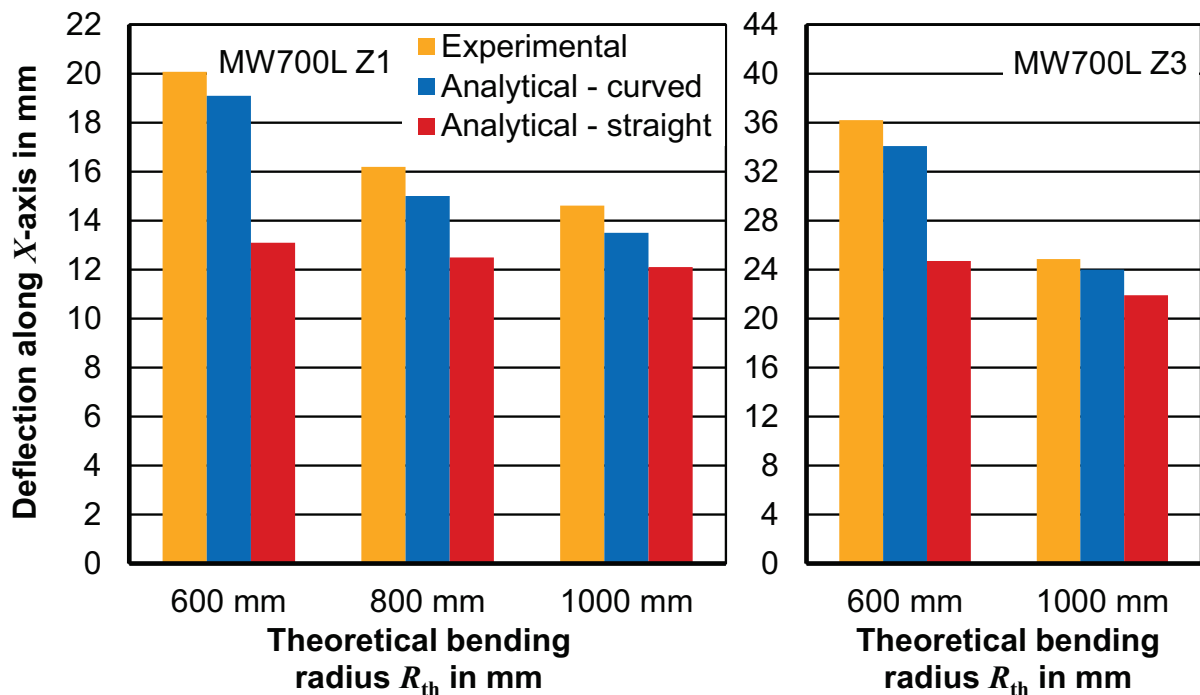


**Figure 6.14:** Specific deflection of curved beam over straight beam with 3 supports of varying distance in relation to the rotation angle  $\beta_1$



**Figure 6.15:** Specific deflection of curved beam with 3 supports of varying distance over curved beam with full moment connection in relation to  $\beta_1$

MW700L Z3: 2.0 mm at  $R_{th} = 1000$  mm and 2.5 mm at  $R_{th} = 600$  mm). Using Eq. (5.7) and reducing  $L_{B,X}$  by said reduced deflection, the theoretical unloaded radii 668.5 mm, 924.0 mm, and 1196 mm are calculated for MW700L Z1 and 745.2 mm and 1396 mm are calculated for MW700L Z3. These are the radii used in the beam deflection calculations, since the radius used in the analytical beam deflection calculation represents the unloaded radius. The Young's modulus degradation, described in Section 5.1 is taken into account by using the average true axial strain over the cross-section at each respective theoretical bending radius as  $\bar{\epsilon}_{pl}$ , thereby calculating a single Young's modulus for the whole cross-section. The resulting analytical beam deflections for the curved beam are in quite good agreement with the experimental data. For MW700L Z1 the deviation is 4.9 % for  $R_{th} = 600$  mm, 7.4 % for  $R_{th} = 800$  mm, and 7.6 % for  $R_{th} = 1000$  mm. In relation, the deviations for the straight beam model are 34.7 % for  $R_{th} = 600$  mm, 22.8 % for  $R_{th} = 800$  mm, and 17.2 % for  $R_{th} = 1000$  mm. As expected, the deviation is lower for larger radii and is predicted to converge with the curved model for  $R_{th} = \infty$ . For MW700L Z3 the deviation is 5.8 % for  $R_{th} = 600$  mm and 3.5 % for  $R_{th} = 1000$  mm. In relation, the deviations for the straight beam model are 31.8 % for  $R_{th} = 600$  mm and 11.9 % for  $R_{th} = 1000$  mm.



**Figure 6.16:** Experimental profile deflection caused by relieving a loaded profile during the bending process in comparison to analytical beam deflection calculations using a curved beam and a straight beam. Data for the materials MW700L Z1 and Z3 are shown.

### 6.3.2 Beam deflection in $z$ -direction

For the deflection in the  $z$ -direction, a set of three differential equations describes beam bending and the resulting deflection:

$$w''_{z,B,1}(s)EI = M_T \sin\left(\beta_1 - \frac{s}{R}\right) + F_{B,z}R \sin\left(\beta_1 - \frac{s}{R}\right) \quad (6.64)$$

$$w''_{z,B,2}(s)EI = M_T \sin\beta_1 \left(1 + \frac{s}{L_{S12}}\right) + F_{B,z}R \sin\beta_1 \left(1 + \frac{s}{L_{S12}}\right) - S_{3,z} \frac{L_{S23}}{L_{S12}} s \quad (6.65)$$

$$w''_{z,B,3}(s)EI = S_{3,z}(s + L_{S12} + L_{S23}) \quad (6.66)$$

As in Section 6.2.2, the twisting curved beam section also causes a deflection in  $z$ -direction. Since  $S_1$  takes up all torque around the  $y$ -axis, the same equations can be used to describe the deflection of the beam as in Section 6.2.2. Eq. (6.67) is equal to the sum of Eqs. (6.38) and (6.43):

$$w_{z,T,1}(s)GJ_T = F_{B,z}R^3 \left[ \frac{s}{R} - \sin\left(\frac{s}{R}\right) \right] + (F_{B,z}R^3 + M_T R^2) \left[ -\sin\left(\frac{s}{R} - \beta_1\right) + \frac{1}{4} \sin\left(2\frac{s}{R} - \beta_1\right) + \frac{1}{2} \frac{s}{R} \cos\beta_1 - \frac{3}{4} \sin\beta_1 \right] \quad (6.67)$$

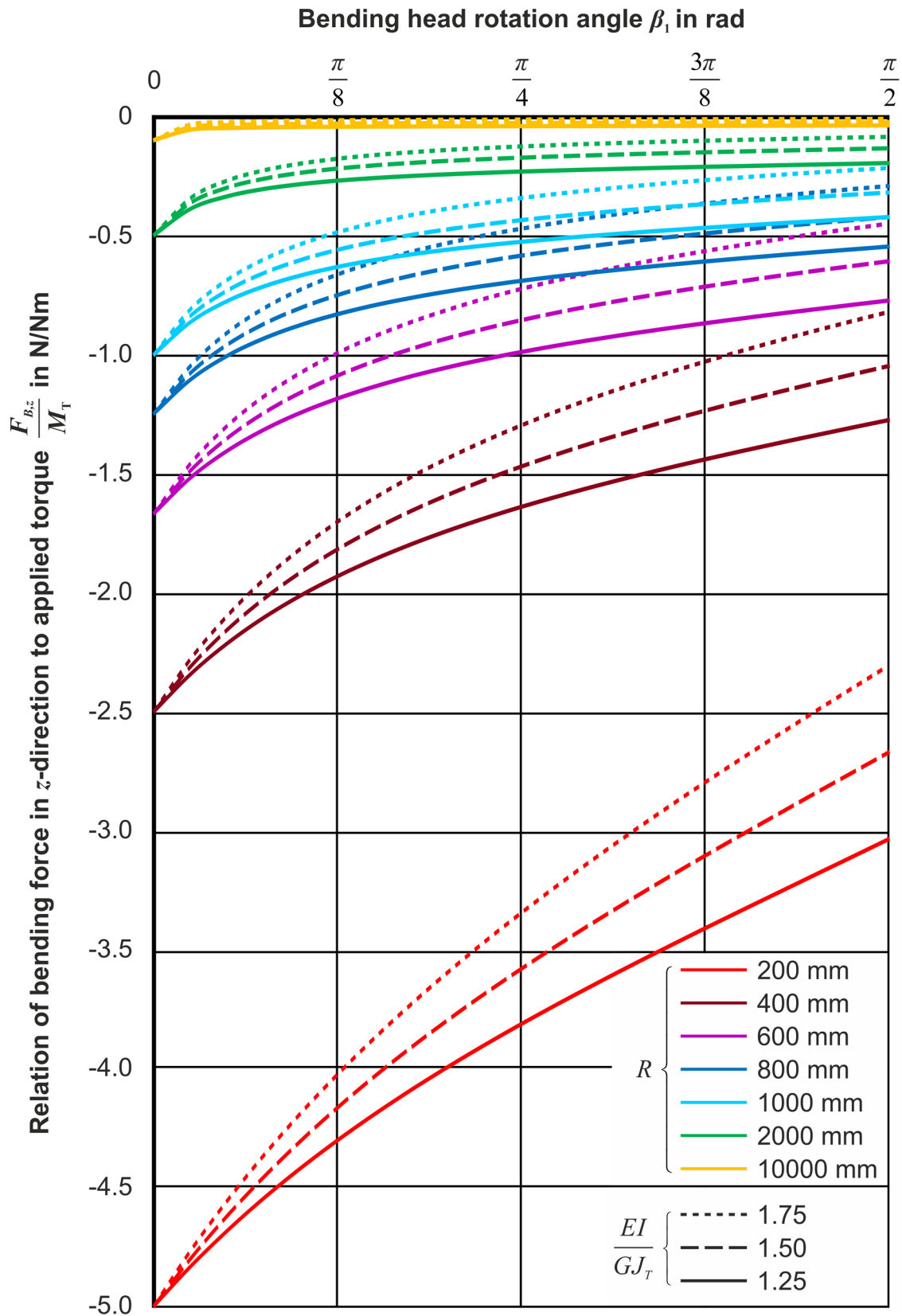
Together with the following boundary conditions in the  $z$ -direction:

$$\begin{aligned} w_{z,B,1}(s_1) + w_{z,T,1}(s_1) &= 0 \\ w_{z,B,1}(0) = w_{z,B,2}(0) = w_{z,B,2}(-L_{S12}) = w_{z,B,3}(-L_{S12}) = w_{z,B,3}(-L_{S12} - L_{S23}) &= 0 \\ w'_{z,B,1}(0) = w'_{z,B,2}(0) & \\ w'_{z,B,2}(-L_{S12}) = w'_{z,B,3}(-L_{S23}) & \end{aligned} \quad (6.68)$$

and using the method of superposition as for the die-based model in Section 6.2, the unknown forces  $F_{B,z}$  and  $S_{3,z}$  can be determined in terms of the applied torque  $M_T$ :

$$F_{B,z} = -\frac{M_T}{R} \left[ \frac{(\sin\beta_1 - \beta_1 \cos\beta_1 + \psi\beta_1) - \frac{EI}{2GI_p}(\sin\beta_1 - \beta_1 \cos\beta_1)}{(\sin\beta_1 - \beta_1 \cos\beta_1 + \psi\beta_1) - \frac{EI}{2GI_p}(3\sin\beta_1 - \beta_1 \cos\beta_1 - 2\beta_1)} \right] \quad (6.69)$$

$$S_{3,z} = -\frac{1}{2}(M_T + F_{B,z}R) \left[ \frac{L_{S12} \sin\beta_1}{L_{S23}(L_{S12} + L_{S23})} \right] \quad (6.70)$$



**Figure 6.17:** Ratio of bending force  $F_{B,z}$  to applied torque  $M_T$  for different radii and ratios of bending stiffness  $EI$  to torsional stiffness  $GJ_T$

with  $\psi$  from Eq. (6.63). It can be noticed that Eq. (6.69) is similar to Eq. (6.45) with the difference of the added term  $\psi$ , which introduces dependencies on the support lengths  $L_{S12}$  and  $L_{S23}$ . Figure 6.17 shows the relation of  $F_{B,z}$  to  $M_T$  in dependence of the beam radius  $R$ , the bending head angle  $\beta_1$ , and the ratio bending stiffness  $EI$  to torsional stiffness  $GJ_T$ . The lengths  $L_{S12} = 325$  mm and  $L_{S23} = 250$  mm were chosen to depict the 5-cDOF TSS bending machine geometry. Comparing Figure 6.17 with Figure 6.12 it can be directly noticed that the influence of the beam support has a dramatic influence on the ratio of  $F_{B,z}$  to  $M_T$ . While the maximum ratio in the full moment support model was -1.9 at a radius of 200 mm the ratio in the 3 support model is -5.0. Using a stiffness ratio of 1.74 as in Section 6.2.2 and a beam radius of 600 mm, the ratio of  $F_{B,z}$  to  $M_T$  is 0.76 1/m, at 800 mm the ratio is 0.59 1/m, and at 1000 mm the ratio is 0.48 1/m. Relative to the full moment support this means that the  $F_{B,z}$  values resulting from a torque application are between 3.6 and 3.7 times higher.

Because of its normal position to the bending force  $F_{B,xy}$ ,  $F_{B,z}$  causes the resultant of the bending force to rotate out of the  $xy$ -plane, resulting in a relocation of the bending plane. For 3D bending a rotating bending plane is absolutely necessary to produce 3D-shapes (see Section 3). If the profile is supposed to be bent in the  $xy$ -plane, however, and additionally twisted, the relocation of the bending plane is unwanted and needs to be predicted in order to be compensated. Figure 6.18 shows the bending plane rotations of three experimentally bent profiles. The profiles were bent to the theoretical plane radii  $R_{th} = 600$  mm, 800 mm, and 1000 mm and additionally twisted with 0.982 rad/m. During bending, the torque and the  $X$ -axis force were measured using the measurement setup described in Section 5.2.3. Using the 3D-contour sensor introduced in Section 5.3 the radius, the torsion, and the bending plane rotation was measured. To define the radius of the curved beam, necessary for the calculation of  $F_{B,z}$ , the radii measured in the loading and steady state region (see Section 5.4.1) were averaged to generate the parameter  $R_{meas,avg}$ . As applied torque, the peak torque measured at the end of the loading stage ( $M_{T,meas}$ ) was used. Because of the difficulties in the extraction of the bending force from experimental measurements as mentioned in Section 5.4, the comprehensive numerical model was used to extract the peak bending force data ( $F_{B,xy,num}$ ) in the loading stage. The low deviations between the numerically calculated peak torque ( $M_{T,num}$ ) and the experimentally measured peak torque ( $M_{T,meas}$ ) – 6.8 % at  $R_{th} = 600$  mm, 5.1 % at  $R_{th} = 800$  mm, and 1.6 % at  $R_{th} = 1000$  mm – support the applicability of the numerical force data (Table 6.1). The angle between the resultant of  $F_{B,xy,num}$  and  $F_{B,z}$  and the  $xy$ -plane is used to determine the angle  $\eta(s_{PS})$  between the machine bending plane  $M$  and the bending plane  $B$  at the profile support  $s_{PS}$  (see Section 4.2.3, Figure 4.11). In the beam calculations in this section the profile support  $S_1$  is positioned at  $s = 0$ . The values are stated in Table 6.1.

Table 6.1: Experimental and analytically calculated parameters for bending plane rotation analysis

$R_{th}$	$R_{meas,avg}$	$F_{B,xy,num}$	$M_{T,num}$	$M_{T,meas}$	$F_{B,z}$	$\eta(SPS)$
600 mm	723 mm	5106 N	963Nm	1033 Nm	-668.5 N	-0.130 rad
800 mm	960 mm	4901 N	1126 Nm	1071 Nm	-532.8 N	-0.108 rad
1000 mm	1265 mm	4739 N	1219 Nm	1200 Nm	-457.8 N	-0.096 rad

Since the  $\alpha_1$ -axis is not rotated, the difference between  $\eta$  and  $\theta$  (Eq. (4.75)) does not change. This means that the apparent twist  $d\phi_{\text{apparent}} = 0$ . According to Eq. (4.36) an apparent twist of 0 combined with a twist per unit length  $d\phi \neq 0$ , results in a bending plane rotation  $d\theta_r = d\phi$ . Hereby, the angle  $\eta$  introduces an additional constant offset of the cross-section.

The bending plane rotation, reduced by the machine stiffness, is calculated by:

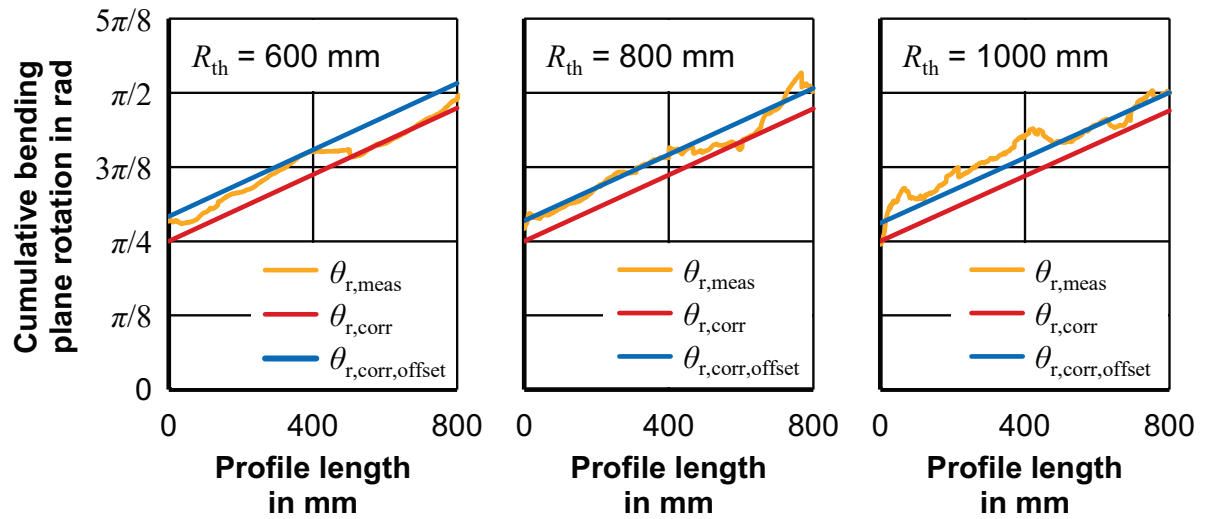
$$d\theta_{r,corr} = d\theta_r - \frac{M_T}{\underbrace{c_m \beta_1 R_{th}}_{\text{machine stiffness}}} \quad (6.71)$$

The term  $\eta$  offsets the bending plane as a whole and, as such, only appears in the calculation of the cumulative rotation. In order to know the initial bending plane orientation relative to the cross-section, the cross-section orientation  $\theta$  is additionally added:

$$\theta_{r,corr} = \int_0^s d\theta_{r,corr} + \theta \quad (6.72)$$

$$\theta_{r,corr,offset} = \theta_{r,corr} - \eta \quad (6.73)$$

Figure 6.18 shows the experimentally measured cumulative bending plane rotation in relation to the theoretical rotation reduced by the machine stiffness and the rotation additionally offset by  $\eta$ . In the present case  $\theta = \pi/4$ . On average, the measured cumulative rotation is in good agreement with the calculated rotation  $\theta_{r,corr,offset}$ . Using the instantaneous force and torque at every bending step would lead to improved local curve agreement. In order to model the profile behavior independently from experimental data, the bending force and torque, and especially the reciprocal effects that each load has on the other during simultaneous application, need to be investigated. The next section focuses on the analysis of stresses and strains during simultaneous bending and twisting and derives bending moment and torque calculations. As a final step the knowledge gained about plastic material behavior is combined with the knowledge on elastic behavior from this chapter and the knowledge about geometric shape definition from Chapter 3 into a comprehensive process model.



**Figure 6.18:** Experimental cumulative bending plane rotation in comparison to the theoretical bending plane rotation, reduced by the machine stiffness, and the offset





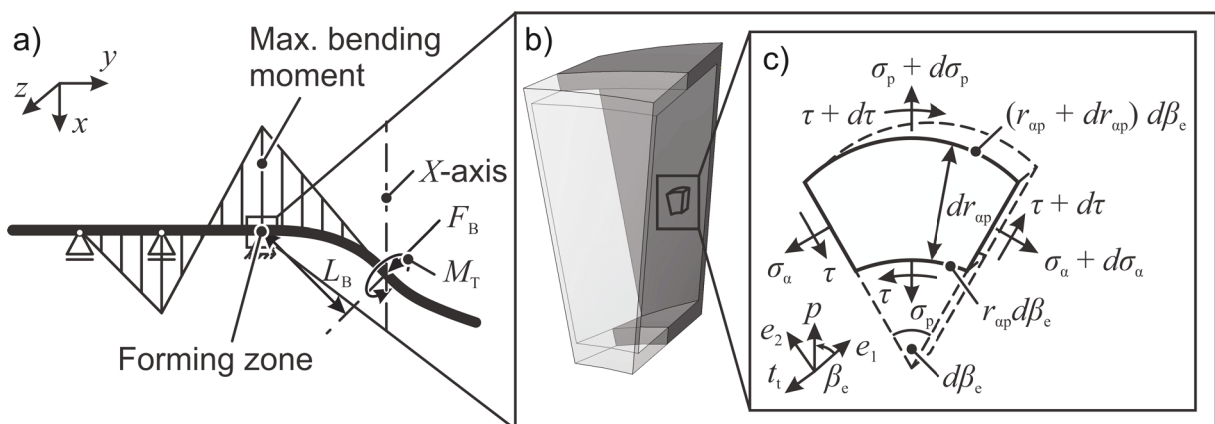
## 7 The reciprocal effects of bending and torsion during 3D profile bending

As described in Section 3, profiles with non-circular cross-sections can only be bent to arbitrary bending contours by changing the bending plane, while simultaneously controlling the torsion angle of the cross-section. By applying mechanical torsion to a profile, shear stresses are induced in the cross-section that interact with the axial stresses generated by the applied bending force. This fundamental aspect of 3D profile bending and its effect on the resulting bending curvature has until now been neglected in analytical process models and is addressed in the following sections.

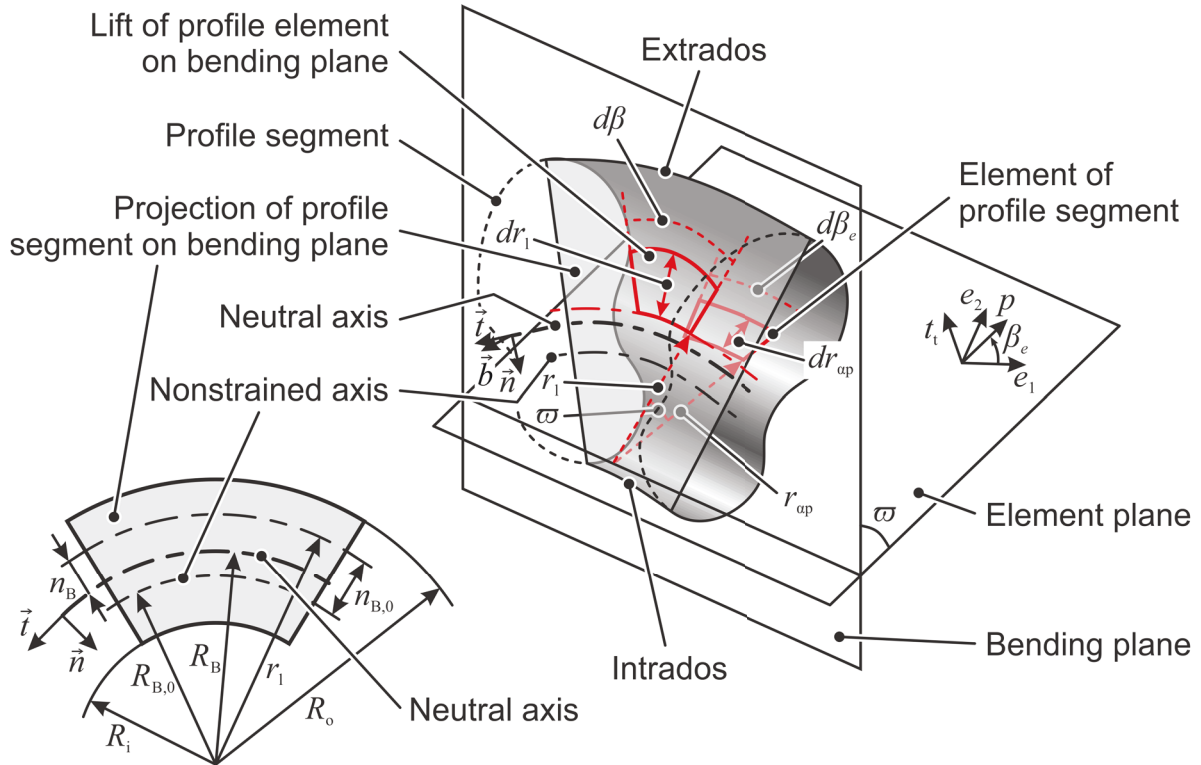
### 7.1 Analytical description of the states of strains and stresses

Figure 6.1 shows the qualitative trends of the bending moment for a 3D-bending process with a die support and roll-based support during bending. These trends can be directly linked to externally applied moments and forces. The challenge in 3D profile bending processes, actually the challenge in all bending processes, is that these forces and moments are initially unknown. What is known, however, is the target contour of the profile. This means that the final deformed geometry can be used to calculate the resistance of the profile against deformation, which, in effect causes the above-mentioned internal moments. These moments in turn cause springback, which is regarded in Chapter 6.

Because this work focuses on thin-walled profiles, plane stress is assumed as a first simplification. Figure 7.1 shows the stresses acting on a single element of a profile with an arbitrary cross-section. Here, the angle  $\beta_e$  describes the rotation around the normal vector of the element in the direction of the wall thickness  $t_t$ , while  $d\beta_e$  describes the incremental bending angle of said element.



**Figure 7.1:** a) simplified supported beam model of the process b) segment of the profile c) element of a profile segment



**Figure 7.2:** Relation of element plane to bending plane

Considering displacements and strains to be small leads to the following equilibrium conditions:

$$\sum F_p:$$

$$0 = -\sigma_p r_{ap} t d\beta_e + (\sigma_p + d\sigma_p)(r_{ap} + dr_{ap}) t d\beta_e - \sigma_\alpha dr_{ap} t d\beta_e - d\sigma_\alpha \frac{d\beta_e}{2} t dr_{ap} - \tau t dr_{ap} + (\tau + d\tau) t dr_{ap}$$

$$0 = \frac{d\sigma_p}{dr_{ap}} + \frac{1}{r_{ap}} \frac{d\tau}{d\beta_e} + \frac{\sigma_p - \sigma_\alpha}{r_{ap}} \quad (7.1)$$

$$\sum F_{\beta_e}:$$

$$0 = -\sigma_\alpha t dr_{ap} + (\sigma_\alpha + d\sigma_\alpha) t dr_{ap} + \tau \frac{d\beta_e}{2} t dr_{ap} + (\tau + d\tau) \frac{d\beta_e}{2} t dr_{ap} + \tau (r_{ap} + dr_{ap}) t d\beta_e + d\tau (r_{ap} + dr_{ap}) t d\beta_e - \tau r_{ap} t d\beta_e$$

$$0 = \frac{d\tau}{dr_{ap}} + \frac{1}{r_{ap}} \frac{d\sigma_\alpha}{d\beta_e} + \frac{2\tau}{r_{ap}} \quad (7.2)$$

The parameters of interest in Eqs. (7.1) and (7.2) are the axial stress  $\sigma_\alpha$ , the perimetral stress  $\sigma_p$ , and the shear stress  $\tau$ . The parameter  $r_{ap}$  describes the projection of the local

bending radius  $r_1$ , lying on the bending plane, onto the plane of the element, while  $dr_{ap}$  represents the height of the element (see Figure 7.2). The angle  $\varpi$  describes the angle between the element plane and the bending plane.

$$r_{ap} = \frac{r}{\cos \varpi} \quad (7.3)$$

$$dr_{ap} = \frac{dr_1}{\cos \varpi} \quad (7.4)$$

If  $r_{ap}$  and  $dr_{ap}$  in Eqs. (7.1) and (7.2) are replaced by Eqs. (7.3) and (7.4), then  $\cos \varpi$  appears in every term and can be cancelled. In order to be independent of  $d\beta_e$  in the following calculations, Eqs. (7.1) and (7.2) can be solved for  $d\beta_e$  and subsequently equated resulting in the following nonlinear differential equation:

$$0 = \frac{\sigma_\alpha}{d\tau} - \frac{\sigma_p}{d\tau} - \frac{r_1}{dr_1} \frac{d\sigma_p}{d\tau} + \frac{2\tau}{d\sigma_\alpha} + \frac{r_1}{dr_1} \frac{d\tau}{d\sigma_\alpha} \quad (7.5)$$

To be able to solve the above equation, a relation of the unknown stress values to plastic strain has to be established. Using the Levy-Mises flow rule, plastic strain increments can be set in relation to deviatoric stress:

$$\dot{\lambda} = \frac{\dot{\epsilon}_\alpha}{\sigma'_\alpha} = \frac{\dot{\epsilon}_p}{\sigma'_p} = \frac{\dot{\epsilon}_{ap}}{\tau'} = \frac{1}{2} \dot{\gamma} \quad (7.6)$$

With the stress tensor being:

$$\sigma_{ij} = \begin{bmatrix} \sigma_\alpha & \tau & 0 \\ \tau & \sigma_p & 0 \\ 0 & 0 & 0 \end{bmatrix} \quad (7.7)$$

The deviatoric stress tensor becomes:

$$\sigma'_{ij} = \sigma_{ij} - \sigma_{ij}^h \text{ with } \sigma_{ij}^h = \sigma_h \delta_{ij} = \frac{1}{3} \text{tr} \sigma_{ij} \delta_{ij} = \frac{1}{3} (\sigma_\alpha + \sigma_p) \delta_{ij} \quad (7.8)$$

$$\sigma'_{ij} = \begin{bmatrix} \frac{2}{3} \sigma_\alpha - \frac{1}{3} \sigma_p & \tau & 0 \\ \tau & \frac{2}{3} \sigma_p - \frac{1}{3} \sigma_\alpha & 0 \\ 0 & 0 & -\frac{1}{3} \sigma_\alpha - \frac{1}{3} \sigma_p \end{bmatrix} \quad (7.9)$$

By inserting the deviatoric stress values from Eq. (7.9) into Eq. (7.6), the following relationship can be found:

$$\tau = \frac{1}{6} \frac{\dot{\gamma}}{\dot{\epsilon}_\alpha} (2\sigma_\alpha - \sigma_p) \quad (7.10)$$

with its two partial derivatives:

$$d\tau = \frac{1}{3} \frac{\dot{\gamma}}{\dot{\epsilon}_\alpha} d\sigma_\alpha \quad (7.11)$$

$$d\tau = -\frac{1}{6} \frac{\dot{\gamma}}{\dot{\epsilon}_\alpha} d\sigma_p \quad (7.12)$$

Inserting Eqs. (7.10) and (7.12) into Eq. (7.5) leads to:

$$0 = \sigma_p \left( 1 + \frac{1}{9} \frac{\dot{\gamma}^2}{\dot{\epsilon}_\alpha^2} \right) - \sigma_\alpha \left( 1 + \frac{2}{9} \frac{\dot{\gamma}^2}{\dot{\epsilon}_\alpha^2} \right) + \frac{r_1}{dr_1} d\sigma_p \left( 1 + \frac{1}{18} \frac{\dot{\gamma}^2}{\dot{\epsilon}_\alpha^2} \right) \quad (7.13)$$

which can be rearranged to:

$$\frac{dr_1}{r_1} = \frac{\left( 1 + \frac{1}{18} \frac{\dot{\gamma}^2}{\dot{\epsilon}_\alpha^2} \right) d\sigma_p}{\sigma_\alpha \left( 1 + \frac{2}{9} \frac{\dot{\gamma}^2}{\dot{\epsilon}_\alpha^2} \right) - \sigma_p \left( 1 + \frac{1}{9} \frac{\dot{\gamma}^2}{\dot{\epsilon}_\alpha^2} \right)} \quad (7.14)$$

Integrating the above differential equation leads to the general solution containing the constant  $C_1$ :

$$C_1 r_1 = \left[ \sigma_p \left( 1 + \frac{1}{9} \frac{\dot{\gamma}^2}{\dot{\epsilon}_\alpha^2} \right) - \sigma_\alpha \left( 1 + \frac{2}{9} \frac{\dot{\gamma}^2}{\dot{\epsilon}_\alpha^2} \right) \right]^{\left( \frac{9\dot{\epsilon}_\alpha^2 + \frac{1}{2}\dot{\gamma}^2}{9\dot{\epsilon}_\alpha^2 + \dot{\gamma}^2} \right)} \quad (7.15)$$

The particular solutions can be found by considering the perimetral stress  $\sigma_p$  to be zero at the inner projected bending radius  $R_i$  and outer projected bending radius  $R_o$ :

$$\sigma_p = \sigma_\alpha \left( \frac{9\dot{\epsilon}_\alpha^2 + 2\dot{\gamma}^2}{9\dot{\epsilon}_\alpha^2 + \dot{\gamma}^2} \right) \left[ 1 - \left( \frac{R_{io}}{r_1} \right)^{\left( \frac{9\dot{\epsilon}_\alpha^2 + \dot{\gamma}^2}{9\dot{\epsilon}_\alpha^2 + \frac{1}{2}\dot{\gamma}^2} \right)} \right] \text{ with } R_{io} = \begin{cases} R_o & \text{for } r_1 > R_{B,0} \\ R_i & \text{for } r_1 < R_{B,0} \end{cases} \quad (7.16)$$

Based on the von Mises yield criterion, the flow stress can be described as:

$$\sigma_f^2 = \frac{1}{2} \left[ (\sigma_\alpha - \sigma_p)^2 + (\sigma_p - \sigma_t)^2 + (\sigma_t - \sigma_\alpha)^2 + 6(\tau_{\alpha p}^2 + \tau_{pt}^2 + \tau_{\alpha t}^2) \right] \quad (7.17)$$

Using the plane stress condition stated in Eq. (7.7), Eq. (7.17) simplifies to:

$$\sigma_f^2 = \sigma_\alpha^2 - \sigma_\alpha \sigma_p + \sigma_p^2 + 3\tau^2 \quad (7.18)$$

By inserting Eqs. (7.10) and (7.16) into Eq. (7.18) the axial stress  $\sigma_\alpha$  and the perimetral stress  $\sigma_p$  can be determined in terms of the axial strain increment  $\dot{\epsilon}_\alpha$ , the shear strain increment  $\dot{\gamma}$ , the flow stress  $\sigma_f$ , the local bending radius  $r_1$  and the projected inner and outer bending radii  $R_i$  and  $R_o$ :

$$\sigma_\alpha = \begin{cases} \frac{\sigma_f}{\sqrt{1 - \xi + \xi^2 + \frac{1}{12} \frac{\dot{\gamma}^2}{\dot{\epsilon}_\alpha^2} (2 - \xi)^2}} & \text{for } R_o \geq r_1 > R_{B,0} \\ -\frac{\sigma_f}{\sqrt{1 - \xi + \xi^2 + \frac{1}{12} \frac{\dot{\gamma}^2}{\dot{\epsilon}_\alpha^2} (2 - \xi)^2}} & \text{for } R_i \leq r_1 < R_{B,0} \end{cases} \quad (7.19)$$

$$\sigma_p = -\frac{\sigma_f}{\sqrt{1 + \frac{1 - \xi}{\xi^2} + \frac{1}{12} \frac{\dot{\gamma}^2}{\dot{\epsilon}_\alpha^2} \left(\frac{2 - \xi}{\xi}\right)^2}} \quad (7.20)$$

$$\text{with } \xi = \left( \frac{9\dot{\epsilon}_\alpha^2 + 2\dot{\gamma}^2}{9\dot{\epsilon}_\alpha^2 + \dot{\gamma}^2} \right) \left[ 1 - \left( \frac{R_{i0}}{r_1} \right)^{\left( \frac{9\dot{\epsilon}_\alpha^2 + \dot{\gamma}^2}{9\dot{\epsilon}_\alpha^2 + \frac{1}{2}\dot{\gamma}^2} \right)} \right] \text{ where } R_{i0} = \begin{cases} R_o & \text{for } r_1 > R_{B,0} \\ R_i & \text{for } r_1 < R_{B,0} \end{cases} \quad (7.21)$$

Inserting Eqs. (7.19) and (7.20) into Eq. (7.10) yields the shear stress  $\tau$ :

$$\tau = \frac{1}{6} \frac{\dot{\gamma}}{\dot{\epsilon}_\alpha} \left[ \frac{2\sigma_f}{\sqrt{1 - \xi + \xi^2 + \frac{1}{12} \frac{\dot{\gamma}^2}{\dot{\epsilon}_\alpha^2} (2 - \xi)^2}} - \frac{\sigma_f}{\sqrt{1 + \frac{1 - \xi}{\xi^2} + \frac{1}{12} \frac{\dot{\gamma}^2}{\dot{\epsilon}_\alpha^2} \left(\frac{2 - \xi}{\xi}\right)^2}} \right] \quad (7.22)$$

Up to now, the behavior of the flow stress, which depends on the equivalent plastic strain increment  $\dot{\epsilon}_{pl}$ , is unknown and, as a result, is derived in the following. Since plane stress is considered, the general state of strain increments can be described as follows:

$$\dot{\epsilon}_{ij} = \begin{bmatrix} \dot{\epsilon}_\alpha & \dot{\epsilon}_{\alpha p} & 0 \\ \dot{\epsilon}_{\alpha p} & \dot{\epsilon}_p & 0 \\ 0 & 0 & \dot{\epsilon}_t \end{bmatrix} = \begin{bmatrix} \dot{\epsilon}_\alpha & \frac{1}{2}\dot{\gamma} & 0 \\ \frac{1}{2}\dot{\gamma} & \dot{\epsilon}_p & 0 \\ 0 & 0 & \dot{\epsilon}_t \end{bmatrix} \quad (7.23)$$

As initially described, the target contour of the profile is supposed to be used to describe the local deformation acting on one element of the profile segment. From the torsion,

the shear strain of one element can be derived, while the curvature of the contour can be used to find the local bending radii and the axial strain. Strain in perimetral direction and in thickness direction are not targeted and, thus, unknown parameters. However, as described in Section 2.2, nearly all analytic approaches to describe tube and profile bending have regarded the bending process as being uniaxial with quite satisfactory results. A uniaxial stress state also results in a three-dimensional strain state but with considering volume constancy:

$$\dot{\varepsilon}_a + \dot{\varepsilon}_p + \dot{\varepsilon}_t = 0 \quad (7.24)$$

and isotropic material behavior, the state of strain increments simplifies to:

$$\dot{\varepsilon}_{ij} = \begin{bmatrix} \dot{\varepsilon}_a & \frac{1}{2}\dot{\gamma} & 0 \\ \frac{1}{2}\dot{\gamma} & -\frac{1}{2}\dot{\varepsilon}_a & 0 \\ 0 & 0 & -\frac{1}{2}\dot{\varepsilon}_a \end{bmatrix} \quad \text{with} \quad \dot{\varepsilon}_p = \dot{\varepsilon}_t = -\frac{1}{2}\dot{\varepsilon}_a \quad (7.25)$$

The equivalent plastic strain increment can, thus, be defined as:

$$\dot{\varepsilon}_{pl} = \sqrt{\frac{2}{3} \left[ \dot{\varepsilon}_a^2 + \dot{\varepsilon}_p^2 + \dot{\varepsilon}_t^2 + 2(\dot{\varepsilon}_{ap}^2 + \dot{\varepsilon}_{pt}^2 + \dot{\varepsilon}_{ta}^2) \right]} = \sqrt{\dot{\varepsilon}_a^2 + \frac{1}{3}\dot{\gamma}^2} \quad (7.26)$$

To be able to link the strain increments directly to the target contour to be bent, linear strain paths are considered. This means that strains are considered to increase with the same proportion until the final strain state is reached. Hereby, it is important to note that the individual strains reach their final states at the same time. From Eq. (7.6) it follows that:

$$\frac{\dot{\varepsilon}_a}{\dot{\gamma}} = \frac{\sigma'_a}{2\tau'} \quad (7.27)$$

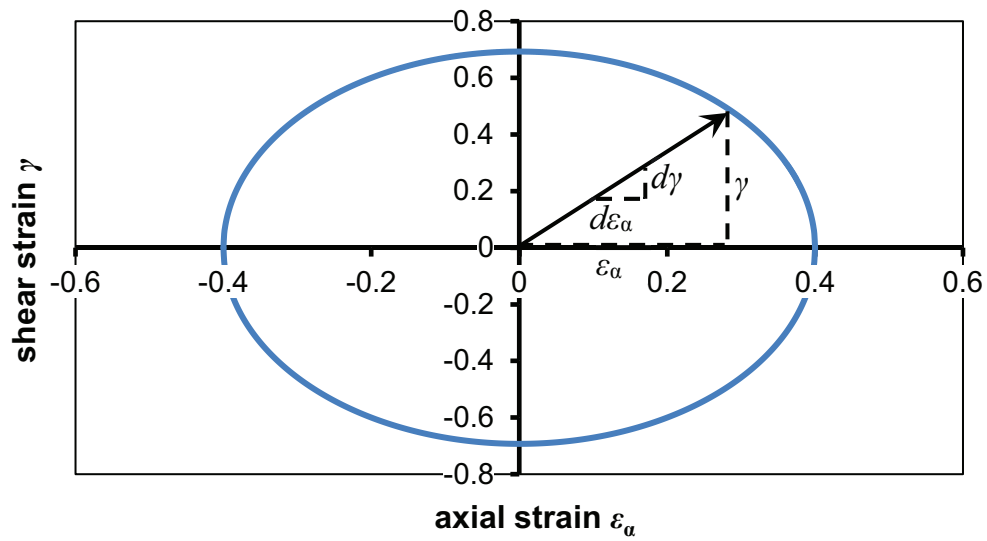
where:

$$\frac{\dot{\varepsilon}_a}{\dot{\gamma}} = \frac{\frac{d\varepsilon_a}{dt}}{\frac{d\gamma}{dt}} = \frac{d\varepsilon_a}{d\gamma} \quad (7.28)$$

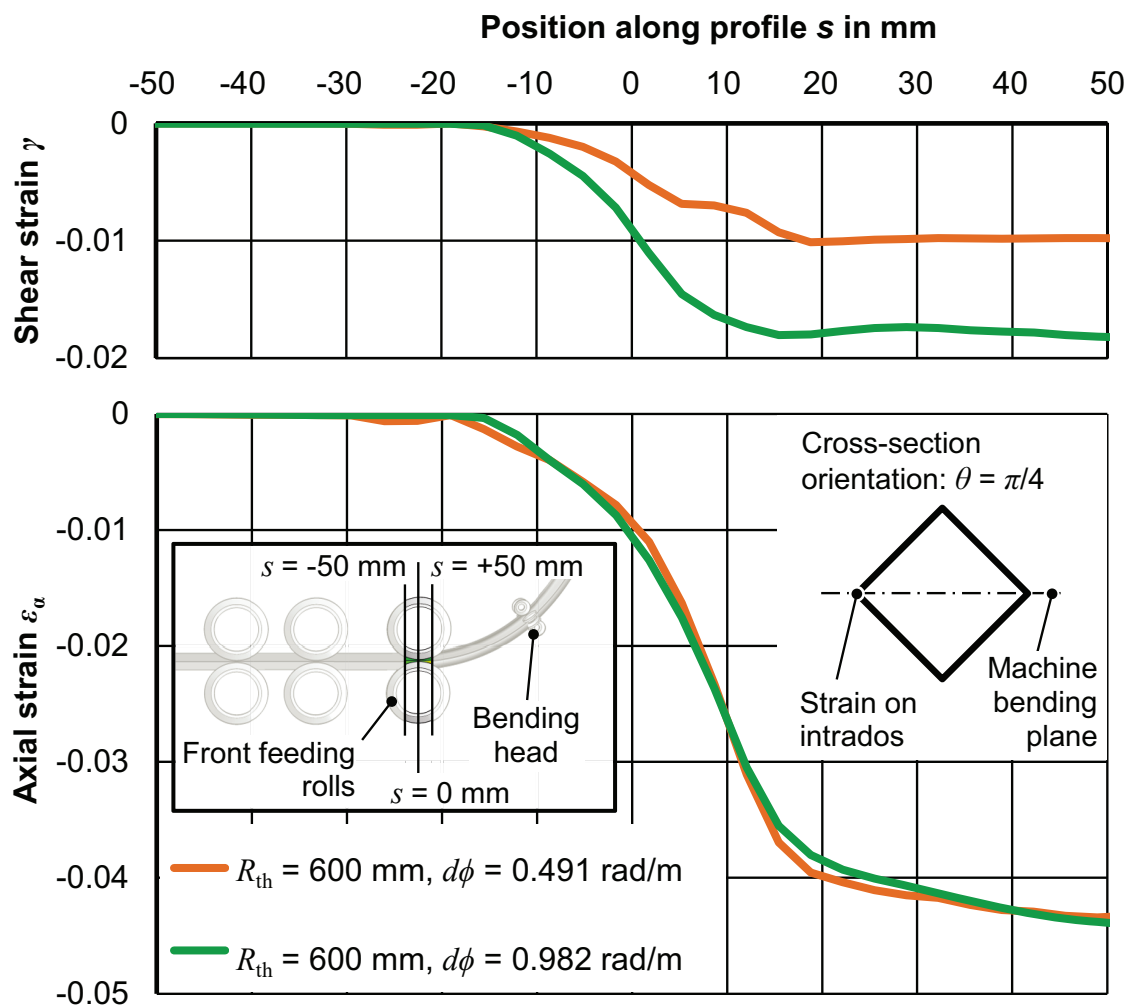
Linearizing the strain increment relationship leads to:

$$\frac{d\varepsilon_a}{d\gamma} = \frac{\varepsilon_a}{\gamma} \quad (7.29)$$

Graphically this relationship is pictured in Figure 7.3. To analyze the validity of the assumption of proportional deformation, the analytical simplification is compared to numerical strain data. Reliable experimental data for shear strain could not be obtained by digital image correlation due to a limited resolution of the available measurement



**Figure 7.3:** Assumption of proportional deformation during 3D bending



**Figure 7.4:** Numerical analysis of the axial and shear strain evolution in the forming zone for MW700L Z1 using the comprehensive numerical model

setup and the resulting high scatter. Therefore, it was only focused on the numerical data shown in Figure 7.4 calculated with the comprehensive numerical model described in Section 5.4.1. The axial and shear deformations evolve along the course of a hyperbolic tangent, which can be effectively linearized in the area surrounding its inflection point. Additionally, it can be seen that the shear deformation as well as the axial deformation begin and end at the same position along the profile. By regarding the feed rate, each position of the profile can be linked to a specific time step, leading to the conclusion that the shear and axial deformations reach their final states at the same time. A linearization of the strain paths, thus, is feasible. This leads to the following set of equations, which describe the stresses in an element of a profile segment purely in terms of deformation:

$$\sigma_\alpha = \begin{cases} \frac{\sigma_f(\bar{\varepsilon}_{pl})}{\sqrt{1-\xi+\xi^2+\frac{1}{12}\frac{\gamma^2}{\varepsilon_\alpha^2}(2-\xi)^2}} & \text{for } R_o \geq r_1 > R_{B,0} \\ -\frac{\sigma_f(\bar{\varepsilon}_{pl})}{\sqrt{1-\xi+\xi^2+\frac{1}{12}\frac{\gamma^2}{\varepsilon_\alpha^2}(2-\xi)^2}} & \text{for } R_i \leq r_1 < R_{B,0} \end{cases} \quad (7.30)$$

$$\sigma_p = -\frac{\sigma_f(\bar{\varepsilon}_{pl})}{\sqrt{1+\frac{1-\xi}{\xi^2}+\frac{1}{12}\frac{\gamma^2}{\varepsilon_\alpha^2}\left(\frac{2-\xi}{\xi}\right)^2}} \quad (7.31)$$

$$\tau = \frac{1}{6} \frac{\gamma}{\varepsilon_\alpha} \left[ \frac{2\sigma_f(\bar{\varepsilon}_{pl})}{\sqrt{1-\xi+\xi^2+\frac{1}{12}\frac{\gamma^2}{\varepsilon_\alpha^2}(2-\xi)^2}} - \frac{\sigma_f(\bar{\varepsilon}_{pl})}{\sqrt{1+\frac{1-\xi}{\xi^2}+\frac{1}{12}\frac{\gamma^2}{\varepsilon_\alpha^2}\left(\frac{2-\xi}{\xi}\right)^2}} \right] \quad (7.32)$$

with:

$$\xi = \left( \frac{9\varepsilon_\alpha^2 + 2\gamma^2}{9\varepsilon_\alpha^2 + \gamma^2} \right) \left[ 1 - \left( \frac{R_{io}}{r_1} \right)^{\left( \frac{9\varepsilon_\alpha^2 + \gamma^2}{9\varepsilon_\alpha^2 + \frac{1}{2}\gamma^2} \right)} \right] \quad \text{with } R = \begin{cases} R_o & \text{for } r_1 > R_{B,0} \\ R_i & \text{for } r_1 < R_{B,0} \end{cases} \quad (7.33)$$

and:

$$\bar{\varepsilon}_{pl} = \sqrt{\varepsilon_\alpha^2 + \frac{1}{3}\gamma^2} \quad (7.34)$$

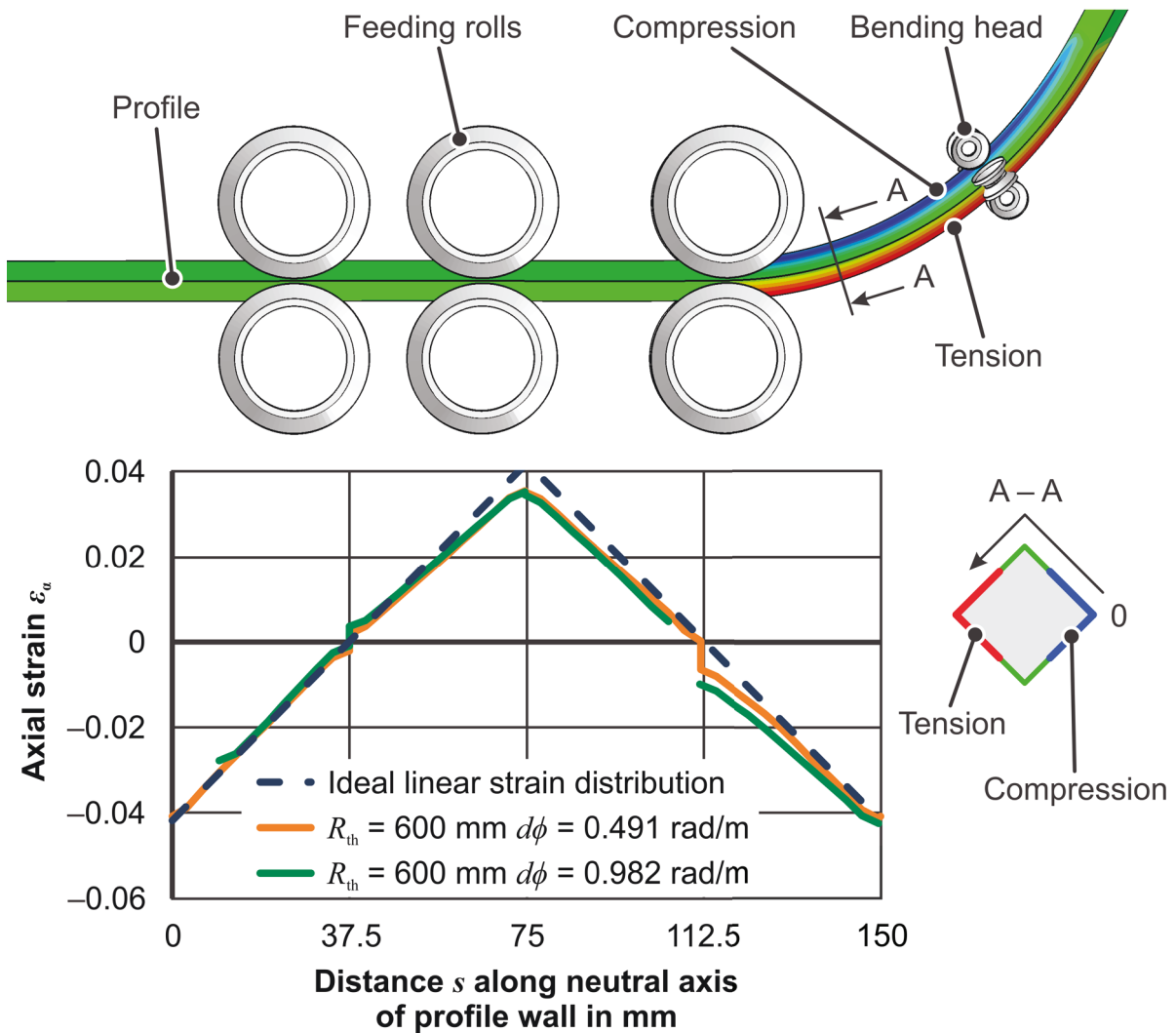


The flow stress  $\sigma_f(\bar{\varepsilon}_{pl})$  is calculated according to the flow curve approximations described in Section 5.1.

The next step is to set the strains in relation to the target contour of the profile. The general analytical approach in bending of sheets as well as tubes and profiles is to consider a linear increase of the axial strain from the neutral axis to the intrados and extrados, with respect to the bending plane, whereby a point symmetry is considered around the point lying on the neutral axis. As mentioned by Franz (1961), in plastic bending the neutral axis actually splits up into a remaining neutral axis with the radius  $R_B$  and a non-strained axis  $R_{B,0}$  with  $R_{B,0} < R_B$  (see Figure 7.2) to maintain the internal force equilibrium. The axial strain is considered to increase linearly from the non-strained axis to the intrados and to the extrados. If a single profile segment under pure bending is considered, such that its cross-section is staying plane and normal to the neutral axis, the slope of the engineering strain from the inner fiber to the outer fiber can be directly related to the bending radius. Inversely this means that if a specific bending radius is defined to which the segment is bent, only one single slope in axial strain over the profile height can result. The shift of the nonstrained axis inwards, hereby, only increases the length of the profile segment, not its bending radius, which is still defined by its neutral axis. In sheet metal bending, this lengthening of the segment is what necessitates a bend deduction during the preparation of the flat specimen. Strain calculations performed by Hill (1950) and Wang et al. (1993) for sheet metal bending, and by Hassan (2017) for rotary draw bending of tubes, actually do not consider this unchanging radius. They defined the maximum strain as the distance from the extrados to the nonstrained axis divided by  $R_{B,0}$  and the minimum strain as the distance from the intrados to the non-strained axis divided by  $R_{B,0}$ , accordingly. The linear slope between these two extrema actually defines a bending radius that is smaller than the one applied to the profile segment. It follows that in a calculation strategy, where the bending radius is used as a controlling parameter, this ratio cannot be used. To keep the slope constant, the strain actually needs to be set in relation to  $R_B$ :

$$\varepsilon_\alpha = \ln\left(1 + \frac{r_1 - R_{B,0}}{R_B}\right) = \ln\left(1 + \frac{n_{B,0}}{R_B}\right) \quad (7.35)$$

The parameter  $n_{B,0}$  describes the distance of a profile element from the non-strained axis, projected onto the bending plane. Numerical data, as shown in Figure 7.5, underline the validity of the hypothesis of a linear strain distribution between the non-strained axis and the extrados and intrados respectively.



**Figure 7.5:** Numerical analysis of the axial strain along the cross-section for MW700L Z1 using the comprehensive numerical model

## 7.2 Influence of perimetral stress on the bending process

Defining an element of a thin-walled tube or profile as a plane stress element, the perimetral stress can be split up in a radial component, lying in the bending plane, and a transverse component, normal to the bending plane. Franz (1961) stated a relation between radial force components and the ovalization of tubes. Paulsen and Welo (2001) analyzed cross-sectional deformation of tubes and profiles by directly regarding the acting perimetral stress. Their focus was on the analysis of bending processes that are greatly affected by cross-section deformation, namely rotary draw bending, stretch bending, and pure bending. In pure bending the forming zone is as large as the area of constant bending moment, leading to an equally constant cross-section deformation in this zone. The cross-section deformation is only hindered in the area of moment application by nondeformed profile segments. In stretch bending the size of the forming zone

or multiple forming zones vary according to the tool geometry, but the applied additional axial tension increases the perimetral stress and, thus, the radial stress components especially on the outer radius of the profile part. Rotary draw bending actually combines elements of pure bending and stretch bending together with bending radii as small as 0.7 times the diameter of the tube ( $0.7xD$ , only possible with a mandrel) (Chatti et al., 2012). The kinematics of the process, which is based on a moment being directly applied to the tube, results in a large forming zone (Hinkel, 2013). Additionally, tensile stresses can be superposed onto the outer radius by the pressure die, which has a similar effect on the radial stress components as in stretch bending.

In kinematic 3D bending processes, targeted bending radii are generally larger than in rotary draw bending. According to J. Neu GmbH, their machines can produce radii down to  $2xD$  (see Section 2.1.3). According to Figure 5.7, the minimum theoretical bending radius, which the 5-cDOF TSS profile bending machine can achieve in the case of arbitrary profile cross-sections, is  $5.5xD_P$  (at a  $D_P$  of  $55\sqrt{2}$  mm). At a  $D_P$  of 40 mm, the theoretical bending radius is equal to  $11xD_P$ , which was also experimentally observed by Staupendahl et al. (2014a) using  $40 \times 1.5$  mm tubes made from MW700L Z1 and Z3. But not only the produced radii are larger in kinematic 3D bending processes, also the forming zone is localized in a smaller region of the profile because the application of a single bending force results in a distinct maximum bending moment in the proximity of the profile support. The non-plastic profile segments surrounding the forming zone stabilize the plastic profile segment and, in turn, reduce cross-sectional deformation (Hermes, 2011).

So apart from cross-section deformation, which will not be covered in this work, the question arises if the occurring perimetral stress significantly affects the axial stress and the shear stress and, consequently, affects the bending outcome. From Eq. (7.18) it can be directly seen that the perimetral stress and the axial stress influence each other more than they do the shear stress. Thus, the following analyses solely focus on the interaction of perimetral and axial stress.

Setting the shear strain  $\gamma$  in Eqs. (7.30), (7.31), and (7.33) to zero, they simplify to:

$$\sigma_\alpha = \begin{cases} \frac{\sigma_f(\varepsilon_\alpha)}{\sqrt{1 + \frac{R_o^2 - r_1 R_o}{r_1^2}}} & \text{for } R_o \geq r_1 > R_{B,0} \\ -\frac{\sigma_f(\varepsilon_\alpha)}{\sqrt{1 + \frac{R_i^2 - r_1 R_i}{r_1^2}}} & \text{for } R_i \leq r_1 < R_{B,0} \end{cases} \quad (7.36)$$

and:

$$\sigma_p = - \begin{cases} \frac{\sigma_f(\varepsilon_\alpha)}{\sqrt{1 + \frac{r_1 R_o}{(r_1 - R_o)^2}}} & \text{for } R_o \geq r_1 > R_{B,0} \\ \frac{\sigma_f(\varepsilon_\alpha)}{\sqrt{1 + \frac{r_1 R_i}{(r_1 - R_i)^2}}} & \text{for } R_i \leq r_1 < R_{B,0} \end{cases} \quad (7.37)$$

To be able to solve Eqs. (7.36) and (7.37),  $R_{B,0}$  needs to be found. As stated before,  $R_{B,0}$  describes the axis, around which the internal forces and moments equalize. Now, the axial stress distribution could be used together with the geometry of a specific profile to calculate the bending moment  $M_{B,o}$  generated by the profile elements in the area greater than  $R_b$  and the bending moment  $M_{B,i}$  generated by the profile elements in the area smaller than  $R_B$ .  $R_{B,0}$  could then be found in an iterative process by minimizing the difference between  $M_{B,o}$  and  $M_{B,i}$ . However, since the perimetral stress is caused by the profile elements in the profile area smaller than  $R_{B,0}$  pushing outward and the profile elements in the profile area greater than  $R_{B,0}$  pushing inward, the stress caused by the inner elements and outer elements must be equal at  $R_{B,0}$ . Thus, by directly equating both cases of Eq. (7.37) and setting  $r_1 = R_{B,0}$ , the radius of the non-strained axis is found:

$$R_{B,0} = \sqrt{R_i R_o} \quad (7.38)$$

Although, starting with a plane stress model, this formula is actually equal to the one used to find the non-strained axis in sheet metal bending, which is derived from a plane strain formulation (Ismar and Mahrenholtz, 1979).

### 7.2.1 Normalized stress-strain relationship

Eqs. (7.36) and (7.37) describe the axial and perimetral stress solely in terms of the radii on the bending plane (radius of the non-strained axis  $R_{B,0}$ , inner radius  $R_i$ , outer radius  $R_o$ , and local bending radius  $r_1$ ). The equations are independent from the cross-section geometry. By stating the bending radius  $R_B$  as a multiple of the profile height  $D_P$ :

$$R_B = \rho D_P \quad \text{with} \quad D_P = R_o - R_i \quad (7.39)$$

Eqs. (7.36) and (7.37) can even be set independent from a specific bending radius and profile height. By rearranging Eqs. (7.38) and (7.39) and normalizing the distance of a profile element to the neutral axis  $n_N$  to the range  $[-1, 1]$ , with  $-1$  describing the location of the intrados and  $1$  that of the extrados, the location of the non-strained axis is

defined by:

$$n_{N,0} = \sqrt{4\rho^2 - 1} - 2\rho \quad (7.40)$$

The axial and the perimetral stress can, thus, be described by:

$$\sigma_\alpha = \begin{cases} \frac{\sigma_f(\varepsilon_\alpha)}{\sqrt{1 + \frac{(2\rho+1)^2 - (2\rho+n_N)(2\rho+1)}{(2\rho+n_N)^2}}} & \text{for } 1 \geq n_N \geq \sqrt{4\rho^2 - 1} - 2\rho \\ -\frac{\sigma_f(\varepsilon_\alpha)}{\sqrt{1 + \frac{(2\rho-1)^2 - (2\rho+n_N)(2\rho-1)}{(2\rho+n_N)^2}}} & \text{for } -1 \leq n_N < \sqrt{4\rho^2 - 1} - 2\rho \end{cases} \quad (7.41)$$

$$\sigma_p = - \begin{cases} \frac{\sigma_f(\varepsilon_\alpha)}{\sqrt{1 + \frac{(2\rho+n_N)(2\rho+1)}{(n_N-1)^2}}} & \text{for } 1 \geq n_N \geq \sqrt{4\rho^2 - 1} - 2\rho \\ \frac{\sigma_f(\varepsilon_\alpha)}{\sqrt{1 + \frac{(2\rho+n_N)(2\rho-1)}{(n_N+1)^2}}} & \text{for } -1 \leq n_N < \sqrt{4\rho^2 - 1} - 2\rho \end{cases} \quad (7.42)$$

with:

$$\varepsilon_\alpha = \ln \left( 2 + \frac{n_N - \sqrt{4\rho^2 - 1}}{2\rho} \right) \quad (7.43)$$

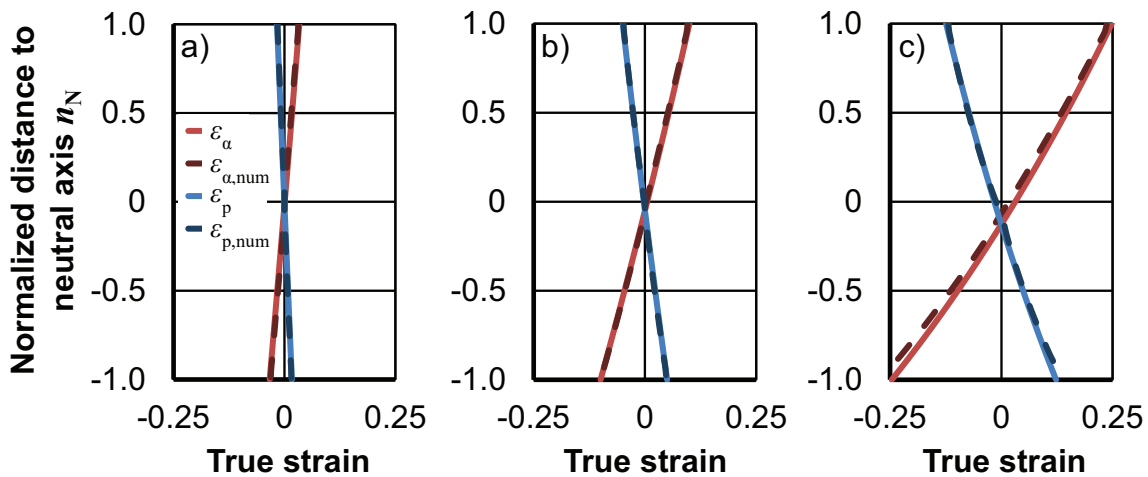
Using the relation of strain rates stated in Eq. (7.25) and the assumption of proportional deformation introduced in Section 7.1, the strains in perimetral as well as in thickness direction can be described as:

$$\varepsilon_p = \varepsilon_t = -\frac{1}{2} \ln \left( 2 + \frac{n_N - \sqrt{4\rho^2 - 1}}{2\rho} \right) \quad (7.44)$$

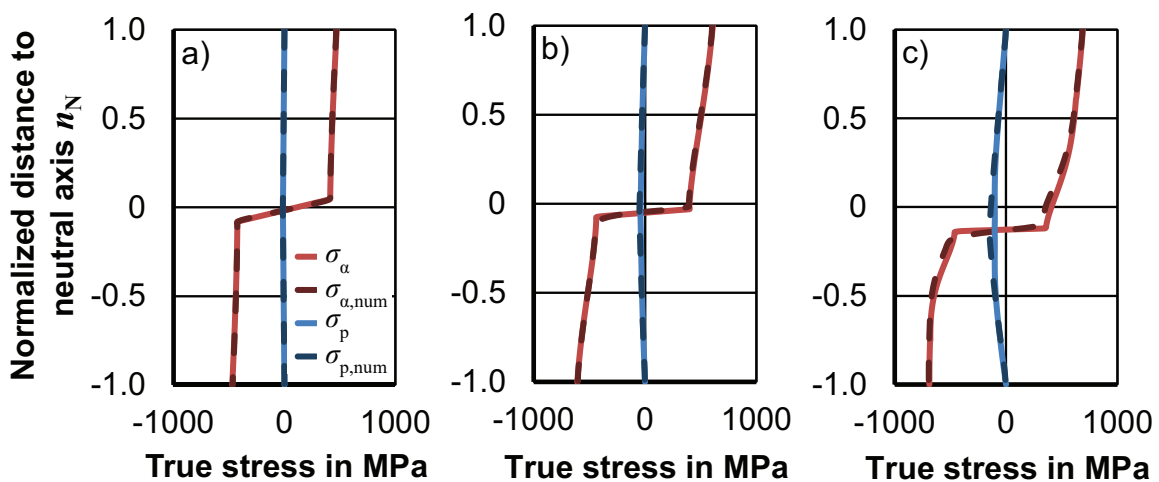
Eqs. (7.41) to (7.44) thus describe the stresses and strains in a profile with an arbitrary cross-section but point symmetrical to the neutral axis.

To quantify the reciprocal influence of the perimetral stress and the axial stress during bending, Eqs. (7.41) to (7.44) are solved for significant values of  $\rho$ . Based on the previously mentioned minimal bending radii of available 3D profile bending processes, bending radii of  $15xD_P$ ,  $5xD_P$ , and  $2xD_P$  are chosen. To validate the results without the influences of friction, contact pressure, and shear, an implicit plane stress FE-model of a pure

bending process is used. The geometrical proportions and boundary conditions were based on a plane strain model by Weinrich (2015). As such, the length of the specimen was set to be 5 times longer than the profile height in order to have a large region in the middle of the profile not affected by the constrained profile ends. The profile height was set to 40 mm and a wall-thickness of 2.5 mm was chosen. The mesh size was defined as 1.0 mm with a linear decrease to 0.2 mm at the neutral axis. The pure bending process was realized by fully constraining one end of the profile, while applying a rotation to a rigid part connected to the other. The rotation was applied at the point of the rigid part lying on the neutral axis of the profile. Figure 7.6 shows the axial and radial strain distribution while Figure 7.7 shows the axial and radial stress distribution for said bending radii. To validate the analytical calculation, the results are shown in comparison to values generated with the plane stress FE-model using material data of MW700L Z1.



**Figure 7.6:** Axial and perimetral strain distribution over a normalized profile height for different ratios of  $R_B$  to  $D_p$ : a)  $\rho = 15$  b)  $\rho = 5$  c)  $\rho = 2$



**Figure 7.7:** Axial and perimetral stress distribution over a normalized profile height for different ratios of  $R_B$  to  $D_p$ : a)  $\rho = 15$  b)  $\rho = 5$  c)  $\rho = 2$

Figures 7.6 and 7.7 show a high agreement between the analytical and numerical stress and strain results. The low deviation supports the hypothesis of a linear nominal strain distribution over the cross-section. Additionally, the assumption of an equal true strain in thickness and in perimetral direction as introduced in Eq. (7.25) is backed. Only at  $\rho = 2$  the analytically calculated position of the non-strained axis deviates noticeable from the numerically calculated axis. This difference can be related to the fact that in the analytical calculation, the total height change of the profile is not regarded. As a result, the nonstrained axis falls together with the nonstressed axis, while in the FE-model, the non-strained and non-stressed axes diverge at lower values of  $\rho$  (see Table 7.1). As seen in Figure 7.7, this simplification actually does not have a significant impact on the resulting stress distribution.

**Table 7.1:** Normalized shift of nonstrained and nonstressed axes

	$\rho = 15$	$\rho = 10$	$\rho = 5$	$\rho = 2$
Analytical nonstrained=nonstressed	-0.017	-0.025	-0.050	-0.127
Numerical nonstressed	-0.016	-0.025	-0.035	-0.144
Numerical nonstrained	-0.015	-0.029	-0.044	-0.080

### 7.2.2 Impact of the neutral axis shift on the bending moment

The most obvious impact of the additional consideration of perimetral stress during bending is the shift of the non-strained axis towards the intrados. Additionally, the axial stress above the non-strained axis is lower in proximity to said axis, while the axial stress is higher below and in proximity to the non-strained axis compared to a uniaxial approach. The differences are shown in Figure 7.8. Here, the uniaxial stress distribution is simply calculated by:

$$\sigma_a = \sigma_f(\varepsilon_a) \quad (7.45)$$

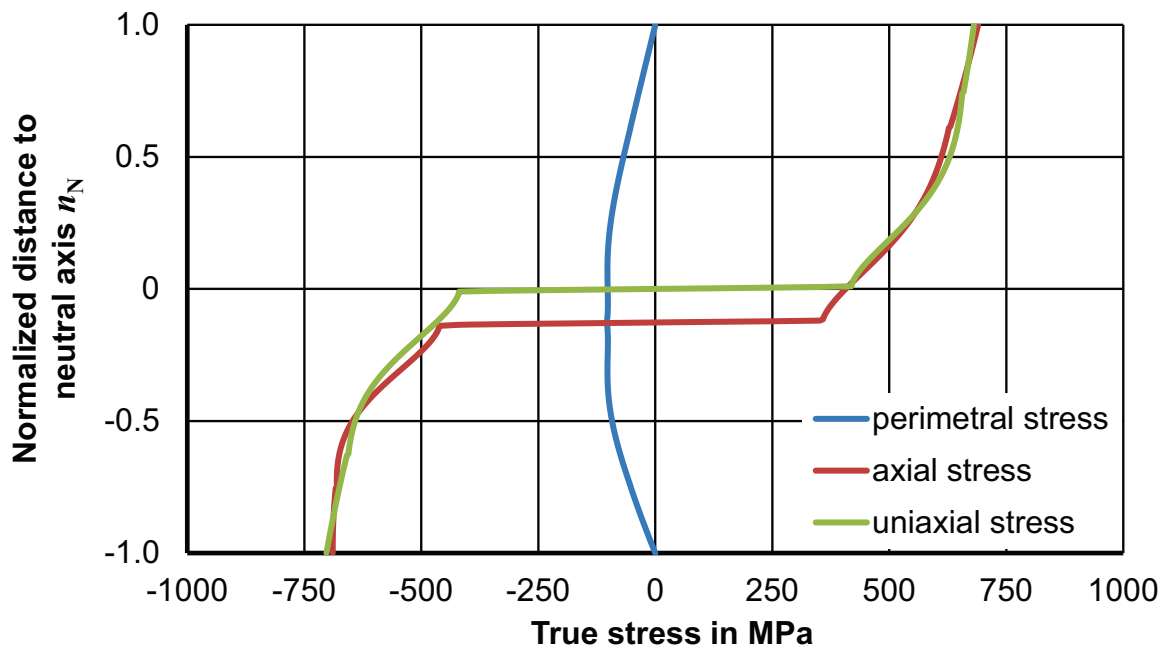
which is essentially mapping the flow curve over the profile height as described in the elementary bending theory. The question now is if this axis shift and stress shift towards the compressive region is relevant for bending moment calculations.

Regarding a normalized profile, the bending moment is calculated as follows:

$$M_B = \int_A \sigma_\alpha(n_N) n_N dA = \underbrace{\int_{-1}^{\sqrt{4\rho^2-1-2\rho}} \sigma_\alpha(n_N) n_N dA}_{M_{B,comp}} + \underbrace{\int_{\sqrt{4\rho^2-1-2\rho}}^1 \sigma_\alpha(n_N) n_N dA}_{M_{B,tens}} \quad (7.46)$$

With the consideration of a uniaxial stress distribution, Eq. (7.46) simplifies to:

$$M_B = \int_A \sigma_\alpha(n_N) n_N dA = \underbrace{\int_{-1}^0 \sigma_\alpha(n_N) n_N dA}_{M_{B,comp}} + \underbrace{\int_0^1 \sigma_\alpha(n_N) n_N dA}_{M_{B,tens}} \quad (7.47)$$



**Figure 7.8:** Difference in stress distribution between a uniaxial stress assumption and a plane stress assumption at  $\rho = 2$  using material data of MW700L Z1 and the numerical model described in Section 7.2.1

In both of the equations,  $dA$  describes a section of the profile cross-section of infinitesimal height. In practice, the nondeformed cross-section is generally used to set up  $dA$ . Additionally, when bending profiles with point symmetric cross-sections, the stress distribution over the cross-section is generally considered point symmetric as well. Using the latter assumption, Eq. (7.46) simplifies to:

$$M_B = 2 \underbrace{\int_0^1 \sigma_\alpha(n_N) n_N dA}_{M_{B,tens}} \quad (7.48)$$

Commonly, Eqs. (7.47) and (7.48) are integrated over the nondeformed cross-section while at the same time assuming a true stress distribution. A more obvious choice would



be to combine the nondeformed, or nominal area, with the nominal stress, but the common practice has proven to lead to acceptable results over a multitude of  $\rho$  values and in modelling different bending processes – form-bound as well as kinematic (see Section 2.2).

Table 7.2 compares the accuracies of different calculation strategies using a normalized profile with a constant mass distribution over the profile height for different values of  $\rho$ . These values can be assigned to hollow cross-sections with a near constant mass distribution as, for instance, square profiles bent over their diagonal axes or non-hollow rectangular profiles bent over their normal axes. Hollow profiles with arbitrary cross-sections tend to have an increasing mass distribution from the neutral axis to the intrados and extrados, with the exact distribution depending on the shape of the cross-section. However, also in the case of arbitrary cross-sections Table 7.2 can be used for a qualitative assessment of the strategies' performance.

**Table 7.2:** Deviation of analytical bending moment calculated using different strategies in relation to numerical data

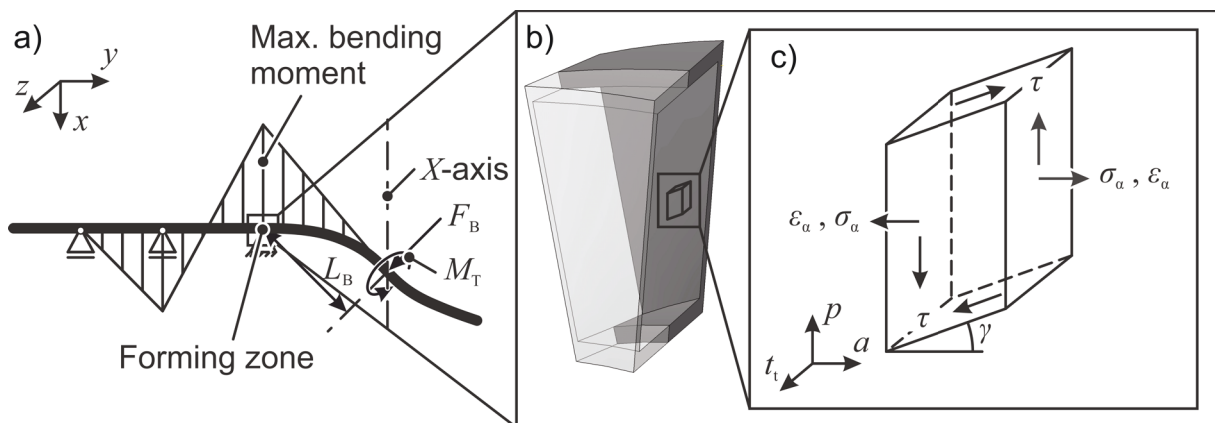
Analytical bending moment calculation strategies			$\rho = 25$	$\rho = 15$	$\rho = 10$	$\rho = 5$	$\rho = 2$
1	Plane stress	<ul style="list-style-type: none"> <li>• True stress</li> <li>• True <math>dA</math></li> </ul>	0.3 %	0.8 %	0.8 %	1.0 %	0.9 %
2	Uniaxial $2M_{B,tens}$	<ul style="list-style-type: none"> <li>• True stress</li> <li>• Nominal <math>dA</math></li> </ul>	0.3 %	0.7 %	0.6 %	0.6 %	2.3 %
3	Uniaxial $2M_{B,tens}$	<ul style="list-style-type: none"> <li>• Nominal stress</li> <li>• Nominal <math>dA</math></li> </ul>	-1.0 %	-1.5 %	-2.7 %	-5.9 %	-12.5 %
4	Uniaxial $2M_{B,tens}$	<ul style="list-style-type: none"> <li>• True stress</li> <li>• True <math>dA</math></li> </ul>					
5	Uniaxial $M_{B,tens} + M_{B,comp}$	<ul style="list-style-type: none"> <li>• True stress</li> <li>• Nominal <math>dA</math></li> </ul>	0.3 %	0.8 %	0.9 %	1.4 %	3.4 %
6	Uniaxial $M_{B,tens} + M_{B,comp}$	<ul style="list-style-type: none"> <li>• Nominal stress</li> <li>• Nominal <math>dA</math></li> </ul>	0.4 %	0.9 %	1.1 %	2.0 %	7.2 %
7	Uniaxial $M_{B,tens} + M_{B,comp}$	<ul style="list-style-type: none"> <li>• True stress</li> <li>• True <math>dA</math></li> </ul>					

Table 7.2 was generated using the numerical model described in Section 7.2.1 and the hardening behavior of the material MW700L Z1 given by Eq. (5.2), which incorporates an elongated yield point and significant material hardening. In comparison, using an elastic-ideally plastic material behavior, at  $\rho = 2$  the deviation between calculation strategies 1 and 2 increases by 1 % while the deviation to strategies 3 and 4 actually reduces by 1.2 %. At increasing values of  $\rho$ , these deviations exponentially decrease with negligible differences at values of  $\rho$  greater 10. The impact on the deviations of strategies 5, 6 and 7 are negligible at all values of  $\rho$  between 2 and 25.

As a conclusion, it can be stated that the bending moments calculated via strategies 2 and 5 most closely resemble the results of the comprehensive plane stress calculation (strategy 1), with strategy 2 producing slightly lower results at  $\rho$  values equal and higher than 5, and with strategy 5 producing slightly higher results in that same range. At values of  $\rho$  lower than 5, the results gained via strategies 2 and 5 diverge significantly from the results gained via the plane stress calculation. In comparison to the plane stress calculation, the uniaxial stress calculation is much simpler to handle, especially in combination with integrating  $dA$  over the original cross-section to gain the bending moment. As a result, it is recommended to use calculation strategy 2 for point symmetrical cross-sections, while strategy 5 is recommended for non-symmetrical cross-sections. The usage of these simplified calculations should be limited to  $\rho$  values equal or higher than 5 in order to keep calculation errors negligible.

### 7.3 Influence of torsion on the bending process

From the outcome of Section 7.2 it can be deduced that for  $\rho$  values equal or higher than 5, perimetral stress can be neglected without causing significant errors in bending moment calculations. Thus, the complex state of stresses acting on a single element of a profile, as shown in Figure 7.1, can be simplified to the state shown in Figure 7.9. Instead of regarding a curved element, the element can be simplified as a parallelepiped.



**Figure 7.9:** a) simplified supported beam model of the process b) segment of the profile c) element of a profile segment

The force equilibria along the  $p$ -axis as well as the  $a$ -axis, hereby, result in no geometric dependency of the axial stress  $\sigma_a$  and the shear stress  $\tau$ . As a result, the interaction of the two parameters can solely be defined by the von Mises yield criterion and the Levy-Mises flow rule. Using the simplified stress state *uniaxial stress + shear*, the stress tensor, set up in Section 7.1, simplifies to:

$$\sigma_{ij} = \begin{bmatrix} \sigma_a & \tau & 0 \\ \tau & 0 & 0 \\ 0 & 0 & 0 \end{bmatrix} \quad (7.49)$$

resulting in the following deviatoric stress tensor:

$$\sigma'_{ij} = \begin{bmatrix} \frac{2}{3}\sigma_a & \tau & 0 \\ \tau & -\frac{1}{3}\sigma_a & 0 \\ 0 & 0 & -\frac{1}{3}\sigma_a \end{bmatrix} \quad (7.50)$$

The Levy-Mises flow rule:

$$\dot{\lambda} = \frac{\dot{\epsilon}_a}{\sigma'_a} = \frac{\frac{1}{2}\dot{\gamma}}{\tau'} \quad (7.51)$$

can be used together with the simplification of linear strain paths from Section 7.1 to define  $\tau$  as a function of  $\sigma_a$ :

$$\tau = \frac{1}{3} \frac{\gamma}{\epsilon_a} \sigma_a \quad (7.52)$$

Inserting Eq. (7.52) into the von Mises yield criterion:

$$\sigma_f \left( \bar{\epsilon}_{pl} \right)^2 = \sigma_a^2 + 3\tau^2 \quad (7.53)$$

yields the following set of equations:

$$\sigma_a = \frac{\sigma_f \left( \bar{\epsilon}_{pl} \right)}{\sqrt{1 + \frac{1}{3} \frac{\gamma^2}{\epsilon_a^2}}} \quad (7.54)$$

$$\tau = \frac{\sigma_f \left( \bar{\epsilon}_{pl} \right)}{\sqrt{3 + 9 \frac{\epsilon_a^2}{\gamma^2}}} \quad (7.55)$$

For  $\bar{\varepsilon}_{pl}$ , Eq. (7.34) from Section 7.1 is used. In Section 7.1 it was also shown that the axial strain  $\varepsilon_\alpha$  can be directly related to the bending radius by Eq. (7.35). Since there is no shift in the nonstrained axis in a uniaxial calculation approach, Eq. (7.35) simplifies to the generally known term:

$$\varepsilon_\alpha = \ln\left(1 + \frac{r_1 - R_B}{R_B}\right) = \ln\left(1 + \frac{n_B}{R_B}\right) \quad (7.56)$$

The question that now arises is how the nominal shear strain  $\gamma$  can be related to the torsion of the profile.

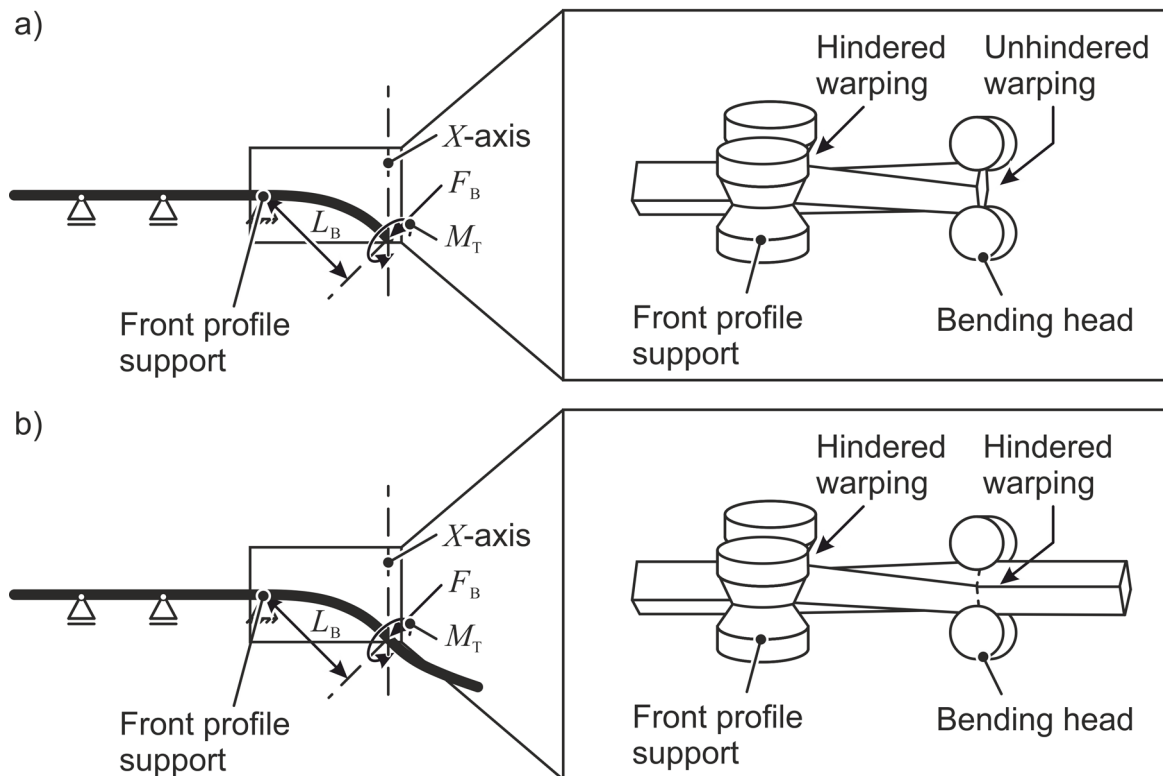
### 7.3.1 Analytical description of pure torsion

Pure torsion of solid profiles with a constant cross-section can be described by the Saint Venant formulation (Saint Venant, 1855). This formulation considers warping of the cross-section in axial direction of the profile to be irrelevant in the calculation of the shear stresses. To apply the theory, the following requirements have to be fulfilled:

- The profile is able to warp freely over the regarded profile length
- Possibly occurring warping is constant over the profile length
- The outer contour of the cross-section is considered to not change
- Twisting only occurs around the longitudinal axis whereby the rotational center has to be able to position itself
- The twist per unit length  $d\phi$  over the longitudinal axis is constant

The first requirement can actually not be fulfilled in 3D bending. At least one end of the profile section being twisted is hindered in its possible warping. If the location of the twisted profile region is directly at the front end of the profile, said end is free to deform in axial direction during moment application by the bending head, while axial warping is hindered at the end held in the profile support by the remaining nondeformed profile directly behind this support. If a twisted region is supposed to be generated in a middle section of the profile then the axial warping is actually hindered at both ends of the twisted profile. Figure 7.10 reflects both stated cases.

But not all cross-sections actually warp when twisted. And if the cross-section does not warp, then it makes no difference if the profile can warp freely or not. The most simple geometry, a cylinder – hollow as well as full – does, for instance, not warp. But there are several other warp-free cross-sections that are especially relevant for 3D profile bending. Figure 7.11 shows an overview of different cross-sections and their tendency to warp. Besides circular cross-sections (a-1), all regular polygons with a constant wall-thickness are warp-free (a-2). In these cases, the center of area  $c_a$  coincides with the shear center  $c_s$ . Additionally, all polygons are warp-free that fulfill the following requirement (a-3) (Roik, 1978): Two vectors are set up in each vertex so that their starting



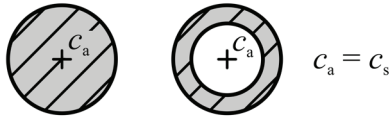
**Figure 7.10:** a) Hindered warping at one end of the profile b) hindered warping at both ends of the profile

point is in the vertex itself and their direction is each parallel to an adjoining side of the polygon. The length of each vector represents the wall thickness of the side of the polygon that it is lying on. If the resultants, set up by the two vectors in each vertex all intersect at a single point, then the cross-section is warp-free. For a rectangular profile with opposite sides of equal wall-thickness, this definition can be specified by saying: if the ratio of the two wall-thicknesses is equal to the ratio of the corresponding side lengths, then the rectangular cross-section is warp free. Also, open thin-walled profiles are warp free that are made up of members that all intersect in one single point (a-4). All of these described shapes are only warp-free if the center of rotation lies on the shear center point  $c_s$ . (Francke and Friemann, 2005)

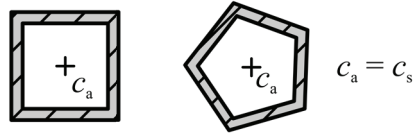
Cross-sections that do warp can be differentiated into two groups. The first group is comprised of arbitrary closed profiles – both solid and hollow. The second group is comprised of arbitrary open profiles that do not fulfil the requirement of having one common intersection point of all of its members. Although, both of these groups do warp, the deformation is small in the case of closed arbitrary profiles and can be neglected according to EN 1993-1-1, Abs. 6.2.7 (7) (Lohse et al., 2016). It can be concluded that, with the exception of arbitrary open shapes and combined open-closed shapes, the Saint Venant formulation can be applied to the profiles relevant for 3D bending.

**a) Warp-free cross-sections**

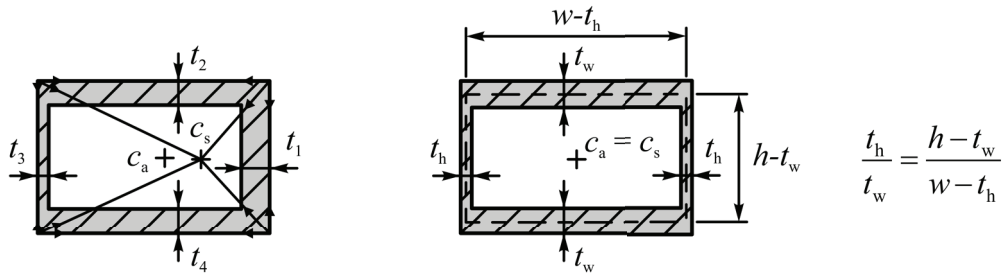
1) Rotationally symmetric



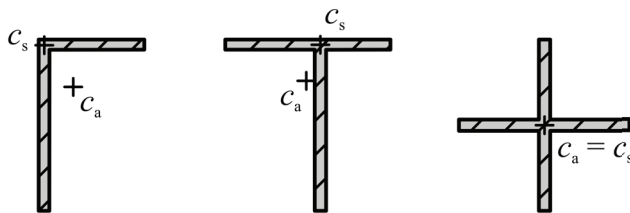
2) Thin-walled regular polygons,  $t = \text{const.}$



3) Thin-walled polygons with specific wall-thickness distributions

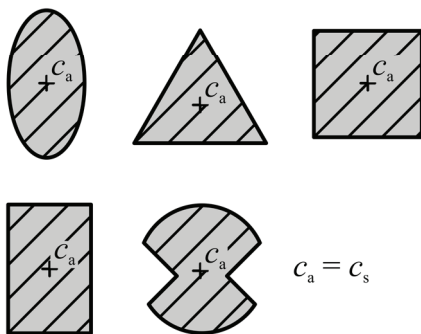


4) Open cross-sections with members intersecting in single point

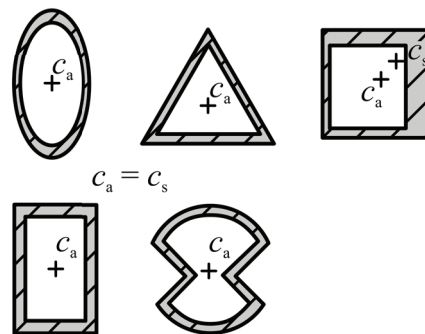


**b) Cross-sections with minor warping**

1) Solid cross-sections



2) Hollow cross-sections



**Figure 7.11:** Warp-free cross sections and cross sections with minor warping (Extended representation of results by Francke and Friemann (2005), Roik (1978), and Lohse et al. (2016))

If an arbitrary hollow profile is regarded (Figure 7.12), the displacement vector of a differential element at the position  $s$  of the cross-section can be described as:

$$\bar{u}(s) = \underbrace{u(s)\bar{e}_{y_{cs}}}_{\substack{\text{Longitudinal} \\ \text{displacement} \\ \text{(causes warping)}}} + \underbrace{\phi(y_{cs})(\bar{e}_{y_{cs}} \times \bar{r}_{cs}(s))}_{\substack{\text{In-plane} \\ \text{displacement}}} \quad (7.57)$$

where  $\phi(y_{cs})$  describes the angle of twist along the longitudinal axis  $y_{cs}$ . To calculate the displacement in tangential direction, the in-plane displacement term is multiplied by the tangent unit vector  $e_p$  and rearranged:

$$v_p = \phi(y_{cs})(\bar{e}_{y_{cs}} \times \bar{r}_{cs}(s)) \cdot \bar{e}_p = \phi(y_{cs})\bar{e}_{y_{cs}} \cdot (\bar{r}_{cs}(s) \times \bar{e}_p) \quad (7.58)$$

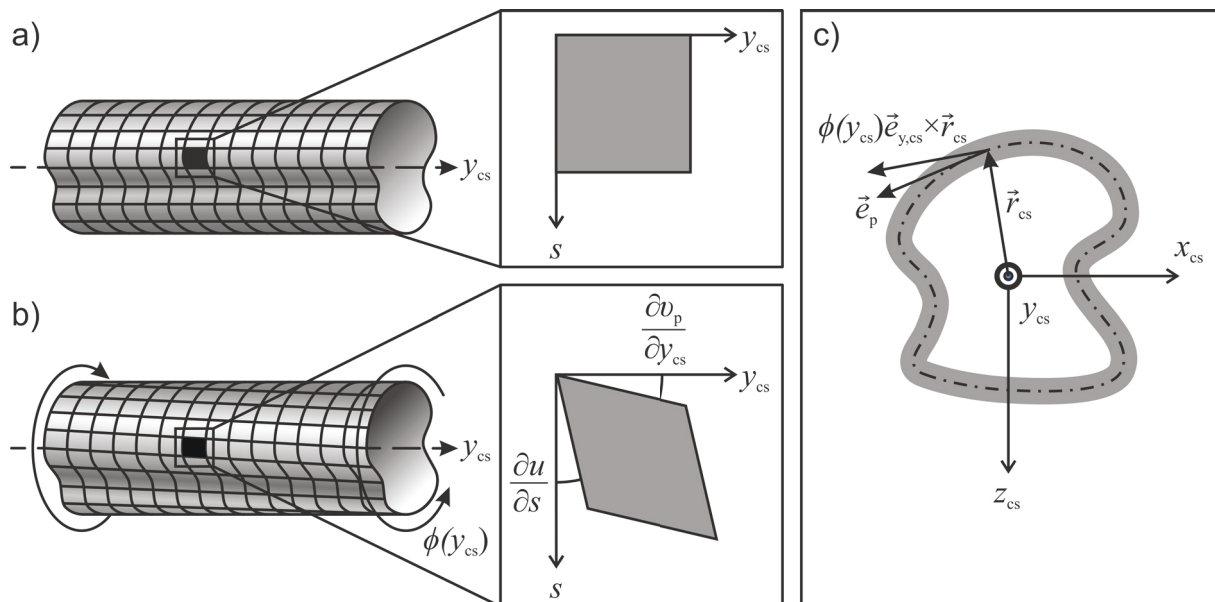
The term:

$$r_{\perp}(s) = \bar{e}_{y_{cs}} \cdot (\bar{r}_{cs}(s) \times \bar{e}_p) \quad (7.59)$$

is a scalar describing the perpendicular distance of the vector  $\bar{e}_p$  at the differential element to the centroid. Using  $r_{\perp}(s)$  as the moment arm, the total torque caused by twisting the profile can be calculated by:

$$M_T = \int_{s=0}^P \tau(s) t r_{\perp}(s) ds \quad (7.60)$$

If the shear stress is assumed constant over  $s$  and  $\frac{1}{2}r_{\perp}(s)ds$  is considered a differential



**Figure 7.12:** a) Arbitrary hollow profile b) arbitrary hollow profile with applied twist c) cross-sectional view of the profile

segment of the cross-sectional surface enclosed by the middle axis of the wall  $A_m$ , then Eq. (7.60) can be rewritten as:

$$M_T = \tau t_t \int_{s=0}^P r_{\perp}(s) ds = 2\tau t_t A_m \quad (7.61)$$

Eq. (7.61) essentially is the first formulation by Bredt (1896). Assuming small displacements and no warping, the shear strain can be described as:

$$\gamma = \left( \underbrace{\frac{\partial u}{\partial s}}_{=0} + \frac{\partial v_p}{\partial y_{cs}} \right) = \phi'(y_{cs}) r_{\perp}(s) \quad (7.62)$$

no warping

Regarding the twist per unit length  $\phi'(y_{cs})$  to be constant over  $y_{cs}$ , the relation of  $\gamma$  to  $\phi'(y_{cs})$  can also be expressed as the more figurative:

$$\gamma dy_{cs} = d\phi(y_{cs}) r_{\perp}(s) \quad (7.63)$$

$$\gamma = \frac{d\phi(y_{cs})}{dy_{cs}} r_{\perp}(s) \quad (7.64)$$

Graphically, this relation is presented in Figure 7.13. The integration of the local shear strains over the perimeter can, as the torque in Eq. (7.61), be related to the area  $A_m$ :

$$\int_{s=0}^P \gamma ds = \int_{s=0}^P [\phi'(y_{cs}) r_{\perp}(s)] ds = 2\phi'(y_{cs}) A_m \quad (7.65)$$

and by dividing this term by the length of the neutral axis of the wall  $P$ , the average shear strain can be written as:

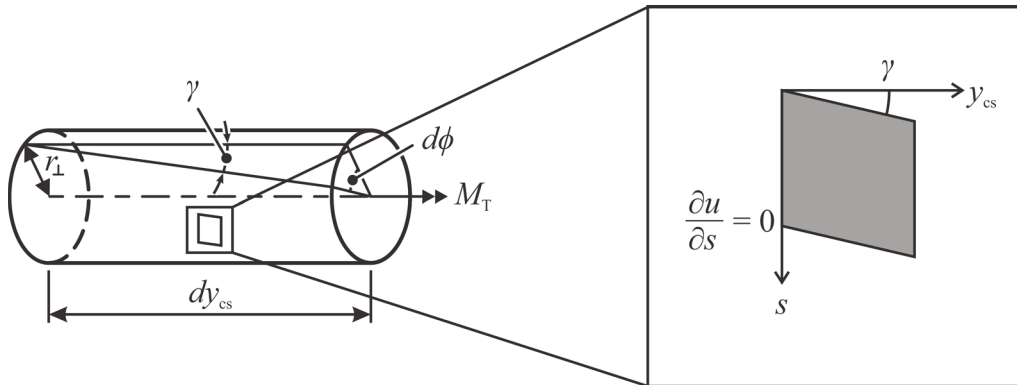
$$\gamma_{\text{avg}} = \phi'(y_{cs}) \frac{2A_m}{P} = \phi'(y_{cs}) \frac{J_T}{W_T} \quad (7.66)$$

Hereby,  $J_T$  is the torsional constant, which in the case of a circular cross-section is equal to the polar moment of inertia, and  $W_T$  is the torsional section modulus. In the case of a rectangular profile with the profile height  $h$ , the profile width  $w$ , and the wall-thickness  $t_t$ , Eq. (7.66) can be specified as:

$$\gamma_{\text{avg}} = \phi'(y_{cs}) \frac{(w-t_t)(h-t_t)}{w+h-2t_t} \quad (7.67)$$

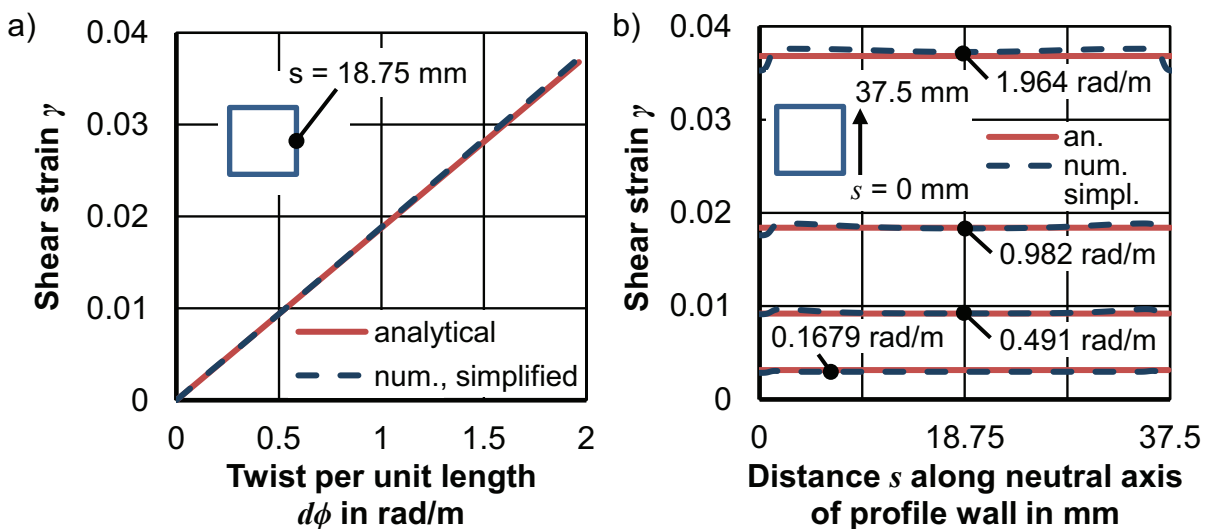
In the case of warp-free pure torsional deformation,  $\gamma$  is equal to  $\gamma_{\text{avg}}$  and, thus, constant over  $s$ . To confirm the validity of Eq. (7.67), the analytic shear strain is compared to numerical strain data calculated with the simplified implicit plane stress FE-model described in Section 5.4.2. As in Section 7.2.1, the model regards a 200 mm long profile



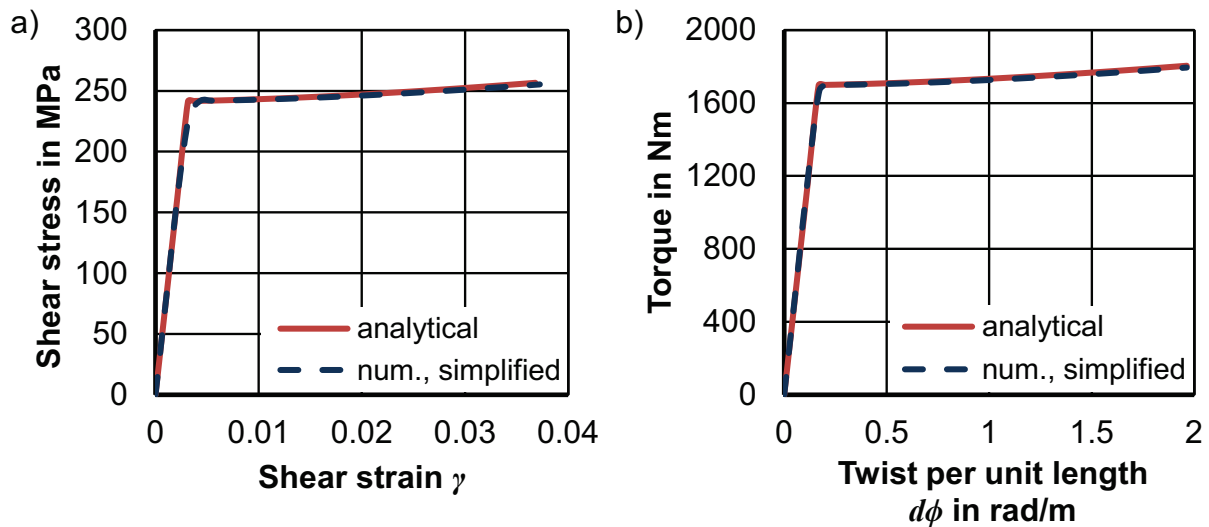


**Figure 7.13:** Geometrical relation between  $\gamma$  and  $d\phi(y_{cs})$

segment with the difference that, instead of simulating only one face of the profile, a whole square cross section with the dimensions 40x40x2.5 mm is modelled. The comparison of the analytical and the numerical strain data at twist per unit length values linearly increasing from 0 to 1.964 rad/m, which represents an angle of twist of 45° on a profile length of 400 mm, is shown in Figure 7.14. The analytically calculated shear strain in the middle of the profile wall (Figure 7.14a) is in good agreement with the numerical strain over the whole range of the twist per unit length with a negligible deviation in proximity to the maximum rate of 1.964 rad/m. Figure 7.14b shows the strain distribution over a single face of the profile cross-section. While the analytical calculation regards the strain as being constant over  $s$ , the numerical analysis shows a slightly increasing shear strain from the middle of the face at  $s = 18.75$  mm to the starting points of the fillets at  $s = 1.25$  mm and  $s = 36.25$  mm.



**Figure 7.14:** a) Shear strain evolution over twist per unit length for the element at  $s = 18.75$  mm b) Shear strain distribution along the neutral axis of the profile wall (Staupendahl and Tekkaya, 2018b), calculations were performed using material data of MW700L Z1



**Figure 7.15:** a) Shear stress evolution over shear strain at  $s = 18.75$  mm b) Torque over twist per unit length for MW700L Z1

The fillets itself are not considered in the comparison due to edge effects in the numerical data. Comparing the average of the numerical strains with the analytical value, the deviation is at maximum 1 %. The shear stress distribution over the cross section behaves similar to the shear strain and can, thus, be defined as constant over  $s$ . To compare the accuracy of the analytical calculation in relation to the numerical data, it is sufficient to compare the shear stress at the point  $s = 18.75$  mm. The shear stress over shear strain is pictured in Figure 7.15a and only shows slight deviations in the transition from elastic to elasto-plastic deformation. The resulting deviation of the analytically calculated torque to the numerical torque is negligible over the whole range of investigated twist per unit length values with the maximum error being 0.6 % at the value 1.964 rad/m.

### 7.3.2 Analytical description of combined bending and torsion

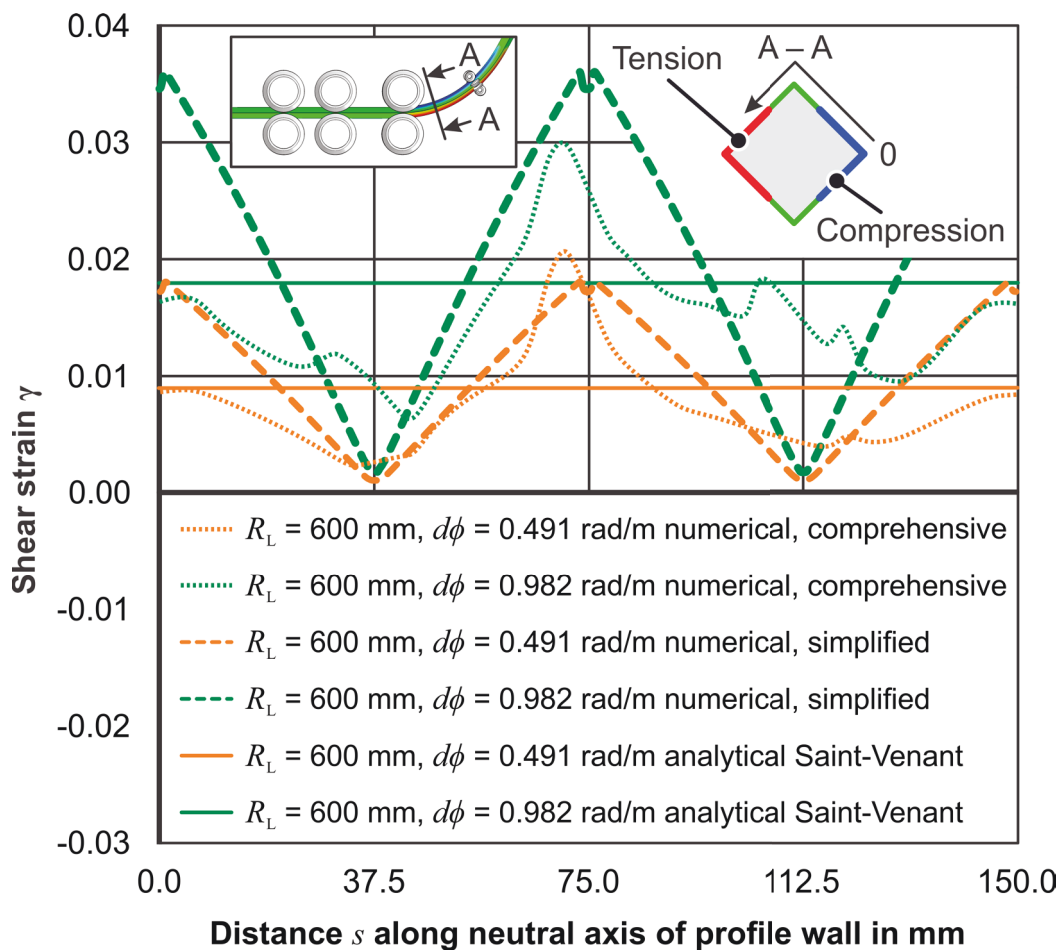
Looking at the well-fitting analytical models for pure bending (Section 7.2) and pure torsion (Section 7.3.1) it might seem straightforward to combine the linear increasing axial strain from the neutral axis to the intrados and extrados due to bending with a uniform shear strain over the cross section. This would result in using Eqs. (7.54) and (7.55) to calculate the axial stress and shear stress in each fiber of the profile and subsequently use Eqs. (7.48) and (7.60) to calculate the bending moment and torque.

However, this is not how strains develop in the case of combined loading. Analyses performed with the comprehensive numerical model described in Section 5.4.1 show that the shear strain, in fact, is not constant over the cross-section during combined loading (Figure 7.16). This observation was also made with the simplified implicit FE model described in Section 5.4.2. Although differences do exist between both curves, which can be attributed to tool contact in the comprehensive numerical model, the general trend of a shear strain starting at a minimal value near to the neutral axis ( $s = 37.5$  mm,

$s = 112.5$  mm) and increasing towards the intrados (the innermost fiber) and extrados (the outermost fiber) of the profile can be observed in both models. Considering a profile that is both bent and twisted simultaneously, the elastic limit is first reached at the intrados and extrados of the profile, as in the case of pure bending. This statement can be directly verified by the von Mises yield criterion (Eq. (7.53)), which, for the elastic case, can be rewritten as:

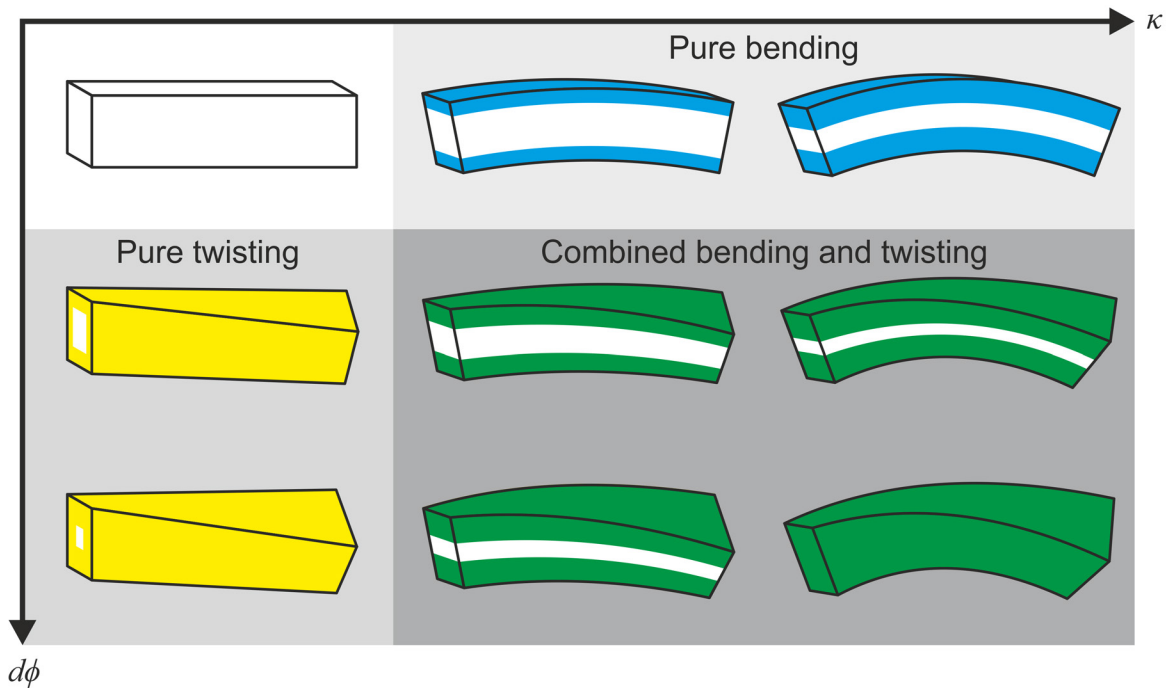
$$\sigma_{el}^2 = (\varepsilon_\alpha E)^2 + 3(\gamma G)^2 \tag{7.68}$$

During elastic deformation, the axial strain is linearly distributed over the profile cross-section with its minimum at the intrados and its maximum at the extrados. The shear strain is distributed homogeneously over the entire cross-section. As a result, the von Mises stress  $\sigma_{el}$  will always be maximum at the intrados and extrados and  $\sigma_{el}$  will reach the yield stress  $\sigma_Y$  at exactly these positions. The strains at the yield point can be defined as  $\varepsilon_Y$  and  $\gamma_Y$ . Once the material yields, plastic deformation initiates in these respective

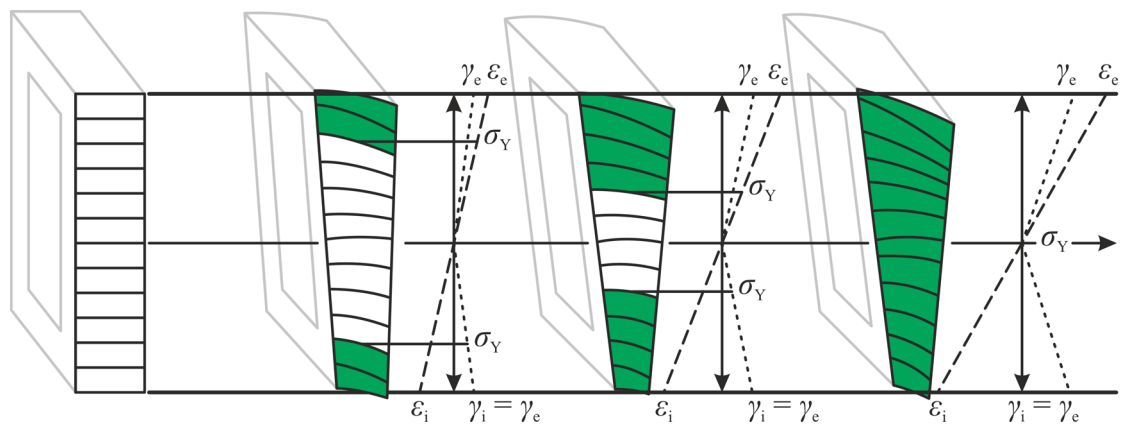


**Figure 7.16:** Shear strain distribution over the cross-section at  $\theta = \pi/4$  calculated for MW 700L Z1 (Staupendahl and Tekkaya, 2018b)

forming zones. With an increasing bending curvature and twisting angle, the forming zones increase toward the neutral axis of the profile until it is completely plastified. Figure 7.17 compares the qualitative development of the forming zone for the three cases: pure bending, pure twisting, and combined bending and twisting. Figure 7.18 qualitatively shows the profile deformation along the diagonal of Figure 7.17 for idealized linear axial as well as shear strain distributions. The validity of a linear axial strain distribution is shown in Section 7.1, Figure 7.5, while the validity of a linear shear strain



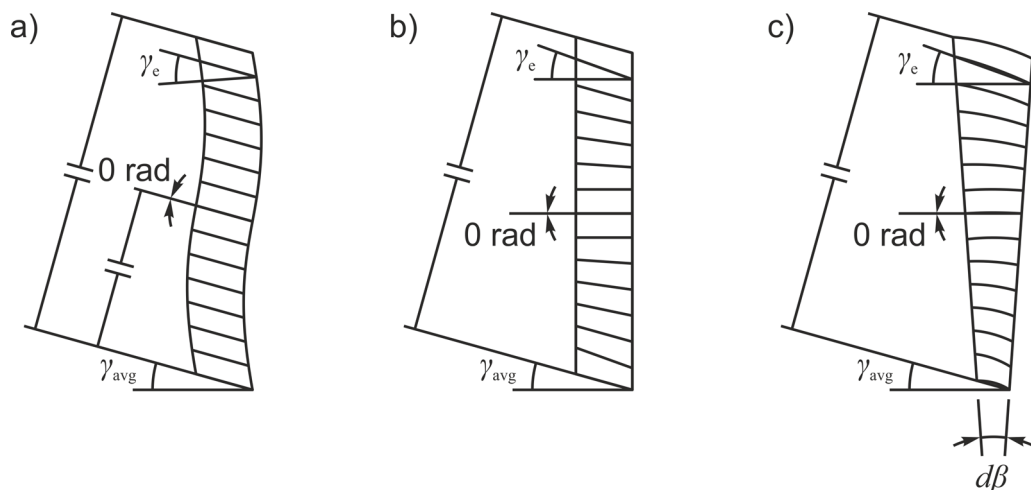
**Figure 7.17:** Development of the forming zone during pure bending, pure twisting and combined bending and twisting



**Figure 7.18:** Development of the forming zone with proportionally increasing curvature and twist per unit length

distribution during simultaneous bending and torsion can be concluded from Figure 7.16. With an increasing bending curvature and twist per unit length, the absolute values of the axial strain and shear strain at the extrados ( $\varepsilon_e$ ,  $\gamma_e$ ) and the intrados ( $\varepsilon_i$ ,  $\gamma_i$ ) also increase, whereby  $\gamma_e$  can be said to equal  $\gamma_i$  for a symmetrical or point symmetrical cross section. With, assuming proportional loading,  $\varepsilon_Y$  and  $\gamma_Y$  being constant, the point of initial yield continuously moves inward until it reaches the neutral axis of the profile.

In Section 7.3.1, warp-free cross sections were defined and it was explained that thin-walled square cross sections are warp-free under pure torsion. If the exemplary square profile segment from Figure 7.18 is now taken, which is simultaneously bent and twisted, and the shear deformation, linearly increasing from the neutral axis to the intrados and extrados, is regarded separately from the axial strain and, thus, without the resulting axial constraints, the cross section would actually warp, generating the S-shape shown in Figure 7.19a. This shows that cross sections that are generally considered to be warp-free in pure torsion lose this property in combined bending and torsion. What also becomes clear when looking at Figure 7.19a is how there can be a difference in  $\gamma_{avg}$  calculated by Eq. (7.66) and the local shear strain  $\gamma$ . In the shown profile segment, even though the local shear strain  $\gamma$  of the elements at the neutral axis is 0 and that of the elements at the intrados and extrados is  $\gamma_e$ ,  $\gamma_{avg}$  is actually equal in all elements of the profile segment. If now warping is considered to be hindered (Figure 7.19b), as this is the constraint of kinematic 3D bending processes (Figure 7.10),  $\gamma_{avg}$  is left to describe the shear angle of the outer edge of the profile segment. The local shear strain  $\gamma$  of the elements at the intrados and extrados is still  $\gamma_e$  as in the case of unhindered warping, which again reduces to 0 in the elements at the neutral axis of the profile segment.



**Figure 7.19:** a) Warping of a profile segment caused by varying shear strains over the cross section b) hindered torsion caused by 3D bending constrains c) actual shear strain distribution in simultaneously bent and twisted profile segment

By superposing the axial deformation of the profile segment caused by bending (Figure 7.19c), the geometry previously shown in the far right of Figure 7.18 is generated. The local shear strains, hereby, stay the same as in Figure 7.19a and b and the average shear strain  $\gamma_{\text{avg}}$  is still measured at the outer edge of the profile segment. In the following calculations, the stiffening effect hindered warping has on the torsional stiffness (Francke und Friemann, 2005) is neglected.

To analytically describe the shear strain distribution for a rectangular cross-section with the profile width  $w$  and the profile height  $h$ , the distribution is idealized as shown in Figure 7.18 and defined to begin at 0 on the neutral axis and linearly increase to the maximum shear strain  $\gamma_m$  (with  $\gamma_m = \gamma_i = \gamma_e$ ) at the intrados and extrados. Specifically, the distribution projected on the bending plane is defined to be linear, while the distribution along the sides of the cross-section are allowed to be bi-linear. Using this simplification, only  $\gamma_m$  needs to be found in order to determine the overall shear strain distribution. In order to calculate  $\gamma_m$  for any given cross-section rotation, two particular cross-section rotation angle cases have to be distinguished. The first case describes the neutral axis intersecting the sides of the rectangle with the length  $w - t_t$ , which occurs in the rotation angle ranges:

$$-\tan^{-1}\left(\frac{1}{q}\right) \leq \theta \leq \tan^{-1}\left(\frac{1}{q}\right) \quad (7.69)$$

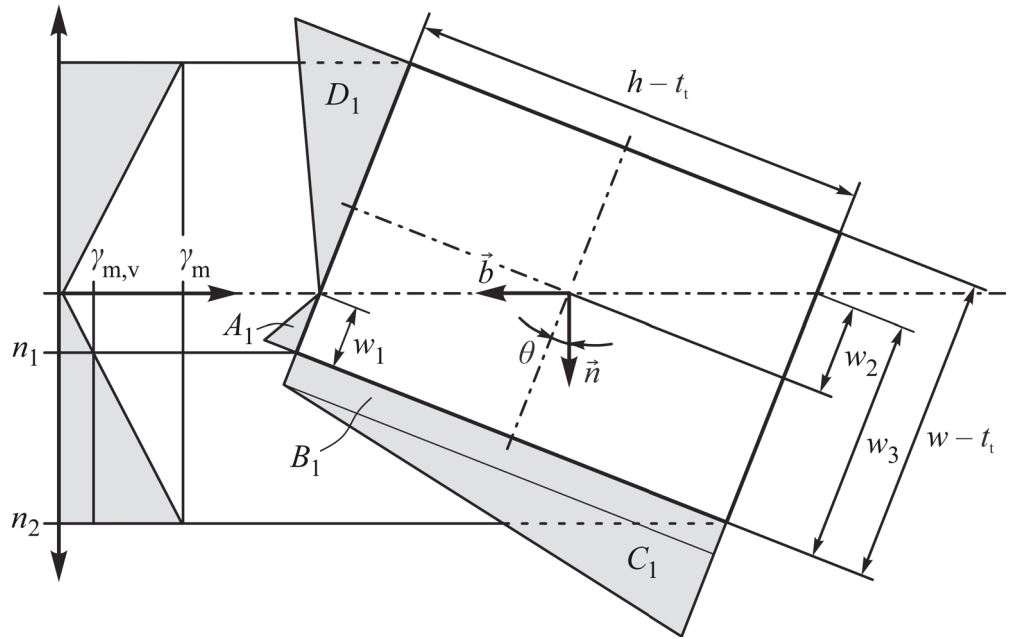
and

$$\pi - \tan^{-1}\left(\frac{1}{q}\right) \leq \theta \leq \pi + \tan^{-1}\left(\frac{1}{q}\right) \quad (7.70)$$

The parameter  $q$ , hereby, describes the ratio of the height to the width of the middle axis of the profile wall:

$$q = \frac{h - t_t}{w - t_t} \quad (7.71)$$

Figure 7.20 shows a qualitative linear shear strain distribution in  $\vec{n}$ -direction from 0 on the neutral axis ( $\vec{b}$ -vector) over the intermediate value  $\gamma_{m,v}$  at position  $n_1$  (vertex nearest to the neutral axis) to the maximum value  $\gamma_m$  at position  $n_2$ . Additionally, the bi-linear projection of this linear shear strain distribution on two sides of the rectangular cross-section is shown for the rotation angle range described by Eq. (7.69). In the interest of clarity, the point symmetric distribution along the other two sides is not displayed. To describe the shear strain distribution for Eq. (7.70), the rectangular cross-section shown in Figure 7.20 simply has to be mirrored around the  $\vec{n}$ -vector.



**Figure 7.20:** Case 1: Qualitative shear strain distribution generated when the neutral bending axis intersects the sides of the rectangle with the length  $w - t_t$  (Staupendahl and Tekkaya, 2018b)

The link of the actual shear strain distribution to the average shear strain can be made by adding individual distributions per side and dividing the sum by the perimeter  $P$ , whereby  $j = \{1,2\}$  depending on the case of cross-section rotation:

$$\frac{2(A_j + B_j + C_j + D_j)}{P} = \gamma_{\text{avg}} \quad (7.72)$$

The shear strain distributions  $A_1$ ,  $B_1$ ,  $C_1$ , and  $D_1$  are, in turn, calculated with the relevant dimensions shown in Figure 7.20. To simplify the equations, the length  $w - t_t$  is normalized to 1 so that, by using Eq. (7.71),  $h - t_t$  equals  $q$ :

$$w_1 = \frac{1}{2} - \frac{1}{2}q \tan \theta \quad (7.73)$$

$$w_2 = \frac{1}{2}q \tan \theta \quad (7.74)$$

$$w_3 = \frac{1}{2} + \frac{1}{2}q \tan \theta \quad (7.75)$$

$$n_1 = \left( \frac{1}{2} - \frac{1}{2}q \tan \theta \right) \cos \theta \quad (7.76)$$

$$n_2 = \left( \frac{1}{2} + \frac{1}{2}q \tan \theta \right) \cos \theta \quad (7.77)$$

Using Eqs. (7.76) and (7.77), the shear strain at the vertex closest to the neutral bending axis is defined:

$$\gamma_{m,v} = \gamma_m \frac{1 - q \tan \theta}{1 + q \tan \theta} \quad (7.78)$$

With the set of Eqs. from (7.73) to (7.78), the shear strain distributions are found:

$$A_1 = \frac{1}{4} \frac{(1 - q \tan \theta)^2}{(1 + q \tan \theta)} \gamma_m \quad (7.79)$$

$$B_1 = \frac{1 - q \tan \theta}{1 + q \tan \theta} q \gamma_m \quad (7.80)$$

$$C_1 = \frac{1}{2} \left( 1 - \frac{1 - q \tan \theta}{1 + q \tan \theta} \right) q \gamma_m \quad (7.81)$$

$$D_1 = \frac{1}{4} (1 + q \tan \theta) \gamma_m \quad (7.82)$$

The second particular case of cross-section rotation describes the neutral axis intersecting the sides of the length  $h - t_t$ , which occurs in the rotation angle ranges:

$$\tan^{-1} \left( \frac{1}{q} \right) < \theta < \pi - \tan^{-1} \left( \frac{1}{q} \right) \quad (7.83)$$

and

$$\pi + \tan^{-1} \left( \frac{1}{q} \right) < \theta < 2\pi - \tan^{-1} \left( \frac{1}{q} \right) \quad (7.84)$$

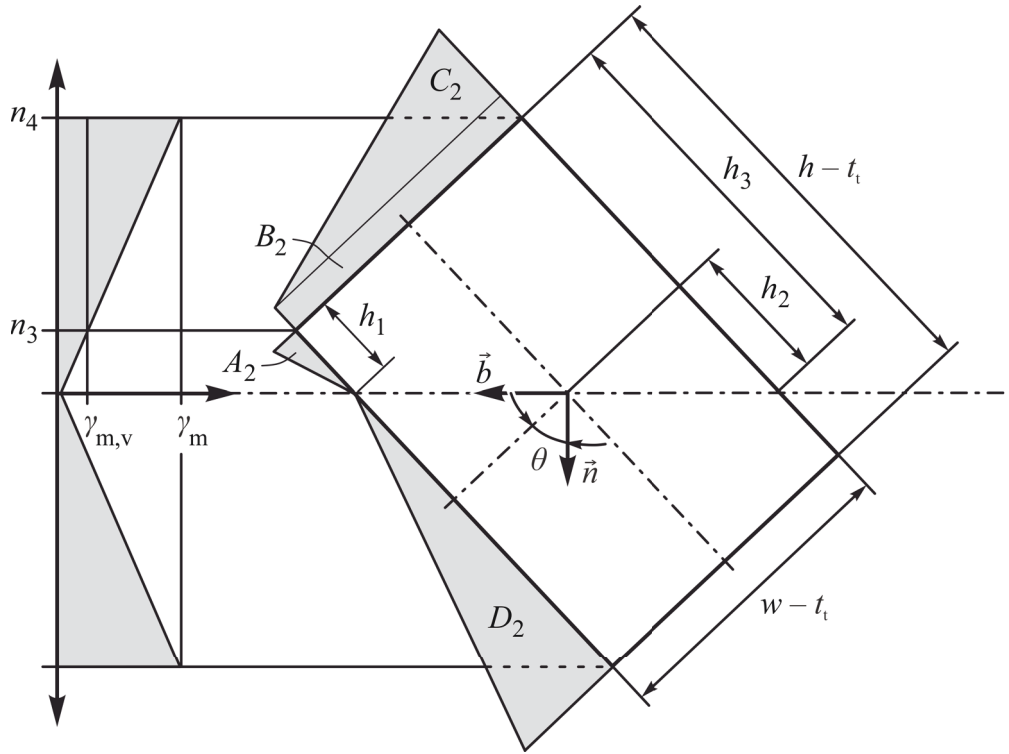
Figure 7.21 shows the qualitative shear strain distribution along two sides of the rectangle for the rotation angle range described by Eq. (7.83). As in Figure 7.20 the point symmetric distribution along the other two sides is not shown. To describe the shear strain distribution for Eq. (7.84), the rectangular cross-section shown in Figure 7.21 simply has to be mirrored around the  $z$ -axis. The relevant dimensions in case 2 are:

$$h_1 = \frac{1}{2} q - \frac{1}{2} \tan \left( \frac{\pi}{2} - \theta \right) \quad (7.85)$$

$$h_2 = \frac{1}{2} \tan \left( \frac{\pi}{2} - \theta \right) \quad (7.86)$$

$$h_3 = \frac{1}{2} q + \frac{1}{2} \tan \left( \frac{\pi}{2} - \theta \right) \quad (7.87)$$





**Figure 7.21:** Case 2: Qualitative shear strain distribution generated when the neutral bending axis intersects the sides of the rectangle with the length  $h - t$  (Staupendahl and Tekkaya, 2018b)

$$n_3 = \left[ \frac{1}{2}q - \frac{1}{2} \tan\left(\frac{\pi}{2} - \theta\right) \right] \cos\left(\frac{\pi}{2} - \theta\right) \quad (7.88)$$

$$n_4 = \left[ \frac{1}{2}q + \frac{1}{2} \tan\left(\frac{\pi}{2} - \theta\right) \right] \cos\left(\frac{\pi}{2} - \theta\right) \quad (7.89)$$

The shear strain at the vertex closest to the neutral bending axis calculated using Eqs. (7.88) and (7.89):

$$\gamma_{m,v} = \gamma_m \frac{1 - q \tan \theta}{1 + q \tan \theta} \quad (7.90)$$

The set of Eqs. from (7.85) to (7.90) leads to the shear strain distributions:

$$A_2 = \frac{1}{4} \frac{\left( q - \tan\left(\frac{\pi}{2} - \theta\right) \right)^2}{q + \tan\left(\frac{\pi}{2} - \theta\right)} \gamma_m \quad (7.91)$$

$$B_2 = \frac{q - \tan\left(\frac{\pi}{2} - \theta\right)}{q + \tan\left(\frac{\pi}{2} - \theta\right)} \gamma_m \quad (7.92)$$

$$C_2 = \frac{1}{2} \left( 1 - \frac{q - \tan\left(\frac{\pi}{2} - \theta\right)}{q + \tan\left(\frac{\pi}{2} - \theta\right)} \right) \gamma_m \quad (7.93)$$

$$D_2 = \frac{1}{4} \left[ q + \tan\left(\frac{\pi}{2} - \theta\right) \right] \gamma_m \quad (7.94)$$

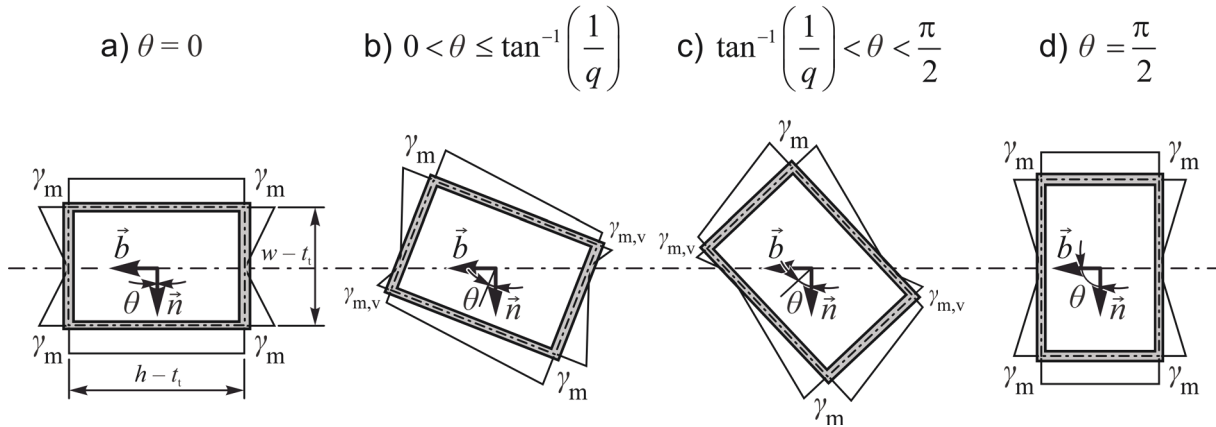
The maximum shear strain  $\gamma_m$  is finally set in terms of the rotation angle of the profile cross-section  $\theta$  and related to  $\gamma_{\text{avg}}$  by solving Eq. (7.72) for cases 1 and 2:

$$\gamma_m(\theta) = \frac{2(1+q)[1+q \tan|\theta|]}{1+q^2 \tan^2(\theta) + 2q} \gamma_{\text{avg}} \quad \text{for} \quad \begin{cases} -\tan^{-1}\left(\frac{1}{q}\right) \leq \theta \leq \tan^{-1}\left(\frac{1}{q}\right) \\ \pi - \tan^{-1}\left(\frac{1}{q}\right) \leq \theta \leq \pi + \tan^{-1}\left(\frac{1}{q}\right) \end{cases} \quad (7.95)$$

$$\gamma_m(\theta) = \frac{2(1+q) \left[ q + \tan\left|\frac{\pi}{2} - \theta\right| \right]}{q^2 + \tan^2\left(\frac{\pi}{2} - \theta\right) + 2q} \gamma_{\text{avg}} \quad \text{for} \quad \begin{cases} \tan^{-1}\left(\frac{1}{q}\right) < \theta < \pi - \tan^{-1}\left(\frac{1}{q}\right) \\ \pi + \tan^{-1}\left(\frac{1}{q}\right) < \theta < 2\pi - \tan^{-1}\left(\frac{1}{q}\right) \end{cases} \quad (7.96)$$

Figure 7.22 sets the two previously shown cross-section rotation angle cases in line with the two normal positions at  $\theta = 0$  and at  $\theta = \pi/2$ . In these positions, the shear strains increase linearly along the two sides normal to the neutral axis from 0 to the maximum shear strain  $\gamma_m$  at the intrados and extrados. The shear strain value along the sides parallel to the neutral axis has the constant value  $\gamma_m$ . For  $\theta = 0$ ,  $\gamma_m$  is calculated with Eq. (7.95), while for  $\theta = \pi/2$ ,  $\gamma_m$  is calculated with Eq. (7.96). The shear strain at each position along the cross-sectional parameter is calculated by:

$$\gamma(n_B) = \gamma_m \frac{|n_B|}{n_m} \quad (7.97)$$



**Figure 7.22:** Shear strain distribution over the profile wall of a rectangular cross-section in the rotation angle range  $\theta = 0$  to  $\pi/2$  (Staupendahl and Tekkaya, 2018b)

Inserting Eq. (7.97) into Eqs. (7.54) and (7.55) leads to:

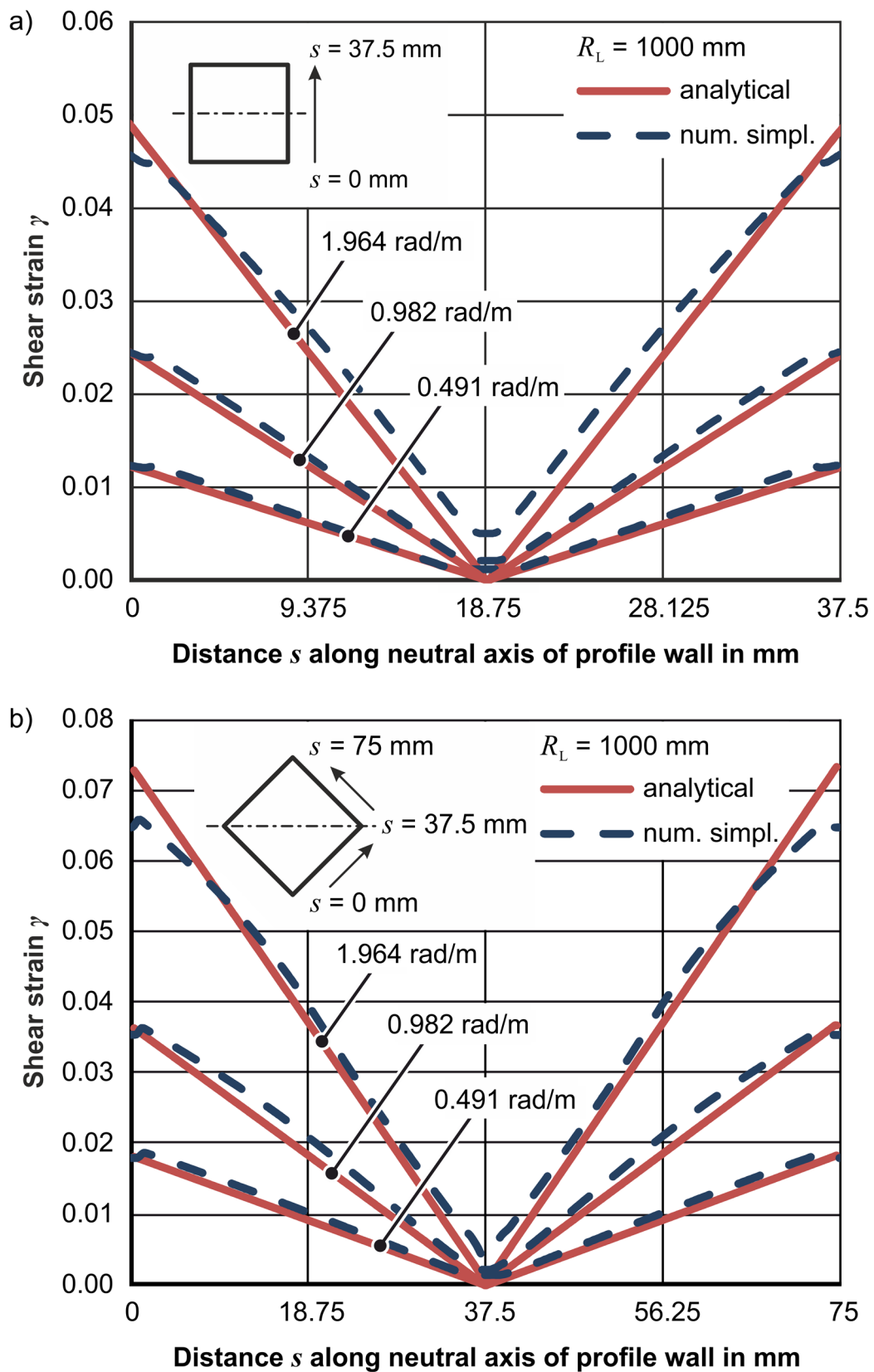
$$\sigma_\alpha = \frac{\sigma_f(\bar{\varepsilon}_{pl})}{\sqrt{1 + \frac{1}{3} \left( \frac{\gamma_m n_B}{\varepsilon_\alpha n_m} \right)^2}} \quad (7.98)$$

$$\tau = \frac{\sigma_f(\bar{\varepsilon}_{pl})}{\sqrt{3 + 9 \left( \frac{\varepsilon_\alpha n_m}{\gamma_m n_B} \right)^2}} \quad (7.99)$$

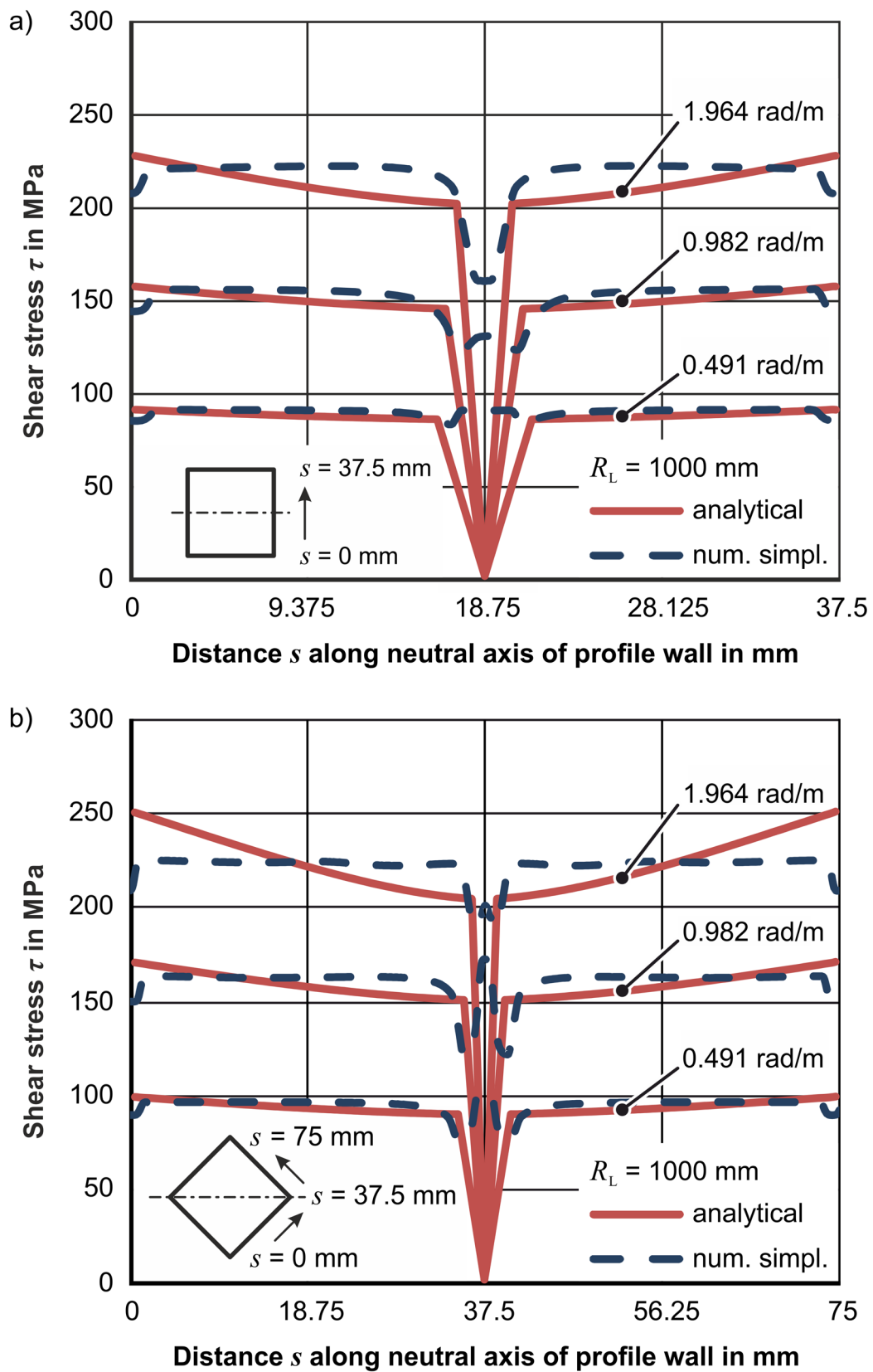
with  $\bar{\varepsilon}_{pl}$ , according to Eq. (7.34) from Section 7.1 being:

$$\bar{\varepsilon}_{pl} = \sqrt{\varepsilon_\alpha^2 + \frac{1}{3} \left( \gamma_m \frac{n_B}{n_m} \right)^2} \quad (7.100)$$

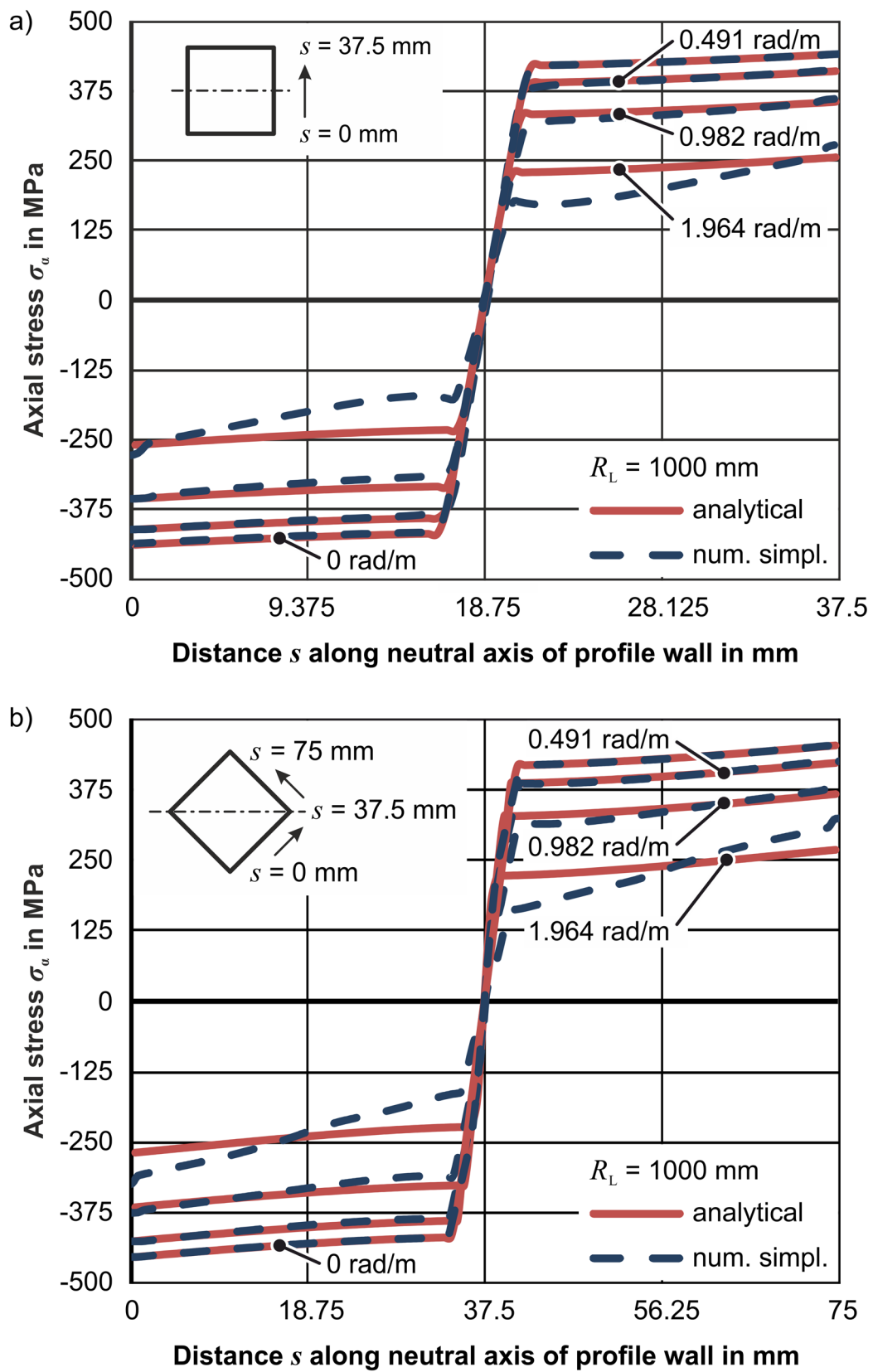
Figure 7.23 shows the comparison between the shear strain calculated numerically with the simplified FE model and the analytically calculated shear strain over the profile wall parallel to the bending plane at  $\theta = 0$  and  $\theta = \pi/4$ . Additionally, Figure 7.24 shows the analytically calculated shear stress in comparison to the numerical data and Figure 7.25 shows the analytically calculated axial stress in comparison to the numerical data. The data is given relative to the perimetral length  $s$ , whereby  $n_B = 0$  at  $s = 18.75$  mm and  $n_m = 18.75$  mm for  $\theta = 0$  and  $n_B = 0$  at  $s = 37.5$  mm and  $n_m = 26.52$  mm for  $\theta = \pi/4$ . The results for three twist per unit length values (0.491, 0.982, and 1.964 rad/m) are shown. The ratios of twist per unit length to bending curvature  $d\phi/R_L$  for each of the trials were chosen to be 0.491, 0.982, and 1.964 rad, respectively. The graphs with the strain and stress results for the radii 600 mm and 800 mm can be found in annex A.1.



**Figure 7.23:** Comparison of analytically calculated shear strain to numerically calculated shear strain for combined bending and torsion at  $\theta = 0$  (a) and  $\theta = \pi/4$  (b) for MW700L Z1 (Staupendahl and Tekkaya, 2018b)



**Figure 7.24:** Comparison of analytically calculated shear stress to numerically calculated shear stress for combined bending and torsion at  $\theta = 0$  (a) and  $\theta = \pi/4$  (b) for the material MW700L Z1



**Figure 7.25:** Comparison of analytically calculated axial stress to numerically calculated axial stress for combined bending and torsion at  $\theta = 0$  (a) and  $\theta = \pi/4$  (b) for the material MW700L Z1

For  $\theta = 0$  the average deviations between the linear shear strain approach, given by Eq. (7.97), and the numerically calculated strains at 0.491, 0.982, and 1.964 rad/m lie at 11 %, 11 %, and 15 %, respectively. For  $\theta = \pi/4$  the average deviations between the linear shear strain approach, given by Eq. (7.97), and the numerically calculated strains at 0.491, 0.982, and 1.964 rad/m lie at 13 %, 14 %, and 12 %, respectively. A major part of these errors is caused by the analytical shear strain starting at 0 on the neutral axis of the profile, whereby the numerical calculation actually shows initial elastic strains.

These initial elastic strains also cause the numerical shear stress to be non-zero (see Figure 7.24), while the analytical model predicts a drop down from  $\sigma_Y$  to 0 MPa on the neutral axis. For  $\theta = 0$  the average deviations between the shear stress, given by Eq. (7.99), and the numerically calculated shear stress at 0.491, 0.982, and 1.964 rad/m lie at 9 %, 7 %, and 8 %, respectively. For  $\theta = \pi/4$  the average deviations between the shear stress, given by Eq. (7.99), and the numerically calculated shear stress lie at 7 % for all three twist per unit length values.

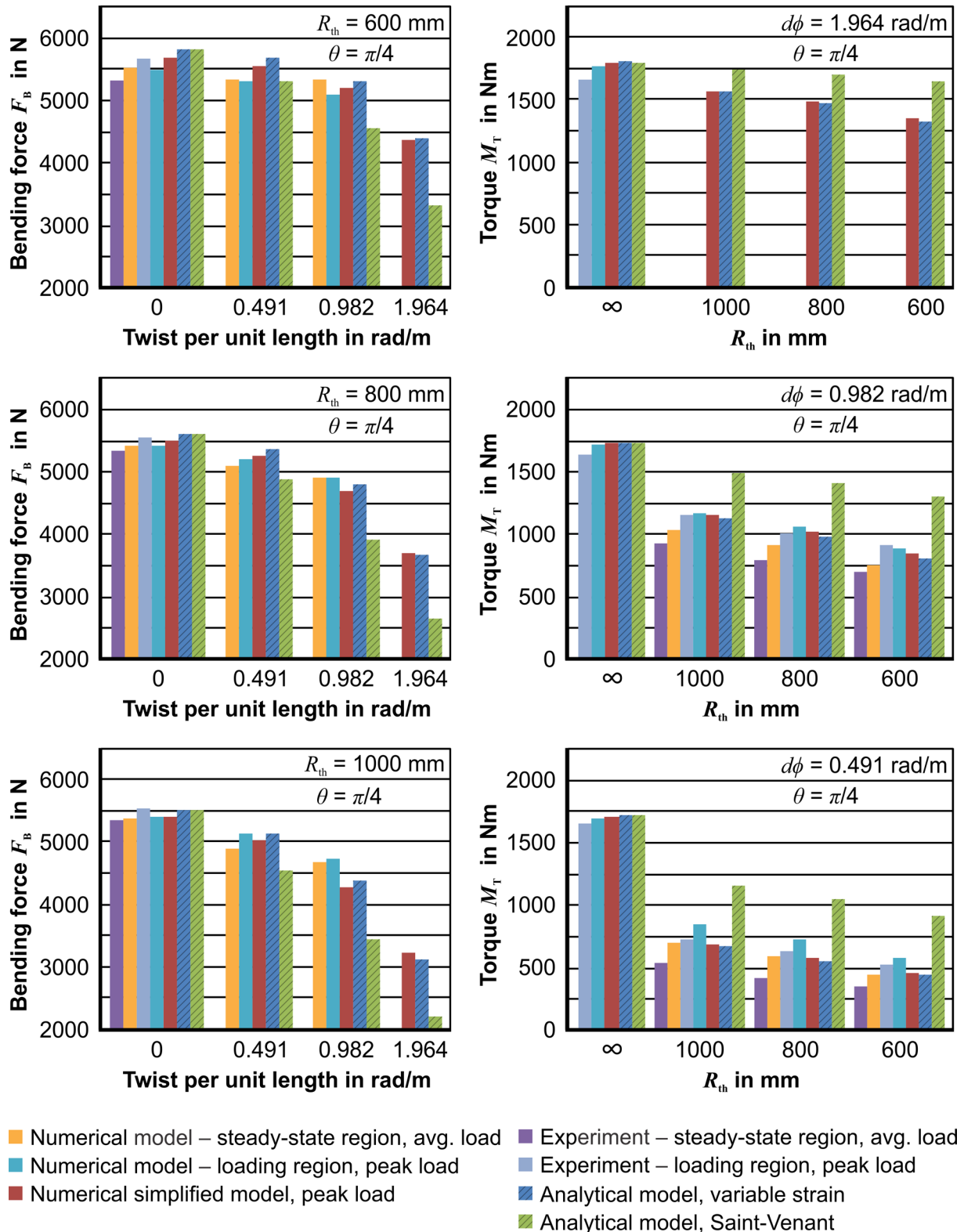
Figure 7.25 shows an increasing deviation between the analytically calculated axial stress, given by Eq. (7.98) and the numerically calculated stress values with an increasing twist per unit length. While the average deviation for  $\theta = 0$  is 4 % at 0 and 0.491 rad/m, this value increases to 6 % at 0.982 rad/m, and to 22 % at 1.964 rad/m. For  $\theta = \pi/4$  the average deviation behaves similarly with the average deviation being 3 % at 0 and 0.491 rad/m, 6 % at 0.982 rad/m, and 20 % at 1.964 rad/m.

### 7.3.3 Performance of the analytical model for combined bending and torsion

Using Eq. (7.98) in combination with the bending moment calculation strategy 2 from table 7.2:

$$M_B = 2 \int_0^{n_m} \sigma_\alpha n_B dA \quad (7.101)$$

the bending force  $F_B = M_B/L_B$  can be calculated. The torque is calculated via Eq. (7.60). Figure 7.26 shows experimental bending force and torque results abreast results from the comprehensive and simplified numerical model in comparison to the results from the analytical model with a uniform shear strain distribution over the cross-section (Saint-Venant) and the variable strain model derived in Section 7.3.2 for  $\theta = \pi/4$ . The results for  $\theta = 0$  can be found in Annex A.2, Figure A.7. The data was produced using the material description for MW700 L Z1. For the comprehensive numerical model (description in Section 5.4.1, Figure 5.21), the NC-data was set up as described in Section 5.4 resulting in a loading region with increasing values of  $X$ ,  $\beta_1$ , and  $\alpha_2$ , a steady-state region with constant values of  $X$ ,  $\beta_1$ , and  $\alpha_2$  and, finally, an unloading region. The average bending force and torque in the steady state region and the peak



**Figure 7.26:** Bending force and torque results for MW700L Z1 at  $\theta = \pi/4$  of the loading region and the steady-state region of the comprehensive numerical model and experiments in comparison to the bending force and torque of the simplified numerical model and the analytical models with a variable strain over the cross-section and a constant shear strain (Saint-Venant) (Staupendahl and Tekkaya, 2018b)



bending force and torque in the loading region are presented. For the simplified numerical model (description in Section 5.4.2, Figure 5.24) the peak bending force and torque are stated, output at the increment when the final loaded radius and twist per unit length is reached in each separate simulation. The comprehensive numerical model could only be used to generate data up to a twist per unit length of 0.982 rad/m. At a twist per unit length of 1.964 rad/m, the twist was not able to be applied uniformly to the profile. Rather, local excessive twisting occurred in the forming zone, resulting in unusable bending force and torque data. Experimental data could also not be consulted for this twist per unit length because the feeding force generated by the friction-based roll feeding system did not have the height required to transport the profile. As a result, only data from the simplified numerical model can be presented alongside the analytical data for the twist per unit length of 1.964 rad/m. While the experimental torque values, measured using the torque sensor introduced in Section 5.2.3, are stated for all producible radius-twist per unit length combinations, the experimental bending force data can only be shown for plane bending (twist per unit length = 0 rad/m) as explained in Section 5.4.

Looking at the three bending force diagrams of Figure 7.26, it can be seen that the bending force decreases with an increased twist per unit length. This decrease is more pronounced with increasing bending radii, which can be explained by the then increased quadratic ratio of shear strain to longitudinal strain as seen in Eq. (7.98). It can also be noticed that the analytical model with a constant shear strain over the cross-section greatly overestimated the bending force reduction  $F_{B,red}$ :

$$F_{B,red} = \frac{F_{B,R_{th},0} - F_{B,R_{th},d\phi}}{F_{B,R_{th},0}} \cdot 100\% \quad (7.102)$$

with  $F_{B,R_{th},0}$  describing the bending force at the theoretical bending radius  $R_{th}$  and a twist per unit length of 0 and  $F_{B,R_{th},d\phi}$  describing the bending force at the theoretical bending radius  $R_{th}$  and the twist per unit length  $d\phi$ . Compared to the numerical simulations and the enhanced analytical model with a variable shear strain over the cross-section, the bending force reduction is significantly overestimated and about three times as high in several combinations of  $R_{th}$ ,  $d\phi$ , and  $\theta$  (e.g. at  $R_{th} = 800$  mm,  $\theta = \pi/4$ , and  $d\phi = 0.491$  rad/m the simplified numerical model shows a bending force reduction of 4.5 %, the comprehensive numerical model shows a bending force reduction of 6.2 % (steady state) and 4.1 % (peak), the enhanced analytical model shows a reduction of 4.4 %, while the analytical model with a constant shear strain over the cross-section shows a reduction of 13.2 %), with a maximum absolute bending force deviation of 32.1 % ( $R_{th} = 1000$  mm,  $\theta = \pi/4$ , and  $d\phi = 1.964$  rad/m) to the simplified numerical model and 26.5 % (steady-state,  $R_{th} = 1000$  mm,  $\theta = \pi/4$ , and  $d\phi = 0.982$  rad/m) and 27.5 % (peak,  $R_{th} = 1000$  mm,  $\theta = \pi/4$ , and  $d\phi = 0.982$  rad/m) to the comprehensive numerical model. The enhanced analytical model, on the other hand, only shows maximum absolute deviations of up to 3.0 % ( $R_{th} = 1000$  mm,  $\theta = \pi/4$ , and  $d\phi = 1.964$  rad/m) to

the simplified numerical model and 6.2 % (steady-state,  $R_{th} = 1000$  mm,  $\theta = \pi/4$ , and  $d\phi = 0.982$  rad/m) and 7.5 % (peak,  $R_{th} = 1000$  mm,  $\theta = \pi/4$ , and  $d\phi = 0.982$  rad/m) to the comprehensive model.

While the analytical model with a constant shear strain overestimates the bending force reduction  $F_{B,red}$ , the model underestimates the torque reduction  $M_{T,red}$ :

$$M_{T,red} = \frac{M_{T,R_{th},0} - M_{T,R_{th},d\phi}}{M_{T,R_{th},0}} \cdot 100\% \quad (7.103)$$

Using the above mentioned example of  $R_{th} = 800$  mm,  $\theta = \pi/4$ , and  $d\phi = 0.491$  rad/m, the simplified numerical model shows a torque reduction of 66.5 %, the comprehensive numerical model shows a bending force reduction of 65.5 % (steady state) and 57.6 % (peak), the enhanced analytical model shows a reduction of 67.8 %, while the analytical model with a constant shear strain over the cross-section only shows a reduction of 38.9 %. The maximum absolute deviation of the torque calculated via the analytical model with a constant shear strain to the simplified numerical model is 101.5 % ( $R_{th} = 600$  mm,  $\theta = \pi/4$ , and  $d\phi = 0.491$  rad/m) and to the comprehensive numerical model is 79.6 % (steady-state,  $R_{th} = 800$  mm,  $\theta = \pi/4$ , and  $d\phi = 0.491$  rad/m) and 46.1 % (peak,  $R_{th} = 800$  mm,  $\theta = \pi/4$ , and  $d\phi = 0.491$  rad/m). In contrast, the enhanced analytical model only shows maximum absolute deviations of up to 4.2 % ( $R_{th} = 600$  mm,  $\theta = \pi/4$ , and  $d\phi = 0.491$  rad/m) to the simplified numerical model and 8.7 % (steady-state,  $R_{th} = 1000$  mm,  $\theta = \pi/4$ , and  $d\phi = 0.982$  rad/m) and 24.2 % (peak,  $R_{th} = 600$  mm,  $\theta = \pi/4$ , and  $d\phi = 0.491$  rad/m) to the comprehensive model.

The higher deviations to the bending force and torque output of the comprehensive numerical model can be explained with the elastic deformation of the profile in the feeding roll system as well as in between the front feeding roll and the bending head, which does not occur in the simplified model. This elastic profile deformation actually causes the effective loaded radii to be larger than the targeted loaded radii (see Section 6.3.1). As the stresses and strains used in both analytical models were generated based on the theoretical radii 600 mm, 800 mm, and 1000 mm, the elastic behavior is not considered in the generation of the shown bending force and torque results and explains the higher agreement with the results of the simplified numerical model.

The combination of the description of plastic 3D-bending behavior with the description of elastic profile behavior from Section 6.3 is presented in the next Chapter.

## 8 Comprehensive process model of 3D profile bending

The results of Chapters 3, 6, and the previous sections of Chapter 7 are now used to setup a comprehensive process model that predicts the bending axes movements needed to produce a targeted profile shape.

### 8.1 Model procedure

The first step is the generation of the geometrical data of the target profile shape in relation to the arc length  $s$  as explained in Section 4.1:

- Curvature  $\kappa$  by Eq. (4.17) (continuous curve description) or Eqs. (4.50), (4.51), or (4.52) (discrete curve description)
- Bending plane rotation  $d\theta_r$  via Eq. (4.18) (continuous curve description) or  $\Delta\theta_r$  via Eq. (4.57) (discrete curve description)
- The twist per unit length  $d\phi$  by Eq. (4.43) (continuous curve description) or  $\Delta\phi$  by Eq. (4.63) (discrete curve description)

For easier legibility, the differential representations will be used in all of the following steps.

The next step is the generation of the raw NC-data based on the target geometry in terms of the arc length  $s$  as explained in Section 4.2.3:

- The rotation angle  $\alpha_1$  is calculated based on Eq. (4.75)
- The resultant  $r$ , which can be directly used as the displacement along the  $X$ -axis ( $L_{B,X}$ ) in the case of a bending process with a single linear axis is calculated with Eq. (4.76)
- The rotation angle  $\alpha_2$  of the torsional cDOF is either calculated with Eq. (4.79) or with Eq. (4.80)
- The rotation angle  $\beta_1$  of the bending head is obtained by Eq. (4.81)
- The rotation angle  $\beta_2$  of the bending head is obtained by Eq. (4.82)

Subsequently, the bending moment (Eq. (7.101)) and torque (Eq. (7.60)) are calculated using the stress distributions determined with Eqs. (7.98) (axial stress) and (7.99) (shear stress). The bending moment is subsequently used in order to calculate the loaded curvature  $\kappa_L$ :

$$\kappa_L = \kappa + \frac{M_B(\kappa_L)}{EI} \quad (8.1)$$

The torque is used in order to calculate the loaded twist per unit length  $d\phi_L$ :

$$d\phi_L = d\phi + \frac{M_T(d\phi_L)ds}{GJ_t} \quad (8.2)$$

Since the bending moment depends on the unknown loaded curvature and the torque depends on the unknown loaded twist per unit length and both loads are related through the state of stresses described by Eqs. (7.98) and (7.99),  $\kappa_L$  and  $d\phi_L$  have to be approximated by the recurrence relations given by Eqs. (8.3) and (8.4). Because of the parameters' reciprocal effects, the parameters have to be approximated simultaneously.

$$\kappa_{L,n} = \kappa + \frac{M_B(\kappa_{L,n-1})}{E(\bar{\varepsilon}_{pl,cs,mid,L})I} \quad \text{with} \quad \bar{\varepsilon}_{pl,cs,mid,L} = \ln\left(1 + \frac{1}{2}n_m\kappa_{L,n-1}\right) \quad (8.3)$$

$$d\phi_{L,n} = d\phi + \frac{M_T(d\phi_{L,n-1})ds}{GJ_t} \quad (8.4)$$

Since the forming zone is defined to be at the front profile support  $S_1$  (see Figures 6.1 and 6.13), the curvature  $\kappa_L$  represents the instantaneous loaded curvature at this position. Using the distance from  $S_1$  to the plane of bending force application  $L_{B,y}$  and  $M_B(\kappa_L)$ , the bending force  $F_B$  is calculated. This bending force is subsequently used to determine the elastic beam deformation. In order to avoid the otherwise necessary constant change of the coordinate system of the elastic beam model,  $F_B$  is used as the in plane bending force  $F_{B,xy}$ . The elastic beam models described in Chapter 6 calculate the beam deformation based on an unloaded beam. As such, for bending of constant curvatures, rather than using  $\kappa_L$  to set up the curved beam model,  $\kappa_U$  is used. Depending on the targeted shape of the profile and the segment of the profile being bent,  $\kappa_U$  is not necessarily constant between  $S_1$  and the point of bending force application  $P_{FB}$ . In order to still be able to use the beam models described in Chapter 6, which are based on constant curvature,  $L_{B,x}$  is used together with  $L_{B,y}$  and Eq. (5.7) to determine the average curvature  $\kappa_{avg} = 1/R_{avg}$  in this segment. Next, the elastic beam deflection in the  $xy$ -plane  $w_{xy,B}$  is calculated according to Eq. (6.62), using the parameters  $F_B$ ,  $R_{avg}$ ,  $\beta_{1,avg}$ , and  $E(\bar{\varepsilon}_{pl,cs,mid,avg})$  with:

$$\bar{\varepsilon}_{pl,cs,mid,avg} = \ln\left(1 + \frac{1}{2}n_m\kappa_{avg}\right) \quad (8.5)$$

The profile deflection  $w_{X,B}$  along the  $X$ -axis is highly affected by  $\beta_1$  as shown in Figure 6.6 and as can be interpreted from the comparison of deflections calculated with a straight beam model and a curved beam model (Figure 6.16). For the calculation of  $w_{X,B}$  Eq. (6.20) is, therefore, modified to:

$$w_{X,B}(F_B, R_{avg}, \beta_1, \beta_{1,avg}) = \frac{w_{xy,B}(F_B, R_{avg}, \beta_{1,avg})}{\cos\left[\beta_1 + w'_{xy,B}(F_B, R_{avg}, \beta_{1,avg})\right]} \quad (8.6)$$

where  $\beta_1$  is the value generated in the raw NC-data generation. The total deflection along

the  $X$ -axis, corrected by the machine stiffness displacement function (Eq. (5.14)) is:

$$w_{X,B,\text{corr}}(F_B, R_{\text{avg}}, \beta_1, \beta_{1,\text{avg}}) = w_{X,B}(F_B, R_{\text{avg}}, \beta_1, \beta_{1,\text{avg}}) + \delta_M(F_B) \quad (8.7)$$

By adding this term to  $L_{B,X}$  of the raw NC-Data in Eq. (5.7) the equivalent loaded curvature can be determined:

$$\kappa_{L,\text{eq}} = \frac{1}{R_{L,\text{eq}}} = 2 \left( \frac{(L_{B,X} + w_{X,B,\text{corr}})^2 + L_{B,Y}^2}{L_{B,X} + w_{X,B,\text{corr}}} \right)^{-1} \quad (8.8)$$

The equivalent loaded twist per unit length is calculated by:

$$d\phi_{L,\text{eq}} = d\phi_L + \frac{M_T(d\phi_L)}{\underbrace{c_m \beta_1 R_{\text{th}}}_{\text{machine stiffness}}} \quad (8.9)$$

Based on the findings of Section 6.3.2 the equivalent loaded bending plane rotation is determined by:

$$d\theta_{r,L,\text{eq}} = d\theta_r + \frac{M_T(d\phi_L)}{\underbrace{c_m \beta_1 R_{\text{th}}}_{\text{machine stiffness}}} \quad (8.10)$$

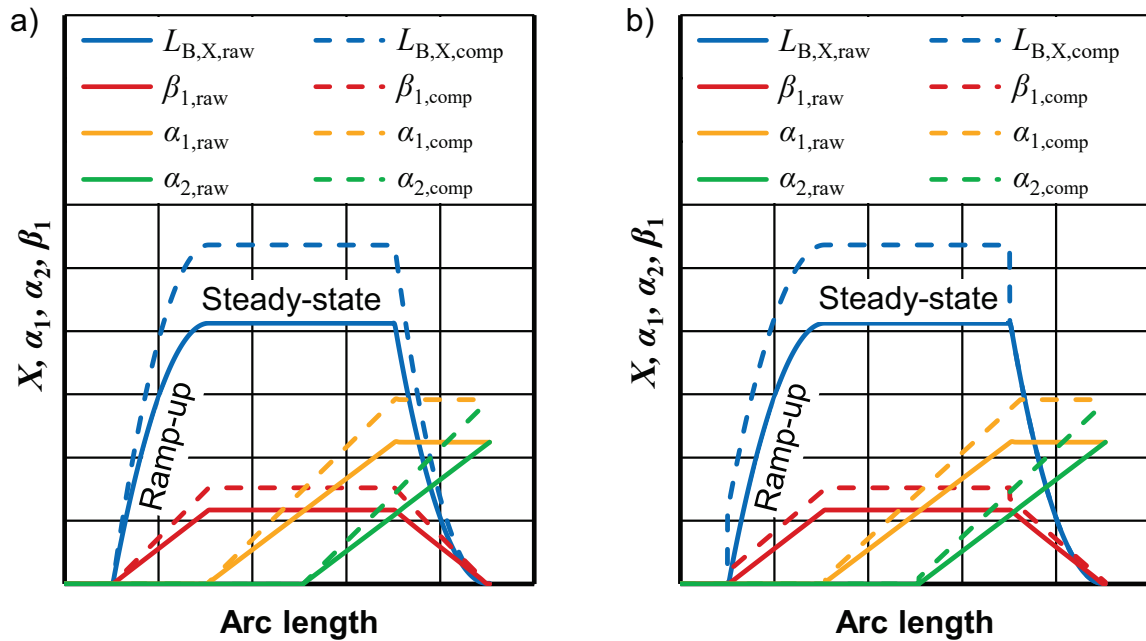
with the equivalent loaded cumulative rotation being:

$$\theta_{r,L,\text{eq,offset}} = \theta_{r,L,\text{eq}} + \theta + \eta \quad \text{with} \quad \eta = \sin^{-1} \left( \frac{F_{B,z}}{F_B} \right) \quad (8.11)$$

## 8.2 Generation of springback-compensated NC-data

Two strategies can now be used in order to determine the springback-compensated NC-data.

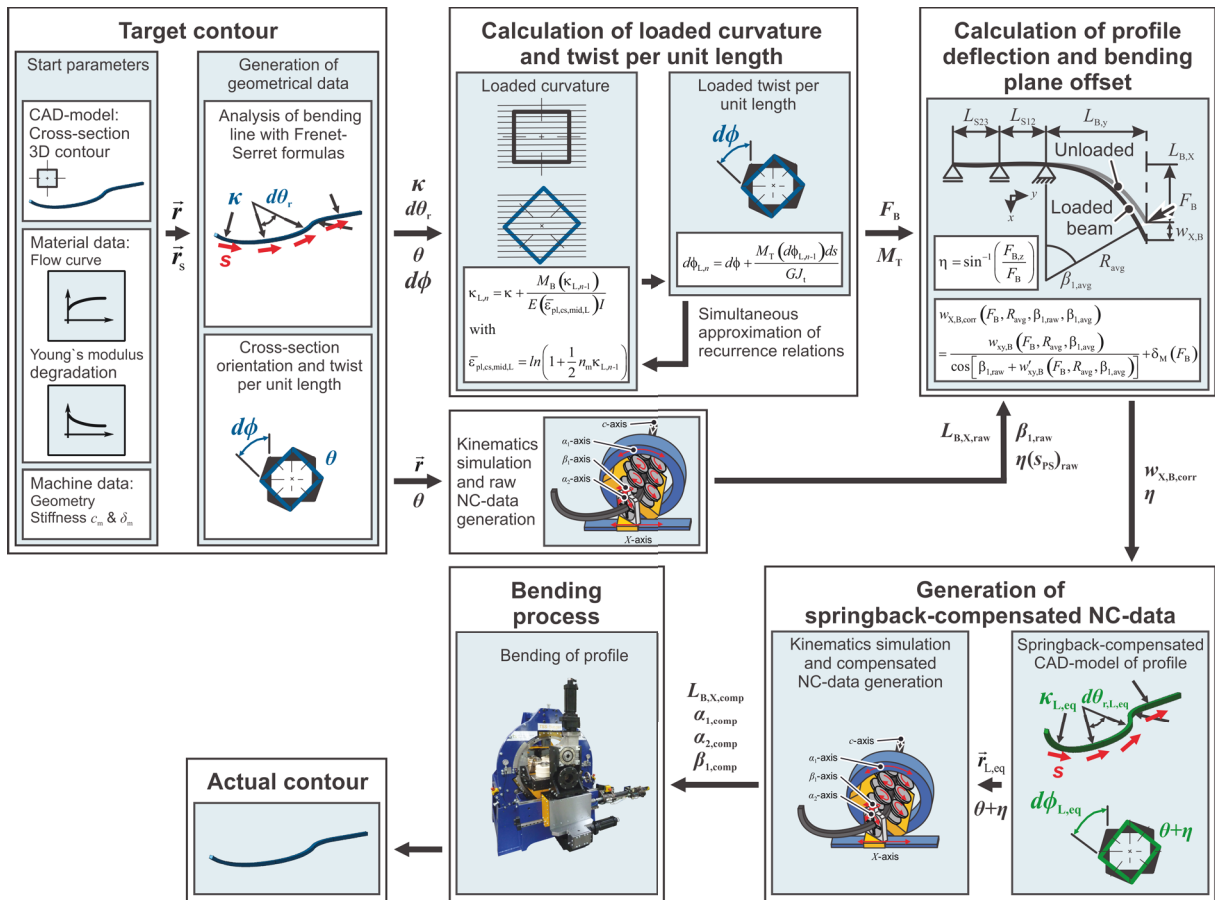
- The first method (a) is similar to the strategy by Hermes (2011): The equivalent loaded curvature, twist and bending plane rotation are used to generate a compensated profile shape, which, in turn, is used to generate the compensated NC-data in terms of the arc length  $s$  as explained in Section 4.2.3. (Figure 8.1a)
- The second method (b) uses the raw NC-data determined with the target profile geometry together with compensatory axis data generated from Eqs. (8.7), (8.9), and (8.11). When using this strategy it has to be respected that  $w_{X,B,\text{corr}}$  represents the deflection in the bending plane and not the deflection along the  $X$ -axis of the bending machine or along the resultant  $r$ . Consequently, when using the 5-cDOF TSS bending process with its single linear axis,  $w_{X,B,\text{corr}}$  has to be split up into an  $X$ -axis component and an  $\alpha_1$ -component. (Figure 8.1b)



**Figure 8.1:** Exemplary springback-compensated NC-data in comparison to raw data using the two above mentioned strategies: a) by the generation of a compensated profile shape, b) by direct compensation of axis data

Comparing the curves shown in Figure 8.1a and b it can be seen that, while the final compensated steady-state axis values are the same, the ramp-up is different. In the first method (a), the raw and compensated NC-Data both initiate at the same start values and smoothly deviate according to part geometry and material data. In the second method (b) the movements of all axes are distinguished by an abrupt data jump at the beginning of the ramp-up and at the end of the steady state region. This behavior can be generalized to all radius, twist, and bending plane rotation transitions. The advantage of these data jumps is the possibility to directly compensate the elasticity from the beginning of a new radius/twist/rotation segment resulting in smaller transition zones in between radii. A disadvantage is the increased complexity of the machine control. While in method (a) the feed speed can be constant, the data jumps in method (b) necessitate variable feed speeds. Also, even if method (b) allows for smaller transition zones, this effect has to be measurable. The 128 mm distance from contact unit 1 to contact unit 3 of the 3D contour sensor (see Section 5.3) results in the limitation that transition zones under 128 mm cannot be properly analyzed.

The process model validation is, thus, performed according to the method (a). The comprehensive process model that includes the generation of springback-compensated NC-data according to method (a) is shown in Figure 8.2.



**Figure 8.2:** Comprehensive process model of 3D profile bending using springback compensation method (a)

### 8.3 Process model demonstration

The process validation is performed using profiles experimentally bent to the theoretical radii 600 mm, 800 mm, and 1000 mm and twisted with 0 rad/m, 0.491 rad/m 0.982 rad/m. The same NC-data was used as for the comprehensive numerical model in Section 7.3.3. As such, the validation is performed inversely: the NC-data is seen as the compensated data, with the theoretical radius, twist, and bending plane rotation seen as the equivalent data. This equivalent data is recursively used to analytically calculate the target curvature, twist, and bending plane rotation, which are in turn compared to the experimentally obtained data. From the analyses in Section 6.3.2 it is known that twisting a profile without rotating the  $\alpha_1$ -axis results in a helix with a theoretical apparent twist per unit length  $d\phi_{\text{apparent}} = 0$ . Figure 8.3 shows the contour data of the experimentally bent helices, measured with the 3D-contour measurement device presented in Section 5.3, compared to the theoretical and analytically calculated data.

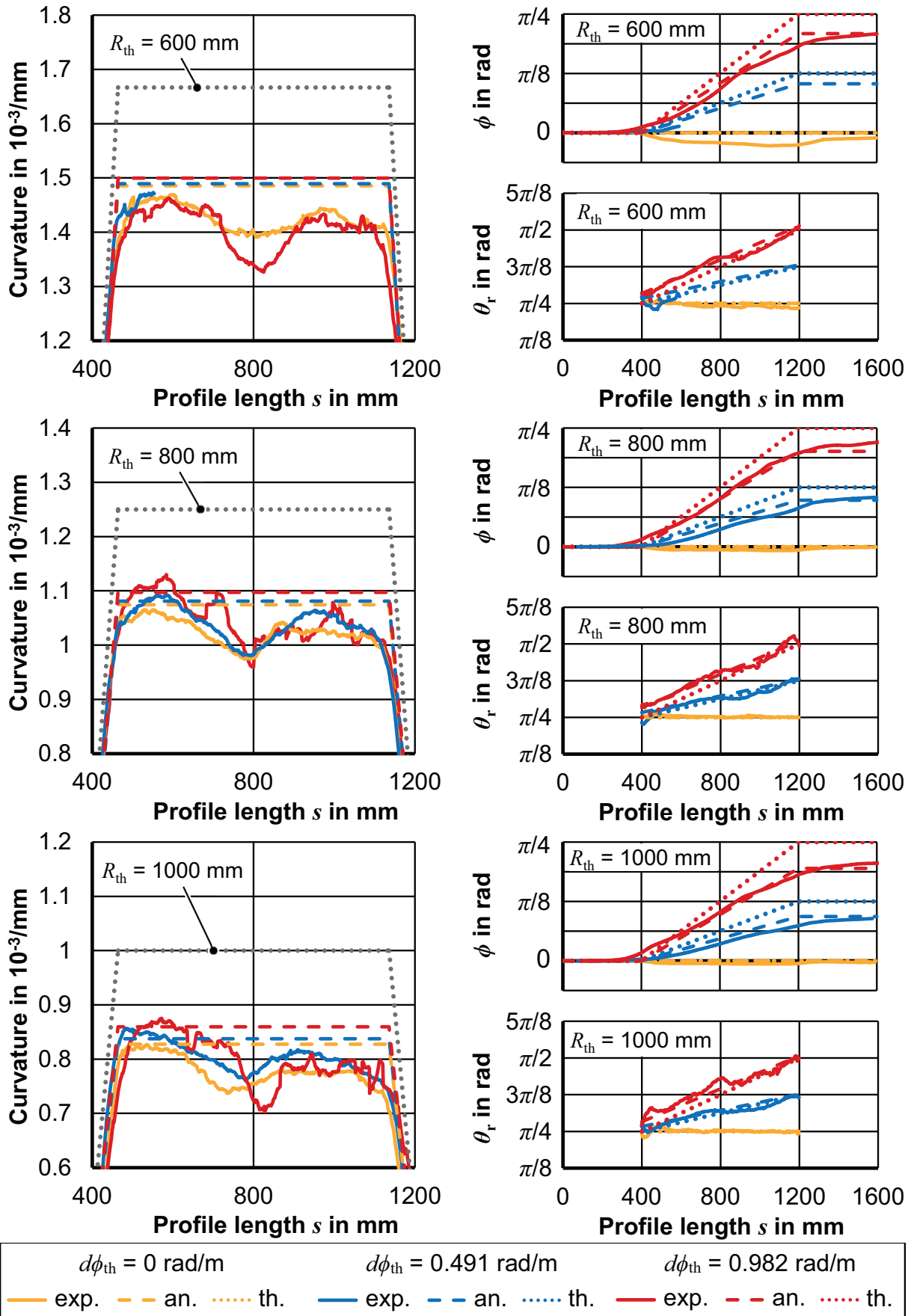
For  $R_{\text{th}} = 600$  mm, the deviation of the analytically calculated to the experimental peak curvature is 1.1 % for  $d\phi_{\text{th.}} = 0$  rad/m and  $d\phi_{\text{th.}} = 0.0491$  rad/m, and 2.5 % for  $d\phi_{\text{th.}} = 0.0982$  rad/m. The deviation of the average curvature in between the profile

lengths 500 mm and 1100 mm is 4.0 % for  $d\phi_{th.} = 0$  rad/m and 6.4 % for  $d\phi_{th.} = 0.0982$  rad/m. Although the deviation in twist per unit length at  $d\phi_{th.} = 0.0982$  rad/m in between profile lengths 500 mm and 1100 mm is on average 14.0 %, the finally reached value only shows a deviation of 0.3 %. This can be explained by the large transition zones that show that during ramp-up and ramp-down actually also the profile in between the bending head and the front profile support  $S_1$  is twisted outside of the forming zone defined by bending. The bending plane rotation shows an average deviation of 3.5 % in the same profile range. The analytically calculated cumulative rotation at a profile length of 1200 mm deviates 2.1 % from the experimentally obtained value.

For  $R_{th} = 800$  mm, the deviation of the analytically calculated to the experimental peak curvature is 0.9 % for  $d\phi_{th.} = 0$  rad/m, 1.1 % for  $d\phi_{th.} = 0.0491$  rad/m, and 2.9 % for  $d\phi_{th.} = 0.0982$  rad/m. The deviation of the average curvature in between the profile lengths 500 mm and 1100 mm is 4.9 % for  $d\phi_{th.} = 0$  rad/m, 4.0 % for  $d\phi_{th.} = 0.0491$  rad/m, and 4.5 % for  $d\phi_{th.} = 0.0982$  rad/m. The deviation in twist per unit length at  $d\phi_{th.} = 0.0491$  rad/m in between profile lengths 500 mm and 1100 mm is on average 14.3 %, while the finally reached cumulative twist value shows a deviation of 5.8 %. At  $d\phi_{th.} = 0.0982$  rad/m the average twist per unit length deviation is 4.3 % and the finally reached cumulative twist value shows a deviation of 8.5 %. The bending plane rotation shows an average deviation of 7.4 % at  $d\phi_{th.} = 0.0491$  rad/m and 1.9 % at  $d\phi_{th.} = 0.0982$  rad/m. The analytically calculated cumulative rotation at a profile length of 1200 mm deviates 0.6 % from the experimentally obtained value at  $d\phi_{th.} = 0.0491$  rad/m and 3.7 % at  $d\phi_{th.} = 0.0982$  rad/m.

For  $R_{th} = 1000$  mm, the deviation of the analytically calculated to the experimental peak curvature is 0.1 % for  $d\phi_{th.} = 0$  rad/m, 2.2 % for  $d\phi_{th.} = 0.0491$  rad/m, and 1.8 % for  $d\phi_{th.} = 0.0982$  rad/m. The deviation of the average curvature in between the profile lengths 500 mm and 1100 mm is 6.4 % for  $d\phi_{th.} = 0$  rad/m, 4.2 % for  $d\phi_{th.} = 0.0491$  rad/m, and 6.5 % for  $d\phi_{th.} = 0.0982$  rad/m. As for  $R_{th} = 600$  mm and 800 mm, the deviation in twist per unit length at  $d\phi_{th.} = 0.0491$  rad/m is relatively high with 20.0 %. As for the two other theoretical radii the finally reached cumulative twist value shows low deviation of 4.8 %. At  $d\phi_{th.} = 0.0982$  rad/m the average twist per unit length deviation is again relatively high with 17.1 % while the finally reached cumulative twist value shows only a deviation of 5.4 %. The bending plane rotation shows an average deviation of 11.5 % at  $d\phi_{th.} = 0.0491$  rad/m and 1.1 % at  $d\phi_{th.} = 0.0982$  rad/m. The analytically calculated cumulative rotation at a profile length of 1200 mm deviates 3.2 % from the experimentally obtained value at  $d\phi_{th.} = 0.0491$  rad/m and 1.4 % at  $d\phi_{th.} = 0.0982$  rad/m.





**Figure 8.3:** Validation of process model by comparison of experimentally bent helices made from MW700L Z1 at  $\theta = \pi/4$  to analytically calculated data

Overall, it can be said that the analytically calculated values for the curvature, twist, and bending plane rotation correlate well with the experimental data. What can be noticed in all curvature graphs is that, after a first curvature peak, a local minimum occurs in the transition from ramp-up to the steady state region after which a plateau develops with a central local maximum. This curvature trend can be explained by the used NC-data compensation method (a) (see exemplary Figure 8.1). This method does not take into account the elastic behavior of the straight profile between the profile support and the bending head prior to load application. With the initial movement of the bending head along the  $X$ -axis, the profile is, thus, not plastically deformed but only elastically. With further movement of the bending head, the profile reaches plastic strains in the forming zone at  $S_1$ . So, instead of a sharp curvature jump from 0 to the target curvature, a smooth trend develops. Since the NC-data assumes said sharp curvature jump, the profile necessarily needs to develop a curvature peak in order to develop a trend, which, on average, is equal to the targeted curvature. The movement of the curvature peak towards the bending head inevitably causes the following curvature to decrease, again, to average out this initial peak. The following plateau with the local maximum develops because of the same reason as the initial curvature peak and can be considered as the second wave in a dampened curvature oscillation. This behavior could be overcome to a certain extent by using method (b) for NC-data generation, whereby ideal curvature jumps will not be achievable and will have to actually be replaced with ramps as shown by Groth et al. (2018c).

In all of the cumulative twist diagrams, large transition zones are visible that begin before ramp-up (400 mm) and end after ramp-down (800 mm). This behavior is in contrast to the curvature graphs in which the transition zones actually begin after ramp-up and end before ramp down. As explained before, this behavior shows that twisting does not necessarily occur only in the forming zone as it was specified in Chapters 6 and 7. Especially during the slight initial  $X$ -axis movements that cause only elastic axial deformation of the profile, or only slight plastic deformation of the extrados and intrados, the resulting stress state in the specified forming zone is not high enough to cause a localization of the twist. This localization could be assisted by using method (b) for the NC-data generation. Here, it should be considered to apply the  $X$ -axis movement before rotating the  $\alpha_2$ -axis in order to generate a region of high axial stress prior to twisting. Another option would be to allow a movement of the bending head towards the profile support  $S_1$ . This would reduce  $L_{B,y}$  and allow a more localized application of the twist, independent of the stress-state in the profile segment in between  $S_1$  and the bending head.

Another interesting aspect that is noticed when comparing the cumulative twist and cumulative bending plane rotation diagrams is that the experimental and analytical cumulative apparent twist ( $\phi - \theta_R$ ) of the profiles is actually non-zero. This is because, while profile twist is dependent on profile springback and machine stiffness, the bending plane

rotation is only dependent on the machine stiffness. This independence of the bending plane rotation on profile springback can be understood when looking back at Section 6.3.2. Here, it was explained that the angle  $\eta$ , which describes the angle between the bending plane and the machine bending plane is only dependent on the bending force components. The good agreement of the analytical and experimental twist and bending plane rotation data show that this behavior is well implemented in the process model.

In Section 4.2.4 it was described how a parasitic torque develops during bending plane changes and it was deduced that this torque was responsible for the deviations of around 15 % between targeted and set bending plane rotations, which were noticed by Hudovernik (2014a) in his 3-cDOF bending tests. The question here is, how this torque can be compensated? In the 5-cDOF process, the resulting torque is directly taken up by a reaction moment in the bending head. In the 3-cDOF TSS bending process and also in the three-roll push bending process, the rotation of the cross-section in the bending head or setting roll is free. No torque can be applied here. However, by using the target contour, in this case solely the bending line since the cross-section rotation cannot be controlled, the bending plane angle  $\eta$  can be determined (Eq. (4.74)). The next steps have to be performed inside a recurrence scheme. Using the initially unknown bending moment and the angle  $\eta$ , the force  $F_{B,z}$  can be determined. Using the elastic beam calculations from Chapter 6 the resulting torque at  $M_{S_{1,y}}$  ( $=M_{T,p}$ ) can be determined – the torque  $M_T$  at  $P_{FB}$  is 0 in this calculation. The torque gives the shear stress distribution (Eq. (7.60)) over the cross-section. Using the axial strain distribution given by the target curvature together with the shear stress distribution and Eqs. (7.98), (7.99), and (7.100), the maximum shear strain  $\gamma_m$  is determined. The average shear strain  $\gamma_{avg}$  is then calculated by Eqs. (7.95) or (7.96) for rectangular cross-sections. For circular cross-sections  $\gamma_{avg}$  is obtained by, first, projecting a linear increasing shear strain onto the circumference (similar to the method shown for a rectangular profile in Figure 7.20) and by then averaging the strain values. Eq. (7.64) is finally used to determine  $d\phi$ , which, in the case of 3-cDOF TSS bending process and three-roll push bending is the unwanted twist per unit length that leads to a reduced bending plane rotation. In order to compensate this unwanted behavior,  $d\phi$  has to be added to the targeted  $d\theta_r$ .



## 9 Conclusion and outlook

Kinematic 3D profile bending opens up a whole new area of geometric freedom, which is inline with with current demands by the industry and consumers regarding natural and aesthetic shapes, lightweight design, and individuality. Profiles with non-circular cross-sections allow geometric function integration by especially selecting cross-sections that are adapted for specific applications and applied loads. Although several 3D bending processes have been developed in the recent decades that allow kinematic 3D profile bending, the process is not yet widely used. A research of the state of the art has shown that the main factor limiting its widespread use, has, up until now, been the limited knowledge of fundamental aspects of 3D bending itself.

The first step towards a fundamental understanding of 3D bending was the setup of a sound mathematical model of a 3D shaped profile with a twisted cross-section. Special care was taken to describe the relationship of cross-sectional twist and bending plane rotation. Beside a continuous mathematical description a discrete description is given, which, depending on the differentiability of the curves, is either a necessity when analyzing 3D shapes or might just be easier to implement in control or analysis software. Next, the fundamental number and positions of actuators was analyzed, needed for the production of a 3D bent profile part with and without a twisted cross-section. This fundamental view allowed a classification of currently available kinematic bending processes with respect to their freedom in shape generation. As a final step in the geometrical analysis of 3D profile bending the mathematical relationship of the profile shape and actuator movements was derived.

Using the knowledge gained in the geometrical analysis, the 3-cDOF TSS bending process was extended to a 5-cDOF-bending process, thereby, expanding the range of producible shapes from simple 3D bending lines to shapes with 3D bending lines and twisted cross-sections. In order to analyze the shapes during and after bending, a flange-based torque sensor was developed and integrated into the bending head. Additionally, a 3D contour sensor was designed and manufactured that allows the time efficient online and offline measurement of 3D shaped profiles. Since kinematic bending is highly affected by springback, not only the flow curve of the investigated material was set up but also the impact of plastic strain on the apparent Young's modulus, or cord modulus, was investigated. Here, it was noticed that the apparent Young's modulus decreases from 199 GPa down to around 175 GPa for both MW700L Z1 and MW700L Z3 at an equivalent plastic strain of only 0.02. Up until a strain of 0.05 the apparent Young's modulus even drops down to below 160 GPa. A comparison with the state of the art showed that this material behavior is actually common in all modern steel grades. Since elastic models generally work with a static Young's modulus, it was proposed to use the average

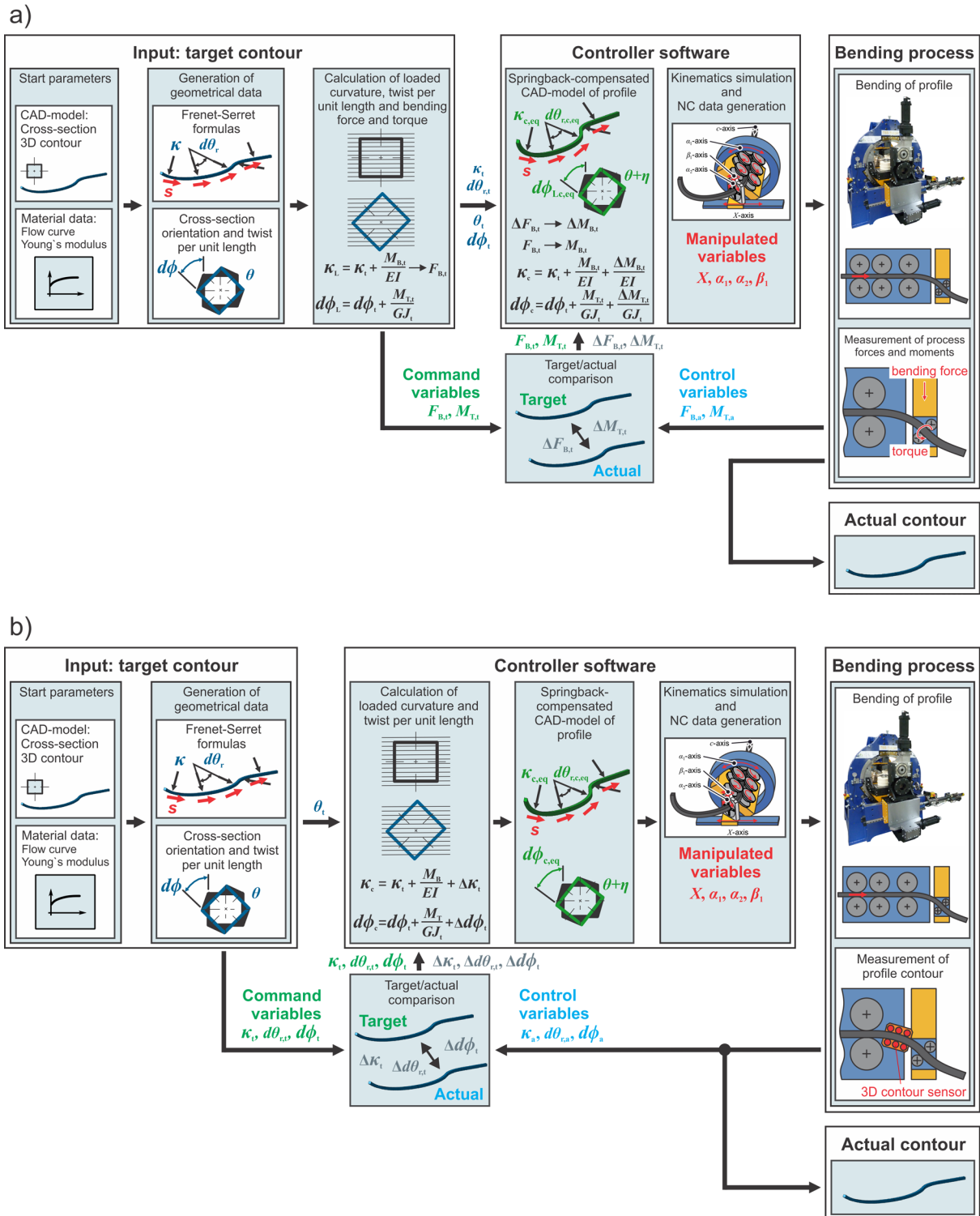
equivalent strain of the cross-section to determine the apparent Young's modulus of the loaded profile.

The assessment of the impact of torsion on the bending process was split up into an elastic analysis and a plastic analysis. In the elastic analysis, a curved beam model was set up and the influence of different profile supports was investigated. The model can be used to represent a beam held by up to three roller/hinged supports, a single full-moment support, or a combination of a single hinged support and a single full-moment support. In the deflection calculation, it became apparent that the curved representation is essential for an accurate calculation of the elastic behavior of bent profiles. While the accuracy of the calculated deflection using a curved beam model is about two times as high as the deflection calculated using a straight beam at a theoretical radius of 1000 mm, the accuracy is actually 7 times as high at a radius of 600 mm. By applying a torque to the curved beam model, an additional force component at the point of bending force application could be determined, which lies orthogonal to the in-plane bending force. By comparing analytical data with experimental investigations, it was found out that this vertical force can be used to determine the actual bending plane position and that it is the cause of a rotation of the bending plane.

In order to feed the elastic beam model with the correct bending force and torque data, the stresses and strains in the forming zone during simultaneous bending and twisting were investigated next. A thorough analysis of an analytical plane stress model showed that the shift of the neutral axis, caused by perimetral stress, has insignificant effects on the finally calculated bending moment. The plane stress model could, as a consequence, be simplified to a uniaxial stress state with additional shear stress. In numerical analyses that were performed alongside the analytical modelling it was observed that the shear strain during combined loading of bending and torsion is not uniform over the cross-section, but rather decreases linearly towards the neutral axis. The integration of this behavior into the analytical model lead to bending forces that are in accordance with targeted values, not only qualitatively but also quantitatively.

Finally, the knowledge about geometric modelling, elastic profile deformation, and plastic profile behavior was merged into a single comprehensive process model. In the model validation, deviations of the curvature, cumulative twist, and cumulative bending plane rotation of around 5 % were achieved, which prove the applicability of the presented model. Additionally to the usability of the model for 3D profile bending to compensate elastic deformation during the process, it was explained how the model could be adapted to determine the bending plane rotation difference noticed during 3D bending using 3-cDOF bending processes as three-roll push bending.

Although the validation of the developed process model has shown well correlating experimental and analytical data, the deviations of the curvature, cumulative twist and cumulative bending plane rotation of around 5 % might still be too high for certain applications. An accuracy increase is expected from using the direct compensation method



**Figure 9.1:** Concepts of a) indirect closed-loop control b) direct closed-loop control (Staupendahl et al., 2016)

of NC-data generation (Figure 8.1b). However, minimal shape deviations will only be achievable through the integration of a closed-loop control system. Figure 9.1a shows the concept of an indirect closed-loop control system, which uses force and torque measurements as control parameters. Figure 9.1b displays the concept of a direct closed-loop control system, which uses the measured contour data – curvature, twist per unit length, and bending plane rotation – as control parameters. The closed-loop control concepts are exemplarily shown for the combination with the NC-data compensation strategy using a compensated profile shape (Figure 8.1a). The advantage of the indirect closed-loop control is the use of the instantaneous load measurements of the currently bent profile segment. This means that only the calculation time of the compensation algorithm appears as a lag element. The disadvantage is that the relationship between process forces and resulting shape data has to be very accurate and might need additional calibration. The advantage of the direct closed-loop control is the direct measurement of the actual profile shape. The disadvantage is that the shape cannot be measured directly in the forming zone due to limited access. The contour sensor is, thus, either placed in between the profile support and the bending head or downstream of the bending head. This means that, additionally to the lag element caused by the compensation calculation, a lag element caused by delayed contour measurement is introduced into the system. The impact of these conditions will have to be investigated in future studies.



## References

- Al-Qureshi, H. A., 1999. Elastic-plastic analysis of tube bending. *International Journal of Machine Tools and Manufacture*, 39 (1), pp. 87-104.
- An, Y. G., Vegter, H., 2005. Analytical and experimental study of frictional behavior in through-thickness compression test. *Journal of Materials Processing Technology*, 160 (2), pp.148-155.
- ASTM E1876-09, 2009. Standard test method for dynamic Young's Modulus, Shear Modulus, and Poisson's ratio by impulse excitation of vibration. *Annual Book of ASTM Standards*. West Conshohocken, PA: ASTM International, pp.1181-1196.
- Atlanta Antriebssysteme, 2012: HT-Servo-Hochleistungsgetriebe [HT-Servo-High-Power Gear Units], p. GA-12, <https://atlantagmbh.de/download/pdf-kataloge/servo-antriebssysteme/>.
- Belytschko, T., Liu, W.K., Moran, B., Elkhodary, K.I., 2014. *Nonlinear Finite Elements for Continua and Structures*, second ed. John Wiley & Sons, Ltd, Chichester, pp. 337-346.
- Becker, C., Tekkaya, A. E., Kleiner, M., 2014. Fundamentals of the incremental tube forming process, *CIRP Ann. Manuf. Technol.* 63 (1), pp. 253-256.
- Beulich, N., Craighero, P., Volk, W., 2017. FEA Simulation of Free-Bending – a Pre-forming Step in the Hydroforming Process Chain, *Journal of Physics: Conf. Series* 896, 012063.
- Boger, R.K., Wagoner, R.H., Barlat, F., Lee, M.G., Chung, K., 2005. Continuous, large strain, tension/compression testing of sheet material. *Int. J. Plasticity*, 21 (12), pp. 2319-2343.
- Bredt, R., 1896. Kritische Bemerkungen zur Drehungselastizität [Critical remarks on torsional elasticity]. *ZVDI*, 40 (28), pp. 785-790 & 40 (29), pp. 813- 817.
- Cao, J., Lee, W., Cheng, H.S., Seniw, M., Wang, H.-P., Chung, K., 2009. Experimental and numerical investigation of combined isotropic-kinematic hardening behavior of sheet metals. *Int. J. Plasticity*, 25 (5), pp. 942-972.
- Chatti, S., 1997. *Optimierung der Fertigungsgenauigkeit beim Profilbiegen [Optimization of the Manufacturing Accuracy During Profile Bending]*. Dissertation, Universität Dortmund.
- Chatti, S., Hermes, M., Tekkaya, A. E., Kleiner, M., 2010. The new TSS bending process: 3D bending of profiles with arbitrary cross-sections. *CIRP Ann. Manuf. Technol*, 59 (1), pp. 315-318.

- Chatti, S., Maevus, F., Hermes, M., Tekkaya, A. E., Kleiner, M., 2012. Biegeumformung. In: Hoffmann, H., Neugebauer, R., Spur, G. (eds), Handbuch Umformtechnik. Carl Hanser Verlag, pp. 573-606.
- Chongthairungruang, B., Uthaisangasuk, V., Suranuntchai, S., Jirathearanat, S., 2012. Experimental and numerical investigation of springback effect for advanced high strength dual phase steel. *Materials & Design*, 2012. 39 (0): pp. 318-328.
- DIN EN ISO 6892-1:2009-12. Zugversuch – Teil 1 Prüfverfahren bei Raumtemperatur. Beuth Verlag, Berlin.
- Dirksen, U., 2008. Testumgebung für Prozessregelungen zum Drei-Rollen-Profilbiegen mit virtuellem und realen Biegeprozess [Testing Environment for Closed-Loop Process Controls for Three-Roll Bending]. Dissertation, Technische Universität Dortmund.
- Döbele, S., Eichhorn, S., Trübswetter, I., Burghardt, R., Obst, T., Lucke, M. Koch, R. Stöckle, U., 2009. Optische Messsysteme ermöglichen die Erfassung von komplexen Bewegungen im Mikrometerbereich [Optical Measurement Systems Allow the Capture of Complex Movements in the Range of Microns]. Verifikation eines innovativen optischen Messsystems der Firma GOM mbH – Gesellschaft für Optische Messtechnik – für biomechanische Anwendungen. Implantate für Orthopädie und Traumatologie & Tissue Engineerte Biomaterialien, Internationale Biomechanik- und Biomaterial-Tage, 11, In: Biomaterialien, 10 (1/2), p. 42.
- Eichhorn, A., 1974. Ein Beitrag zur Untersuchung technologisch bedingter Formabweichungen am Werkstück beim Profilieren von Metallbändern [A Contribution to the Investigation of Technologically Based Form Deviations of the Workpiece During Roll Forming of Metal Strips]. Dissertation, TH Magdeburg.
- El Megharbel, A., El Nasser, G.A., El Domiaty, A., 2008. Bending of tube and section made of strain-hardening materials, *Journal of Materials Processing Technology*, 203 (1-3), pp. 372-380.
- Engel, B., Gerlach, C., Cordes, S., 2008. Biegemomentabschätzung des Dornbiegeverfahrens [Bending Moment Approximation of Rotary Draw Bending], *UTF science*, 2, pp. 1-8.
- Engel, B., Kersten, S., 2011. Analytical Models to Improve the Three-Roll-Pushbending Process of Tube-Profiles. *Steel Research International*, special edition. ICTP 2011, pp. 355–360.
- Engel, B., Groth, S., 2015. Analyse der Torsionsverformung beim Drei-Rollen-Schubbiegen von Rundrohren [Analysis of the Torsion Deformation During Three-Roll Push Bending of Tubes]. In: Proc. of the XXXIV Verformungskundliches Kolloquium. Leoben, Austria. pp. 87–92.

- Flehmg, T., Kibben, M., Kühni, U., Ziswiler, J., 2009. Device for the free forming and bending of longitudinal profiles, particularly pipes, and a combined device for free forming and bending as well as draw-bending longitudinal profiles, particularly pipes. European patent: EP1863604 B1, priority date: 22.03.2005.
- Francke, W., Friemann, H., 2005. Schub und Torsion in geraden Stäben. Vieweg & Sohn Verlag/GWV Fachverlage GmbH, 3. Edition, Wiesbaden, p. 160.
- Franz, W.-D., 1961. Das Kalt-Biegen von Rohren [Bending of Tubes at Room Temperature]. Springer-Verlag, Berlin/Göttingen/Heidelberg.
- Frenet, F., 1852. Sur les courbes à double courbure, *Journal de mathématiques pures et appliquées*, 17, pp. 437-447.
- Gantner, P.; Bauer, H.; Harrison, D. K.; DeSilva, A. K. M.: The Investigation of a Close-to-Reality Simulation Model for the Free-Bending Technique. In: 19<sup>th</sup> Int. Conf. CAPE 2005: Computer-Aided Production Engineering, pp. 109-118.
- Gerlach, C., 2010. Ein Beitrag zur Herstellung definierter Freiformbiegegeometrien bei Rohren und Profilen [A Contribution to the Manufacturing of Tubes and Profiles with Free Form Bending Geometries]. Shaker Verlag, Aachen.
- Gerstein, G., Clausmeyer, T., Isik, K., Nürnberger, F., Tekkaya, A. E., Bruchanov, A. A., Maier, H. J., 2017. Experimental analysis of anisotropic damage in dual-phase steel by resonance measurement. *International Journal of Damage Mechanics*, 26 (8), pp. 1147-1169.
- Ghiotti, A., Simonetto, E., Bruschi, S., Bariani, P. F., 2017. Springback measurement in three roll push bending process of hollow structural sections. *CIRP Ann. Manuf. Technol.* 66 (1), pp. 289-292.
- Goto, H., Ichiryu, K., Saito, H., Ishikura, Y., Tanaka, Y., 2008. Applications With a New 6-DOF Bending Machine in Tube Forming Processes. In: Proceedings of the 7th JFPS International Symposium on Fluid Power, TOYAMA, September 15-18, pp.183-188.
- Goto, H., Ichiryu, K., Saito, H., Ishikura, Y., Tanaka, Y., 2012. 3D Tube Forming and Applications of a New Bending Machine with Hydraulic Parallel Kinematics. *Int. J. of Automation Technology*, 6 (4), pp. 509-515.
- Groche, P., Schneider, R., 2000. Umformtechnik für die Produkte von morgen [Forming Technology for the Products of Tomorrow]. In: Groche, P. (Ed.), Anforderungen – Innovationen – Perspektiven: 7. Umformtechnisches Kolloquium Darmstadt, Bamberg, Meisenbach.

- Groth, S., Engel, B., 2017. Determination of the bending line of bent tubes by an analytical plasticity model considering process kinematics. In: Proceedings Conference on Plasticity, Damage and Fracture, Puerto Vallarta (Mexico).
- Groth, S., Engel, B., 2018a. A method for manufacturing bent profiles with open cross-section by die-push-bending. In: ITAtube Journal 2018 (1), pp. 44-49.
- Groth, S., Engel, B., Frohn, P., 2018b. Approach to a manufacture-oriented modeling of bent tubes depending on the curvature distribution during three-roll-push-bending. In: Proceedings of the 21st International ESAFORM Conference on Material Forming, AIP Conf. Proc. 1960, 110006.
- Groth, S., Engel, B., Langhammer, K., 2018c. Algorithm for the quantitative description of freeform bend tubes produced by the three-roll-push-bending process. Prod. Eng. Res. Devel., 12 (3-4), pp. 517-524.
- Grzancic, G., Löbbe, C., Ben Khalifa, N., Tekkaya, A. E., 2019. Analytical prediction of wall thickness reduction and forming forces during the radial indentation process in Incremental Profile Forming. Journal of Materials Processing Technology, 267, pp. 68-79.
- Guo, X., Xiong, H., Xu, Y., Ma, Y., Abd El-Aty, A., Tao, J., Jin, K., 2018. Free-bending process characteristics and forming process design of copper tubular components. The International Journal of Advanced Manufacturing Technology, 96 (9-12), pp. 3585-3601.
- Hagenah, H., Vipavc, D., Plettke, R., Merklein, M., 2010. Numerical model of tube free-form Bending by Three-roll-push-bending. In: 2<sup>nd</sup> Int. Conf. on Engineering Optimization. Lisbon, Portugal. pp. 1-10.
- Halmos, G. T., 2006. Roll Forming Handbook, CRC Press, Taylor & Francis Group, Boca Raton, pp. 6-10.
- Hassan, H. R., 2017. Plasto-Mechanical Model of Tube Bending in Rotary Draw Bending Process. Dissertation, Universität Siegen.
- Heath, T. L., 1921. A History of Greek Mathematics (Vol II). Oxford University Press. pp. 321-323.
- Hermes, M., Chatti, S., Weinrich, A., Tekkaya, A. E., 2008. Three-Dimensional Bending of Profiles with Stress Superposition. International Journal of Material Forming, 1 (1), pp. 133-136.
- Hermes, M. 2011. Neue Verfahren zum rollenbasierten 3D-Biegen von Profilen [New Processes for Roll-Based 3D Bending of Profiles]. Dissertation, Technische Universität Dortmund.

- Hermes, M., Kleiner, M., 2013. Method and Device for Profile Bending, European patent EP 2 144 720 B1, priority date: 20.03.2007.
- Hill, R., 1950. A theory of the plastic bulging of a metal diaphragm by lateral pressure. *Philosophical Magazine Series 7*, 41 (322), pp. 1133-1142.
- Hinkel, M., 2013. Prozessfenster für das Spannen von Rohrprofilen beim Rotationszugbiegen unter Berücksichtigung der Tribologie [Process Window for the Clamping of Tubes During Rotary Draw Bending Considering Tribology]. Dissertation, Universität Siegen.
- Hockett, J. E., Sherby, O. D., 1975. Large strain deformation of polycrystalline metals at low homologous temperatures. *Journal of the Mechanics and Physics of Solids*, 23 (2), pp. 87-98.
- Hoffmann, K., 1987. Eine Einführung in die Technik des Messens mit Dehnungsmessstreifen [An Introduction to the Technique of Measuring using Strain Gauges], Hottinger Baldwin Messtechnik GmbH, Darmstadt, p. 240.
- Hoffmann, Michael; Leischnig, Steffen; Naumann, Christian; Otto-Adamczak, Tobias; Priber, Ulrich; Strauß, Michael; Tropper, Matthias. 2013, HexaBend – Freiformbiegen auf einer parallelkinematischen Biegemaschine [HexaBend – Free-Form Bending on a Parallel Kinematics-Type Bending Machine], Verbundprojekt im Rahmenkonzept "KMU-Innovativ" des Bundesministeriums für Bildung und Forschung (BMBF). In: Fraunhofer-Institut für Werkzeugmaschinen und Umformtechnik (Ed.), Technische Informationsbibliothek u. Universitätsbibliothek, Chemnitz [u.a.], Hannover.
- Hollomon, J. H., 1945. Tensile deformation. *Transactions of the American Institute of Mining, Metallurgical and Petroleum Engineers (AIME)*, 162, pp. 268-290.
- Hubmer, G., Klein, M., Spindler, H., Sonnleitner, M., Wagner, J., Aigner, A., 2017. Roll-formed HF welded tubes and sections made from ultra-high strength martensitic steels with yield strength 960 MPa – and beyond. In: *Proceedings of the SCT 2017 – 5th Intern. Conf. on Steels in Cars and Trucks, Future Trends in steel development, processing technologies and applications*, Noordwijkerhout/Amsterdam, The Netherlands.
- Hudovernik, M., Staupendahl, D., Gharbi, M., Hermes, M., Tekkaya, A.E., Kuzman, K., Slabe, J.M., 2013. 3D numerical analysis of 2D profile bending with the torque superposed spatial bending method. *Strojniški vestnik – J. Mech. Eng.*, 59 (3), pp. 139-147.
- Hudovernik, M., 2014a. Characterisation of the Process for 3D Bending of Profiles. Dissertation. Faculty of Mechanical Engineering, University of Ljubljana.

- Hudovernik, M., Kosel, F., Staupendahl, D., Tekkaya, A.E., Kuzman, K., 2014b. Application of the bending theory on square-hollow sections made from high strength steel with a changing angle of the bending plane. *J. Mat. Proc. Technol.*, 214 (11), pp. 2505-2513.
- Ismar, H., Mahrenholtz, O., 1979. *Technische Plastomechanik*. Vieweg & Sohn Verlagsgesellschaft, Braunschweig.
- Iwata, N., Matsui, M., Kato, T., Kaneko, K., Tsutamori, H., Suzuki, N., Gotoh, M., 2001. Numerical prediction of spring-back behavior of a stamped metal sheet by considering material nonlinearity during unloading. In: Mori, K. (Ed.), *Proceedings of the Seventh International Conference on Numerical Methods in Industrial Forming Processes*, Balkema, Lisse, pp. 693-698.
- Kersten, S., 2013. *Prozessmodelle zum Drei-Rollen-Schubbiegen von Rohrprofilen* [Process Models for Three-Roll Push Bending of Tubes]. Shaker Verlag, Aachen.
- Kibben, M., Mertens, O., Flehmig, T., Van der Heiden, A. T., Mulder, G. J. J., De Jong, R. B., De Graaf, M. G., 2013. Device and Method for Manufacturing Profiles with Shape That is Variable According to the Position and is Oriented in the Length Direction. European patent: EP2780126 B1, priority date: 15.11.2011.
- Klaus, A., 2002. *Verbesserung der Fertigungsgenauigkeit und der Prozesssicherheit des Rundens beim Strangpressen* [Increase of the Manufacturing Accuracy and the Process Stability of Curved Profile Extrusion], Shaker Verlag, Aachen.
- Krautkrämer, J., Krautkrämer, H., 1990 (reprint 2002). *Ultrasonic Testing of Materials*. Translation of: *Werkstoffprüfung mit Ultraschall*. 5th rev. ed. 1987, Springer, Berlin, Heidelberg, New York, pp. 533–535.
- Kuwabara, T., Kumano, Y., Ziegelheim, J., Kurosaki, I., 2009. Tension–compression asymmetry of phosphor bronze for electronic parts and its effect on bending behavior. *International Journal of Plasticity*, 25 (9), pp. 1759–1776.
- Lems, W., 1963. *The change of Young's modulus after deformational at low temperature and its recovery*. Dissertation, Delft University of Technology.
- Lohse, W., Laumann, J., Wolf, C., 2016. *Bemessung von Stahlbauten* [Structural Design of Steel Structures]. In: *Stahlbau 1*. Springer Vieweg, Wiesbaden, pp.100-101.
- Ludwik, P., 1903: *Technologische Studie über Blechbiegung – ein Beitrag zur Mechanik der Formänderungen* [Technological Study on Sheet Metal Bending – a Contribution on the Mechanics of Deformation]. *Technische Blätter – Zeitschrift des Deutschen Polytechnischen Vereins in Böhmen*, 35, pp. 133-159.
- Ludwik, P., 1909. *Elemente der technologischen Mechanik*, [Elements of Technological Mechanics]. J. Springer-Verlag, Berlin.

- Magro, T., Simonetto, E., Ghiotti, A., Savio, E., Brushi, S., 2019. Testing the accuracy of in-process springback measurements in tube draw bending. In: AIP Conference Proceedings 2113, 170013.
- Merklein, M., Biasutti, M., 2011. Forward and reverse simple shear test experiments for material modeling in forming simulations. In: Hirt, G., Tekkaya, A.E. (Eds.), International Conference on Technology of Plasticity, Aachen, pp. 702-707.
- Morestin, F., Boivin, M., 1996. On the necessity of taking into account the variation in the Young modulus with plastic strain in elastic-plastic software. Nuclear Engineering and Design, 162 (1): pp. 107-116.
- Murata, M., Ohashi, N., Suzuki, H., 1989. New flexible penetration bending of a tube: 1<sup>st</sup> report, a study of MOS bending method. Trans. Jpn. Soc. Mech. Eng., C 55, pp. 2488-2492.
- Murata, M., Yamamoto, S., Suzuki, H., 1994. Development of CNC machine for tube bending. Journal of JSTP 35, pp. 262-267.
- Murata, M., 1996. Experimental study of square tube bending by MOS bending method. Journal of JSTP, 37, pp. 515-520.
- Nazari, E., Staupendahl, D., Löbke, C., Tekkaya, A. E., 2019. Bending moment in incremental tube forming. International Journal of Material Forming, 12 (1), pp. 113-122.
- Neugebauer, R., Drossel, W.-G., Blau, P., 2001. 3D-Freiformbiegen von Profilen. HexaBend – ein neuartiges Konzept [3D Free-Form Bending of Profiles. HexaBend – a Novel Concept]. ZWF – Zeitschrift für wirtschaftlichen Fabrikbetrieb, 96 (11-12), pp. 611-615.
- Oehler, G.W., 1951. Gestaltung gezogener Blechteile [Design of Drawn Sheet Metal Parts]. In: Cornelius, E.-A. (Ed.), Konstruktionsbücher, Springer-Verlag Berlin Heidelberg, p. 102.
- Olympus, 2018: <https://www.olympus-ims.com/de/applications/elastic-modulus-measurement/>. Last access on 25 February, 2019.
- Pahl, G., Beitz, W., 1977. Konstruktionslehre [Engineering Design], 1st ed., Springer, Berlin.
- Paulsen, F., Welo, T., 2001. Cross-sectional deformations of rectangular hollow sections in bending: Part II — analytical models. International Journal of Mechanical Sciences, 43 (1), pp. 131-152.
- Plettke, R., Vatter, P.H., Vlpavc, D., 2012. Basics of process design for 3D freeform bending. Steel research international. 14<sup>th</sup> Int. Conf. on Metal Forming, special edition. pp. 307-310.

- Popov, V. L., 2010. Kontaktmechanik und Reibung - Von der Nanotribologie bis zur Erdbebendynamik [Contact Mechanics and Friction], 2nd ed., Springer-Verlag Berlin Heidelberg, p. 65.
- Roik, K H., 1978. Vorlesungen über Stahlbau (Grundlagen) [Lectures about Steelwork (Basic Principles)]. Verlag Wilhelm Ernst & Sohn, Berlin, München, Düsseldorf.
- Saint Venant, A. J.-C. B. de, 1855. Mémoire sur la Torsion des Prismes, avec des considérations sur leur flexion, ainsi que sur l'équilibre intérieur des solides élastiques en général, et des formules pratiques pour le calcul de leur résistance à divers efforts s'exerçant simultanément [Essay on the torsion of prisms, with considerations on their springback, as well as on the internal equilibrium of elastic solids in general, and practical forms for the calculation of their resistance to various simultaneous forces]. Mémoires présentés par divers savants à l'Académie des Sciences de l'Institut Impérial de France. Recueil des savants étrangers, 14, pp. 233-560.
- Serret J.-A., 1851. Sur quelques formules relatives à la théorie des courbes à double courbure [On Some Formulas Related to the Theory of Double-Curvature Curves], Journal de mathématiques pures et appliquées, 16, pp. 193-207.
- Shackelford, J. F., 1992. Introduction to Materials Science for Engineers, third ed., MacMillan, New York, p. 349.
- Sloan, Alfred P. Jr., 1963 (Reissue, 2015). My Years with General Motors, eNet Press Inc. Lake Oswego, p. 205.
- Staupendahl, D., Becker, C., Hermes, M., Tekkaya, A.E., Kleiner, M., 2011. New methods for manufacturing 3D-bent lightweight structures. In: Wieland, H.J., TEMA Technologie Marketing AG (Eds.), SCT 2011. 3<sup>rd</sup> Intern. Conf. on Steels in Cars and Trucks, Future Trends in Steel Development, Processing Technologies and Applications, Verlag Stahleisen, Düsseldorf, pp. 120-129.
- Staupendahl, D., Becker, C., Hermes, M., Tekkaya, A.E., Hudovernik, M., Quintana, G., Cavallini, B., Esteve Oró, F., Tassan, M., Servoli, G., Di Rosa, S., Tolazzi, M., Sulaiman, H., Salomon, R., 2014a. Flexible and cost-effective innovative manufacturing of complex 3D-bent tubes and profiles made of high-strength steels for automotive lightweight structures (ProTuBend). Luxembourg, Publication Office of the European Union.
- Staupendahl, D., Löbbe, C., Becker, C., Tekkaya, A.E., 2014b. Process Combinations for the Production of Load-Optimized Structural Components. In: Wieland, H.J., Brockmann, S., TEMA Technologie Marketing AG (Eds.), SCT 2014. 4<sup>th</sup> Intern.



- Conf. on Steels in Cars and Trucks, Future Trends in steel development, processing technologies and applications, Verlag Stahleisen, Düsseldorf, pp. 638-645.
- Staupendahl, D., Becker, C., Tekkaya, A.E., 2015. The impact of torsion on the bending curve during 3D bending of thin-walled tubes – a case study on forming helices. *Key Eng. Mater.*, 651-653, pp. 1595-1601.
- Staupendahl, D., Chatti, S., Tekkaya, A.E. 2016. Closed-loop control concept for kinematic 3D-profile bending. In: *AIP Conference Proceedings*, 1769, 150002.
- Staupendahl, D., Tekkaya, A.E., 2017a. Inline-measurement of complex profile contours for the generation of process parameters used in 3D-bending, In: *Proceedings of the SCT 2017 – 5th Intern. Conf. on Steels in Cars and Trucks, Future Trends in steel development, processing technologies and applications*, Noordwijkerhout/Amsterdam, The Netherlands.
- Staupendahl, D., Tekkaya, A.E., 2017b. The reciprocal effects of bending and torsion on springback during 3D bending of profiles. *Procedia Eng.*, 207, 2322-2327.
- Staupendahl, D., Schultz, D., Tekkaya, A.E., 2018a. Device for Tactile Detection and Analysis of the Geometry of Bent Profiles or Tubes. European patent EP 3 315 221 B1, priority date: 31.10.2016.
- Staupendahl, D., Tekkaya, A.E., 2018b. Mechanics of the reciprocal effects of bending and torsion during 3D bending of profiles. *Journal of Materials Processing Tech.*, 262, pp. 650–659
- Swift, H.W., 1952. Plastic instability under plane stress. *Journal of the Mechanics and Physics of Solids*, 1 (1), pp. 1-18.
- Tisza, M., Lukacs, Z., 2014. Springback analysis of high strength dual-phase steel. *Procedia Engineering*, 81, pp. 975-980.
- Torkabadi, A., Perdahcioğlu, E.S., van den Boogaard, A.H., 2017. Modelling of anelastic deformation in dual-phase steel for improved springback simulation. *Procedia Engineering*, 207, pp. 185-190.
- Ul Hassan, H., Maqbool, F., Güner, A., Hartmaier, A, Ben Khalifa, N., Tekkaya, A. E., 2015. Springback prediction and reduction in deep drawing under influence of unloading modulus degradation. *International Journal of Material Forming*. pp. 1-15.
- Vatter, P.H., Plettke, R., 2013. Process model for the design of bent 3-dimensional freeform geometries for the three-roll-push-bending process. *Procedia CIRP*, 7, pp. 240-245.

- VDI-Fachbereich Produktentwicklung und Mechatronik, 1993. VDI 2221:1993-05. Methodik zum Entwickeln und Konstruieren technischer Systeme und Produkte [Systematic Approach to the Development and Design of Technical Systems and Products]. Beuth Verlag, Berlin.
- VDI-Fachbereich Produktentwicklung und Mechatronik, 1998. VDI 2225 Blatt 3: 1998-11. Konstruktionsmethodik – Technisch-wirtschaftliches Konstruieren – Technisch-wirtschaftliche Bewertung [Design Engineering Methodics - Engineering Design at Optimum Cost - Valuation of Costs]. Beuth Verlag, Berlin.
- VDI-Fachbereich Produktionstechnik und Fertigungsverfahren. VDI 3431: 2016-08. Bending of profiles – Testing notes for profile bending elements. Beuth Verlag, Berlin.
- Vdovin, S. I., 1980. Berechnung der Rückfederung des Werkstoffs beim Biegen von Profilen mit Hilfe einer EDV-Anlage [Calculation of Material Springback During Bending of Profiles Using an EDP System]. In: Kuznecno-stampovocnoe proizvodstvo, 22 (7), pp. 22-24.
- Verma, R. K., Kuwabara T., Chung, K., Haldar A., 2011. Experimental evaluation and constitutive modeling of non-proportional deformation for asymmetric steels, International Journal of Plasticity, 27 (1), pp. 82-101.
- Viète, F., 1600. Apollonius Gallus, Seu, Exsuscitata Apollonii Pergaei Geometria [The French Apollonius or the Revival of Apollonian Geometry], David Leclerc, Paris.
- Voce, E., 1948. The relationship between stress and strain for homogeneous deformation. Journal of the Institute of Metals, 74, pp. 537-562.
- Walther, A., 1931. Der Kreis durch drei Punkte. Mathematische Zeitschrift, 33 (1), pp. 796-800.
- Wang, C., Kinzel, G., Altan, T., 1993. Mathematical modeling of plane-strain bending of sheet and plate. Journal of Material Processing Technology, 39, pp. 279-304.
- Weimar, G., 1966. Längsdehnungen und Verwerfungen beim Bandprofilwalzen (Walzprofilieren) [Longitudinal Strain and Warping During Roll Forming]. Dissertation, Technische Hochschule Hannover.
- Weinrich, A., 2015. Das Freibiegen mit inkrementeller Spannungsüberlagerung [Free Bbending with Incremental Stress Superposition]. Dissertation, Technische Universität Dortmund.
- Wiederhorn, S., Fields, R., Low, S., Bahng, G.-W., Wehrstedt, A., Hahn, J., Tomota, Y., Miyata, T., Lin, H., Freeman, B., Aihara, S., Hagihara, Y., Tagawa, T., 2006. Mechanical Properties. In: Czichos H., Saito, T., Smith, L. E. (Eds.), Springer

- Handbook of Materials Measurement Methods, Springer Handbooks, Springer, Berlin, Heidelberg, pp. 283-397.
- Yin, Q., Brosius, A., Tekkaya, A. E., 2011. Modified plane torsion tests for sheet metal characterization. *Steel research international*, Special Edition: 10th International Conference on Technology of Plasticity, ICTP 2011, 1, pp. 696-701.
- Yin, Q., 2014a. Verfestigungs- und Schädigungsverhalten von Blechwerkstoffen im ebenen Torsionsversuch [Strain Hardening and Damage Behavior of Metal Sheets in the In-Plane Torsion Test]. Dissertation, Technische Universität Dortmund.
- Yin, Q., Zillmann, B., Suttner, S., Gerstein, G., Biasutti, M., Tekkaya, A. E., Wagner, M. F.-X, Merklein, M., Schaper, M., Halle, T., Brosius, A., 2014b. An experimental and numerical investigation of different shear test configurations for sheet metal characterization. *International Journal of Solids and Structures*, 51 (5), pp. 1066-1074.
- Yin, Q., Soyarslan, C., Isik., K., Tekkaya, A. E., 2015. A grooved in-plane torsion test for the investigation of shear fracture in sheet materials. *International Journal of Solids and Structures*, 66, pp. 121-132.
- Yoshida, F., Uemori, T., Fujiwara, K., 2002. Elastic–plastic behavior of steel sheets under in-plane cyclic tension–compression at large strain. *International Journal of Plasticity*, 18 (5–6), pp. 633–659.
- Zillmann, B., Wagner, M. F.-X, Schmaltz, S., Schmidl, E., Lampke, T., Willner, K., Halle, T., 2015. In-plane biaxial compression and tension testing of thin sheet materials. *International Journal of Solids and Structures*, 66, pp. 111-120.

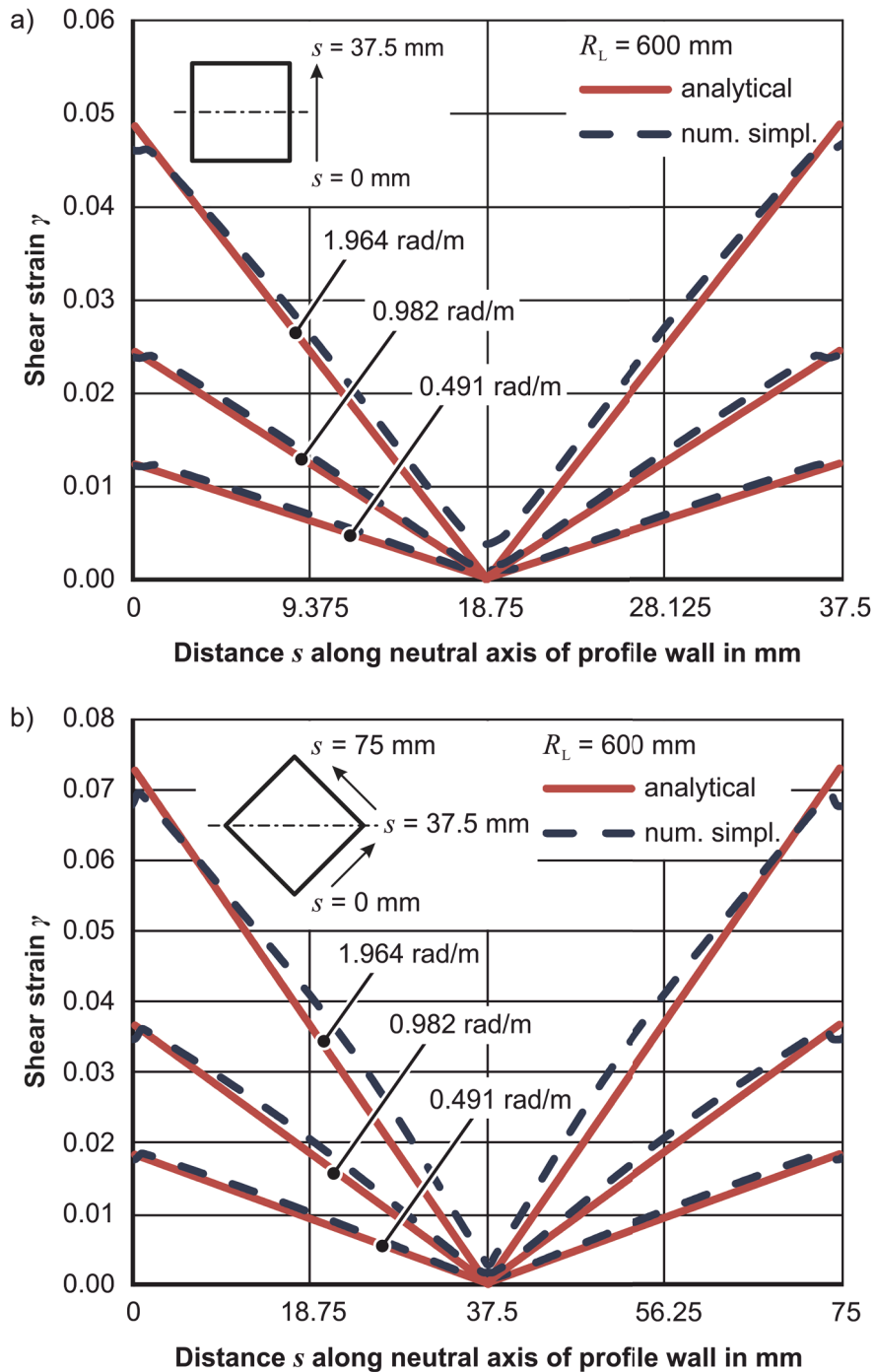
## Further reading

- Allister, W. D. Jr., 2003. *Materials Science and Engineering—An Introduction*, sixth ed., John Wiley, New York (NY), p. 139.
- Bhav Singh, B., Sivakumar, K., Balakrishna Bhat, T., 2009. Effect of cold rolling on mechanical properties and ballistic performance of nitrogen-alloyed austenitic steels, *International Journal of Impact Engineering*, 36 (4), pp. 611-620.
- Brooks, I., Lin, P., Palumbo, G., Hibbard, G. D., Erb, U., 2008. Analysis of hardness–tensile strength relationships for electroformed nanocrystalline materials, *Materials Science and Engineering: A*, 491 (1-2), pp. 412-419.
- Chattarji, P. P., 1958. Torsion of curved beams of rectangular cross-section having transverse isotropy. *ZAMM - Journal of Applied Mathematics and Mechanics*, 38 (3-4), pp.157-159.

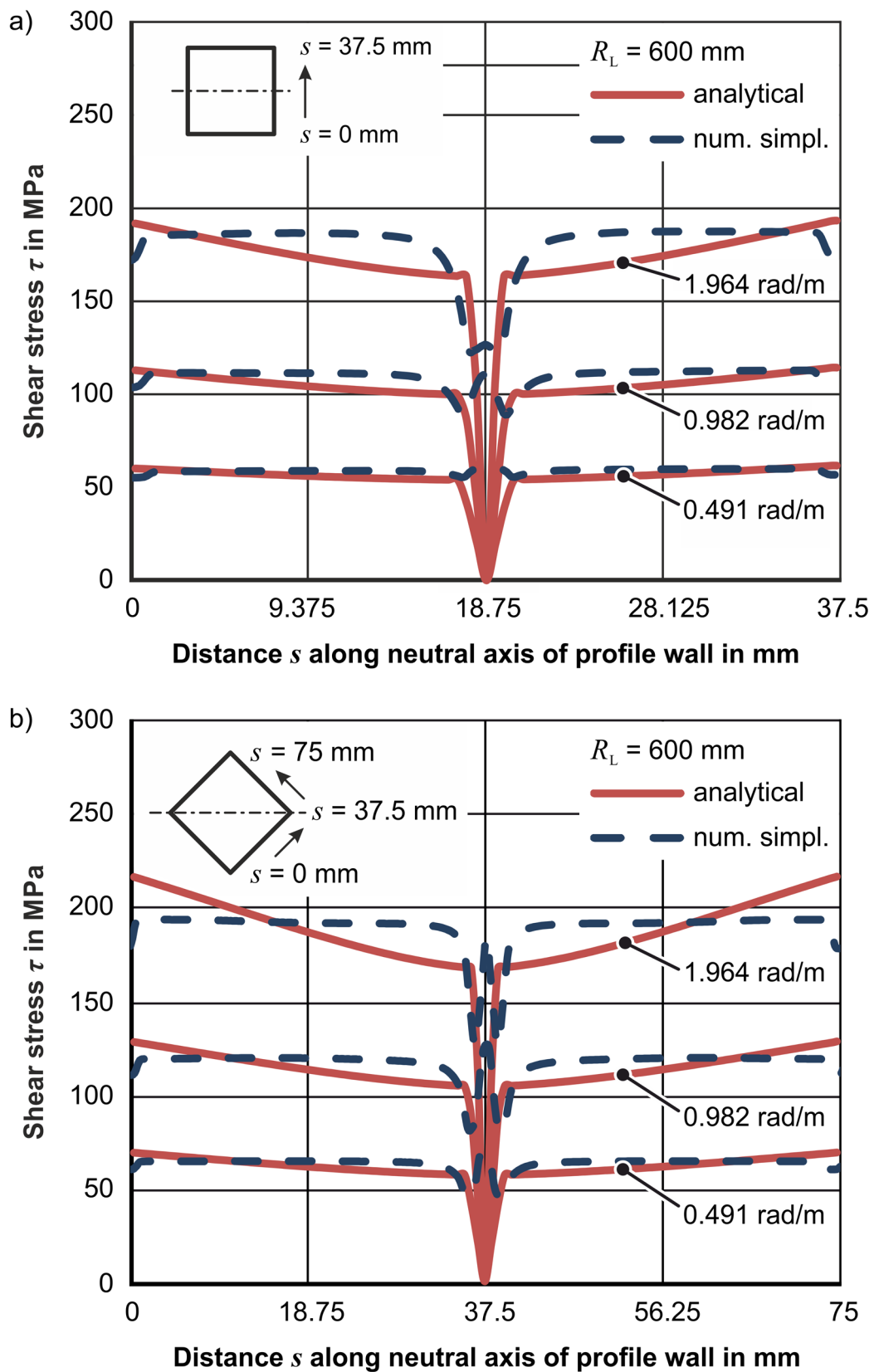
- Flinn, R.A., Trojan, P.K., 1986. *Engineering Materials and Their Applications*, third ed., Houghton Mifflin, Boston (MA), p. 84.
- Hedayati, A., Najafizadeh A., Kermanpur, A., Forouzan, F., 2010. The effect of cold rolling regime on microstructure and mechanical properties of AISI 304L stainless steel. *Journal of Materials Processing Technology*, 210 (8), pp. 1017-1022.
- Heymans, P., Heymans, W. J., 1925. The Torsion Problem of Curved Beams. In: *Proceedings of the National Academy of Sciences of the United States of America*, 11 (2), pp. 161-166.
- Hill, R., 1948. A theory of the yielding and plastic flow of anisotropic metals. In: *Proceedings of the Royal Society of London. Series A, Mathematical and Physical Sciences*, 193 (1033), pp. 281-297.
- Hill, R., 1990. Constitutive modelling of orthotropic plasticity in sheet metals. *Journal of the Mechanics and Physics of Solids*, 38 (3), pp. 405-417.
- Khodabakhshi, F., Haghshenas, M., Eskandari, H., Koohbor, B., 2015. Hardness–strength relationships in fine and ultra-fine grained metals processed through constrained groove pressing, *Materials Science and Engineering: A*, 636, pp. 331-339.
- Kreis, O., Hein, P., 2001. Manufacturing system for the integrated hydroforming, trimming and welding of sheet metal pairs. *Journal of Materials Processing Technology*, 115, pp. 49–54.
- Lung-Wen TSAI, 1999. *Robot Analysis: The Mechanics of Serial and Parallel Manipulators*. John Wiley & Sons Inc. New York, pp.151-154.
- Milad, M., Zreiba, N., Elhalouani, F., Baradai, C., 2008. The effect of cold work on structure and properties of AISI 304 stainless steel. *Journal of Materials Processing Technology*, 203 (1-3), pp. 80-85.
- Thile, J., 2009. Kosten Optimierung der Rohrleitungsfertigung - Wirtschaftlich denken heißt fortschrittlich messen [Cost Optimization of the Production of Tubular Structures- Thinking Economically Means Measuring Progressively]. *Inspect 11*, GIT VERLAG GmbH & Co. KG, Darmstadt, pp. 42-44.
- Van Vlack, L.H., 1975. *Elements of Materials Science and Engineering*, third ed., Addison-Wesley, Reading (MA), p. 9.
- Zhang, Z.K., Wu, J.J., Guo, R.C., Wang, M.Z., Li, F.F., Guo, S.C., Wang, Y.A., Liu, W.P., 2016. A semi-analytical method for the springback prediction of thick-walled 3D tubes. *Mater. Des.*, 99, pp. 57-67.

## Annex

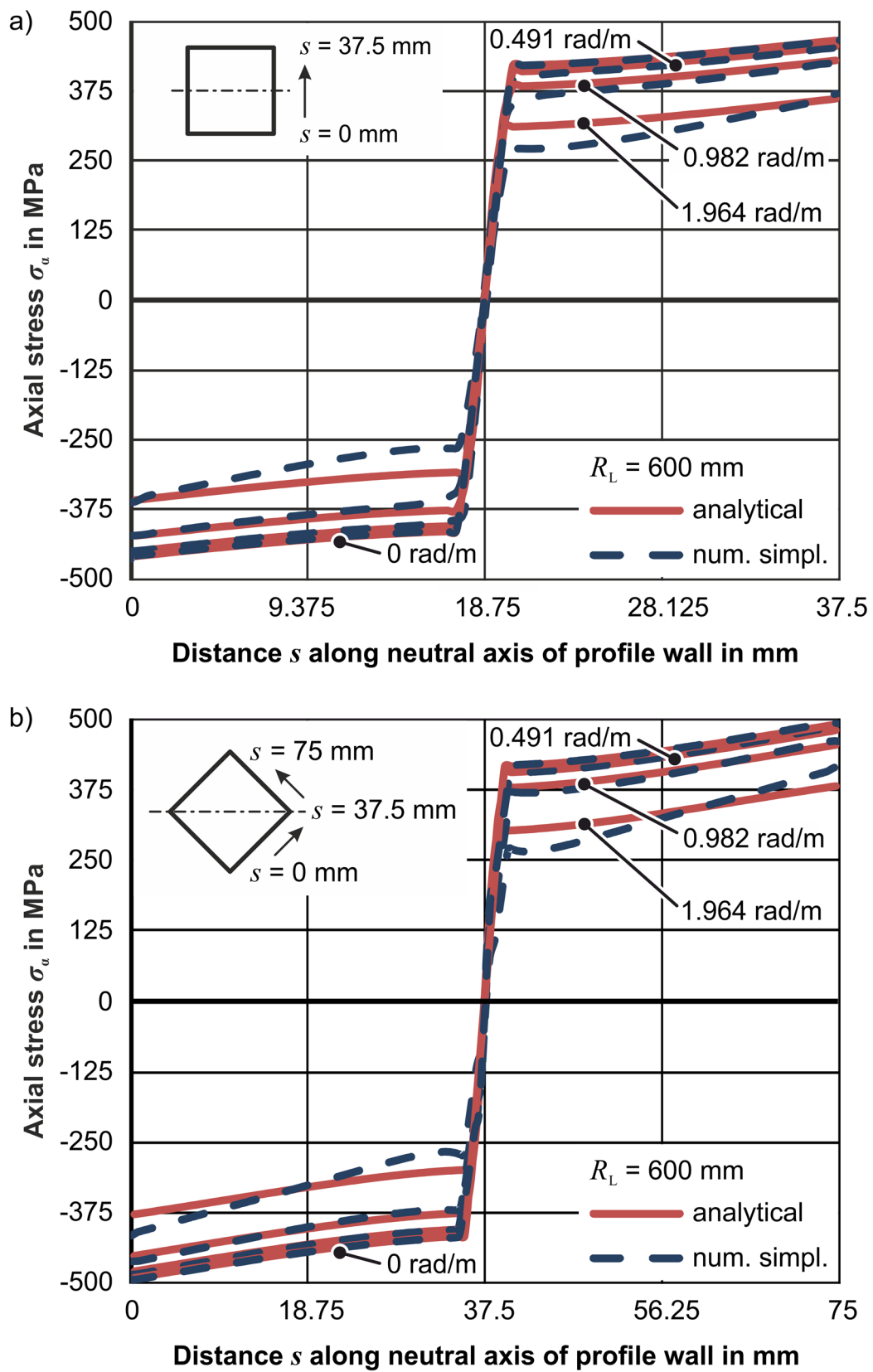
A.1 Comparison of analytically calculated shear strain, shear stress, and axial stress to numerical data, generated with the simplified numerical model introduced in Section 5.4.2, for  $R_L = 600$  mm and 800 mm at  $\theta = 0$  and  $\theta = \pi/4$



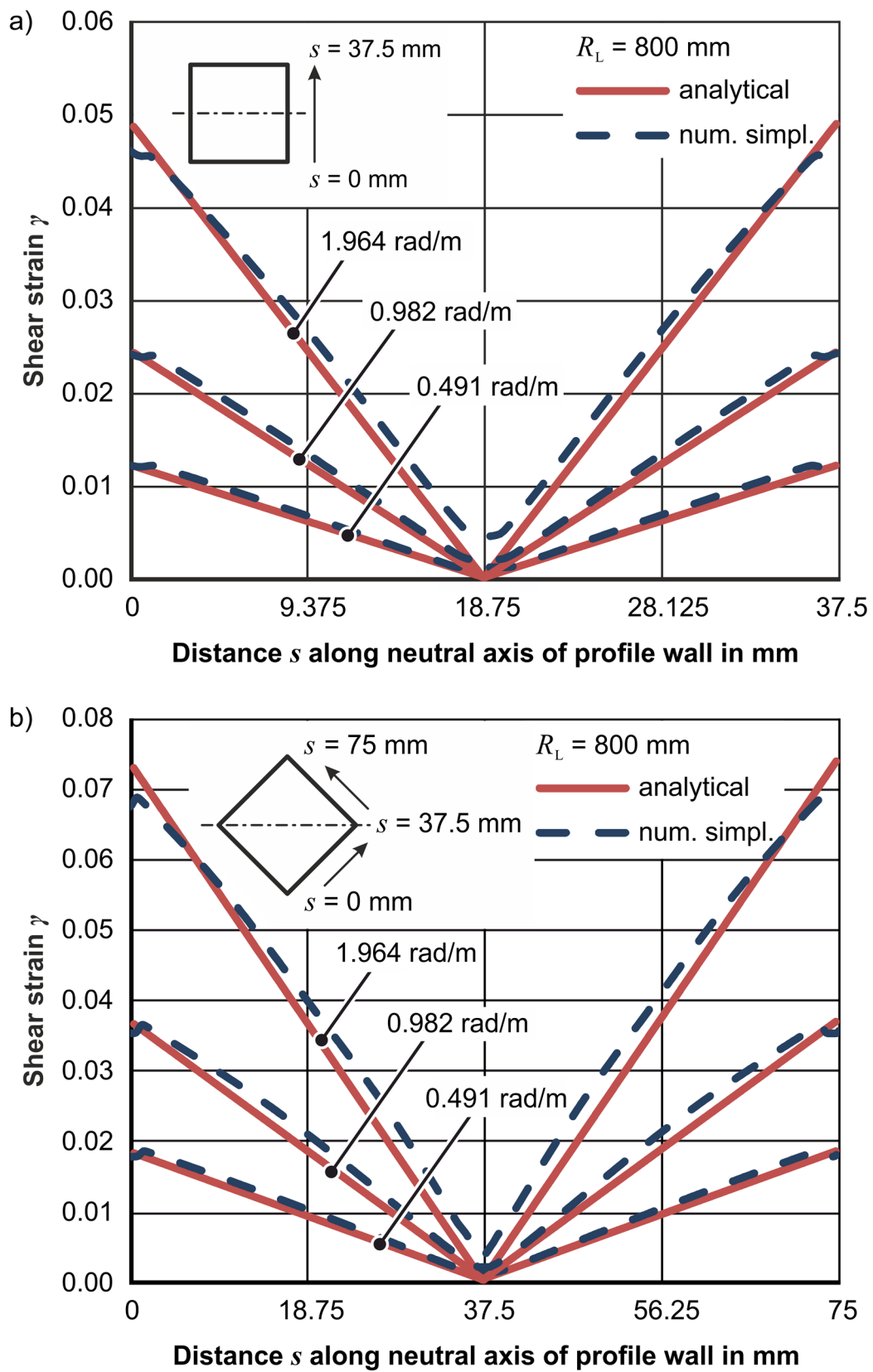
**Figure A.1:** Comparison of analytically calculated shear strain to numerically calculated shear strain for combined bending and torsion at  $\theta = 0$  (a) and  $\theta = \pi/4$  (b) for the material MW700L Z1



**Figure A.2:** Comparison of analytically calculated shear stress to numerically calculated shear stress for combined bending and torsion at  $\theta = 0$  (a) and  $\theta = \pi/4$  (b) for the material MW700L Z1

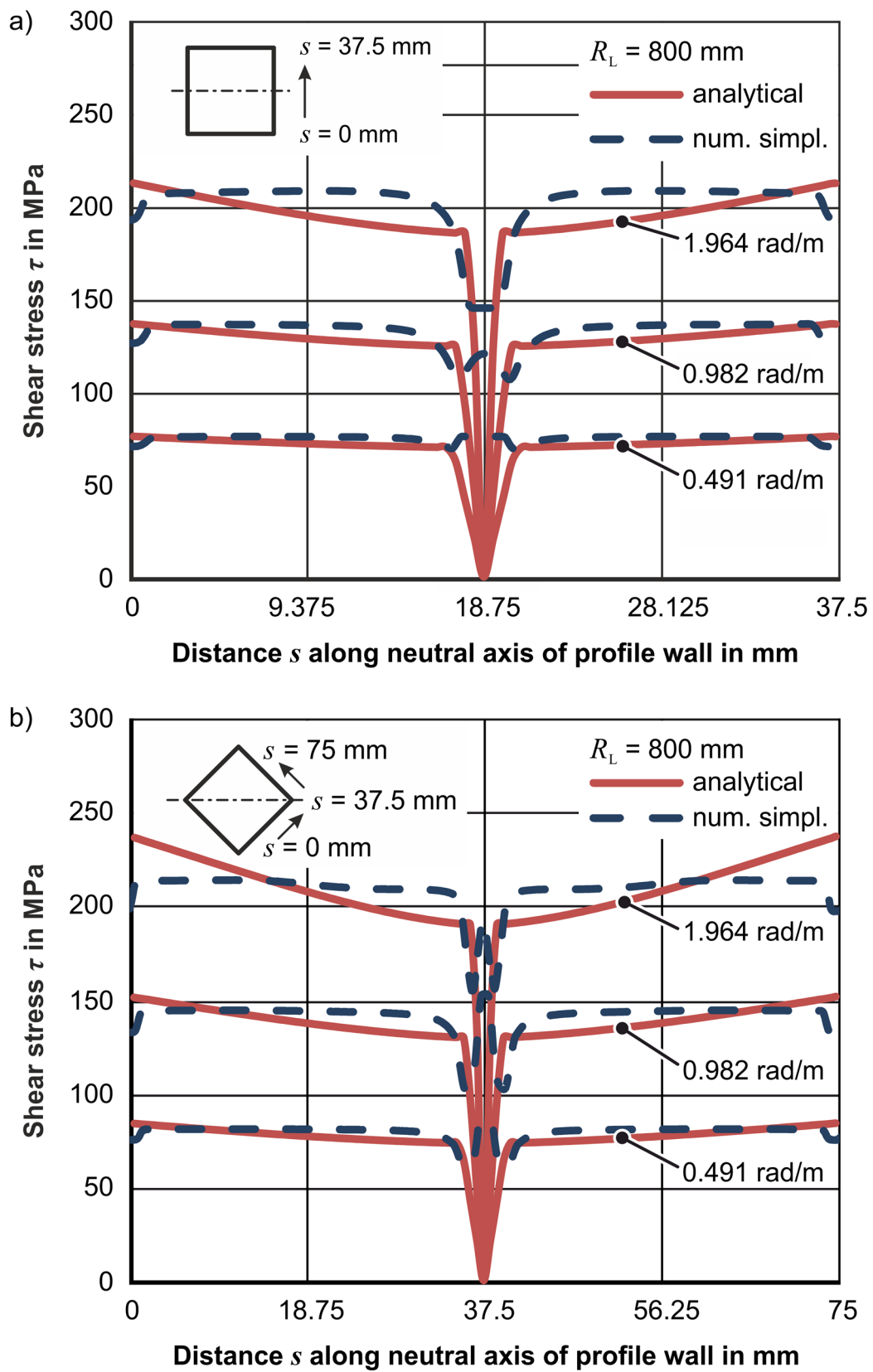


**Figure A.3:** Comparison of analytically calculated axial stress to numerically calculated axial stress for combined bending and torsion at  $\theta = 0$  (a) and  $\theta = \pi/4$  (b) for the material MW700L Z1

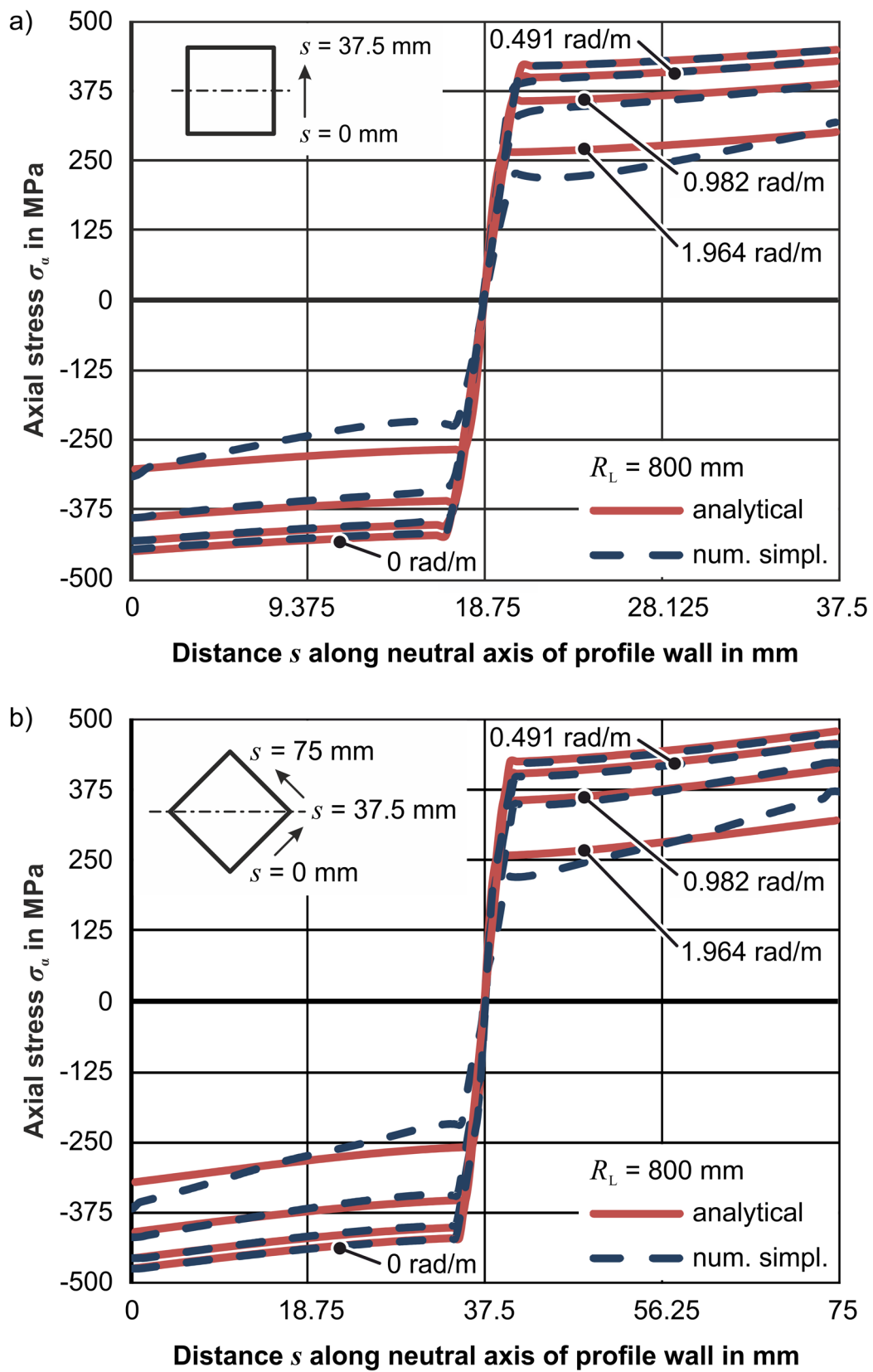


**Figure A.4:** Comparison of analytically calculated shear strain to numerically calculated shear strain for combined bending and torsion at  $\theta = 0$  (a) and  $\theta = \pi/4$  (b) for the material MW700L Z1





**Figure A.5:** Comparison of analytically calculated shear stress to numerically calculated shear stress for combined bending and torsion at  $\theta = 0$  (a) and  $\theta = \pi/4$  (b) for the material MW700L Z1



**Figure A.6:** Comparison of analytically calculated axial stress to numerically calculated axial stress for combined bending and torsion at  $\theta = 0$  (a) and  $\theta = \pi/4$  (b) for the material MW700L Z1

A.2 Comparison of the bending force and torque results from the comprehensive and simplified numerical model to the results from the analytical model with a uniform shear strain distribution over the cross-section (Saint-Venant) and the variable strain model derived in Section 7.3.2 at  $\theta = 0$

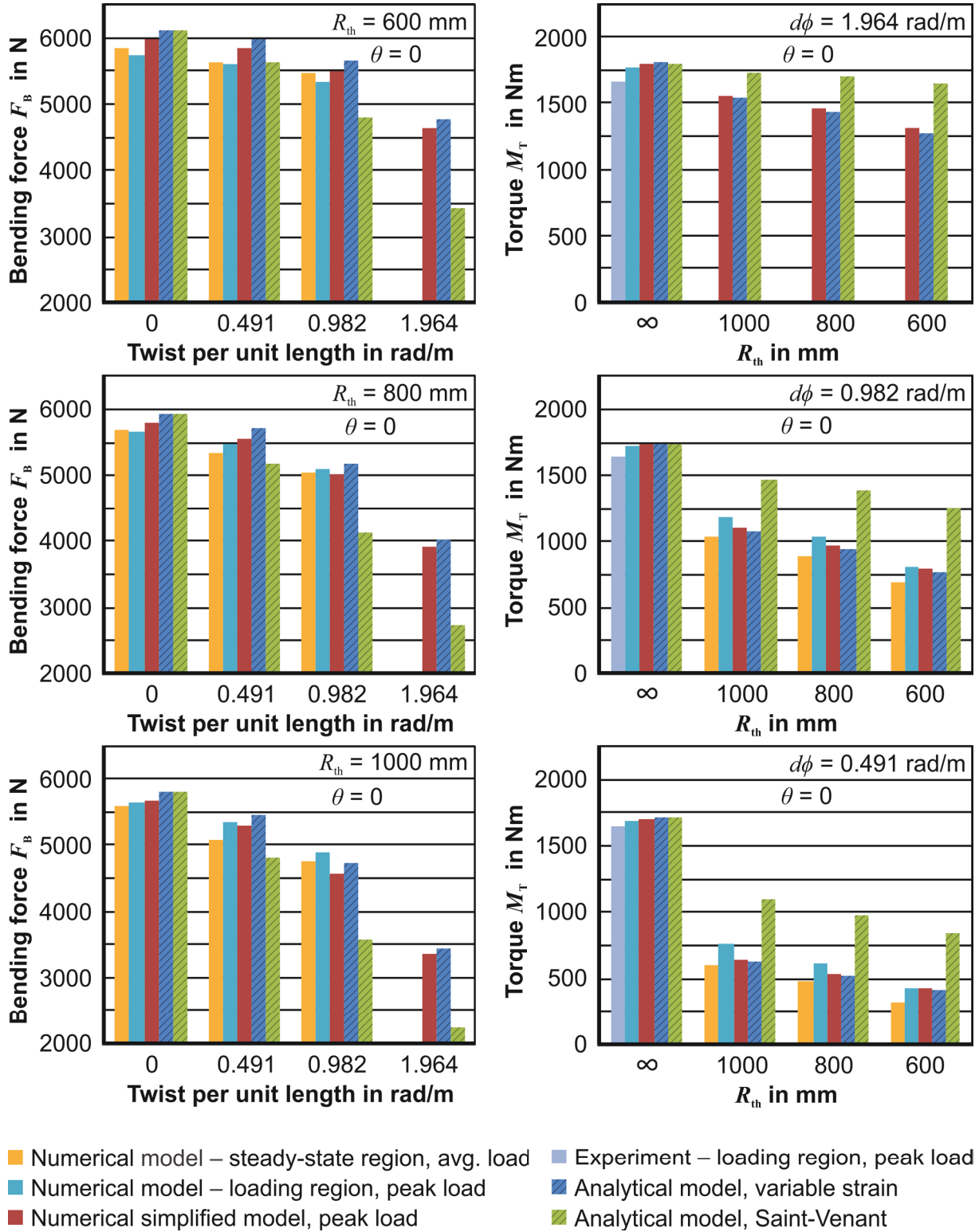


Figure A.7: Bending force and torque results for MW700L Z1 at  $\theta = 0$



# Curriculum vitae

## Personal details

Name: Daniel Staupendahl  
Date and place of birth: 13 August 1984 in Dortmund, Germany  
Nationality: German

## Professional experience

Since June 2019 Head of Research and Development, Erichsen GmbH & Co. KG, Hemer, Germany  
May 2018 – February 2019 Head of Project Planning, Institute of Forming Technology and Lightweight Components (IUL), Technische Universität Dortmund, Germany  
September 2013 – April 2018 Manager of the ReCIMP – Research Center for Industrial Metal Processing, IUL, Technische Universität Dortmund, Germany  
September 2009 – August 2013 Researcher at the IUL, Technische Universität Dortmund, Germany  
October 2007 – January 2008 Internship at ThyssenKrupp Ingeniería Chile, Santiago de Chile

## Education

October 2003 – September 2009 Study of mechanical engineering at the Technische Universität Dortmund, Germany  
Specialization: machine technology  
Degree: Diplom-Ingenieur  
1998 – 2002 The Woodlands High School, The Woodlands, Texas, USA  
Certificate: High School Diploma  
1994 – 1998 Phoenix-Gymnasium, Dortmund, Germany  
1990 – 1992 Deutsche Schule zu Johannesburg, South Africa



**Aus der Dortmunder Umformtechnik sind im Shaker Verlag bisher erschienen:**

- A. Adelhof: Komponenten einer flexiblen Fertigung beim Profilrunden.  
ISBN 3-86111-601-4
- G. Reil: Prozeßregelung numerisch gesteuerter Umformmaschinen mit Fuzzy Logic. ISBN 3-86111-862-9
- F. Maevus: Rechnerintegrierte Blechteilefertigung am Beispiel des Gesenkbiegens. ISBN 3-8265-0104-7
- R. Warstat: Optimierung der Produktqualität und Steigerung der Flexibilität beim CNC-Schwenkbiegen. ISBN 3-8265-1170-0
- H. Sulaiman: Erweiterung der Einsetzbarkeit von Gesenkbiegepressen durch die Entwicklung von Sonderwerkzeugen. ISBN 3-8265-1443-2
- Ch. Smatloch: Entwicklung eines numerisch einstellbaren Werkzeugsystems für das Tief- und Streckziehen. ISBN 3-8265-1465-3
- T. Straßmann: Prozeßführung für das Walzrunden auf der Basis Neuronaler Netze. ISBN 3-8265-1966-3
- L. Keßler: Simulation der Umformung organisch beschichteter Feinbleche und Verbundwerkstoffe mit der FEM. ISBN 3-8265-2256-7
- E. Szücs: Einsatz der Prozeßsimulation bei der Entwicklung eines neuen Umformverfahrens - der Hochdruckblechumformung. ISBN 3-8265-3119-1
- S. Chatti: Optimierung der Fertigungsgenauigkeit beim Profilbiegen.  
ISBN 3-8265-3534-0
- F. Haase: Eigenspannungen an dünnwandigen Bauteilen und Schichtverbunden. ISBN 3-8265-4312-2
- N. Austerhoff: Integrierte Produkt- und Prozeßgestaltung für die Herstellung von Blechbiegeteilen. ISBN 3-8265-6613-0
- D. Arendes: Direkte Fertigung gerundeter Aluminiumprofile beim Strangpressen. ISBN 3-8265-6442-1
- R. Kolley: Finite-Element-Simulation wirkmedienbasierter Blechumformverfahren als Teil einer virtuellen Fertigung. ISBN 3-8265-6566-5
- T. Weidner: Untersuchungen zu Verfahren und Werkzeugsystemen der wirkmedienbasierten Blechumformung. ISBN 3-8265-6602-5
- W. Homberg: Untersuchungen zur Hochdruckblechumformung und deren Verfahrenskomponenten. ISBN 3-8265-8684-0

M. Rohleder: Simulation rückfederungsbedingter Formabweichungen im Produktentstehungsprozess von Blechformteilen. ISBN 3-8265-9977-2

V. Hellinger: Untersuchungen zur Methodik der Berechnung und Herstellung von leichten Stützkernverbunden. ISBN 3-8322-0104-1

A. Klaus: Verbesserung der Fertigungsgenauigkeit und der Prozesssicherheit des Rundens beim Strangpressen. ISBN 3-8322-0208-0

B. Heller: Halbanalytische Prozess-Simulation des Freibiegens von Fein- und Grobblechen. ISBN 3-8322-0923-9

A. Wellendorf: Untersuchungen zum konventionellen und wirkmedienbasierten Umformen von komplexen Feinstblechbauteilen. ISBN 3-8322-2435-1

C. Klimmek: Statistisch unterstützte Methodenplanung für die Hochdruck-Blechumformung. ISBN 3-8322-2994-9

R. Krux: Herstellung eigenschaftsoptimierter Bauteile mit der Hochdruck-Blechumformung und Analyse der induzierten Eigenspannungen. ISBN 3-8322-3551-5

S. Jadhav: Basic Investigations of the Incremental Sheet Metal Forming Process on a CNC Milling Machine. ISBN 3-8322-3732-1

C. Beerwald: Grundlagen der Prozessauslegung und -gestaltung bei der elektromagnetischen Umformung. ISBN 3-8322-4421-2

A. Brosius: Verfahren zur Ermittlung dehnratenabhängiger Fließkurven mittels elektromagnetischer Rohrumformung und iterativer Finite-Element-Analysen. ISBN 3-8322-4835-8

R. Ewers: Prozessauslegung und Optimierung des CNC-gesteuerten Formdrückens. ISBN 3-8322-5177-4

T. Langhammer: Untersuchungen zu neuen Konzepten für PKW-Kraftstoffbehälter. ISBN 3-8322-5300-9

M. Schikorra: Modellierung und simulationsgestützte Analyse des Verbundstrangpressens. ISBN 3-8322-5506-0

M. Schomäcker: Verbundstrangpressen von Aluminiumprofilen mit endlosen metallischen Verstärkungselementen. ISBN 978-3-8322-6039-2

N. Ridane: FEM-gestützte Prozessregelung des Freibiegens. ISBN 978-3-8322-7253-1

R. Shankar: Surface Reconstruction and Tool Path Strategies for Incremental Sheet Metal Forming. ISBN 978-3-8322-7314-9



- U. Dirksen: Testumgebung für Prozessregelungen zum Drei-Rollen-Profilbiegen mit virtuellem und realem Biegeprozess.  
ISBN 978-3-8322-7673-7
- D. Risch: Energietransfer und Analyse der Einflussparameter der formgebundenen elektromagnetischen Blechumformung.  
ISBN 978-3-8322-8360-5
- M. Marré: Grundlagen der Prozessgestaltung für das Fügen durch Weiten mit Innenhochdruck. ISBN 978-3-8322-8361-2
- D. Becker: Strangpressen 3D-gekrümmter Leichtmetallprofile.  
ISBN 978-3-8322-8488-6
- V. Psyk: Prozesskette Krümmen - Elektromagnetisch Komprimieren - Innenhochdruckumformen für Rohre und profilmäßige Bauteile.  
ISBN 978-3-8322-9026-9
- M. Trompeter: Hochdruckblechumformung großflächiger Blechformteile.  
ISBN 978-3-8322-9080-1
- H. Karbasian: Formgenauigkeit und mechanische Eigenschaften pressgehärteter Bauteile. ISBN 978-3-8322-9250-8
- M. J. Gösling: Metamodell unterstützte Simulation und Kompensation von Rückfederungen in der Blechumformung. ISBN 978-3-8322-9355-0
- H. Pham: Process Design for the Forming of Organically Coated Sheet Metal.  
ISBN 978-3-8440-0309-3
- B. Rauscher: Formschlüssig verbundene Metall-Kunststoff-Hybridbauteile durch Integration von Blechumformung und Spritzgießen.  
ISBN 978-3-8440-0655-1
- T. Cwiekala: Entwicklung einer Simulationemethode zur zeiteffizienten Berechnung von Tiefziehprozessen.  
ISBN 978-3-8440-0701-5
- M. Hermes: Neue Verfahren zum rollenbasierten 3D-Biegen von Profilen.  
ISBN 978-3-8440-0793-0
- N. Ben Khalifa: Strangpressen schraubenförmiger Profile am Beispiel von Schraubenrotoren.  
ISBN 978-3-8440-0969-9
- J. Kolbe: Thermisch beschichtete, faserverstärkte Polymerwerkzeuge für die Umformung höherfester Blechwerkstoffe.  
ISBN 978-3-8440-1353-5

L. Kwiatkowski: Engen dünnwandiger Rohre mittels dornlosen Drückens.  
ISBN 978-3-8440-1381-8

T. Kloppenborg: Analyse- und Optimierungsmethoden für das  
Verbundstrangpressen.  
ISBN 978-3-8440-1384-9

A. Schuster: Charakterisierung des Faserverlaufs in umgeformten Stählen  
und dessen Auswirkung auf mechanische Eigenschaften.  
ISBN 978-3-8440-1581-2

A. Jäger: Strangpressen von Aluminiumprofilen mit prozessintegrierter  
umformtechnischer Weiterverarbeitung.  
ISBN 978-3-8440-1654-3

M. M. Hussain: Polymer Injection Sheet Metal Forming – Experiments and  
Modeling.  
ISBN 978-3-8440-2041-0

M. S. Aydın: Efficient Parameter Characterization for Hardening and Yield Lo-  
cus Models for Sheet Metals.  
ISBN 978-3-8440-2118-9

A. Canpolat: Experimentelle und numerische Bewertung der  
Fließortbestimmung mittels Kreuzzugversuch.  
ISBN 978-3-8440-2126-4

V. Güley: Recycling of Aluminum Chips by Hot Extrusion.  
ISBN 978-3-8440-2476-0

D. Pietzka: Erweiterung des Verbundstrangpressens zu höheren  
Verstärkungsanteilen und funktionalen Verbunden.  
ISBN 978-3-8440-2538-5

M. Haase: Mechanical Properties Improvement in Chip Extrusion with  
Integrated Equal Channel Angular Pressing.  
ISBN 978-3-8440-2571-2

Q. Yin: Verfestigungs- und Schädigungsverhalten von Blechwerkstoffen im  
ebenen Torsionsversuch.  
ISBN 978-3-8440-2839-3

C. Becker: Inkrementelles Rohrumformen von hochfesten Werkstoffen.  
ISBN 978-3-8440-2947-5

R. Hölker: Additiv hergestellte Werkzeuge mit lokaler Innenkühlung zur  
Produktivitätssteigerung beim Aluminium-Strangpressen.  
ISBN 978-3-8440-3149-2

C. Weddeling: Electromagnetic Form-Fit Joining.  
ISBN 978-3-8440-3405-9

A. Güner: In-situ stress analysis with X-ray diffraction for yield locus  
Determination.  
ISBN 978-3-8440-3414-1

A. Güzel: Microstructure Evolution during Thermomechanical Multi-Step  
Processing of Extruded Aluminum Profiles.  
ISBN 978-3-8440-3428-8

S. Hänisch: Verzugsanalyse kaltmassivumgeformter und wärmebehandelter  
Bauteile.  
ISBN 978-3-8440-3761-6

A. Foydl: Strangpressen partiell verstärkter Aluminiumprofile.  
ISBN 978-3-8440-3875-0

A. Weinrich Mora: Das Freibiegen mit inkrementeller Spannungsüberlagerung.  
ISBN 978-3-8440-4221-4

S. Cai: Tailored and double-direction pressure distributions for vaporizing-foil  
Forming.  
ISBN 978-3-8440-4255-9

G. Sebastiani: Erweiterung der Prozessgrenzen inkrementeller Blechumform-  
verfahren mittels flexibler Werkzeuge.  
ISBN 978-3-8440-4359-4

C. Pleul: Das Labor als Lehr-Lern-Umgebung in der Umformtechnik.  
Entwicklungsstrategie und hochschuldidaktisches Modell.  
ISBN 978-3-8440-4569-7

H. Hassan: Springback in deep drawing – Accurate prediction and reduction.  
ISBN 978-3-8440-4924-4

L. Chen: An Investigation of Failure Mechanisms in Forming of Monolithic and  
Composite Sheets.  
ISBN 978-3-8440-5168-1

L. Hiegemann: Glattwalzen beschichteter Oberflächen.  
ISBN 978-3-84440-5419-4

G. Georgiadis: Hot stamping of thin-walled steel components.  
ISBN 978-3-8440-5435-4

S. P. Afonichev: Numerische Simulation der Umformung von  
Sandwichblechen unter Berücksichtigung großer Krümmungen.  
ISBN 978-3-8440-5471-2

- D. May: Globally Competent Engineers. Internationalisierung der Ingenieurausbildung am Beispiel der Produktionstechnik.  
ISBN 978-3-8440-5615-0
- H. Chen: Granular medium-based tube press hardening.  
ISBN 978-3-8440-5701-0
- G. Grzanic: Verfahrensentwicklung und Grundlagenuntersuchungen zum Inkrementellen Profilverfahren.  
ISBN 978-3-8440-5889-5
- S. Alkas Yonan: Inkrementelle Kaltumformung von Thermoplasten.  
ISBN 978-3-8404-6026-3
- P. Sieczkarek: Inkrementelle Blechmassivumformung.  
ISBN 978-3-8440-6118-5
- S. Ossenkemper: Verbundfließpressen in konventionellen Fließpresswerkzeugen.  
ISBN 978-3-8440-6175-8
- K. Isik: Modelling and characterization of damage and fracture in sheet-bulk metal forming.  
ISBN 978-3-8440-6278-6
- S. Gies: Thermische Spulenverluste bei der elektromagnetischen Blechumformung.  
ISBN 978-3-8440-6468-1
- C. H. Lötters: Temperaturunterstütztes Biegen und Wärmebehandeln in mehrstufigen Werkzeugen.  
ISBN 978-3-8440-6485-8
- J. Lueg-Althoff: Fügen von Rohren durch elektromagnetische Umformung – Magnetpulsschweißen.  
ISBN 978-3-8440-6558-9
- C. Dahnke: Verbundstrangpressen adaptiver Leichtbaukomponenten aus Aluminium und Formgedächtnislegierungen.  
ISBN 978-3-8440-6630-2
- O. K. Demir: New test and interpretation of electromagnetic forming limits of sheet metal.  
ISBN 978-3-8440-6986-0
- M. Schwane: Entwicklung und Eigenschaften von Längspressnähten beim Aluminiumstrangpressen.  
ISBN 978-3-8440-6994-5

R. Meya: Schädigungskontrolliertes Blechbiegen mittels  
Druckspannungsüberlagerung.  
ISBN 978-3-8440-7510-6

O. Hering: Schädigung in der Kaltmassivumformung: Entwicklung,  
Auswirkungen und Kontrolle.  
ISBN 978-3-8440-7525-0

H. Traphöner: Erweiterung der Anwendungsgrenzen des ebenen  
Torsionsversuchs.  
ISBN 978-3-8440-7737-7

O. Napierala: Tiefzieh-Verbundfließpressen: Analyse, Bauteileigenschaften  
und Potentiale.  
ISBN 978-3-8440-7856-5

S. Wernicke: Inkrementelle Blechmassivumformung belastungsangepasster  
Funktionsbauteile.  
ISBN 978-3-8440-7980-7